DESIGN, SYNTHESIS AND CHARACTERIZATION OF THIAZOLE-BASED CONJUGATED POLYMERS AND THEIR APPLICATIONS TO *N*-CHANNEL ORGANIC ELECTRONICS

A Dissertation
Presented to
The Academic Faculty

by

Zhibo Yuan

In Partial Fulfillment
of the Requirements for the Degree
Doctor of Philosophy in the
School of Chemistry and Biochemistry

Georgia Institute of Technology
December 2018

DESIGN, SYNTHESIS AND CHARACTERIZATION OF THIAZOLE-BASED CONJUGATED POLYMERS AND THEIR APPLICATIONS TO *N*-CHANNEL ORGANIC ELECTRONICS

Approved by:

Dr. Elsa Reichmanis, *Professor*, Advisor
School of Chemical & Biomolecular Engineering
Georgia Institute of Technology

Dr. Charles Liotta, *Professor*
School of Chemistry and Biochemistry
Georgia Institute of Technology

Dr. David Collard, *Professor*
School of Chemistry & Biochemistry
Georgia Institute of Technology

Dr. Stefan France, *Professor*
School of Chemistry & Biochemistry
Georgia Institute of Technology

Dr. Natalie Stingelin, *Professor*
School of Material Sciences and Engineering
Georgia Institute of Technology

Date Approved: October 25, 2018

Dedication

I dedicate this thesis to my dearest parents, Mr. Yuan, Peizheng and Ms. Lei, Huamin!

ACKNOWLEDGEMENTS

The Ph.D. training at Georgia Institute of Technology for the past 5 years is a truly valuable, memorable, and pleasant journey for me. This experience improved my insight, capability, confidence, and courage of discovering, thinking and resolving challenges not only in scientific research and development, but also in my entire life.

Herein, I would like to firstly give thanks to my advisor, Prof. Elsa Reichmanis. It was my great honor and pleasure to join Prof. Reichmanis' research group and to be her student over the past five years. During these five years, I received an enormous amount of encouragement, guidance, and kind advice from her, both in my academic life and personal life. Prof. Reichmanis is not only an innovative, knowledgeable, and insightful scholar, but also a patient, friendly, and helpful mentor whom people enjoy and love to work with. Countless times can I remember as I sought for help from her, and I have never left without her valuable guidance and a "can-do" attitude. I would not have been able to finish my Ph.D. without her guidance!

I would like to also express my sincere thanks to Prof. Charles Liotta, Prof. David Collard, Prof. Stefan France, and Prof. Natalie Stingelin for agreeing to be in my thesis committee. I have learned a lot in my studies of organic and polymeric syntheses, fundamentals of physical organic chemistry, organic electronics, as well as journal publication writings. I had an enjoyable time of working with them and their research group members; and gained significant amount of guidance and help from them. In addition, I would like to thank Prof. Jean-Luc Brédas, Prof. John Reynolds and Prof. Seth Marder for

their great guidance, help, and comments on developing my knowledge in polymer chemistry and physical organic chemistry.

I truly appreciate our group members and lab-mates, especially Dr. Boyi Fu, Dr. Guoyan Zhang, Dr. Ping-Hsun Chu, Dr. Nabil Kleinhenz, Dr. Dalsu Choi, Dr. Yo-Han Kwon, Dr. Rui Chang, Carolyn Buckley, Giovanni DeLuca, Mike McBride, and Brian Khau. Also, I would like to thank the undergraduate researchers who worked with me: Yundi Jiang, Harrison Kreafle, Lauren Lopez, Amanda Tonnaer, Chase Eckert Neal Patel, Chaker Fares, Qianyi "Beth" Qu, Kyle Hamrock, and Kristina Marquardt for their excellent and dedicated work. It has been a wonderful time of working with them during the past few years in our lab.

I also would like to gratefully acknowledge all our collaborators and people who provided us help and guidance in our research, especially Prof. Jean-Luc Brédas, Prof. Carlos Silva, and Prof. Dennis Hess. Special thanks to Prof. E. Kent Barefield at Georgia Tech and Prof. Harry Gray at Caltech (fellow Western Kentucky University alumni! Go Hilltoppers!) and Dr. Rui Zhang from Western Kentucky University for their inspirations and encouragements early in my Ph.D. studies. It was my great fortune to work with and share my thoughts amongst these innovative, insightful and helpful scholars, who truly are real life role models that I look up to. Also, my gratitude goes to my fellow colleagues: Dr. Simil Thomas, Dr. Ilaria Bargigia, Dr. Siyuan Zhang, Dr. Gang Wang, Dr. Brian Schmatz, who made this ride much more enjoyable.

Furthermore, I would like to thank my friends, Zhixian He, Dr. Huayu Li, Dr. Chong Han, Dr. Zhen Huang, Dr. Zhanjun Guo, Rui Chen, Hongduo Zhou, Eric Vanover, Yutong Wu, and Haochen Yang, who helped me in many different ways during my Ph.D.

studies. Our friendship will be something I cherish for life. Special thanks goes to Zhixian and Rui for their excellent graphic designs for illustrations in my publications and my thesis!

My Ph.D. research was funded in part by the National Science Foundation (DMR-1507205), the Georgia Institute of Technology, and the Center for Science and Technology of Advanced Materials and Interfaces (STAMI) Fellowship at Georgia Tech. GIWAXS measurements were carried out at Stanford Linear Accelerator Center. Special thanks to Dr. Mike Toney and Dr. Stefan Oosterhout for providing their assistance at Stanford University.

Last, but not the least, I would reserve my deepest gratitude to my dearest family, especially to my parents and my grandparents. I appreciate all their contributions and sacrifices to my entire life. I feel so loved, supported and fortunate to have such wonderful families, and I just could not ask for more! During the ten long years of seemingly endless pursue of knowledge in the United States, my family, in particularly my parents, supported me both financially and mentally in every way possible. Bearing the pain of missing their only child, my parents still encourage me to keep going forward in my life, and constantly remind me to become a righteous, kind, and honest person. I always naturally miss them whenever I enjoy the happiness or encounter difficulties. I dedicate my Ph.D. dissertation to my dearest parents and family.

TABLE OF CONTENTS

ACKNOWLEDGEMENTS iv

LIST OF TABLES v

LIST OF SCHEMES vi

LIST OF FIGURES vii

LIST OF SYMBOLS AND ABBREVIATIONS xvi

SUMMARY xviii

CHAPTER 1. Introduction 1

1.1 Organic and Polymer Semiconductors 1

1.2 *n*-Channel Polymer Semiconductors 6

1.3 Thiazoles and Thiazole-based Conjugated Polymers 9

1.4 Charge Transport in Polymer Semiconductors 11

1.5 Organic Field-Effect Transistors (OFETs) 14

1.6 OFET Device Fabrication and Processing 15

1.6.1 OFET Device Structure and Properties 15

1.6.2 Dielectric materials for OFETs 23

1.6.3 Organic and Polymeric Semiconductor Thin-Film Deposition 25

CHAPTER 2. Design, Synthesis and Characterization of Diketopyrrolopyrrole-Thiazole All-Acceptor (A-A) *n*-channel Polymeric Semiconductors and Applications in OFETs 29

2.1 Abstract 29

2.2 Introduction 30

2.3 Results and Discussions 31

2.3.1 Synthesis and Characterizations of **PDPP2Tz** and **PDPP4Tz** 31

2.3.2 **PDPP4Tz** Photophysical Properties 36

2.3.3 DFT Studies of **PDPP4Tz** oligomers and their subunits 39

2.3.4 **PDPP4Tz** Thin-film Morphology and Crystallinity 44

2.3.5 Thiazole-DPP A-A Copolymers for OFET Applications 47

2.4 Conclusion 51

CHAPTER 3. Design, Synthesis and Characterization of Naphthalene Diimide-Thiazole *n*-channel Polymeric Semiconductors and Applications in OFETs 53

3.1 Abstract 53

3.2 Introduction 54

3.3 Results and Discussion 55

3.3.1 Synthesis and Characterization of **PNDI2Tz** 55

3.3.2 Photophysical properties of **PNDI2Tz** 57

3.3.3 **PNDI2Tz** Electrochemical Properties 61

3.3.4 Computational Modeling 62

3.3.5 Thin-film morphology and solid-state crystallinity 65

3.3.6 Charge Transport Performance 67

3.4 Conclusion 70

CHAPTER 4. Nanofiber formation in Naphthalene Diimide-Thiazole based conjugated polymer OFETs via Dielectric Surface Processing 71

4.1 Abstract 71

4.2 Introduction 72

4.3 Results and Discussions 74

4.3.1 Semiconducting polymer synthesis 74

4.3.2 Dielectric layer processing 75

4.3.3 Polymer thin-film microstructures and morphology 77

4.3.4 **PNDI2Tz** Charge Transport Performance 81

4.3.5 Process Versatility-comparison with benchmark D-A conjugated polymers 83

4.3.6 Nanofiber Formation and Charge Transport 85

4.4 Conclusion 90

CHAPTER 5. Thiazole-Naphthalene Diimide Conjugated Polymers for Acid Sensing Applications 91

5.1 Abstract 91

5.2 Introduction 91

5.3 Experimental 93

5.3.1 Materials and Measurements 93

5.3.2 UV-vis Measurements 95

5.3.3 Thin Film Preparation and Device fabrication 97

5.4 Results and Discussion 98

5.4.1 **PNDI2Tz** Halochromism in Solution 99

5.4.2 BF_3 Interaction with **PNDI2Tz** in Solid State 103

5.4.3 **PNDI2Tz** OFET for BF_3 sensor 105

5.5 Conclusion 108

CHAPTER 6. Conclusions 109

CHAPTER 7. Future work 112

7.1 Structure-Property Relationship Study: Impacts of Thiazole/Thiophene on Diketopyrrolopyrrole Polymeric Semiconductor Fundamentals and Performance to Their Applications in OFETs 112

7.2 Investigation of Dielectric Layer Processing and Molecular Interactions at Interfaces and their Impacts to OFET Performance 116

7.3 Thiazole-based Conjugated Polymers for Metal Ion Sensor Applications 117

APPENDIX. SYNTHESIS DETAILS 121

REFERENCES 145

LIST OF TABLES

Table 2.1. Calculated valence band (VB) width, conduction band (CB) width, band gap, and hole and electron effective masses for the **PDPP4Tz** polymer. 41

Table 2.2. Electron transport properties of **PDPP4Tz** fabricated on bottom-gate-bottom-contact OFETs 50

Table 4.1. Electron transporting properties of **PNDI2Tz** based OFET devices fabricated under high temperature blade coating conditions on processed wafer devices. 80

Table 4.2. OFET performances of **PDPP4T** and **N2200** under proposed blade coating conditions (same as the highest performing condition in **Table 4.1**). 84

Table 7.1. Chloroform gel permeation chromatography (GPC) results of DPP-thiazole/thiophene polymers. 113

Table 7.2. Photophysical characteristics of **PDPP4T (P1)**, **PDPP2Tz2T (P2)** and **PDPP2T2Tz (P3)**. 114

LIST OF SCHEMES

Scheme 2.1. Stille polymerization of monomer DTzDPP with hexamethylditin or 5,5'-bis(trimethylstannyl)-2,2'-bithiazole to afford **PDPP2Tz** and **PDPP4Tz**, respectively. 33

Scheme 3.1. Synthesis of poly(2,7-bis(2-decyltetradecyl)-4-methyl-9-(5'-methyl-[2,2'-bithiazol]-5-yl)benzo[lmn][3,8]phenanthroline-1,3,6,8(2H,7H)-tetraone) (**PNDI2Tz**). 54

Scheme 7.1. Proposed **PNDI2Tz**-based conjugated polymer and fluoro- surface modifiers. 116

LIST OF FIGURES

Figure 1.1. Applications based on organic semiconductors.[34-36] 1

Figure 1.2. Schematic representation of both intermolecular and intramolecular charge transport pathways in donor-acceptor (D-A) conjugated polymers. 3

Figure 1.3. Typical electron rich (top) and electron deficient (bottom) organic semiconductor building blocks for *p*-channel and *n*-channel organic. 4

Figure 1.4. Examples of conjugated polymers utilized the concept of side-chain engineering.[81-83] 6

Figure 1.5. Design principles of DPP-based and NDI-based polymers. 8

Figure 1.6. Visualization of nitrogen lone pair and carbon–sulfur antibonding orbitals. Reprinted with permission. Reprinted from Chem. Mater. **2013**, 25, 4239. Copyright 2013 American Chemical Society. 10

Figure 1.7. Schematic representation of four OFET architectures. 16

Figure 1.8. Schematic representation of OFET working mechanism and the effect of gate voltage (V_G) on charge injection into organic/polymeric semiconductors. ... 17

Figure 1.9. (a) Three-dimensional structure of bottom contact bottom gate OFET showing definition of channel dimensions. (b, c, d) Schematic representation of linear regime with $V_D << V_G - V_{th}$ (b), the onsite of saturation regime with $V_{D,sat} = V_G - V_{th}$, where the pitch-off point exhibits at drain electrode (c); and saturation regime with $V_{(x)} = V_G - V_{th}$, at which $V_D > V_{D,sat}$ (d), respectively. Figure

reprinted with permission from *Chem. Mater., Vol. 16, No. 23,* **2004,** 4437-4439. Copyright 2004 American Chemical Society. 18

Figure 1.10. Schematic representation of self-assembly monolayer (SAM) functionalization to SiO_2 surface. 23

Figure 1.11. (a) Schematic illustration of the charge transport model in lamellae stacking conjugated polymer; (b) face-on texture of polymeric crystallites; (c) edge-on stacking texture, the π-stacking and the chain to chain packing of polymers. Reprinted with permission from *Mater. Today.* **2007**, 10 (3), 38-45. Copyright **2007** Elsevier. 25

Figure 2.1. Comparison of 2,2'-bithiazole and 2,2'-bithiophene in HOMO energy level and molecular geometry. 32

Figure 2.2. Gel permeation chromatography (GPC) characterization of **PDPP4Tz** with TCB under 135 °C. 34

Figure 2.3. (top) TGA of polymer **PDPP4Tz** in a nitrogen atmosphere (25 mL/min) at a heating rate of 5 °C/min; (bottom) thermal transition characterization of **PDPP4Tz**. DSC characterization was based on the 2nd heating and cooling process in a nitrogen atmosphere with a nitrogen flow rate of 50 mL/min and a heating/cooling rate of 5 °C/min. 35

Figure 2.4. UV-*vis* absorption spectra of **PDPP4Tz** in solution and thin-film state (1×10^{-6} M; chloroform, *p*-xylene). Film UV-*vis* spectra were obtained by spincoating solutions onto UV-ozone cleaned SiO_2 slides before thermal annealing. 37

Figure 2.5. (left) UPS characterization of as-spun **PDPP4Tz** film on gold-coated Si wafer; (right) zoomed-in of lower binding energy region of the UPS spectrum. 38

Figure 2.6. (a) Illustration of the torsion potentials related to the rotation of the adjacent units in the monomer of **PDPP4Tz**; (b) relative DFT energies at the tuned-ωB97XD/6-31G(d,p) (dashed lines) and B3LYP (solid lines) levels; (c) tuned-ωB97X-D/6-31G(d,p) natural transition orbitals with the largest weight (78%) for the S_0 to S_1 transition in the **PDPP4Tz** tetramer. 39

Figure 2.7. Electron-hole pair natural transition orbitals (isovalue surface 0.02 a.u.) for the S_0 to S_1 transition of the **PDPP4Tz** tetramer calculated by TD-DFT at tuned-wB97X-D/6-31G(d,p) level of theory. The weights of the particle-hole contribution to the excitation are included. 40

Figure 2.8. Tuned-ωB97X-D spin density plots for the anion of the **PDPP4Tz** tetramer (the red and blue colors represents spin up and spin down electron densities, respectively). 41

Figure 2.9. HSEsol//B3LYP electronic band structure of the **PDPP4Tz** chain. The zero of energy corresponds here to the top of the valence band. 42

Figure 2.10. Tapping mode AFM height (top row) and phase (bottom row) images of **PDPP4Tz** blade coated films recorded after thermal annealing each film at 150 ^{o}C for 90 min followed by rapid cooling to room temperature in a nitrogen filled glove box. 44

Figure 2.11. GIWAXS area detector images of **PDPP4Tz** films cast from (a,b) chloroform by spincoating; (c,d) chloroform by blade coating; (e,f) *p*-xylene by blade

coating. (a,c,e) pristine films; (b,d,f) samples after annealing at 150 °C for 90 min followed by rapid cooling to room temperature. 45

Figure 2.12. Polarized Optical Microscope (POM) images of blade-coated **PDPP4Tz** films on glass slides (chloroform as solvent). 46

Figure 2.13. Output characteristics of the bottom-gate/bottom-contact (BG/BC) transistors fabricated by spincoating *p*-xylene solution of **PDPP4Tz.** 47

Figure 2.14. Transfer characteristics of the bottom-gate/bottom-contact (BGBC) transistors fabricated by spincoating *p*-xylene solution of **PDPP4Tz**..... 48

Figure 2.15. PDPP4Tz OFET stability under ambient conditions (25 °C and 50-60% RH). Devices are fabricated on Si-wafers based on the BGBC configuration. Mobility data were measured in a nitrogen filled glovebox with devices stored in vacuum chamber for 12 hours to remove moisture and residual air. 50

Figure 3.1. Thermal transition characterization of **PNDI2Tz**. DSC characterization was based on the 3rd heating and cooling process in a nitrogen atmosphere with a nitrogen flow rate of 50 mL/min and a heating/cooling rate of 5 °C/min. 56

Figure 3.2. a) UV-*vis* spectra of **PNDI2Tz** in various organic solvents; b) Comparison of **PNDI2Tz** solution and thin-film UV-*vis* spectra. 57

Figure 3.3. Ultraviolet photoelectron spectrum (UPS) for **PNDI2Tz** thin film cast on Au-coated silicon wafer. 58

Figure 3.4. Temperature-dependent UV-*vis* spectroscopy on a *p*-xylene solution of **PNDI2Tz**. 59

Figure 3.5. Photoluminescence of **PNDI2Tz** in *p*-xylene and in solid state, compared to the UV-*vis* absorptions in solution and in thin film..... 60

Figure 3.6. CV and DPV results for **PNDI2Tz** thin film drop-cast on a glassy carbon button. 62

Figure 3.7. a) Torsion potentials related to the rotation of the adjacent units in the monomer of **PNDI2Tz**; relative energies determined at the tuned-ωB97X-D/6-31G(d,p) level. b) Evolution of the optical gap *vs.* oligomer size for **PNDI2Tz** as calculated at the TD-DFT (tuned-ωB97X-D/6-31G(d,p)// ωB97X-D/6-31G(d,p) level of theory). (c) TD-DFT (tuned-ωB97X-D) natural transition orbitals (bottom: hole wavefunction; top: electron wavefunction) with the largest contribution to the $S_0 \rightarrow S_1$ transition in the **PNDI2Tz** trimer. 64

Figure 3.8. Atomic force microscopy (AFM) images of **PNDI2Tz** films cast on UV-ozone SiO_2 surfaces and OTS-processed SiO_2 surfaces..... 66

Figure 3.9. Grazing-incidence wide-angle X-ray scattering (GIWAXS) results of pristine and annealed **PNDI2Tz** on Si wafers. 66

Figure 3.10. PNDI2Tz transfer curves measured on bottom-gate-bottom-contact OFETs (devices were coated at 3 mm/s; five device results overlapped showing consistent performances; devices are annealed in a N_2 glovebox at 150 °C for 30 min followed by cooling)..... 69

Figure 4.1. Chemical structures of conjugated polymers studied, **PNDI2Tz** (left), **P(NDI2OD-T2)** (middle), and **PDPP4T** (right). 73

Figure 4.2. a) Chemical structures of hexamethyldisilazane (HMDS), phenyltrichlorosilane (PTS) and octadecyltrichlorosilane (OTS); b) Optical images showing the contact angles of the HMDS, PTS and OTS processed SiO_2 surfaces and surface free energy calculation results. Contact angles in table is the average value of 8 measured spots. 76

Figure 4.3. AFM images of **PNDI2Tz** thin films fabricated on HMDS, PTS and OTS surfaces showing the development of polymer nanofiber network. Bottom row is the three-dimensional representation of the height images for clear view. Scale bars are all 400 nm. 77

Figure 4.4. a) GIWAXS image of **PNDI2Tz** thin-films on HMDS, PTS and OTS processed SiO_2 surfaces; b) 1D line cut along Chi = 15° with zoomed-in plot on q_z = 0.6~1.8 A^{-1}; c) π- π stacking Chi plot from *xy*-plane (Chi = 0°) to *z*-axis (Chi = 90°). 78

Figure 4.5. PNDI2Tz AFM height and phase image with blade coating speeds. Scale bar is 400 nm..... 79

Figure 4.6. Transfer curve of **PNDI2Tz** devices coated on HMDS, PTS and OTS processed bottom-gate-bottom-contact transistors. Solid dots are I_D vs V_G curve, and hollow-dots are $I_D^{1/2}$ vs V_G curve. Devices were fabricated at a blade-coating speed of 3 mm/s. 82

Figure 4.7. AFM height and phase images of two other polymers (**N2200**/n-channel, **PDPP4T**/p-channel) indicating the formation of nanofiber networks on OTS-

processed devices at blade-coating speed of 3 mm/s and 4 mm/s, respectively. Scale bar is 400 nm. 83

Figure 4.8. Transfer curves of **PDPP4T** (*p*-channel), and **N2200** (*n*-channel) showing processing versatility. Solid lines are source-drain current of OFETs, and dashed lines are source-drain current square roots. 85

Figure 4.9. Schematic representation of the proposed conjugated polymer nanofiber network formation process on OTS-processed substrates. 87

Figure 5.1. Chemical structure of PNDI2Tz showing nitrogen atom lone pairs. 92

Figure 5.2. PNDI2Tz OFET-based BF_3 sensor in custom-built gas chamber for sensing test. 96

Figure 5.3. (left) **PNDI2Tz** halochromic effect in solution with HNO_3 addition; (right) UV-*vis* spectra of **PNDI2Tz** solution during acidification cycles. 99

Figure 5.4. Stoichiometric addition of HNO_3 in **PNDI2Tz** solution with HNO_3 molar equivalences. 100

Figure 5.5. PNDI2Tz solution UV-*vis* relative absorbance (A_{540}/A_{450}) with respect to different HNO_3 molar equivalences. 101

Figure 5.6. Proposed mechanism of PNDI2Tz interaction with acids. 102

Figure 5.7. (left) **PNDI2Tz** halochromic effect in solid state with BF_3 fume; (right) UV-vis spectra of **PNDI2Tz** thin film during BF_3 cycles. 103

Figure 5.8. Overlaid UV-*vis* spectra of PNDI2Tz recovery process after BF_3 exposure. 104

Figure 5.9. Demonstration of PNDI2Tz OFET-based BF_3 sensor with transfer curves. 105

Figure 5.10. PNDI2Tz OFET-based BF3 sensor stability test and performance summary in 50 BF_3 treating cycles. 106

Figure 5.11. Real-time **PNDI2Tz** OFET source-drain current (I_D) with BF_3 fume addition and ether fume addition (as blank). 107

Figure 7.1. Chemical structure of four DPP-thiazole/thiophene polymers and building block electron deficiency in an increasing order. 113

Figure 7.2. Solution and thin film UV-*vis* spectra of DPP-thiazole/thiophene polymers. 114

Figure 7.3. GIWAXS images of DPP-thiazole/thiophene polymers on UV-ozoned SiO_2 and OTS-processed SiO_2 substrates..... 115

Figure 7.4. (left) Synthesis of Poly(1,4-bis-(8-(4-phenylthiazole-2-thiol)-octyloxy)-benzene: (a) K_2CO_3, dry acetone, 1,8-dibromooctane, 50 °C; (b) $FeCl_3$, nitrobenzene, RT; and (c) K_2CO_3, 4-phenylthiazole-2-thiol, THF, Reflux, 12 h; (right) proposed detection mechanism of mercury ion with PPT polymer. Reprinted from article *ACS Appl. Mater. Interfaces* **2013**, *5* (6), 2234-2240. Copyright 2013 American Chemical Society. 117

Figure 7.5. Color changes of PPT solution in a THF/water solution upon the addition of (a) anions and (b) halides; in both panels a and b. (c) Color changes of PPT–I^- solution in a THF/water solution upon the addition of metal salts in water. Reprinted with permission from *ACS Appl. Mater. Interfaces* **2013**, *5* (6), 2234-2240. Copyright 2013 American Chemical Society..... 118

Figure 7.6. Proposed new NDI-thiazole based polymer with vinyl linkage for potential metal ion detection..... 119

LIST OF SYMBOLS AND ABBREVIATIONS

μ	Charge carrier transport mobility, $cm^2V^{-1}s^{-1}$
μ_e	Electron mobility, $cm^2V^{-1}s^{-1}$
HOMO	Highest occupied molecular orbital, eV
LUMO	Lowest unoccupied molecular orbital, eV
UV-*vis*	Ultraviolet-visible spectroscopy
IP	Ionization potential, eV
EA	Electron affinity, eV
$I_{ON/OFF}$	Current on and off ratio
V_{th}	Threshold voltage, V
V_G	Gate voltage, V
V_D	Source-drain voltage, V
I_D	Source-drain current, V

E_g	Bandgap, eV
E_g^{opt}	Optical bandgap, eV
E_g^{elec}	Fundamental bandgap (or electronic bandgap), eV
λ	Wavelength, nm
λ_{max}	Wavelength at highest intensity, nm
DSC	Differential scanning calorimetry
T_g	Glass transition temperature, °C
TGA	Thermal gravimetric analysis
CV	Cyclic voltammetry
DPV	Differential pulse voltammetry
AFM	Atomic force microscopy
GIWAXS	Grazing incidence wide angle X-ray scattering
DFT	Density functional theory

SUMMARY

In the past several decades, π-conjugated organic and polymeric semiconducting materials have attracted significant attention due to their promising electronic and optoelectronic properties. Therefore, their potential in applications to electronic and optoelectronic devices have been investigated, including applications in organic field-effect transistors (OFETs), organic photovoltaics (OPVs), and organic light-emitting diodes (OLEDs), etc. In the past two decades, a great number of conjugated polymers with mobility surpassing that of amorphous silicon have been reported. However, most of these high-mobility conjugated polymers are either hole transport or ambipolar (electron and hole transport) semiconductors; only a few electron transport conjugated polymers with high electron mobility (μ_e) have been reported to date. The development of high-mobility electron transporting conjugated polymers falls behind advances in their hole transporting counterparts. However, high-performance pure electron-transporting conjugated polymers for pure *n*-channel organic electronic devices are highly desirable in applications such as metal-oxide-semiconductor (CMOS)-like complementary circuits, organic thermoelectrics, and all-polymer solar cells. Among many electron-poor units, thiazoles stand out as a promising building block for high performance organic semiconductors. This dissertation discusses the development of thiazole-based π-conjugated semiconducting polymers to enhance the electron field-effect mobilities by advancing intra- and inter-molecular interactions between polymer chains, and the enhancement of ambient stability by decreasing the energy levels of frontier molecular orbitals.

The structure-process-property relationships of thiazole-based *n*-channel conjugated polymers are studied in this thesis. Three new thiazole-based conjugated polymers, poly(diketopyrrolopyrrole-bithiazole) (**PDPP2Tz**), poly(diketopyrrolopyrrole-terthiazole) (**PDPP4Tz**), and poly(naphthalenediimide-bithiazole) (**PNDI2Tz**) have been developed, as shown in Chapter 2 and Chapter 3. By incorporating thiazole into the polymer repeating units, the frontier molecular orbital energy levels were effectively reduced, resulting in a new series of *n*-channel semiconducting polymers. Among these polymers, **PDPP4Tz** and **PNDI2Tz** showed unipolar *n*-channel characteristics in OFETs. Surface effects of the dielectric layer on device performance were investigated with three different self-assembled monolayer (SAM) in OFETs in Chapter 4. Polymer nanofiber networks form on hydrophobic SAM-processed SiO_2 dielectric surfaces. This promote polymer packing in thin film and enhance charge transport in OFETs. In Chapter 5, the application of **PNDI2Tz** as an acid sensor was studied. The lone pair on the nitrogen of thiazole can act as Lewis base. **PNDI2Tz** is shown to be halochromic in the presence of Brønsted acids (such as nitric acid and sulfuric acid) or a Lewis acid (such as boron trifluoride). A **PNDI2Tz** OFET-based sensor was designed that showed excellent sensitivity and durability.

CHAPTER 1. INTRODUCTION

1.1 Organic and Polymer Semiconductors

Organic semiconductors have drawn significant attention in the past several decades for their major improvements in material design and purification that led to a significant boost in the materials performance.[1-9] Quite different from conventional silicon based electronics, organic semiconductors are light weight, low cost, amenable to high throughput processing and exhibit excellent flexibility for the potential of fabricating large-area, printable electronics.[10-15] Thus, they may lead to a new generation of products such as conformable and rollable electronic displays, solar energy harvesting devices, radio frequency identification (RFID) tags and convenient medical diagnostics devices.

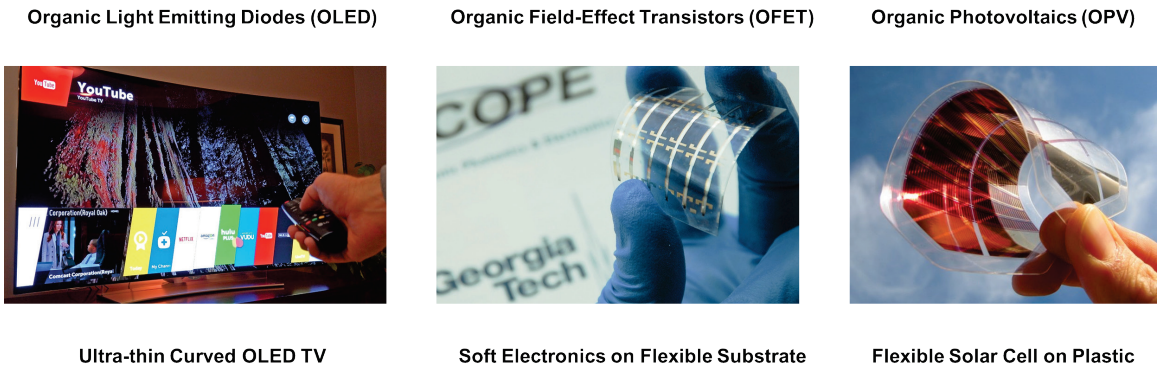

Figure 1.1. Applications based on organic semiconductors.[34-36]

There are two major classes of organic semiconductors that are mainly discussed in this field of research: conjugated small molecules and conjugated polymers with advanced optoelectronic performance. Conjugated small molecules are attractive because they can be efficiently purified, and their ability to form ordered

structures (via various deposition techniques) has enabled charge carriers to gain high mobilities in the solid state.[16] They have also served as model systems for a broad variety variety of fundamental studies of exciton diffusion and charge carrier dynamics.[17-19] On the other hand, conjugated polymers are advantageous for their excellent solubility in a variety of solvents allowing for solution processing, and their desirable mechanical properties for large-area device fabrication. Currently, conjugated materials receive considerable attention due to their applications in organic field-effect transistors (OFETs), organic CMOS (complementary metal-oxide-semiconductor)-like logic, and organic sensors; displays such as organic light-emitting diodes (OLEDs); solar and thermal energy harvesting such as organic photovoltaics (OPVs) and organic thermoelectrics (**Figure 1.1**).[6, 7, 16, 20-36]

Polymer semiconductors are one class of material that is of interest for such applications due to their solution processability, mechanical robustness, inexpensiveness, and light weight. Therefore, polymer semiconductors for organic electronic applications have been attracting tremendous attention since the 1970's.[10, 11, 37-43] Researchers have developed effective design principles for the design of high-performance organic semiconductors to enhance their corresponding effectiveness in devices over the past few decades.[7, 16, 44-47] One of the popular design principles is to incorporate fused aromatic rings in the polymer backbone. The fused ring aromatic structures introduce planarity to the polymer, which in turn leads to higher order molecular organization.[3, 16, 48-50] Such high level organization enhances bulk crystallinity and brings with it a strong tendency for the polymer to form π-π stacks with a large overlapping area that is preferable for charge carrier transport through intramolecular charge transfer and intermolecular hopping.[51, 52] Another

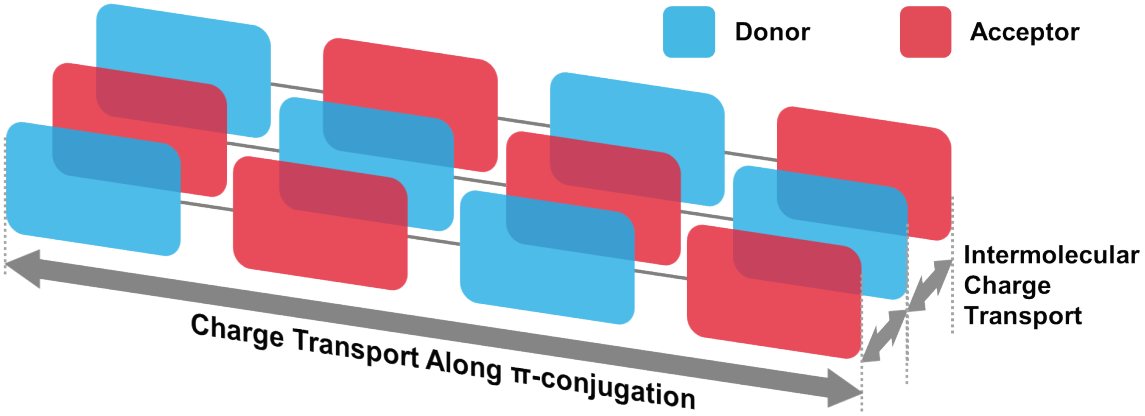

Figure 1.2. Schematic representation of both intermolecular and intramolecular charge transport pathways in donor-acceptor (D-A) conjugated polymers.

approach is to synthesize Donor-Acceptor (D-A) copolymers, which consist of an alternating arrangement of electron-donating (D) and electron-accepting (A) units. Donor-Acceptor copolymers commonly have shorter interchain distances due to strong intermolecular D-A interactions in the solid state.[41, 53, 54] (**Figure 1.2**) Partial intermolecular charge transfer (ICT) between D and A moieties within these polymers can readily manipulate their electronic structures (HOMO/LUMO levels), as well as electronic and optoelectronic properties.[55] The strength of ICT can be tuned through the careful design and selection of D and A building blocks, allowing D-A copolymers to possess small band gaps, broad optical absorption bands, short distances between the polymer chains and high charge carrier mobilities.

Owing to the extensive research efforts of materials scientists and device engineers, a number of polymer semiconductors showing mobility values over 0.5 $cm^2V^{-1}s^{-1}$ up to even 10 $cm^2V^{-1}s^{-1}$ have been developed in research laboratories in the last few years.[53, 55-60] Design and optimization of polymer structures have contributed most significantly to the recent improvements in mobility for polymer

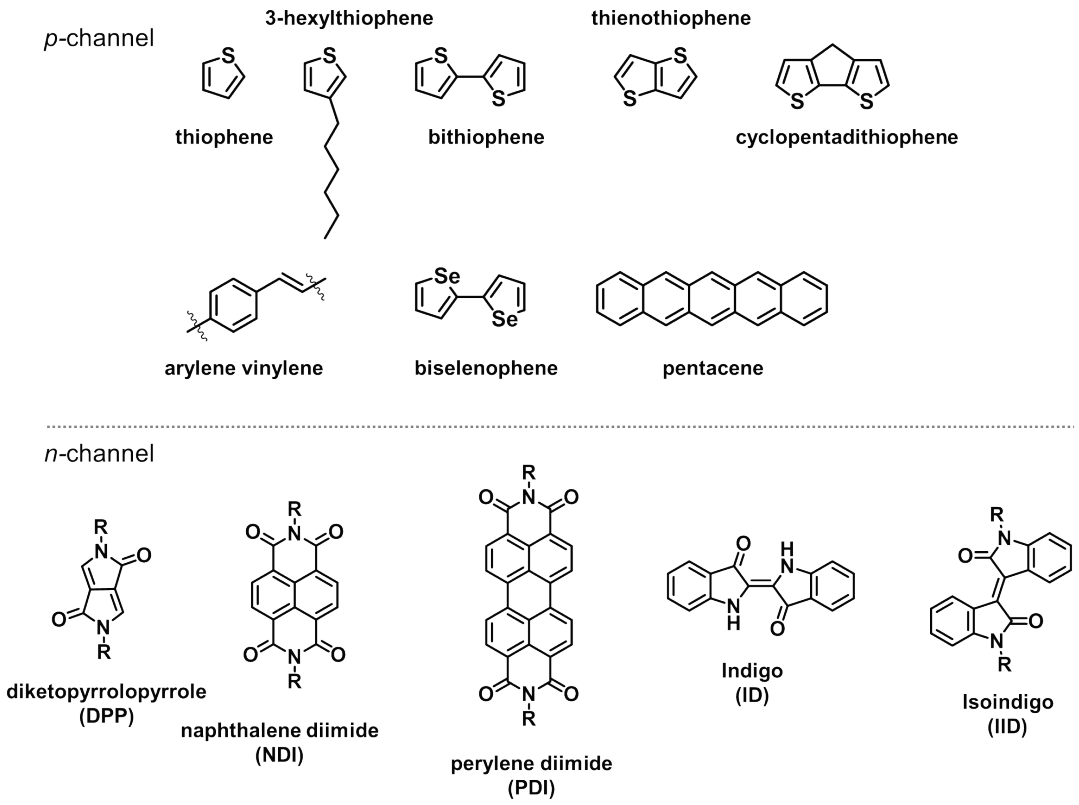

Figure 1.3. Typical electron rich (top) and electron deficient (bottom) organic semiconductor building blocks for *p*-channel and *n*-channel organic.

semiconductors. From molecular engineering perspectives, a large number of highly efficient donor and acceptor structures that are often seen in modern conjugated polymer structures have been developed. Thiophene, alkylthiophene, bithiophene, thienothiophene, cyclopentadithiophene, biselenophene, acenes and arylene vinylene are the typical donor blocks, whereas diketopyrrolopyrrole (DPP) and its derivatives, isoindigo and its derivatives, thiazoles, benzothiadiazole, naphthalene diimide (NDI), perylene diimide (PDI) are known electron acceptor blocks. (**Figure 1.3**) Although the electron donor units play an important role for achieving high mobility values, the electron acceptor building blocks are considered to be the determining factor. The majority of the high mobility polymers are based only on a few types of electron acceptors such as diketopyrrolopyrrole

(DPP)[56, 61-66] and naphthalene diimide (NDI)[14, 67-72].

One of the main concerns associated with organic electronics is the stability of organic semiconductor materials. Elements such as oxygen, UV light, and moisture are detrimental to organic semiconductors during manufacturing or operation in the ambient environment. The impact of these effects can be alleviated through designing different donor and acceptor building blocks to alternate the energy levels of the copolymers. By incorporating electron poor units or electronegative atoms, the highest occupied molecular orbital (HOMO) energy levels can be effectively lowered, leaving the resulting polymer less prone to oxidation. Over the years, researchers have developed and synthesized a number of more stable organic/polymer semiconductors with high mobility and low bandgaps using the concept of molecular engineering.[2, 12, 14, 73-77] Another highly important design principle in conjugated polymer development is related to solution processability. Unlike their small molecule or oligomeric counterparts, conjugated polymers with high molecular weights cannot easily be deposited on substrates by vacuum deposition techniques. Thin-films are typically cast onto device substrates via solution processing, during which a given polymer is first dissolved in a solvent to afford the polymer solution; a subsequent casting or printing step is then used to apply the semiconductor onto the device substrate.[73] Solvent evaporation also impacts polymer thin-film formation. Therefore, the semiconductor film morphology and electronic performance significantly depend on the solution processing.[78] The solubility of π-conjugated polymers depends on both the structure of the polymer backbone and the side chains incorporated into the structure.[3, 25]

Linear and branched alkyl groups have been widely incorporated into π-conjugated polymers with the aim of improving polymer solubility in common organic solvents such as chloroform and chlorobenzene.[77] (**Figure 1.4**) Typically, increasing the density of side chains will lead to increased solubility.[2, 3, 25, 79] The incorporation of side chains, however, might induce steric hindrance within the polymer backbone, resulting in a reduction of π-conjugation along the polymer backbone and thus lowered charge carrier transport properties.[80-83]

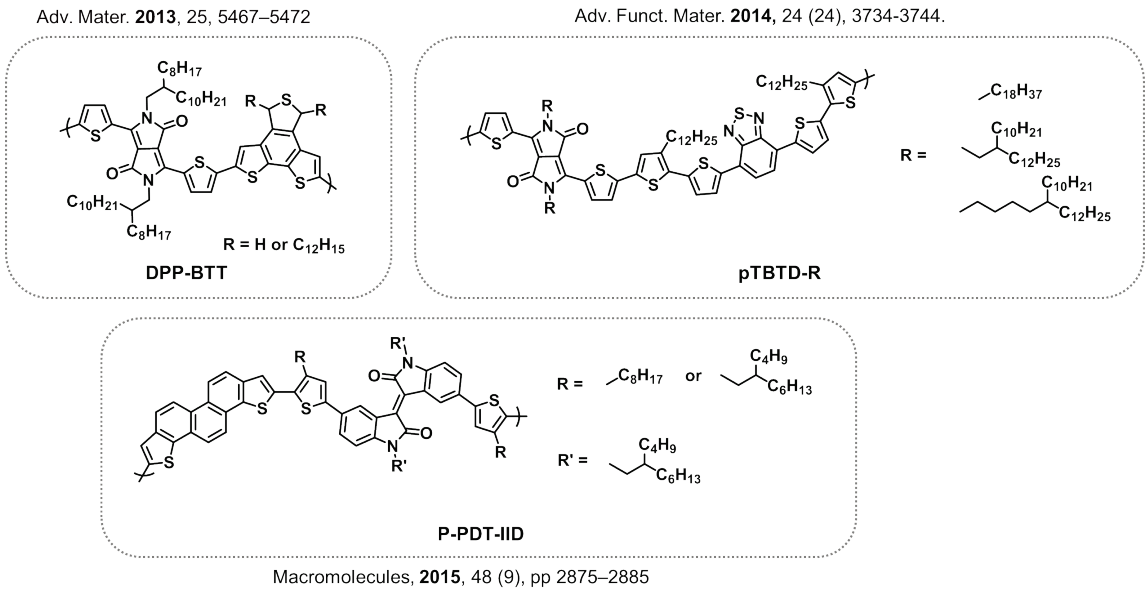

Figure 1.4. Examples of conjugated polymers utilized the concept of side-chain engineering.[81-83]

1.2 *n*-Channel Polymer Semiconductors

As discussed above, significant advances in OFET device performance have been achieved via the development of new conjugated polymers and device optimization, and a great number of conjugated polymers with mobility surpassing that of amorphous silicon have been reported.[9, 84, 85] However, most of these high mobility conjugated polymers are

hole transport or ambipolar (electron and hole transport) semiconductors; only a few electron transport conjugated polymers with high electron mobility (μ_e) have been reported to date.[86, 87] The development of high mobility n-channel conjugated polymers fall behind their p-channel counterparts. Whereas, high-performance unipolar n-channel conjugated polymers are highly desirable in applications such as complementary metal-oxide-semiconductor (CMOS)-like complementary circuits,[86-90] organic thermoelectrics,[91] and all-polymer solar cells.[39, 58, 92-94]

Alternately linking an electron donor (such as thiophene, thienothiophene, acenes) and a strong electron acceptor, such as diketopyrrolopyrrole (DPP)[56, 62-64, 66, 95], naphthalenediimide (NDI)[67-71, 96-99] and isoindigo (IID) derivatives[100-102] via covalent bonds to afford donor–acceptor (D–A) conjugated polymers is a practical way to construct n-channel conjugated polymers. However, weak *p*-channel characteristics are often observed for OFET devices based on n-channel D–A conjugated polymers.[86, 103, 104] The unwanted hole injection and transport at biases lower than threshold voltage result in devices that are difficult to switch off.[105] This phenomenon might be related to the polymer highest occupied molecular orbital (HOMO) energy levels (E_{HOMO}), which are not low enough to block hole injection from the commonly used Au contacts.

Diketopyrrolopyrrole (DPP) is a strongly electron-deficient unit with a relatively planar and rigid skeleton.[106] The structural characteristics of DPP unit have been reported to be more preferable for high mobility conjugated polymers.[40, 107, 108] In fact, very high hole mobility has been achieved in OFETs by using DPP-based polymers.[109] These polymers are generally composed of four parts: (1) the diketopyrrolopyrrole unit, (2) an

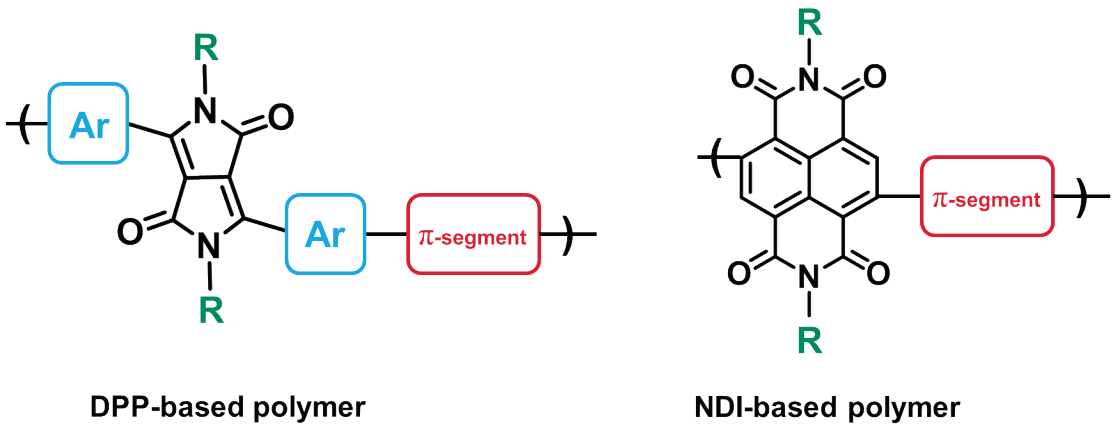

Figure 1.5. Design principles of DPP-based and NDI-based polymers.

adjacent aromatic substituent, (3) a π-conjugated segment, and (4) alkyl side chains on the DPP unit. (**Figure 1.5**) The aromatic substituents connect the DPP to the conjugated segment and originate from the aromatic nitrile precursors used to synthesize DPP. The π-conjugated segment may consist of electron rich or electron deficient units or combinations thereof. By varying the aromatic substituents or changing the π-conjugated segments, the optoelectronic properties (such as optical bandgap, ionization potential, electron affinity, etc.) of the DPP polymers can be easily tuned. The side chains attached to the DPP unit enhance polymer solubility for solution processing, and provide a handle to modify and adjust the aggregation and crystallization of DPP polymers during thin film formation. Therefore, DPP-based polymers have been shown to be a promising family of materials for high performance electron transporting materials.

Another heavily studied family of *n*-channel conjugated polymers are naphthalene diimide (NDI)-based conjugated polymers.[110] Naphthalene diimide (NDI) is the smallest homologue of the rylene diimides.[111-113] NDIs possess high electron affinity, good charge carrier mobility, and excellent thermal and oxidative stability. In the design of electronic

conducting functional materials, NDIs are among the most versatile and fascinating class of aromatic molecules.[25, 71] Nevertheless, functionalization through core-substitution produces NDI analogues whose absorption and fluorescence properties are variable.[114] Furthermore, the electron withdrawing groups at the imide position cause a strong polarization of the π-systems, and the aromatic naphthalene core thus possesses a low π-electron density. Imide substitution has very little effect on the optical and electrochemical properties of NDIs, and NDIs can be functionalized with a variety of groups at the imide position without changing the electronic properties of the π-scaffold in the development of aggregation behavior. Therefore, NDI-based conjugated polymers are promising candidates for organic electronics applications, photovoltaic devices, and flexible displays.[13, 112, 115, 116]

1.3 Thiazoles and Thiazole-based Conjugated Polymers

Mentioned in the sections above, most commonly studied polymeric materials are based on electron-rich aromatic moieties, such as thiophene, selenophene, fluorene, pyrrole, carbazole, and thieno[3,4-b]pyrazine, which have been reviewed on numerous occasions.[2, 3, 7, 23, 79, 117-119] A particularly interesting building block, 1,3-thiazole, for the development of high-performing polymeric semiconductors, however, has received considerably less attention in current literature.[120]

Although thiazole is often considered to be an electron deficient version of thiophene, its reactivity is quite different from thiophene and is a factor that has to be considered when synthesizing thiazole-based monomers. Due to the asymmetric nature of the thiazole ring, the π-electron density is highest on the C5 and lowest on the C2 carbon, which is also

reflected in the reactivity of the thiazole moiety.[76] Among many thiazole derivatives, 2,5-dibrominated thiazole is a useful monomer for conjugated polymer design. In addition to the more complex reactivity, thiazole-containing building blocks also present a more versatile regio-chemistry due to the carbon symmetry of the thiazole ring.

The 2,2'-bithiazole unit exhibits a number of features that could be attractive in the search for electron-transport conjugated polymers.[76] The presence of electronegative nitrogen atoms lowers the LUMO energy in comparison to analogs that consist of electron-rich units such as thienyl derivatives.[121-125] The *trans*- conformation of 2,2'-bithiazole (with a dihedral angle between the thiazole rings close to 180°, as confirmed by density functional theory, DFT, in this study, *vide infra*) can promote polymer backbone planarity,

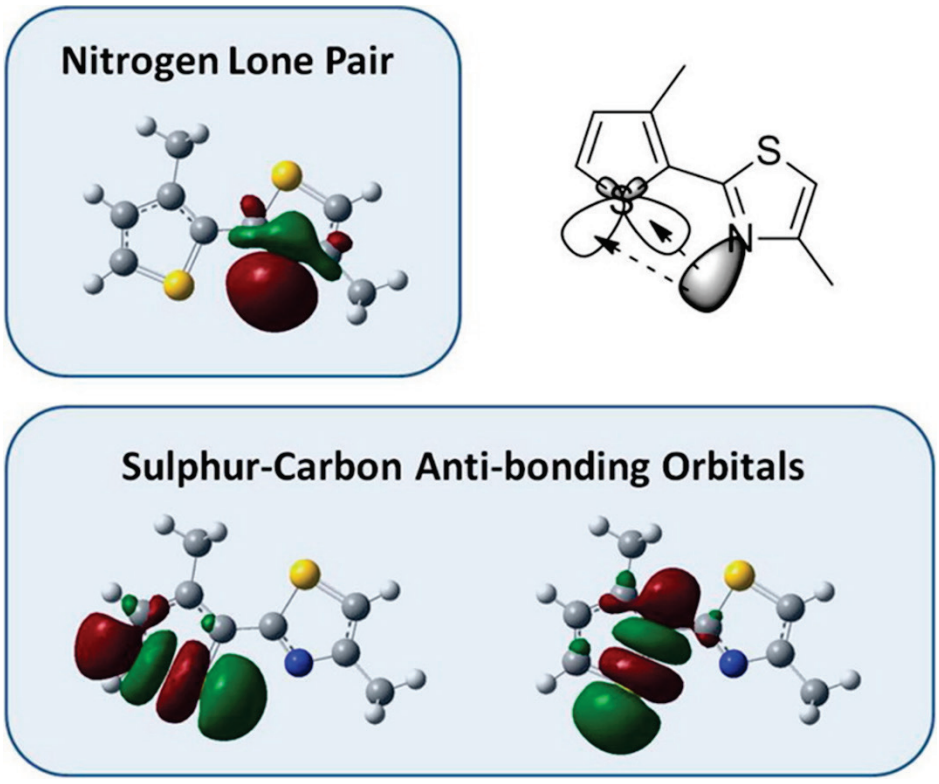

Figure 1.6. Visualization of nitrogen lone pair and carbon–sulfur antibonding orbitals. Reprinted with permission. Reprinted from Chem. Mater. **2013**, 25, 4239. Copyright 2013 American Chemical Society.

which extends intra-chain π-conjugation and interchain π−π stacking, in comparison to analogs such as biphenyl or bithiophene that are not coplanar.[118, 126, 127] Thiazole has a net zero dipole due to its antiparallel alignment between the two thiazole moieties. Such antiparallel conformation leads to a "conformational lock" mechanism, in which the nitrogen lone pair of the thiazole ring interacts with the antibonding orbitals in the adjacent ring (**Figure 1.6**), thus favoring the planarization of the ring system.[128] Additionally, the large dipole of the thiazole unit could impart strong dipole−dipole interactions between bithiazole-based polymer chains.[129]

The bithiazole unit has been primarily used to build hole transport donor−acceptor π-conjugated copolymers;[76] bithiazole was considered as a weak acceptor. Recent studies indicated the feasibility of using bithiazole in developing electron-transport small molecule semiconductors;[129, 130] and in a few cases, bithiazole-based polymers exhibited ambipolar properties.[131] Hence, the development of electron-transport polymeric semiconductors based on bithiazole could be envisioned.[76] One significant challenge lies in the development of an efficient synthetic pathway to incorporate bithiazole units into π-conjugated molecules and polymers.[123, 129]

1.4 Charge Transport in Polymer Semiconductors

Heeger, MacDiarmid and Shirakawa discovered that doping π-conjugated polymers could convert them into conductors,[8] which is against the common notion that polymers are electrical insulators. Unlike the backbone of non-conjugated polymers, which relies on the connection of sp^3 hybridized carbon atoms, conjugated polymers comprise alternating single and double (or triple) bonds. The resultant

conjugated π bonds lead to a relatively small energy gap, which is usually in the range of 1~3 eV, greatly facilitating electron delocalization from HOMOs to LUMOs.[5, 6] Similar to band transport in inorganic materials like silicon, these delocalized π-electrons may move along the polymer chains as charge carriers, resulting in intramolecular transport. (**Figure 1.2**) A highly coplanar polymer backbone can provide an extended π-electron delocalization pathway for efficient charge carrier transport, while a twisted conjugated backbone usually interrupts the intramolecular charge transport resulting in low field-effect mobilities.[43, 132-136]

Charge carrier transport in polymer semiconductors can be viewed at three levels: i) intramolecular (or intrachain), ii) intermolecular (or interchain), and iii) interdomain (or intergranular).[137] The intramolecular charge transport is mainly determined by the effective π-conjugation length along the polymer backbone.[1, 138-142] For aromatic ring systems, a highly coplanar polymer backbone can provide an extended π-electron delocalization pathway for efficient charge carrier transport. A proper choice of building blocks that can minimize main chain twisting and enhance backbone planarity is the key for achieving high intramolecular charge transport performance. On the other hand, intermolecular charge transport is governed by the intermolecular distances as well as the intermolecular π-π overlapping area. The charge transport between polymer chains is highly anisotropic. The most favored path is along the π-π stacks, which usually has the shortest interchain distance among all directions and beneficial for charge hopping between chains. Although debates on charge transport mechanism still remain, a significant body of evidence suggests that charge carrier transport along the π-π stacking direction is not as fast as intramolecular charge transport, but it can still be quite efficient if a short π-π distance and a large π-

overlap area are achieved.[139, 143, 144] In an OFET device, an edge-on chain orientation, where the π-π stacking direction is parallel to the dielectric surface, is highly desirable.[134, 143]

Due to weak intermolecular interactions (Van der Waals forces or electrostatic forces), intermolecular transport becomes the bottle neck of charge transport in organic semiconductors. The intermolecular distance in organic materials is usually around 4 Å, which means that electrons have to hop from one molecule to the next by overcoming the energy barrier induced by intermolecular separation. Thus, this kind of "hopping transport" is strongly field-dependent. This is also the starting point for the idea to synthesize D-A polymers with a shorter π-π distances in order to improve charge carrier hopping.

Unlike most inorganic materials and small organic molecules, single crystals of polymer semiconductors are extremely difficult, if not impossible, to obtain due to their long and polydisperse chains. Consequently, polymer semiconductors inevitably comprise a significant fraction of amorphous phase. Polymer chains in the amorphous regions are twisted, randomly oriented, and loosely contacted, leading to poor intramolecular and intermolecular charge transport properties. In a semi-crystalline polymer thin films, the charge transport between crystalline domains, i.e., the interdomain charge transport, is determined by the size and the packing density of the amorphous region between the crystalline domains.[139, 141, 145-147] To design polymers with intrinsically high charge transport performance at the intramolecular, intermolecular, and interdomain levels is a challenging task for polymer chemists, while to obtain highly crystalline, highly molecularly oriented polymer

semiconductor thin films requires collective efforts from polymer physicists and device engineers.

1.5 Organic Field-Effect Transistors (OFETs)

Of many applications of organic semiconductors, organic field-effect transistors have drawn quite significant attention by researchers.[7, 45, 148] As the fundamental building block for electronic circuits, field-effect transistors utilize an electric field to drive and manipulate the charge carrier conductivity of semiconducting materials in the transistor channel, and thus the signal can be switched and amplified.[9]

Transistors are generally classified as *p*- or *n*-channel, which refer to transistors having hole or electron transport within the transistor channel, respectively. A transistor that exhibits both hole and electron mobility simultaneously is called an ambipolar transistor, and the corresponding semiconducting material is an ambipolar semiconductor.[31, 149, 150] In OFETs, electron rich (hole transport) or electron deficient (electron transport) organic semiconductors replace the inorganic semiconductors, e.g. silicon and zinc oxide, within the transistor channel to afford p-channel and *n*-channel OFETs. The coupling of *p*- and *n*-channel transistors allows for fabrication of CMOS-like logic devices, which are widely used in digital integrated circuits including microprocessors, microcontrollers, and static and dynamic random access memory devices. In more recent research, OFETs have been incorporated into artificial electronic skin, which has significant potential in robotics, wearable electronics, soft displays, and biomedical devices.[151, 152] Transistors are often used as electronic switches that control the electrical current between the source and drain electrodes via an applied input voltage on the third terminal, known as the "gate". The transistor effect was first observed in 1947 by

John Bardeen and Walter Brattain in Bell Labs, and was further studied by William Shockley.[6, 153] In 1960, Kang and Atalla developed the first metal-oxide-semiconductor field-effect transistor (MOSFET) based on silicon.[6, 153] Transistors replaced vacuum tubes shortly thereafter, and became the basic components of integrated circuits.

Today in industry, most transistors are still made of inorganic semiconductors (monocrystalline silicon, polycrystalline silicon, III-V elements, rare earth metals, etc.).[9, 154-157] However, the costly inorganic materials and a complicated fabrication process for MOSFETs limit this technology in certain applications. In 1983, Nara and coworkers reported the first organic field-effect transistor (OFET).[158] In the past two decades, OFETs are becoming increasingly attractive since they not only can meet the requirements for large area coverage and flexibility, but also have achieved the high charge carrier mobility necessary to compete with silicon based transistors.[4, 5, 7] Since then, OFETs have received tremendous attention and are expected to be the key elements for next generation flexible electronics. The operation mechanism of OFETs is similar to that of MOSFETs.[6, 7] However, fabrication of most OFETs does not require high vacuum and high temperature. Instead, OFETs can be fabricated using low-cost solution processing techniques such as spin coating, blade coating, inkjet printing, etc., in ambient conditions.[3, 25]

1.6 OFET Device Fabrication and Processing

1.6.1 OFET Device Structure and Properties

Four typical organic field-effect transistor (OFET) device configurations are

shown in **Figure 1.7**, including bottom-gate/bottom contact (BGBC), bottom-gate/top-contact (BGTC), top-gate/bottom-contact (TGBC), and top-gate/top-contact (TGTC) architectures, in which organic or polymeric semiconductors are employed as the charge carrier transport layers.[159] Each configuration consists of a dielectric layer and three electrodes including the source, drain, and gate electrodes. The source-drain channels are typically 500 - 3000 μm in length and 20 - 100 μm wide. The source electrode is grounded and defined as $V_S = 0$. Unlike inorganic semiconductors, which must be, pre- *p*- or *n*-doped, organic semiconductors used in OFET architectures should be neutral with no free charge carriers available within the semiconductor layer. However, in a real system, organic semiconducting materials inevitably contain trace amounts of impurities which result from syntheses and purification processes, and these impurities will act as dopants. An increase in degree of doping can convert organic semiconductors to conducting materials, as the bands formed between the HOMO/LUMO extend and eventually fill the bandgap.

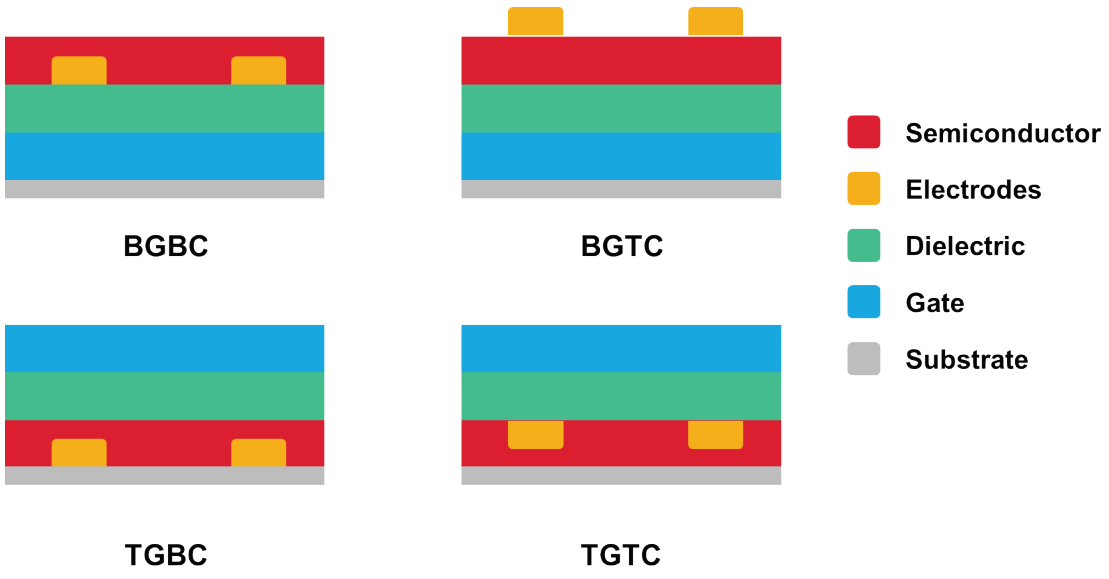

Figure 1.7. Schematic representation of four OFET architectures.

Application of a voltage (V_G) to the gate electrode leads to polarization of the dielectric layer. In BGBC-OFET devices, the injected charge carriers accumulate within the semiconductor adjacent to the semiconductor-dielectric interface. Similarly, the application of $V_G > 0$ induces electron injection and accumulation within semiconductors close to the semiconductor-dielectric interface, as shown in **Figure 1.8**.[16] When there is no bias between the source and drain electrodes ($V_D = 0$), charge carriers are uniformly distributed between the source-drain channel. Once V_D is applied, the movement of charge carriers takes place under the electric field driving force. In the case of $V_G > 0$ and $V_D > 0$, the injected electrons flow from the

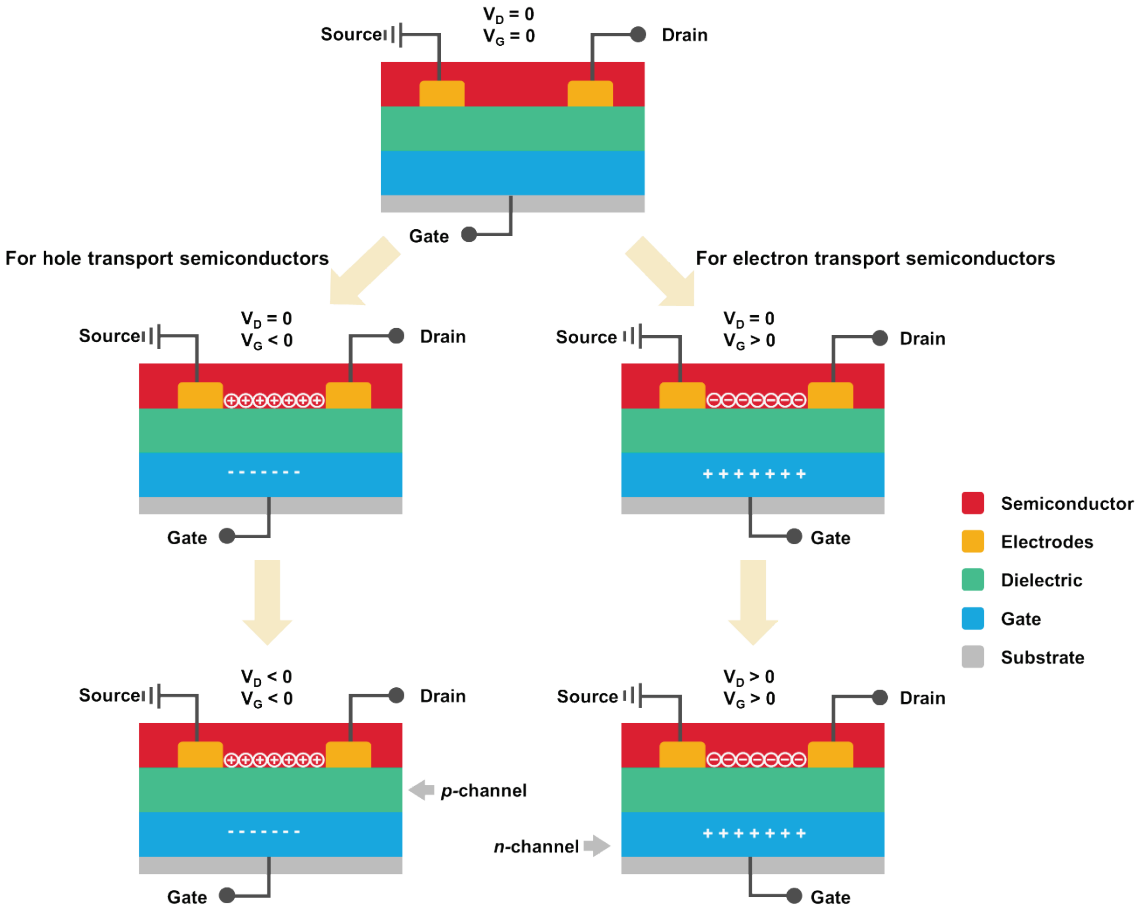

Figure 1.8. Schematic representation of OFET working mechanism and the effect of gate voltage (V_G) on charge injection into organic/polymeric semiconductors.

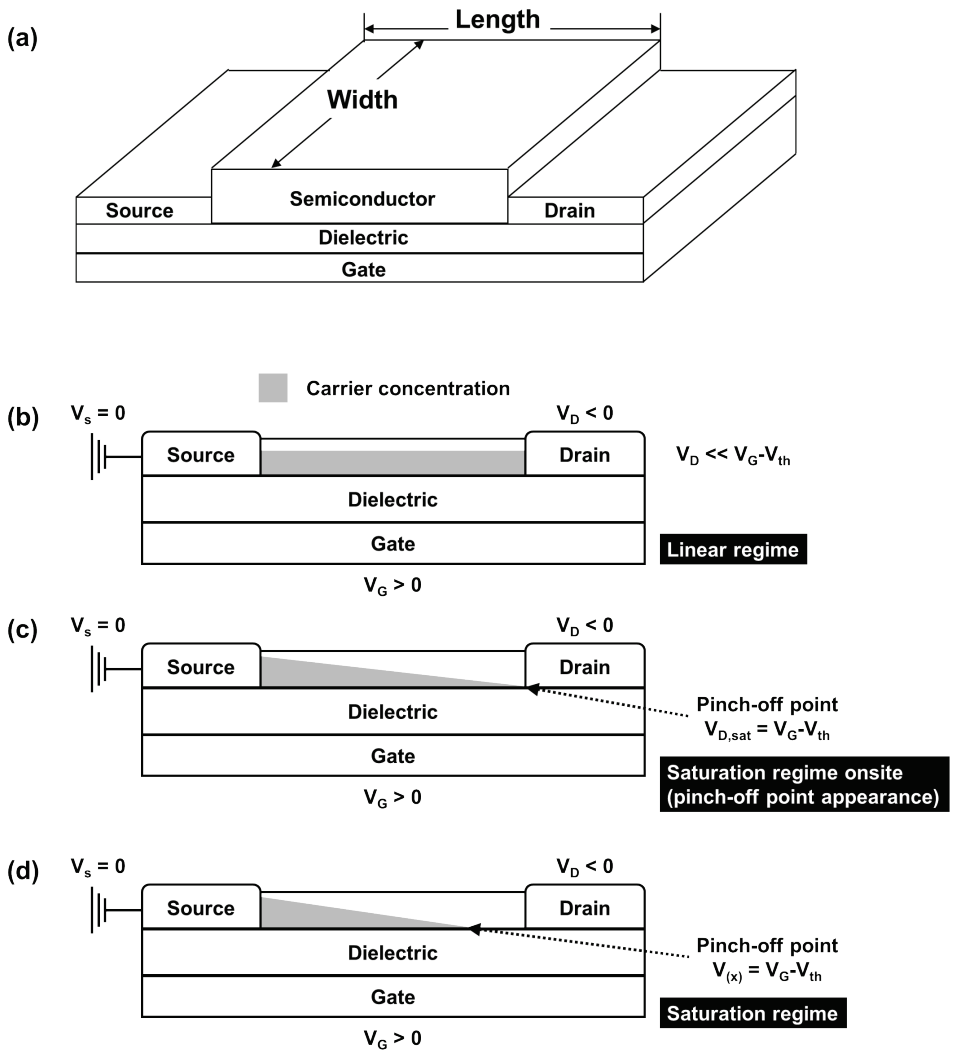

Figure 1.9. (a) Three-dimensional structure of bottom contact bottom gate OFET showing definition of channel dimensions. (b, c, d) Schematic representation of linear regime with $V_D << V_G - V_{th}$ (b), the onsite of saturation regime with $V_{D,sat} = V_G - V_{th}$, where the pitch-off point exhibits at drain electrode (c); and saturation regime with $V_{(x)} = V_G - V_{th}$, at which $V_D > V_{D,sat}$ (d), respectively. Figure reprinted with permission from *Chem. Mater., Vol. 16, No. 23,* **2004,** 4437-4439. Copyright 2004 American Chemical Society.

source to the drain electrode; while for $V_G < 0$ and $V_D < 0$, the injected holes flow from the from the source to drain electrodes.

Charge carrier mobility is the most important parameter for FETs. For commercial FETs, the maximum operation frequency of a device mainly depends on mobility of the semiconductor, as higher mobility would shorten the response time of the field effect

transistors.[39] When the conducting channel just begins to form between the source and drain electrodes under a source-drain voltage (V_D), the value of the gate voltage is defined as the threshold voltage (V_{th}). There are a variety of factors, such as built-in dipoles, impurities, interface states and charge traps, that can impact the value of V_{th} of a FET. Such factors are mainly related to the organic semiconductor materials, the insulating materials, and the fabrication process. $I_{on/off}$ stands for the on-to-off current ratio, which is determined by the highest current when an FET is turned on and the average current level when an FET is turned off. Usually an adequately large I_{on}/I_{off} is required for the transistor to be a qualified switch. The charge carrier density Q_{SD} hence is represented as:[16]

$$Q_{SD} = neh = C_{ox}(V_G - V_{th}) \tag{1.1}$$

where C_{ox} refers to the capacitance of dielectrics within unit area with the unit of $nF \cdot cm^{-2}$, e is the charge per charge carrier (hole or electron) with a constant value of 1.602×10^{-19} C, n denotes the charge density within unit area, and h is the thickness of the charged layer in the channel.

As $V_D << V_G - V_{th}$, Q_{SD} is reduced from the source (x = 0) to drain electrodes (x = L) in a linear manner (**Figure 1.9a**):

$$Q_{SD} = n(x)eh = C_{ox}(V_G - V_{th} - V_{(x)}) \tag{1.2}$$

where $V_{(x)}$ is the impact of source-drain voltage on Q_{SD} with the boundary conditions of $V_{(x)} = 0$ at x = 0 and $V_{(x)} = V_D$ at x = L. This regime is defined as the linear regime. The electric current within the charged layer (I_D) in the channel could be noted as:

$$I_D = n(x)ehW\mu E \tag{1.3}$$

where W is the width of the channel shown in **Figure 1.9a**, μ refers to the field effect mobility with the unit of $cm^2V^{-1}s^{-1}$. E is the electric field between source and drain electrode equals to dV/dx. Thereby,

$$I_D = C_{ox}(V_G - V_{th} - V_{(x)})W\mu\frac{dV}{dx} \tag{1.4}$$

During the charge transport I_D keeps constant along x-direction. According to the boundary conditions that $V_{(x)} = 0$ at $x = 0$, and $V_{(x)} = V_D$ at $x = L$, equation (1.4) is integrated as:

$$I_D = \left(\frac{W}{L}\right)C_{ox}\mu((V_G - V_{th})V_D - \frac{{V_D}^2}{2}) \tag{1.5}$$

As $V_D << V_G - V_{th}$ (linear regime), the equation (1.5) is simplified as:

$$I_D = \left(\frac{W}{L}\right)C_{ox}\mu((V_G - V_{th})V_D) \tag{1.6}$$

As $V_D = V_G - V_{th}$, the "pinch-off" appears inside the channel closed to the drain electrode where I_D reaches a saturated value (**Figure 1.9 b,c,d**). This regime is defined as the saturated regime. Equation (1.6) is converted to:

$$I_D = (\frac{W}{2L})C_{ox}\mu(V_G - V_{th})^2 \tag{1.7}$$

Taking partial derivatives of I_D versus V_G results in Equation (1.8) :

$$\frac{\partial I_D^{1/2}}{\partial V_G} = (\mu C_{ox} \frac{W}{2L})^{1/2} \quad (1.8)$$

where I_D is the source-drain current (A); V_G is the gate voltage (V) in the transfer plot. W and L refer to the channel width and length, respectively; μ represents the electron field-effect mobility in the saturation regime.

Therefore, mobility can be noted as:

$$\mu = (\frac{2L}{WC_{ox}})(\frac{\partial I_D^{1/2}}{\partial V_G}|V_D)^2 \quad (1.9)$$

In the saturation regime, μ is proportional to the slope of the plot of $I_D^{1/2}$ versus V_G, and the threshold voltage V_{th} value can be estimated by the intercept. Otherwise the mobility will be overestimated.[15] Several other factors must be taken into account when using the above equations. The mobility obtained by the method above may not be accurate, since Equations (1.9) are only valid when the mobility is constant, while the mobility in OFETs may depend on the gate voltage. In addition, the mismatch between the work function of metal electrodes and energy levels of the organic semiconductor would lead to the existence of contact resistance, which would affect the mobility value.

Obvious gate leakage currents are often observed in OFETs. A gate leakage current originates from two contributions. The first contribution comes from the current flowing from the drain to the gate through the dielectric layer due to the gate-drain voltage difference, which exists in all transistor operation conditions (on and off). This portion of the gate leakage current is insignificant and can be ignored if an excellent dielectric such as thermal silicon dioxide is used.[160]

The second contribution only exists when a gate voltage is applied. If the organic semiconductor is *p*-channel, holes would be induced to form a conductive layer with the influence of gate voltage, which would act as an electrode to conduct current, causing a shift of the onset current on the output plots. This part of leakage current could be reduced by patterning the semiconducting material or isolating the individual devices to reduce the outside area of the organic semiconductor layer.[161]

Among the four OFET configurations depicted in **Figure 1.7**, BGBC and TGTC have source and drain electrodes placed at the semiconductor and dielectric layer interface that allows direct charge carriers. Alternatively, semiconductors are placed between the dielectric and two (source and drain) electrodes in BGTC and TGTC configurations, where charge carriers injected from the source electrode need to move through the semiconducting layer (10-100 nm in general depending on coating conditions). In BGBC and BGTC architectures, charge carrier transport occurs at the bottom surface of the semiconductor layer; whereas in TGBC and TGTC architectures, charges are conducted along the top surface of the semiconductor. The morphology of the bottom and top surfaces of the organic semiconductor thin film has distinct impact on the four transistor configurations. The electron traps commonly exist at the semiconductor-dielectric interface, leading to trap states.[88, 162] Thereby, these traps have to be first filled before charge carriers can flow through from source electrode to drain electrode. The threshold voltage (V_{th}) includes the impacts of impurities within semiconductors, electron traps within the semiconductor-dielectric interface, and contact resistance at the metal-semiconductor interface.[46] In general, in *p*-channel transistors impurities would move V_{th} positively, the direction is reversed in *n*-channel transistors.

1.6.2 Dielectric materials for OFETs

As discussed above, dielectric materials can significantly impact charge carrier transport. BGBC transistors typical test devices use 200-300 nm of SiO_2 thermally grown onto heavily doped Si gate electrodes.[163] In general, defects and electron withdrawing functional groups exist on the surface of SiO_2 that might negatively affect the efficiency of charge carrier transport at the semiconductor-dielectric interface. One approach to address this challenge is to grow a silane or amine based self-assembled monolayers (SAM) on the top surface of the SiO_2.[164, 165] The silane (active Si-Cl or Si-OMe) or amine (N-H) groups are able to bond to the surface functional groups to afford siloxane (Si-O-Si) or silazane (Si-N) bonds, as shown in **Figure 1.10**.

Typical silane SAMs include alkyltrichlorosilane, perfluorinated alkyltrichlorosilane, alkyltrimethoxylsilane, and bis(trimethylsilyl)amine

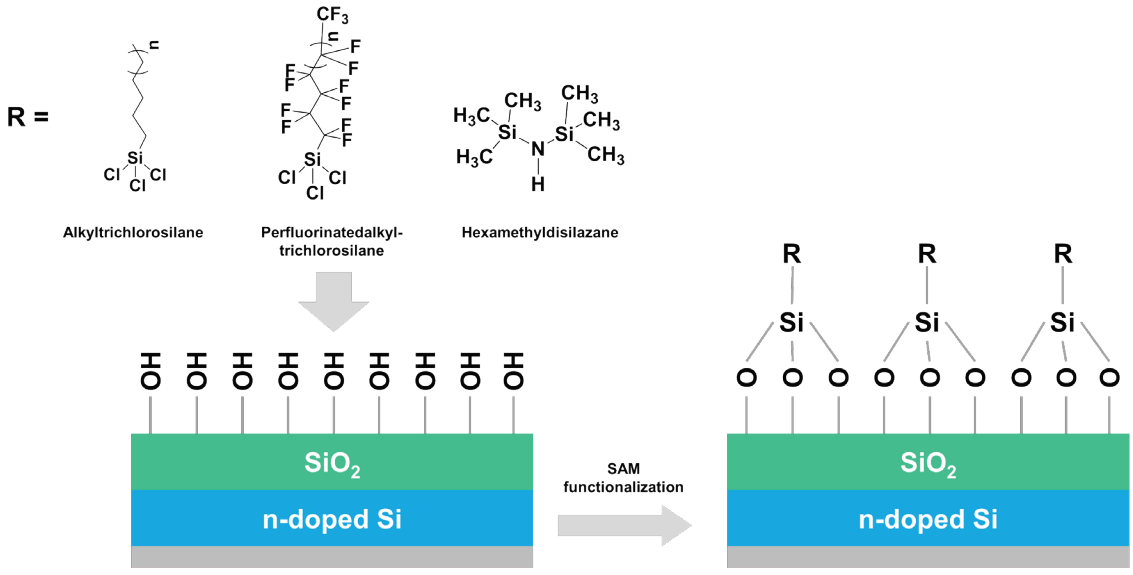

Figure 1.10. Schematic representation of self-assembly monolayer (SAM) functionalization to SiO_2 surface.

(HMDS).[166-168] The resulting surface turns from hydrophilic (water contact angle < 20°) to hydrophobic (water contact angle > 95° for SAMs with alkyl groups and 80-85° for HMDS).[169] The perfluorinated SAM treated surface in particular shows superhydrophobic characteristics, with a contact angle > 130°, which might lead to polymer ink dewetting on the substrate. Field-effect transistors often show approximately an order of magnitude enhancement in hole mobility when a SAM treatment is used in the device fabrication process. Possible reasons include that defects and silanol surface groups were largely eliminated through treatment; and/or that the presence of alkyl chains induces polymer semiconductor packing to turn from a "face-on" orientation to an "edge-on" orientation,[143, 170] which benefits the in-plane carrier transport from source to drain as shown in **Figure 1.11**.

In the real cases, however, it proves difficult to remove all electron traps with the SAM treatment. Therefore, *n*-channel transistors which are quite sensitive to electron traps generally require hydrophobic polymers as dielectrics, such as divinyltetramethylsiloxane-bis(benzocyclobutene) (BCB),[171-173] amorphous fluoropolymer CYTOP,[174, 175] polystyrene (PS),[176, 177] polyvinylpyrrolidone (PVP)[178], and poly(methyl methacrylate) (PMMA)[179]. These polymers have no hydrophilic functional groups and thus minimize electron traps on the dielectric layers. Compared with inorganic dielectrics such as SiO_2, and Al_2O_3, polymeric dielectric materials provide better interfacial interaction with organic and polymeric semiconductors.[180, 181] The resulting *n*-channel transistors generally show enhanced electron transport characteristics (higher mobility, higher $I_{ON/OFF}$, and reduced V_{th}) and minimized ambipolar features compared with devices fabricated with SAM pre-treated SiO_2 dielectric layers. For instance, **P(NDI2OD-T2)** (also known as "**N2200**")

showed an electron mobility close to 1 $cm^2V^{-1}s^{-1}$ based on OFETs with PS as the dielectric. Further, these amorphous polymer dielectrics can be used in fabrication of flexible and stretchable OFET devices based on PET substrates. It is worthy to mention that BCB needs to be formed via polymerization at 300-350 °C. It is thus commonly applied on BGTC transistor configurations, before casting organic and polymeric semiconductors; while the fluorinated CYTOP which has a low surface tension is primarily used in TGBC transistor configurations where it is coated on top of organic or polymeric semiconductors. The encapsulation of organic and polymeric FETs is necessary since the devices are in general sensitive to humidity and oxygen. Polymers such as CYTOP and perylene can be combined with inorganic materials including SiO_2 and Al_2O_3 to form organic- inorganic hybrid encapsulation layers.[175, 182, 183]

1.6.3 Organic and Polymeric Semiconductor Thin-Film Deposition

Small molecule semiconductors are frequently deposited onto FET substrates under high vacuum, where under optimized conditions it is possible to grow single-crystal thin-films. This deposition process needs to be conducted under thermal

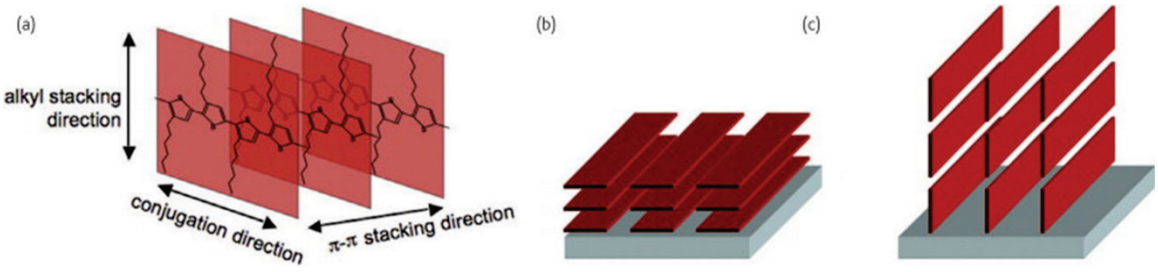

Figure 1.11. (a) Schematic illustration of the charge transport model in lamellae stacking conjugated polymer; (b) face-on texture of polymeric crystallites; (c) edge-on stacking texture, the π-stacking and the chain to chain packing of polymers. Reprinted with permission from *Mater. Today.* **2007**, 10 (3), 38-45. Copyright **2007** Elsevier.

evaporation rather than electron-beam evaporation conditions due to the high-energy associated with electron-beams: exposure of organic materials to an electron-beam often leads to film damage. Thin-film deposition approaches have significant impacts on the resulting thin-film morphology such as molecular orderings and orientation distributions, and thus the charge carrier transport behavior. Previously, it was thought that small molecule thin-films grown from vacuum deposition are superior to ones fabricated from solution-processes such as spin-coating. The spin-cast films are generally more disordered and have multi-crystalline characteristics compared with thermally deposited counterparts, which can severely limit charge carrier transport efficiency due to grain boundaries. However, studies have shown that for certain organic semiconductors, such as BTBT-C8 and pentacene, single-crystal thin-films could be formed through inkjet printing and solution shearing coating (blade coating).[184-188] Giri et al. reported their approach of obtaining lattice-strained TIPS-pentacene crystals via solution shearing on patterned substrates leading to the formation of highly strained, aligned, and single-crystalline TIPS-pentacene regions with mobility as high as 2.7 $cm^2 V^{-1} s^{-1}$.[187] Yuan et al. reported the alignment of BTBT-C8 parallel or perpendicular to source-drain electrodes on OFETs based on an off-center spin coating approach, during which the centrifugal force aligns the thin films.[184] The X-ray scattering characteristics unveiled a new packing structure that differed from the single-crystal film, demonstrating the feasibility that selected metastable molecular packing configurations may possess more efficient charge carrier transport pathways compared with the single-crystal packing that is typically observed.[184] It had been previously believed that the molecular packing associated with single crystal materials is the optimum for achieving the highest possible charge carrier transport for any one

material.

The high MW of polymers prevents film formation via thermal deposition. Spin-coating is widely used to afford uniform and isotropic thin films in lab environments. Film thickness is typically 50-100 nm, depending on the ink concentration, solvent, spinning speed (500-5000 rpm), and spinning time. Over the past decade, doctor blading, dip coating[189], strain stretching[190], poor solvent addition[191], topographical patterning[192], and thermal[193] or solvent vapor[194] annealing, among many others, have all been shown to cause significant enhancement of the charge carrier mobility in π-conjugated polymer-based OFET devices. The results of these studies have revealed the microstructural features that give rise to high-mobility devices: (i) highly ordered crystals with a high degree of electronic delocalization[142], (ii) edge-on orientation relative to the dielectric surface,[145, 195] and (iii) long-range interconnectivity between crystalline domains to form a percolation network for charge transport on the device scale.[196, 197]

An alternative approach for polymeric film formation is based on inkjet printing. The significant operational parameters include ink viscosity and surface tension, which could be manipulated through adjusting the material's concentration in the ink formulation and if necessary, the addition of additives. In comparison to traditional coating methods, inkjet printing allows fine control of the dose and position of active material and thus, the thickness, size and position of the semiconductor film formed on the device substrate, which potentially reduces ink consumption and issues associated with ink solvent emission; also, expensive photolithographic-patterning of the semiconductor films is avoided. Polymeric field-

effect transistors based on inkjet printing have been reported, and similar mobilities compared with transistors fabricated using the spin-coating approach were demonstrated.[175]

CHAPTER 2. DESIGN, SYNTHESIS AND CHARACTERIZATION OF DIKETOPYRROLOPYRROLE-THIAZOLE ALL-ACCEPTOR (A-A) *N*-CHANNEL POLYMERIC SEMICONDUCTORS AND APPLICATIONS IN OFETS

(This chapter is partially published in Chemistry of Materials **(2016)**, Yuan, Z. B.; Fu, B. Y.; Thomas, S.; Zhang, S. Y.; DeLuca, G.; Chang, R.; Lopez, L.; Fares, C.; Zhang, G. Y.; Bredas, J. L.; Reichmanis, E., 28 (17), 6045-6049.)

2.1 Abstract

In order to investigate the impacts of thiazoles in conjugated polymers, two all new thiazole-DPP based conjugated polymers, **PDPP2Tz** and **PDPP4Tz**, were designed and synthesized *via* Stille coupling. Unlike traditional donor-acceptor copolymers, thiazole-DPP based polymers consist of all electron poor units, which independently would act as electron acceptors. Frontier molecular orbital simulation results reveal that in **PDPP4Tz**, there is no clear electron donating nor electron accepting unit. Both holes and electrons are effectively delocalized along polymer conjugated backbone. Preliminary characterization suggested that **PDPP4Tz** possesses electron mobility reaching 0.07 $cm^2V^{-1}s^{-1}$ when incorporated into an organic field-effect transistor. Current *n*-channel and ambipolar conjugated polymers possess a donor-acceptor repeating unit configuration that contains electron donors such as bithiophene or vinylene, which dilute the electron deficiency. The concept identified in this study that couples one electron acceptor (distannane bithiazole) with a second electron acceptor to afford a pure *n*-channel conjugated polymer can be

considered as a general, efficient approach for the development of the next generation of *n*-channel conjugated polymers for device applications.

2.2 Introduction

As discussed in Chapter 1, conjugated polymers have attracted considerable attention for applications in organic electronic devices due to their easily modifiable structures, excellent solution processability, and potential for low-cost device fabrication.[7, 14, 16, 45, 198] Extensive synthetic research has enabled identification of several classes of high performance *p*-channel semiconductors[199, 200]; however, full realization of many potential applications requires access to effective electron transport or rather, *n*-channel solution processed organic/polymeric semiconductors. In particular, demands exist for high performance unipolar electron transporting polymers in applications such as organic field-effect transistors (OFETs), complementary metal-oxide-semiconductor (CMOS)-like logic circuits,[31, 88, 201] organic thermoelectrics,[91] all-polymer heterojunction photovoltaics,[200, 202-204] and organic light-emitting diodes.[29, 30] While ambipolar materials are an attractive alternative, their development has reached a 'glass ceiling' in that their hole and electron mobilities and current on/off ratios ($I_{ON/OFF}$) are generally far from equivalent. Thus, application of ambipolar organic or polymer semiconductors to devices such as CMOS circuits presents significant complications. As a result, it becomes necessary to employ both, unipolar *p*-channel and *n*-channel semiconductors in the design and fabrication of individual devices.[76]

Hence, viable approaches towards the design, synthesis and processing of purely electron transporting organic semiconducting polymers are critically needed.[64, 200, 201, 205-

[207] Not only are such materials essential to achieve advanced device performance, they are also required to ascertain critical structure-property relationships that govern the performance of active organic materials. This chapter talks about the homocoupling of bisthiazole-diketopyrrolopyrrole and the copolymerization of diketopyrrolopyrrole (DPP) with thiazole to afford two all-acceptor (A-A) conjugated polymers, **PDPP2Tz** and **PDPP4Tz**, respectively. Unfortunately, only **PDPP4Tz** shows promising characteristics for potential OFET application, while **PDPP2Tz** only possesses very low FET mobility. Therefore, this chapter mainly discuss the development of **PDPP4Tz** and its application in OFETs.

2.3 Results and Discussions

*2.3.1 Synthesis and Characterizations of **PDPP2Tz** and **PDPP4Tz***

Currently, examples of *n*-channel polymeric semiconductor platforms, which include **P(NDI2OD-T2)** and BDOPV-2T based polymers, are quite limited.[14, 72, 208, 209] The reported materials generally comprise one strong electron withdrawing moiety, such as NDI or BDOPV, coupled with one electron rich unit such as bithiophene, or a substituted vinylene within the repeating unit. The resulting polymers have typical donor-acceptor (D-A) features; whereby, the electron rich units tend to elevate the HOMO and LUMO energy levels of the system impairing efficient electron transport and oxidation resistance which are of critical significance for *n*-channel semiconductors.

The 2,2'-bithiazole unit is attractive for the development of organic[129] and polymeric semiconductors[76, 122, 210] due to molecular features that impart significant differences in electronic characteristics in comparison with bithiophene which is widely

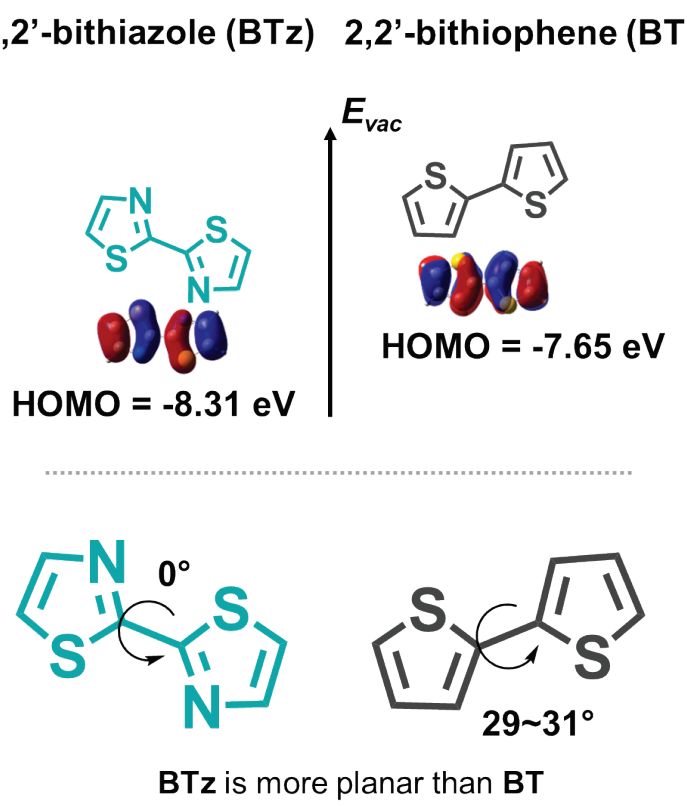

Figure 2.1. Comparison of 2,2'-bithiazole and 2,2'-bithiophene in HOMO energy level and molecular geometry.

used in many current D-A copolymers.[68, 124, 129, 210] (**Figure 2.1**) In particular, the presence of electronegative nitrogen atoms lowers the LUMO energy level; while the planarized *trans*-conformation and large dipole benefit intra-chain π-conjugation and inter-chain π–π interactions.[76, 125, 129, 211] Our recent study discussed a facile approach of metalation of bithiazole to afford a distannane monomer, and its facile coupling with brominated aromatic moieties to afford high molecular weight and strong electron withdrawing polymers was demonstrated.[76]

The bithiazole distannane monomer was co-polymerized with a brominated dithiazolediketopyrrolopyrrole (DTzDPP) to afford, the unipolar all acceptor *n*-channel conjugated polymer, poly(diketopyrrolopyrrole-tetrathiazole), **PDPP4Tz**. (**Scheme 2.1**)

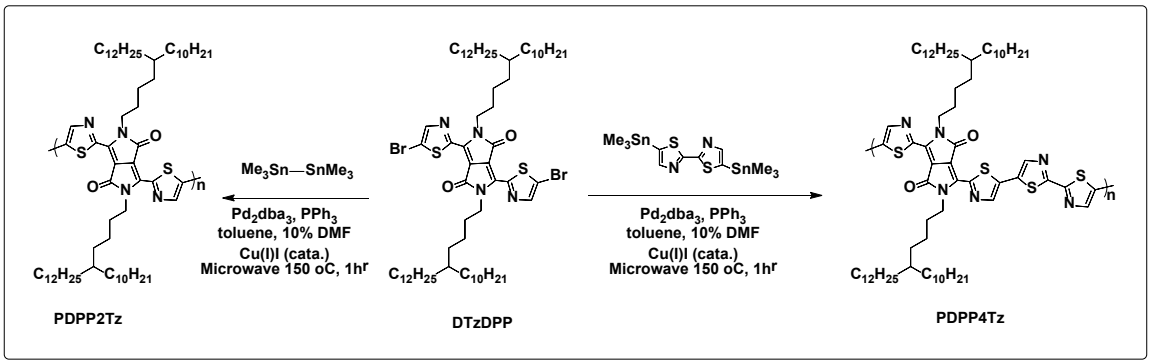

Scheme 2.1. Stille polymerization of monomer DTzDPP with hexamethylditin or 5,5'-bis(trimethylstannyl)-2,2'-bithiazole to afford **PDPP2Tz** and **PDPP4Tz**, respectively.

This polymer is among only a few reported cases of unipolar electron transport, *n*-channel polymers: the preliminary OFET characterization suggests that PDDP4Tz possesses promising macroscale, unipolar field-effect electron mobility as high as 0.067 $cm^2V^{-1}s^{-1}$. The choice of DTzDPP derives from its strong electron acceptor characteristics and recently shown promising electron transport properties in photovoltaic and OFET applications.[61, 64] To the best of our knowledge, this study, for the first time, demonstrates the feasibility of electron withdrawing bithiazole distannane to be coupled with other brominated electron acceptors to afford unipolar *n*-channel polymers; furthermore, PDDP4Tz represents the first example of an *n*-channel conjugated polymer comprised of all electron deficient moieties, which could be considered as an acceptor-acceptor, A-A, backbone structure. This suggests a potential approach to the development of the next generation of "all electron acceptor" A-A conjugated polymers having improved ambient stable, unipolar electron transport performance for organic electronic devices.

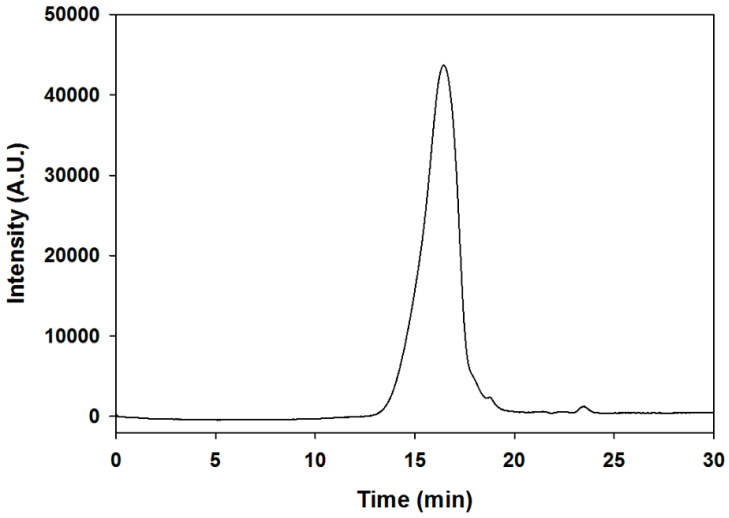

Peak#	Mn	Mw	Mz	Mz1	Mw/Mn	Mz/Mw
Total	26391	35687	51173	91104	1.35222	1.43395
1	26391	35687	51173	91104	1.35222	1.43395

Figure 2.2. Gel permeation chromatography (GPC) characterization of **PDPP4Tz** with TCB under 135 °C.

A branched 5-decylheptadecyl alkyl side chain is incorporated into brominated DTzDPP monomer to enhance polymer solubility.[76, 82] The freshly prepared trimethylstannyl bithiazole monomer was copolymerized with **DTzDPP** to afford the all electron acceptor conjugated polymer **PDPP4Tz**, via Stille step-growth polymerization[64, 76, 205-207] in toluene under microwave irradiation (150 °C for 1 hr) (**Scheme 2.1**). Gel permeation chromatography (GPC; 135 °C with 1,2,4-trichlorobenzene (TCB) as eluent) of **PDPP4Tz** revealed a number-average molecular weight (Mn) of 26 kg mol^{-1} and polydispersity index (PDI) of 1.3.(**Figure 2.2**) Thermogravimetric analysis (TGA, see S.I.) revealed a decomposition temperature greater than 410 °C; and differential scanning calorimetry (DSC) shows the presence of an endothermic transition upon heating (T_1 = 67

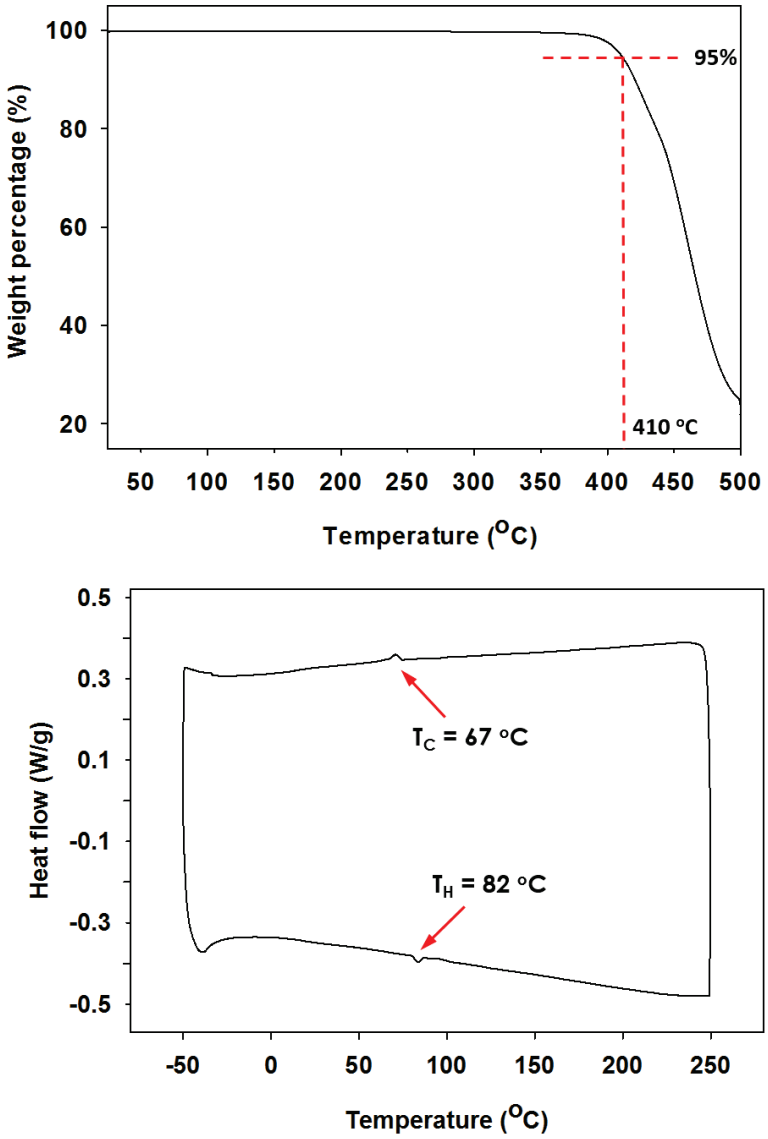

Figure 2.3. (top) TGA of polymer **PDPP4Tz** in a nitrogen atmosphere (25 mL/min) at a heating rate of 5 °C/min; (bottom) thermal transition characterization of **PDPP4Tz**. DSC characterization was based on the 2nd heating and cooling process in a nitrogen atmosphere with a nitrogen flow rate of 50 mL/min and a heating/cooling rate of 5 °C/min.

°C) and an exothermic transition during the cooling process (T_2 = 82 °C), suggesting the presence of ordered phases.[82] Such temperature transitions (higher than room temperature) are believed to represent a phase transition attributed to polymer backbone instead of alkyl side chains before entering an isotropic phase.[82] (**Figure 2.3**)

The initial approach to afford the A-A copolymer was through homo-coupling of brominated dithiazolediketopyrrolopyrrole (**DTzDPP**) monomer using hexamethylditin (**Scheme 2.1**). Such homo-coupling would afford a new A-A copolymer, poly(diketopyrrolopyrrole-bithiazole) (**PDPP2Tz**) that is likely to possess pure *n*-channel transport characterisitics. Preliminary results indeed show weak pure *n*-channel transport characteristics. However, the mobility was only in the range of 10^{-5}~10^{-4} $cm^2V^{-1}s^{-1}$ with a quite low on/off ratio of 10^1, leaving **PDPP2Tz** not suitable for OFET applications.

*2.3.2 **PDPP4Tz** Photophysical Properties*

PDPP4Tz UV-*vis* absorption spectra as shown in **Figure 2.4** exhibit similar absorption bands in both solution and thin films, with a maximum (λ_{max}) at 715 nm, which suggests that the polymer backbone experiences significant rigidity and aggregation in solution and thin-film form. The broader thin film absorption in the range of 750-770 nm suggests the probable self-assembly of **PDPP4Tz** into ordered aggregates that experience enhanced π-π intermolecular interactions.[76] A weak shoulder at ~765 nm in the solution spectra suggests that aggregates also form in the solution phase. Such low band-gap polymers have been found to enhance intramolecular charge transfer, which in turn improves charge carrier mobility.[7, 130, 212, 213] The optical gap evaluated from the solid-state absorption onset is *ca*. 1.34 eV.

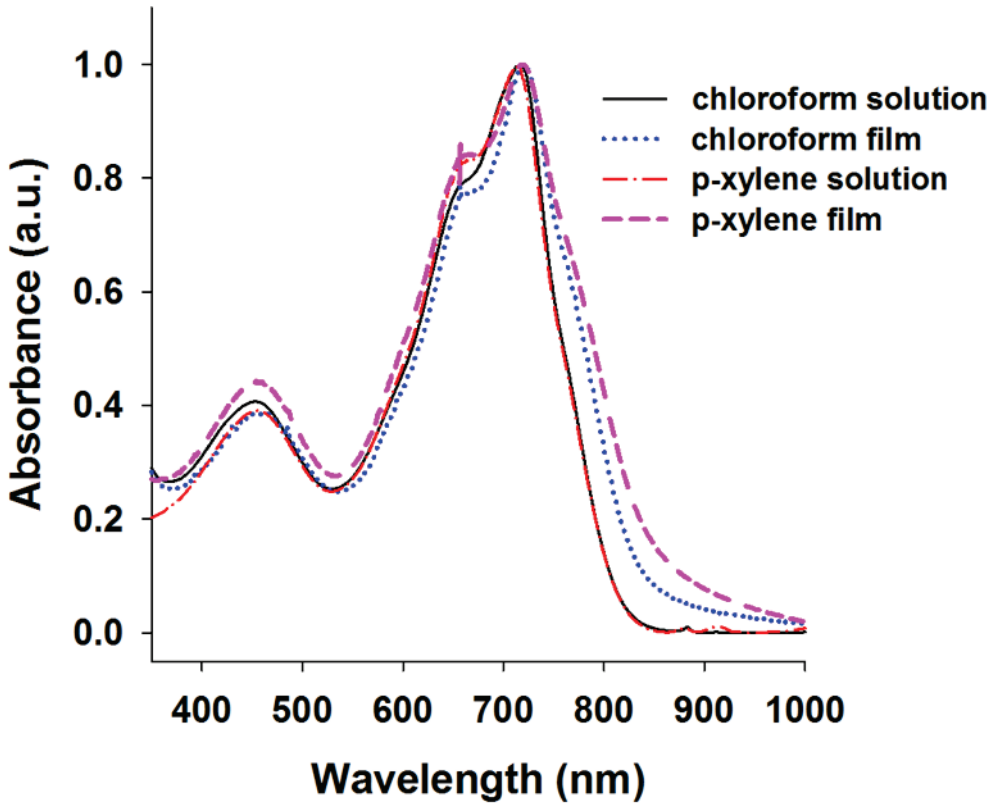

Figure 2.4. UV-*vis* absorption spectra of **PDPP4Tz** in solution and thin-film state (1×10^{-6} M; chloroform, *p*-xylene). Film UV-*vis* spectra were obtained by spincoating solutions onto UV-ozone cleaned SiO_2 slides before thermal annealing.

Ultraviolet Photoemission Spectra (UPS) were measured on a Kratos Axis UltraDLD XPS/UPS system, using He-I lamp radiation at 21.2 eV. All samples were in electronic equilibrium with the spectrometer via a metallic clip on the surface, and were run at a base pressure of 10^{-5} Torr. The Fermi level was calibrated using atomically clean silver. UPS were acquired at a 5 eV pass energy and 0.05 eV step size with the aperture and iris set to 55 μm. The secondary electron edge (SEE) of the UPS the work function (ϕ = 21.22-SEE) was calculated for each polymer, and from the emission close to the Fermi

level the position of valence band maximum was determined. IP (= –HOMO) and ϕ were calculated by equations (2.1) and (2.2):

$$IP = hv - \left(E_{cutoff} - \varepsilon_V^F\right) \tag{2.1}$$

$$\phi = hv - E_{cutoff} \tag{2.2}$$

where hv, E_{cutoff}, and ε_V^F denote the incident photo energy (He I, 21.22 eV), the high binding energy cutoff, and the lowest binding energy point, respectively.

Due to the effect of polymer/gold contact, there is a push-back effect (pillow effect) which leads to a significant decrease in work-function for the modified gold surface[214]. The modified work function of gold is closer to 4.3 eV, compared to the (111) surface of super clean gold in ultra-high vacuum (Φ_{Au} at 5.2 – 5.3 eV)[47, 214]. Therefore, the modified gold work function is closer to the EA of **PDPP4Tz** than the IP. The intrinsic ionization potential (IP) of **PDPP4Tz** is estimated to be 5.71 eV suggesting excellent ambient stability towards oxidation[7].(**Figure 2.5**) Taking into account an optical gap of *ca*. 1.34 eV and an exciton binding energy in the range of 0.3−0.5 eV, the electron affinity (EA) is estimated to be on the order of −3.9 to −4.1 eV[76, 215], which implies an electron transport potential with good

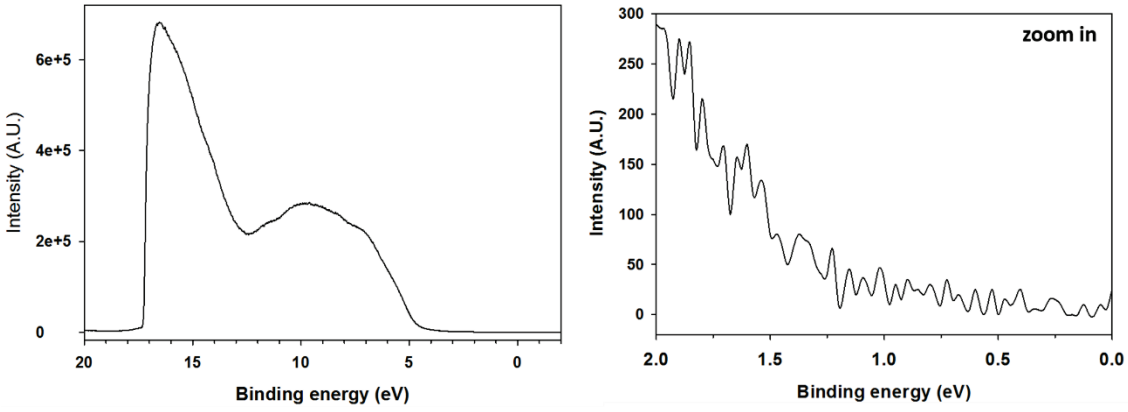

Figure 2.5. (left) UPS characterization of as-spun **PDPP4Tz** film on gold-coated Si wafer; (right) zoomed-in of lower binding energy region of the UPS spectrum.

ambient stability[86, 216]. Compared with our previous investigation on polymer PDBTz[76], in which the peripheral two thiazoles adjacent to DPP in **PDPP4Tz** were substituted by two thiophenes, **PDPP4Tz** has a *ca*. 0.2 eV increase in IP and EA under the identical measurement environment. The results indicate more stable charge carrier transport for the thiazole analog than thiophene.

*2.3.3 DFT Studies of **PDPP4Tz** oligomers and their subunits*

*(Section 2.3.3 is completed in collaboration with Dr. Simil Thomas and Dr. Jean-Luc Bredas at King Abdullah University of Science and Technology, Saudi Arabia, currently at Georgia Institute of Technology, Atlanta, Georgia, USA. **(2016)**)*

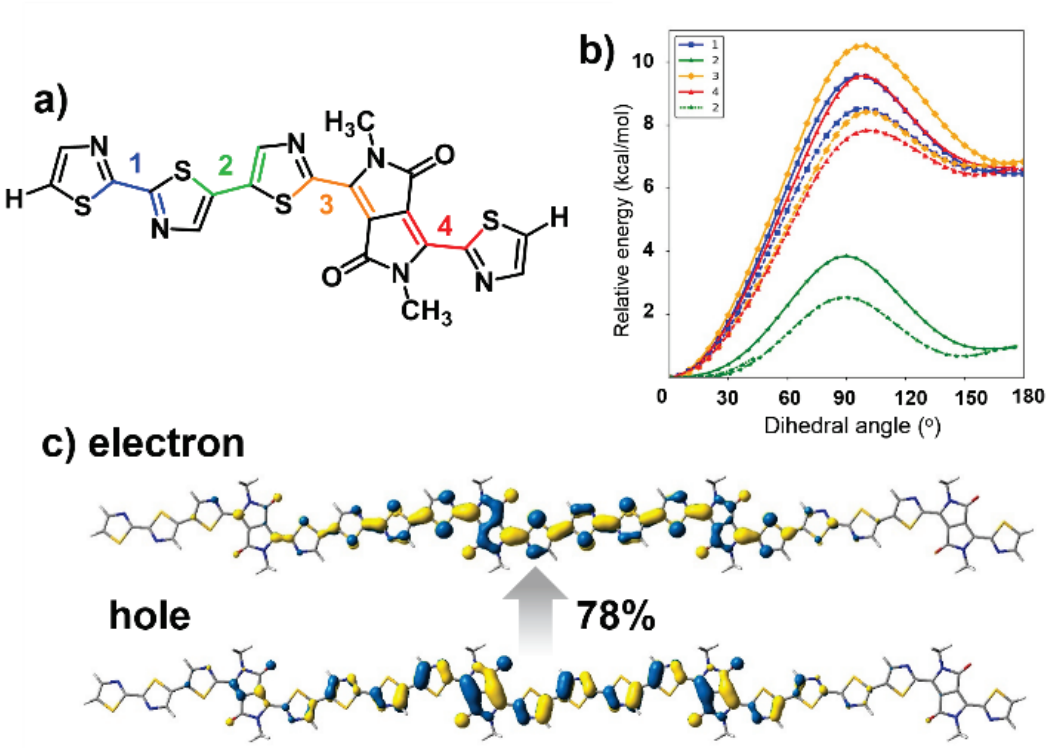

Figure 2.6. (a) Illustration of the torsion potentials related to the rotation of the adjacent units in the monomer of **PDPP4Tz**; (b) relative DFT energies at the tuned-ωB97XD/6-31G(d,p) (dashed lines) and B3LYP (solid lines) levels; (c) tuned-ωB97X-D/6-31G(d,p) natural transition orbitals with the largest weight (78%) for the S_0 to S_1 transition in the **PDPP4Tz** tetramer.

DFT calculations were carried out on oligomers of **PDPP4Tz** with the Gaussian 09 Revision D.01 suite of programs;[217] we considered the tuned-ωB97X-D functional along with the 6-31G(d,p) basis set for the time-dependent density functional theory (TDDFT) calculations (for the sake of comparison with many other results reported in the literature, we also considered the B3LYP functional, even though it is well established to wrongly overdelocalize wavefunctions and thus maximize torsion potential barriers in conjugated polymers). The IP-tuning procedure[218, 219] is carried out with chloroform taken as the dielectric medium (ε = 4.71) to be consistent with experiment, within the self-consistent reaction field (SCRF) framework, to calculate the range separation parameter (ω). The

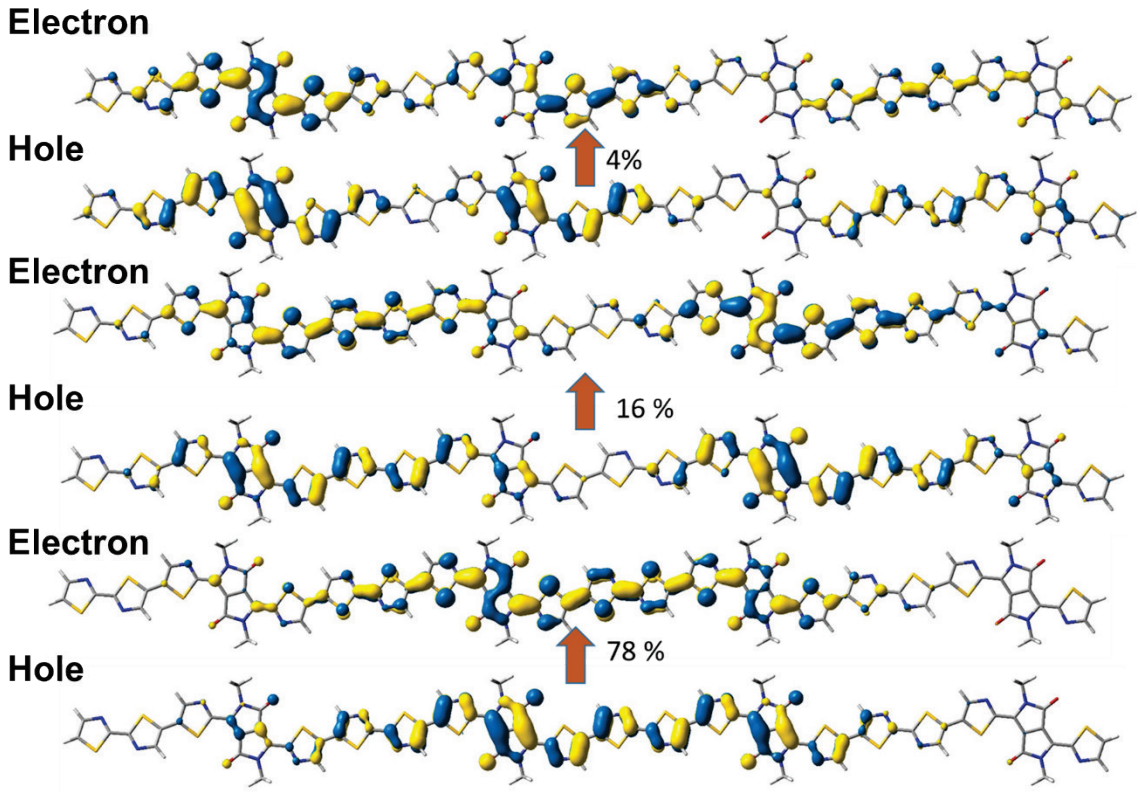

Figure 2.7. Electron-hole pair natural transition orbitals (isovalue surface 0.02 a.u.) for the S_0 to S_1 transition of the **PDPP4Tz** tetramer calculated by TD-DFT at tuned-wB97X-D/6-31G(d,p) level of theory. The weights of the particle-hole contribution to the excitation are included.

Table 2.1. Calculated valence band (VB) width, conduction band (CB) width, band gap, and hole and electron effective masses for the **PDPP4Tz** polymer.

Polymer	Width of VB (eV)	Width of CB (eV)	Band Gap (eV)	m_h/m_0	m_e/m_0
PDPP4Tz	0.25	0.34	1.32	0.18	0.15

optical gap of the **PDPP4Tz** oligomers levels off at 4 repeat units (**Figure 2.6)**; it corresponds to 1.74 eV at this oligomer size, which is close to the experimental optical gap of 1.72 eV estimated from the UV−*vis* absorption maxima in chloroform (experimental optical gap evaluated from the onset of absorption is *ca*. 1.34 eV).

The dominant natural transition orbital (NTO) of the **PDPP4Tz** tetramer for the S_0 to S_1 transition, at tuned-ωB97X-D/6-31G(d,p) level of theory, is well delocalized along the polymer backbone for both hole and electron (**Figure 2.7**); the spin density for the unpaired electron corresponding to the electron-polaron (anion) of the **PDPP4Tz** tetramer is calculated to be delocalized over one full repeat unit, or about 8 to 10 rings (**Figure 2.8**). The electronic band structure of the polymer chain has been modeled using the CRYSTAL14 code.[220] In that instance, the polymer geometry was optimized at the B3LYP level,[221] and the electronic band structure calculated at the HSEsol functional level.[222] The Peintinger-Oliveira-Bredow triple-ζ valence plus polarization (POB-TZVP) basis set[223] using 2k points as set by the Pack-Monkhorst method,[224] was considered for all these

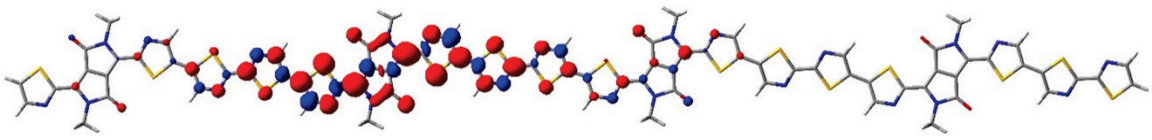

Figure 2.8. Tuned-ωB97X-D spin density plots for the anion of the **PDPP4Tz** tetramer (the red and blue colors represents spin up and spin down electron densities, respectively).

calculations. The effective mass for the polymer chain was calculated at the bottom of the conduction band using the band fitting method.[225]

The electronic band structure of the polymer chain was also calculated with the CRYSTAL14 code[226], using the HSEsol functional[222]. The band structure of the **PDPP4Tz** polymer is shown in **Figure 2.9**. The band gap of the **PDPP4Tz** polymer is calculated here to be 1.32 eV. The effective mass of an electron (at the bottom of the conduction band) and hole (at the top of the valence band) are calculated (See **Table 2.1**).Importantly, the electron effective mass for the polymer chain evaluated at the bottom of the conduction band is very small, on the order of 0.15 m_0, the free electron mass. This result underlines that well-oriented **PDPP4Tz** chains should display very high electron mobilities[227].

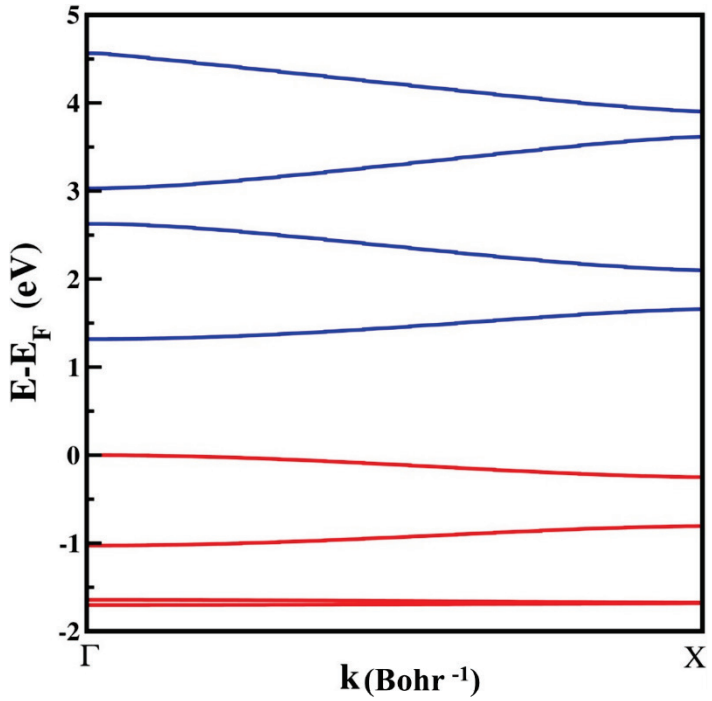

Figure 2.9. HSEsol//B3LYP electronic band structure of the **PDPP4Tz** chain. The zero of energy corresponds here to the top of the valence band.

The range-separation parameter (ω, in $Bohr^{-1}$) of the ωB97X-D functional was optimized for the oligomers of **PDPP4Tz** using the IP tuning procedure.[228, 229] The alkyl chains in the **PDPP4Tz** unit were replaced with methyl groups to reduce the computational time. The geometry was first optimized at the ωB97X-D/6-31G(d,p) level of theory; the IP tuning procedure was then applied to calculate the optimal ω-value for this geometry. The geometry was then re-optimized using the new ω-value and this procedure was iterated until the change in ω became less than 10^{-3} $Bohr^{-1}$ (the tuned ω-value for the optimized monomer geometry is used throughout the subsequent torsion potential scans). The torsion potentials between adjacent units of **PDPP4Tz** were computed at 5° intervals by fixing the dihedral angle and relaxing all other geometrical degrees of freedom (from -180° to 180°) using the tuned-ωB97X-D and B3LYP functionals. All the PES curves in **Figure 2.6b** have two minima with the minimum at 0° lower-lying in energy than that near 180°. The energy barrier heights separating these two minima are 8.6 [9.6], 2.5 [3.8], 8.5 [10.5], and 7.8 [9.6] kcal mol^{-1} respectively for 1, 2, 3, and 4 using tuned-ωB97XD [B3LYP] functional as shown in **Figure 2.6a** and **b**. Since these barrier heights are significantly higher than thermal energy at room temperature (0.6 kcal mol^{-1}), the **PDPP4Tz** polymer backbone is expected to be largely planar in the solid state. Importantly, the dominant tuned-ωB97X-D/6-31G(d,p) natural transition orbital (NTO) describing the S_0 to S_1 transition in the **PDPP4Tz** tetramer, is delocalized along the polymer backbone for *both* the hole and electron (**Figure 2.6c**). This feature underlines the difference between **PDPP4Tz** with regard to typical D-A copolymers that generally display a localized electron NTO.

2.3.4 ***PDPP4Tz*** *Thin-film Morphology and Crystallinity*

PDPP4Tz thin-film surface morphologies were investigated using tapping mode atomic force microscopy (AFM) as shown in **Figure 2.10.** Polymer films were spin-cast and blade-coated onto OTS-18 functionalized SiO_2 on Si substrates. All blade-coated

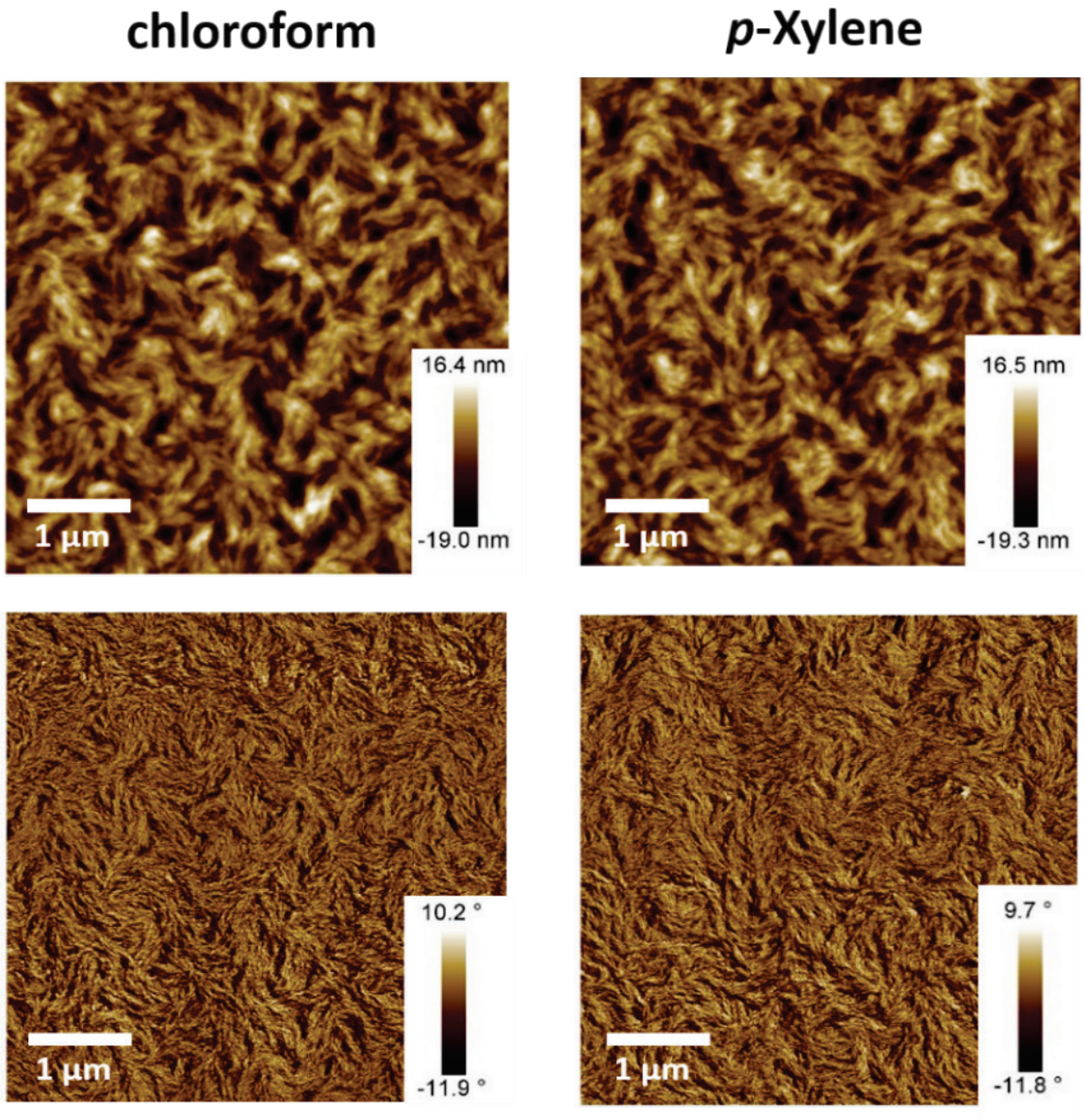

Figure 2.10. Tapping mode AFM height (top row) and phase (bottom row) images of **PDPP4Tz** blade coated films recorded after thermal annealing each film at 150 °C for 90 min followed by rapid cooling to room temperature in a nitrogen filled glove box.

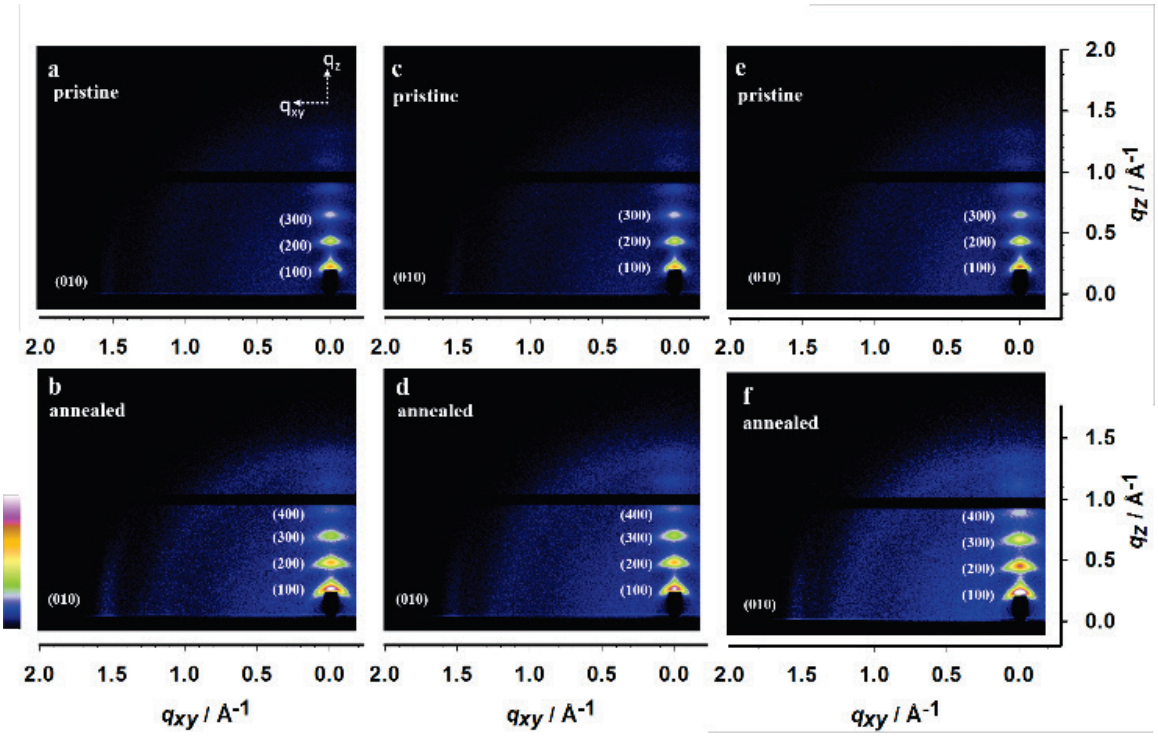

Figure 2.11. GIWAXS area detector images of **PDPP4Tz** films cast from (a,b) chloroform by spincoating; (c,d) chloroform by blade coating; (e,f) *p*-xylene by blade coating. (a,c,e) pristine films; (b,d,f) samples after annealing at 150 °C for 90 min followed by rapid cooling to room temperature.

polymer films exhibited consistent surface morphology patterns, appearing highly ordered with a feathery-like texture. The annealed films appeared with a nano-granular character, which is consistent with the high crystallinity revealed by GIWAXS.

Polymer thin-film microstructure was investigated by grazing incidence wide angle X-ray scattering (GIWAXS). Films were prepared by spin- and blade-coating solutions of **PDPP4Tz** onto Si-substrates. Both pristine and thermally annealed films were studied and exhibited well-defined (*h*00) diffraction patterns along the q_z (out of plane) axis corresponding to a highly ordered lamellar structure; and (010) peaks along the q_{xy} (in-plane) axis arising from π-π stacking of polymer backbones, as shown in **Figure 2.11**. A lamellar *d* spacing of 26.4 Å was derived from the (*h*00) peak, and the π-π stacking (010)

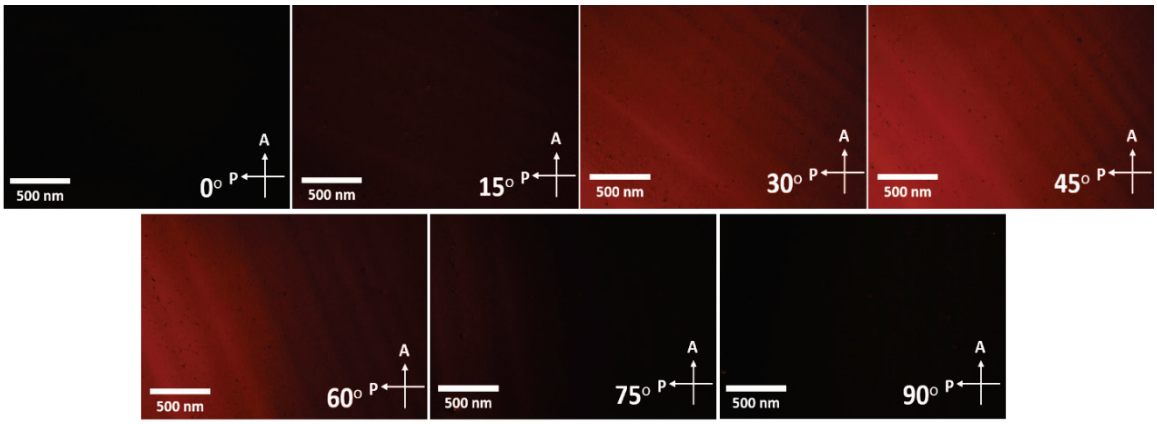

Figure 2.12. Polarized Optical Microscope (POM) images of blade-coated **PDPP4Tz** films on glass slides (chloroform as solvent).

peak has an associated *d* spacing of 3.4 Å. The fact that both (*h*00) and (010) exhibited enhanced intensities after thermal annealing (**Figure 2.11**) demonstrates an improvement in ordering within thin films and a more desirable edge-on orientation due to the annealing process, which, in turn, is believed to constructively favor polymer field-effect charge carrier transport in solid-state films.

Given the importance of molecular order in determining the charge transport characteristics in π-conjugated polymers, **PDPP4Tz** exhibits anisotropy within thin films fabricated with blade-coating, as observed under polarized optical microscopy (**Figure 2.12**). Thin films were cast from both filtered **PDPP4Tz** chloroform and *p*-xylene solutions (4~6 mg/mL) onto UV-ozone cleaned glass slides at room temperature. The observed birefringence indicates that **PDPP4Tz** polymer chains adopt a highly self-organized morphology, which allows the chains to form ordered anisotropic domains in thin-films. As intermolecular charge transport across grain boundaries, or through disordered domains is not as efficient as within ordered domains, increasing the grain size is expected to be a favorable approach to increase charge-carrier mobility.

2.3.5 *Thiazole-DPP A-A Copolymers for OFET Applications*

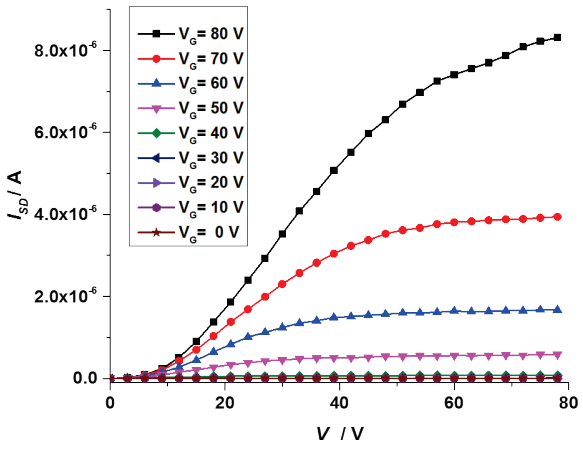

Figure 2.13. Output characteristics of the bottom-gate/bottom-contact (BG/BC) transistors fabricated by spincoating *p*-xylene solution of **PDPP4Tz.**

The charge carrier transport properties of **PDPP4Tz** were investigated using a bottom-gate/bottom-contact (BGBC) OFET device architecture. BGBC OFETs were fabricated on a heavily *p* doped silicon wafer (100) as the gate electrode with a 300 nm thick layer of thermally grown SiO_2 as the gate dielectric. Au source and drain contacts (50 nm of Au contacts with 3 nm of Cr as the adhesion layer) with fixed channel dimensions (50 μm in length and 2 mm in width) were deposited via E-beam using a photolithography lift-off process. Prior to deposition of polymer semiconductors, the devices were cleaned in acetone for 30 min and subsequently rinsed sequentially with acetone, methanol and isopropanol. The SiO_2 surface was pretreated by UV/ozone for 30 min followed by immersion into a 2.54 x 10^{-3} M (1 µL mL^{-1}) solution of OTS-18 in anhydrous toluene. The devices were then cleaned by sonication in toluene for 10 min, followed by rinsing sequentially with acetone, methanol and isopropanol, and drying under a flow of nitrogen. The H_2O contact angle for the SiO_2 surface after OTS-18 treatment was in the range of 95–

105°; the OTS-18 modified SiO_2 dielectric has a capacitance of *ca*. 1.1 x 10^{-4} Fm^{-2}. **PDPP4Tz** solutions were then spin-coated onto substrates inside a N_2 filled glovebox or blade coated in ambient condition.

In this study, the threshold voltage, V_{th}, was calculated by extrapolating $V_{th} = V_G$ at $I_D = 0$ in the V_G *vs.* $I_D^{1/2}$ curve. Current on/off ratio, $I_{ON/OFF}$, was determined through dividing maximum I_D (I_{ON}) by the minimum I_D at about V_G in the range of -20 to 0 V (I_{OFF}). It is noted that **PDPP4Tz** field-effect mobility was more stable and hysteresis was reduced after thermal annealing at 150 °C for 90 min in OFETs and no obvious improvement was observed at annealing temperatures above 150 °C. The thermal annealing treatment was hence fixed at 150 °C for 90 min.

Unlike many D-A π-conjugated polymers which show ambipolar transport characteristics such as PDBTz, **PDPP4Tz** based OFETs exhibited purely *n*-channel

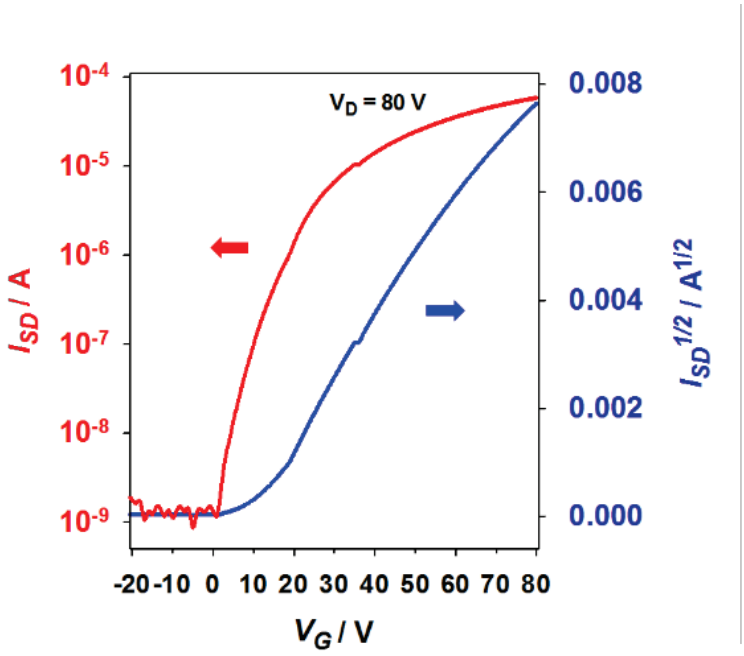

Figure 2.14. Transfer characteristics of the bottom-gate/bottom-contact (BGBC) transistors fabricated by spincoating *p*-xylene solution of **PDPP4Tz**.

transport feature even using Au electrodes as shown in **Figure 2.13**: no obvious source-drain current (I_D) was detected under negative gate voltage (V_G); while $I_D > 1$ μA with V_G < -40V was observed for a **PDBTz** based OFET with Au electrodes in a side-by-side comparison. **PDPP4Tz** output scans were performed in range of VG from 0V to 80V with VD from 0 V to 80 V (**Figure 2.14**). Shown in **Table 2.2**, **PDPP4Tz** exhibited an electron mobility (μ_e) in a range of 0.02~0.07 $cm^2V^{-1}s^{-1}$ with current on-and-off ratio ($I_{ON/OFF}$) of 10^4-10^5 based on spin-cast and blade-coated films. These results, for the first time, confirm the concept of developing unipolar *n*-channel conjugated polymers via constructing an all electron acceptor A-A polymer backbone. It is noteworthy that the field-effect μ_e of **PDPP4Tz** on OFETs could be further improved after in-depth device design and optimization, for example, by incorporation into bottom-gate/top-contact or top-gate/bottom-contact FETs, such as previously reported for **P(NDIOD2-T2)**[14] and BDOPV based polymers.[150, 230] Interestingly, μ_e of **PDPP4Tz** solution processed from *p*-xylene is

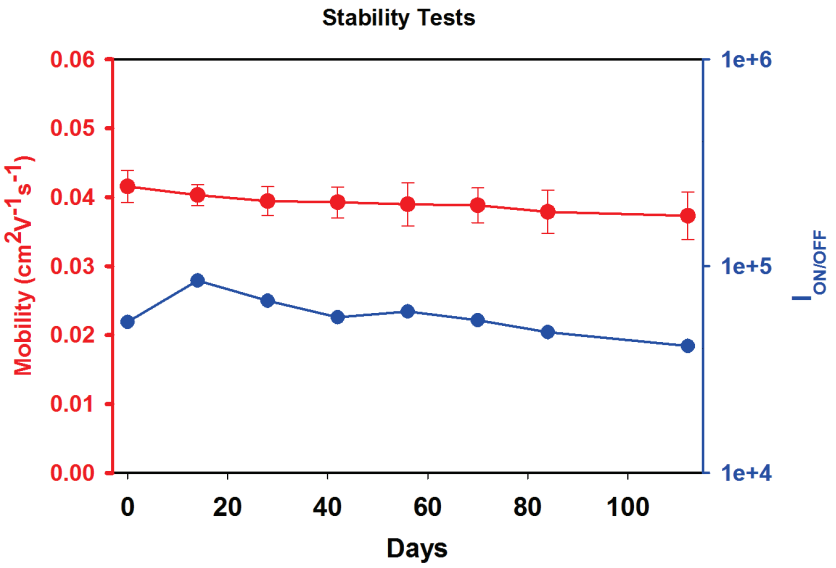

Figure 2.15. PDPP4Tz OFET stability under ambient conditions (25 ºC and 50-60% RH). Devices are fabricated on Si-wafers based on the BGBC configuration. Mobility data were measured in a nitrogen filled glovebox with devices stored in vacuum chamber for 12 hours to remove moisture and residual air.

Table 2.2. Electron transport properties of **PDPP4Tz** fabricated on bottom-gate-bottom-contact OFETs

Sample	Solvent	Coating	Annealed	μ_{eFET} ($cm^2V^{-1}s^{-1}$)		V_{th} (V)	$I_{ON/OFF}$
				avg.	max		
a	chloroform	Spincoating	No	0.020 ± 0.004	0.026	6.2 ± 1.8	10^4 -10^5
b	chloroform	Spincoating	Yes	0.044 ± 0.006	0.052	0.6 ± 0.4	10^4 -10^5
c	chloroform	Blade coating	No	0.018 ± 0.001	0.020	16.2 ± 0.9	10^4 -10^5
d	chloroform	Blade coating	Yes	0.034 ± 0.002	0.037	28.3 ± 3.5	10^4 -10^5
e	*p*-xylene	Blade coating	No	0.015 ± 0.001	0.017	31.5 ± 4.6	10^4 -10^5
f	*p*-xylene	Blade coating	Yes	0.053 ± 0.009	0.067	5.7 ±2.6	10^4 -10^5

BG/BC characterization results were based on 6 devices prepared using each fabrication condition. Devices (b, d, and f) were thermally annealed at 150 °C for 90 min followed by rapid cooling to room temperature.

about twice that for devices fabricated from chloroform. These results suggest the feasibility to produce *n*-channel polymeric OFETs using nonhalogenated, more environmentally benign solution process options. Thermally annealed films exhibited a 2-4 fold increase in μ_e over pristine films, which correlates well with the observed GIWAXS

results. To explore **PDPP4Tz** air stability, devices were stored at 25 °C and 50−60% RH, and were characterized periodically over 4 months. No appreciable decline was observed in μ_e and $I_{ON/OFF}$ over this period (**Figure 2.15** Effect of OFET stability under ambient conditions (25 ^oC and 50-60% RH). Devices are fabricated on Si-wafers based on the BGBC configuration. Mobility data were measured in a nitrogen filled glovebox with devices stored in vacuum chamber for 12 hours to remove moisture and residual air.). The ambient stability correlates with the low frontier energy levels of the system.

2.4 Conclusion

In conclusion, two electron deficient conjugated polymers, **PDPP2Tz** and **PDPP4Tz**, were designed and synthesized *via* Stille coupling. Copolymerization of 2,2'-bithiazole with bithiazole-diketopyrrolopyrrole afforded a new "all-acceptor" (A-A) conjugated polymer, **PDPP4T**. By characterizations based on OFETs, **PDPP4Tz** was proven to be suitable for *n*-channel organic electronic applications. Another A-A copolymer, **PDPP2Tz**, was also synthesized via homocoupling of bisthiazole-diketopyrrolopyrrole, but **PDPP2Tz** showed a very low FET mobility and is not desirable for OFET applications.Unlike traditional D-A copolymers, **PDPP4Tz** provides the first case study of a unipolar *n*-channel polymeric semiconductor comprised of all electron withdrawing moieties. For example, in comparison to the D-A PDBTz having electron rich thiophenes, **PDPP4Tz** exhibited unipolar field-effect electron mobility in OFETs even using Au electrodes, indicative of enhanced electron deficiency due to the presence of thiazole, and thus pure *n*-channel transport behavior. Current *n*-channel and ambipolar conjugated polymers widely adopt a D-A structure with repeating units that couple one acceptor with one donor; the donor moieties in turn dilute polymer electron deficiency. The

concept presented in this study that couples one electron acceptor (distannane bithiazole) with another to afford an *n*-channel conjugated polymer can be considered as an alternate, effective approach for developing the next generation of electron tranport conjugated polymers for device applications.

CHAPTER 3. DESIGN, SYNTHESIS AND CHARACTERIZATION OF NAPHTHALENE DIIMIDE-THIAZOLE *N*-CHANNEL POLYMERIC SEMICONDUCTORS AND APPLICATIONS IN OFETS

(This chapter is partially published in Macromolecules (2018), Yuan, Z.; Buckley, C.; Thomas, S.; Zhang, G.; Bargigia, I.; Wang, G.; Fu, B.; Silva, C.; Brédas, J.-L.; Reichmanis, E., 51 (18), 7320-7328.)

3.1 Abstract

Conjugated monomers and polymers containing 2,2'-bithiazole (BTz) and naphthalene diimide (NDI) units in the main chain were prepared. Polymer **PNDI2Tz** was obtained via palladium-catalyzed Stille polycondensation of a dibromo-substituted NDI derivative with distannyl-2,2'-bithiazole. The optical and electronic properties were investigated using UV-*vis* absorption spectroscopy and ultraviolet photoelectron spectroscopy. It was found that the polymers show very broad absorption bands in the 540 nm region, and **PNDI2Tz** has an optical bandgap of 1.87 eV. Computational analysis demonstrates that holes and electrons are mainly localized on the 2,2'-bithiazole and NDI units, respectively. Organic field-effect transistors (OFETs) fabricated with **PNDI2Tz** exhibit unipolar *n*-channel characteristics with mobility as high as 0.05 $cm^2V^{-1}s^{-1}$.

3.2 Introduction

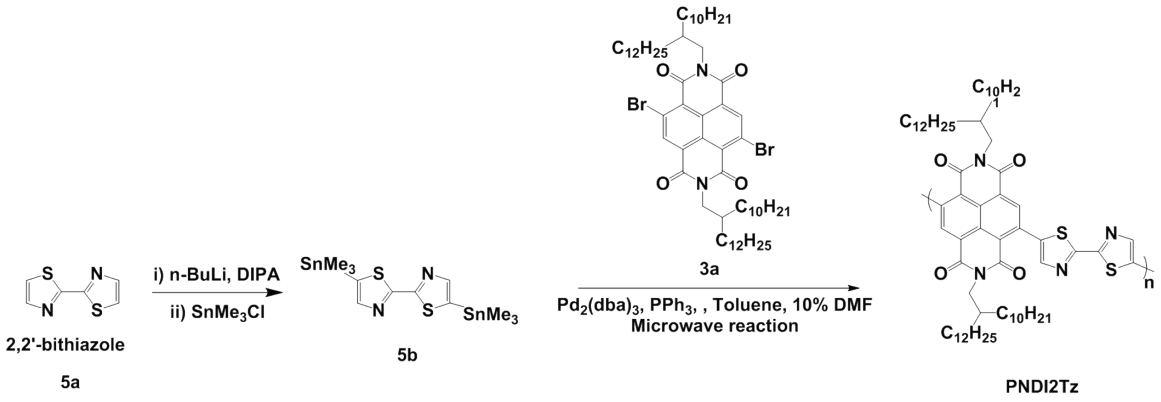

Scheme 3.1. Synthesis of poly(2,7-bis(2-decyltetradecyl)-4-methyl-9-(5'-methyl-[2,2'-bithiazol]-5-yl)benzo[lmn][3,8]phenanthroline-1,3,6,8(2H,7H)-tetraone) (**PNDI2Tz**).

Organic semiconducting materials, and the organic field-effect transistors (OFETs) they facilitate, have received tremendous attention in recent years because of their promising future applications in several technology sectors.[119, 231-234] As a number of organic *p*-channel (hole transporting) and ambipolar semiconductors with relatively high hole mobilities ($\mu > 1$ $cm^2V^{-1}s^{-1}$) have become commercialized,[62, 63, 65] attention is shifting to the design and development of their *n*-channel (electron transporting) counterparts.[119, 235, 236] Potentially useful *n*-channel building blocks can be found among the various electron deficient organic structures.[16] Among these, naphthalene diimide (NDI) has been extensively studied for its planarity and high ionization potential (*i.e.*, low lying HOMO energy level) that can significantly contribute to the *n*-channel characteristics of resulting polymers.[14, 67, 69, 70, 98] Another electron deficient building block, 2,2'-bithiazole (BTz) has attracted growing interest.[64, 76, 90, 120, 121] For instance, Fu *et al.* demonstrated that compared to electron-rich bithiophene (BT), bithiazole can significantly increase the ionization

potential and electron affinity (lower the HOMO and LUMO energy levels) of resulting copolymers comprising the thiazole and diketopyrrolopyrrole conjugated polymers.[76]

In this chapter, the synthesis and characterization of the naphthalene diimide-bithiazole based conjugated polymer, **PNDI2Tz** (**Scheme 3.1**) *via* palladium-catalyzed Stille polycondensation is reported. Computational studies were conducted to characterize the nature of the frontier energy levels, electron density distributions, and molecular geometries. The polymer electronic performance was also evaluated by incorporating the conjugated polymer as the semiconducting layer in organic field-effect transistor (OFET) devices.

3.3 Results and Discussion

*3.3.1 Synthesis and Characterization of **PNDI2Tz***

The electron deficient thiazole ring was recently introduced as a viable acceptor in the search for efficient electron transporting semiconducting polymers.[76, 90, 120, 121, 237] Previous studies explored the copolymerization of thiazoles with electron donors such as thiophene[213, 238] and thienothiophene[48-50] and the electron acceptor, diketopyrrolopyrrole (DPP)[56, 63, 65, 205], revealing the potential of thiazoles as viable units that could be incorporated into organic and polymeric electronic materials.[90, 121, 239-241] As bithiazole is intrinsically planar (with a torsion angle between the two thiazole rings of essentially 180 °C),[90] integrating bithiazole into the design of semiconducting polymers would be expected to promote electron delocalization and afford higher electron affinities (lower resultant polymer lowest unoccupied molecular orbital (LUMO) energy level). In this study, thiazole was co-polymerized with an alkyl substituted NDI through Stille step-growth

polymerization in a microwave reactor to afford the polymer, poly(2,7-bis(2-decyltetradecyl)-4-methyl-9-(5'-methyl-[2,2'-bithiazol]-5-yl)benzo[lmn][3,8]phenanthroline-1,3,6,8(2H,7H)-tetraone) (**PNDI2Tz**) **(Scheme 3.1)**. The as obtained **PNDI2Tz** had a mass average molecular weight of 45,000 g mol^{-1} and polydispersity index (PDI, $Đ$) of 3.5. The 2-decyltetradecyl side-chain was introduced to enhance solubility in common organic solvents,[76, 90] such as chloroform, dichlorobenzene, and xylenes. Note that the polymer chemical structure is such that the thiazole nitrogen atoms point away from the NDI moieties: this molecular architecture minimizes the possibility of unfavorable thiazole nitrogen – NDI oxygen interactions.

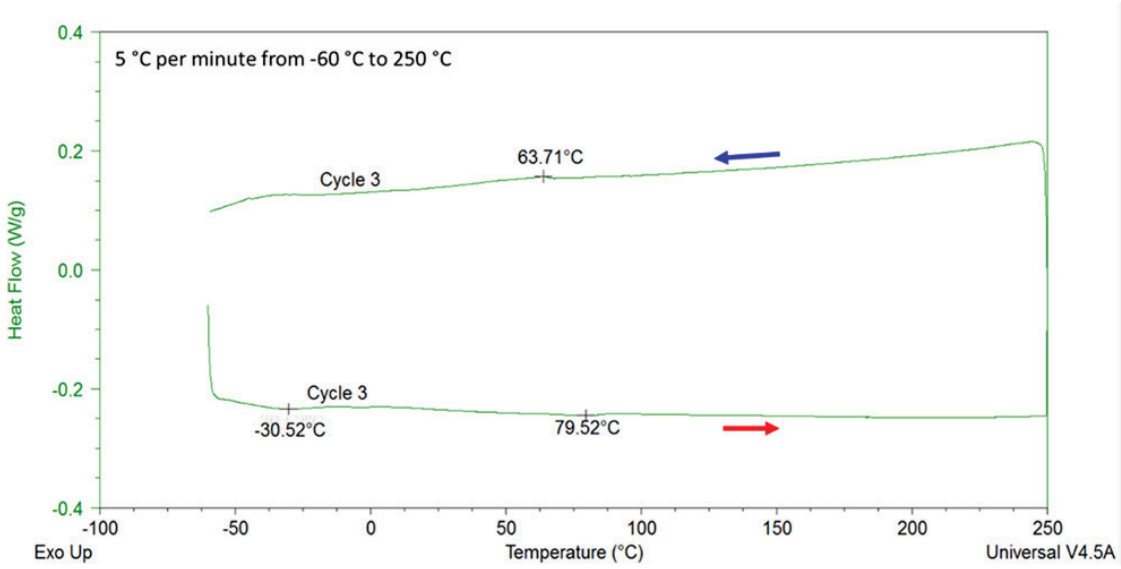

Figure 3.1. Thermal transition characterization of **PNDI2Tz**. DSC characterization was based on the 3rd heating and cooling process in a nitrogen atmosphere with a nitrogen flow rate of 50 mL/min and a heating/cooling rate of 5 °C/min.

PNDI2Tz exhibited excellent thermal stability up to 427 °C as determined by thermogravimetric analysis (TGA). Differential scanning calorimetry (DSC) was used to elucidate additional polymer physical properties such as glass transition temperature (T_g)

and melting behavior. **PNDI2Tz** has a T_g at 63.7 °C which most likely originates from the branched alkyl side chains. No melting transitions were identified within the temperature range from -60 °C up to 250 °C, suggesting that **PNDI2Tz** has a low degree of crystallinity. TGA and DSC scans are provided in **Figure 3.1**. In addition to exhibiting high thermal stability, **PNDI2Tz** was found to be chemically stable in both the solid and solution states for at least 12 months when stored under ambient conditions. No efforts were made to exclude light during this period.

*3.3.2 Photophysical properties of **PNDI2Tz***

PNDI2Tz optical characteristics were evaluated through UV-*vis* (**Figure 3.2**) and ultraviolet photoelectron spectroscopy (UPS) (**Figure 3.3**). The solution spectra (**Figure 3.2a**) display no significant solvatochromism in common organic solvents (chloroform, toluene, *p*-xylene, chlorobenzene, and dichlorobenzene). A minor bathochromic shift was observed for solution spectra of **PNDI2Tz** in 1,2,4-trichlorobenzene (TCB), which is believed to be due to lower solubility of the polymer in TCB leading to enhanced polymer-

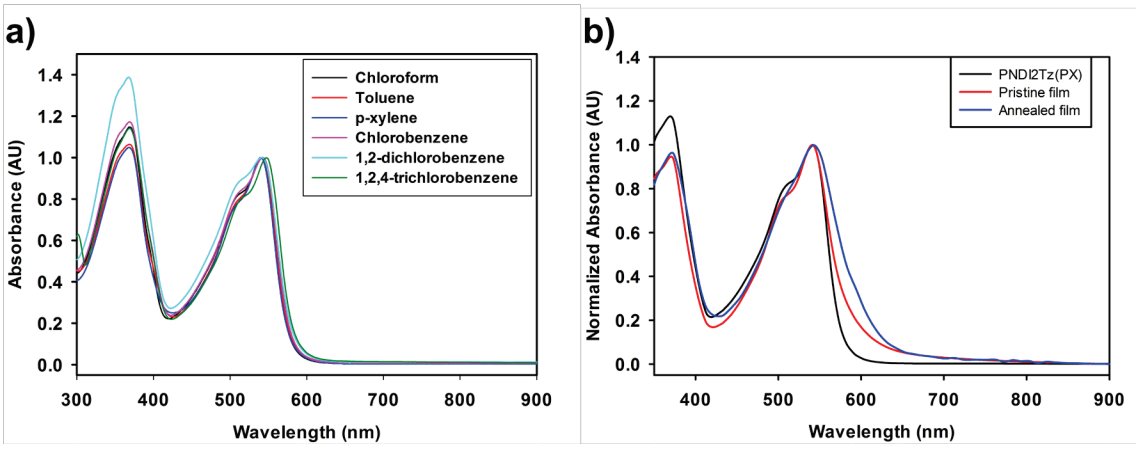

Figure 3.2. a) UV-*vis* spectra of **PNDI2Tz** in various organic solvents; b) Comparison of **PNDI2Tz** solution and thin-film UV-*vis* spectra.

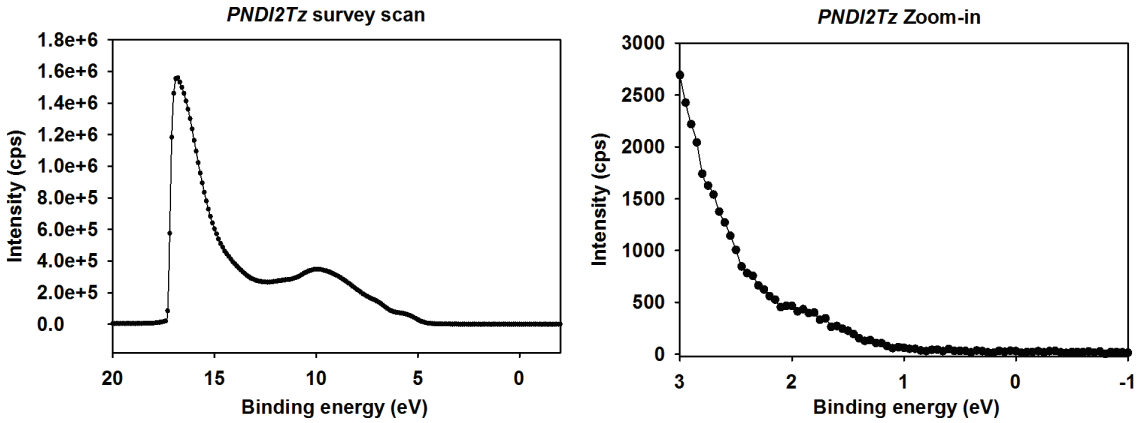

Figure 3.3. Ultraviolet photoelectron spectrum (UPS) for **PNDI2Tz** thin film cast on Au-coated silicon wafer.

polymer interactions. For **PNDI2Tz** *p*-xylene solutions, the polymer absorption maxima remained at ~540 nm (2.3 eV) even when the temperature was increased to 100 ^{o}C (**Figure 3.3**), suggesting that the copolymer does not tend to self-assemble into aggregated structures at room temperature. The small 5 nm blue-shift in λ_{max} and decreasing intensity over the 25 – 100 ^{o}C temperature range can be attributed to decreases in conjugation length with increasing molecular disorder at higher temperatures.[148, 242, 243]

Figure 3.2b provides a perspective on differences observed in the UV-*vis* spectra of **PNDI2Tz** in solution *vs.* solidified thin-film state. Spectra of thin-films prepared from the polymer in *p*-xylene solution and then blade coated onto glass substrates at room temperature, displayed an increase in the onset of absorption upon thermal annealing above the polymer T_g. Pristine **PNDI2Tz** thin films exhibit an optical bandgap (E_g^{opt}) of *ca*. 2.04 eV as determined from the UV-*vis* absorption onset at *ca*. 608 nm (2.03 eV). After thermal annealing, the absorption onset shifted to *ca.* 657 nm, resulting in a narrower optical bandgap of 1.89 eV. As shown in **Figure 3.2b**, E_g^{opt} for the thermally annealed films was *ca*. 0.2 eV (55±13 nm) lower than that for samples that had not been subject to the

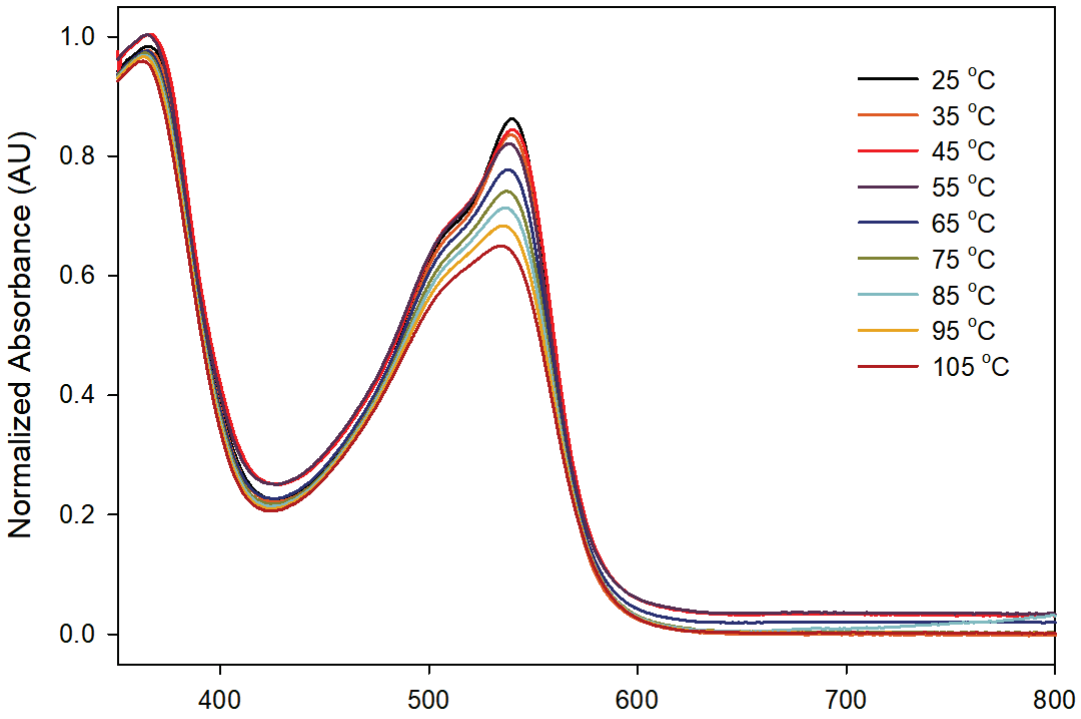

Figure 3.4. Temperature-dependent UV-*vis* spectroscopy on a *p*-xylene solution of **PNDI2Tz**.

annealing step. It can thus be inferred that the thermal treatment enabled the polymer chains to rearrange themselves more effectively into more highly ordered states. For comparison, thin films of the copolymer of NDI with bithiophene, namely **N2200**, exhibited an absorbance with λ_{max} at 594 nm with an onset of absorption at 642 nm (E_g^{opt} = 1.93 eV).[69, 72] **PNDI2Tz** solution temperature-variable UV-*vis* spectra were collected in *p*-xylene (2 mg/mL) at 10 ºC intervals from 25 ºC to 105 ºC. **(Figure 3.4)** Results show no clear bathochromic shifts in main absorption peak of **PNDI2Tz**, but a decrease in peak intensity at 540 nm was recorded.

PNDI2Tz was further evaluated by ultraviolet photoelectron spectroscopy to extract an estimate of the polymer's ionization potential (IP). As presented in **Figure 3.3**, the bithiazole based conjugated polymer exhibited an IP of 5.78 eV, compared to 5.36 eV

for **N2200.**[67, 72] The high IP observed for **PNDI2Tz** suggests that the system should possess excellent ambient stability toward oxidation, and supports the anecdotal observations that

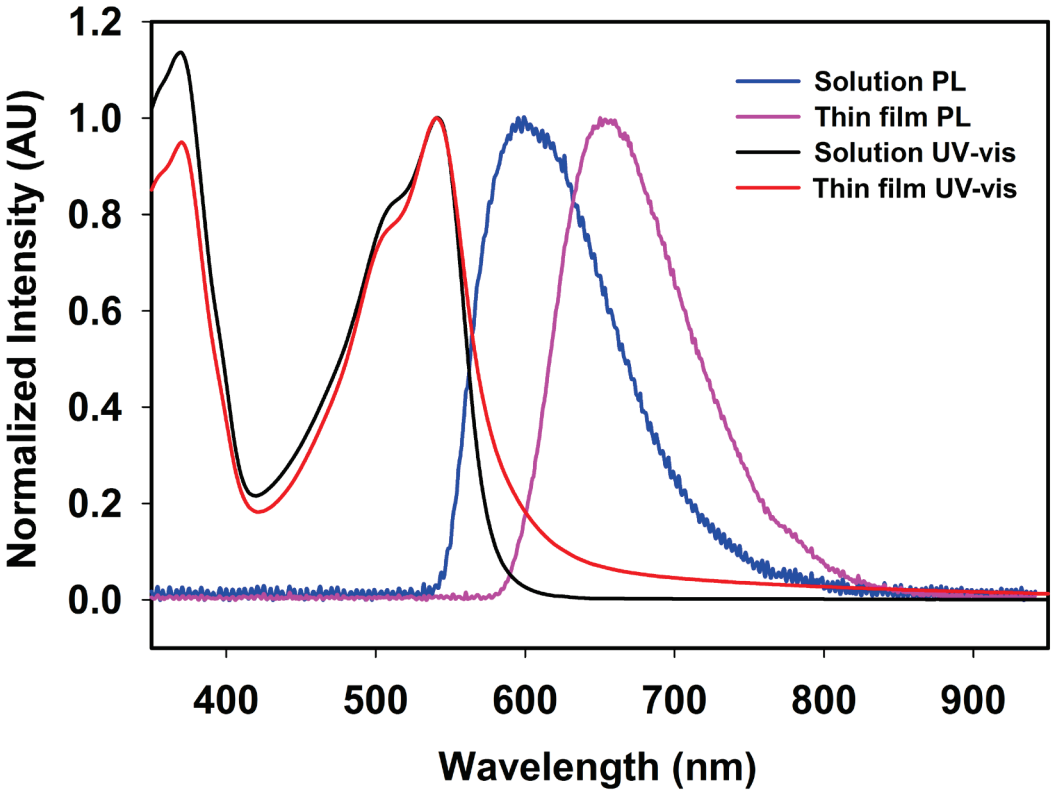

Figure 3.5. Photoluminescence of **PNDI2Tz** in *p*-xylene and in solid state, compared to the UV-*vis* absorptions in solution and in thin film.

PNDI2Tz is stable in ambient environments for over 6 months (*vide supra*).[7]

Photoluminescence spectroscopy was used to further understand the photophysical properties of **PNDI2Tz** in solution and thin film form (**Figure 3.5**). A 532 nm continuous-wave laser was used as the light source, and the light was focused on the sample with a lens of 75 mm focal length. **PNDI2Tz** fluorescence spectra exhibit a λ_{max} at 601 nm in solution, while thin-films exhibit a bathochromic shift to 656 nm. **PNDI2Tz** exhibits a small degree of fluorescence in solution with a quantum yield of 0.06, displays a large

Stokes shift, and polymer thin-films were found to be weakly emissive. Note that the Stokes shifts observed in the photoluminescence spectra were 0.23 eV and 0.41 eV for the solution and thin-film, respectively (61 nm for solution, and 116 nm for thin film). This large Stokes shifts strongly suggests that the structures of the emitting state and ground state are substantially different.

*3.3.3 **PNDI2Tz** Electrochemical Properties*

The electrochemical potentials of **PNDI2Tz** thin films were evaluated using cyclic voltammetry (CV) and differential pulse voltammetry (DPV) (**Figure 3.6**). Cyclic voltammetry (CV) and differential pulse voltammetry (DPV) measurements of PNDI-2Tz were performed in a one-compartment three-electrode electrochemical cell with a platinum flag as the counter electrode and an Ag/Ag^+ reference electrode. Polymer films were drop-cast onto a glassy carbon button (0.02 cm^2) working electrode from a 2 mg/mL polymer solution in $CHCl_3$. All measurements were taken in a 0.5M $TBAPF_6$/PC supporting electrolyte solution at a scan rate of 50 mV/s. For DPV experiments, a step size of 2 mV, step time of 100 ms, and a pulse amplitude of 100 mV was used.

PNDI2Tz exhibits two reversible reduction peaks, with the onset for reduction at -0.69 V (*vs.* Fc/Fc^+) by CV, and -0.64 V (*vs.* Fc/Fc^+) by DPV. No oxidative potentials were observed out to a potential of 1.2 V. Using the approximation of the formal potential of Fc/Fc^+ to be -5.1 eV on the Fermi scale,[102, 244, 245] the reduction potentials would correspond to an electron affinity of 4.40 to 4.46 eV. These values are lower than the LUMO estimates of the bithiophene analog N2200 (4.0 eV), which is an expected result of replacing the bithiophene with bithiazole.[72] Interestingly, the recently reported isomeric **P(NDI2OD-**

Tz2) with a 5,5'-bithiazole unit exhibited a slightly lower estimated LUMO energy of 4.10 eV.[246] Conceivably, the 5,5'-bithiazole analog may have a relatively higher degree of torsional disorder compared to **PNDI2Tz** (*vide infra*), which would result in a lower degree of electronic coupling along the linear chain. **PNDI2Tz** photophysical characterization suggests that **PNDI2Tz** has potential as an ambient stable electron transport material.[86, 216]

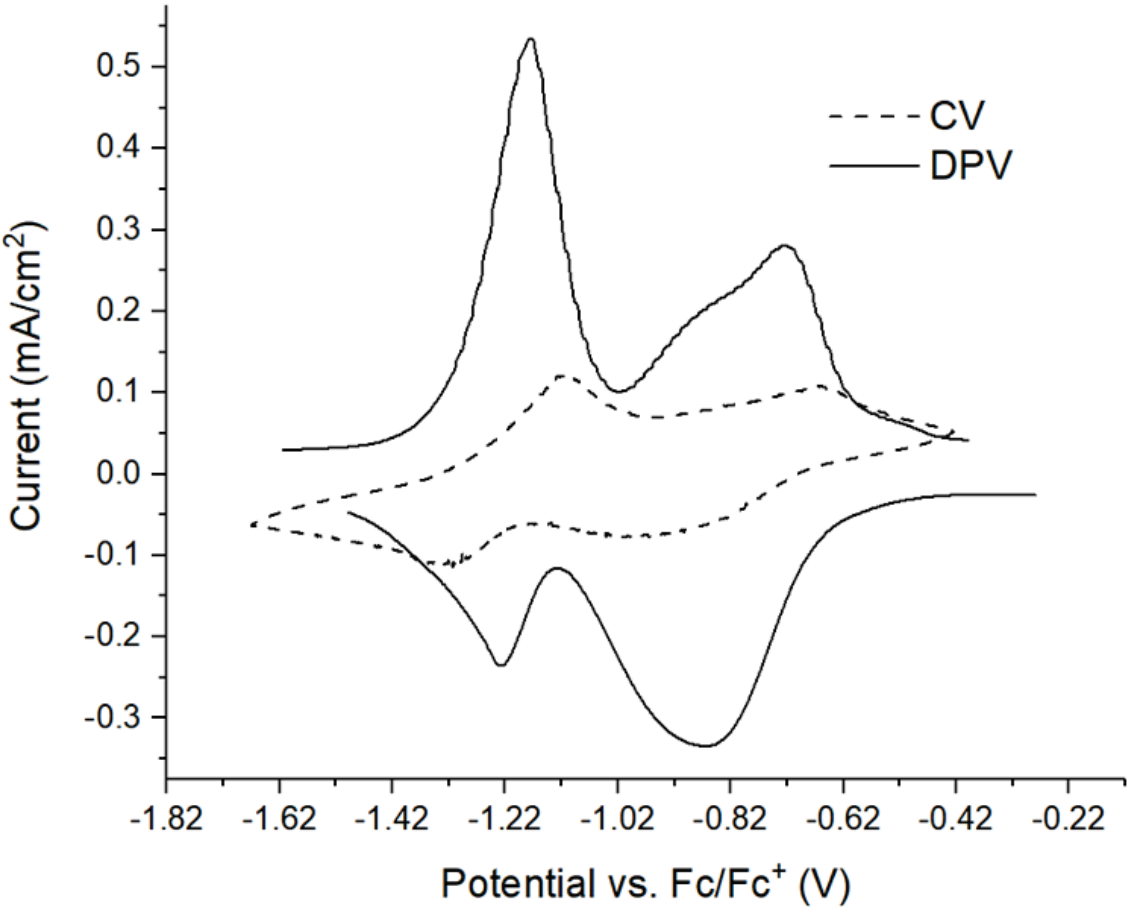

Figure 3.6. CV and DPV results for **PNDI2Tz** thin film drop-cast on a glassy carbon button.

3.3.4 Computational Modeling

*(Section 3.3.4 is completed in collaboration with Dr. Simil Thomas and Dr. Jean-Luc Bredas at Georgia Institute of Technology, Atlanta, Georgia, USA. (**2018**))*

In order to fully characterize the molecular geometry, nature of the frontier HOMO/LUMO energy levels, and first optical absorption of **PNDI2Tz**, a series of Density Functional Theory (DFT) calculations were conducted at the long-range corrected ωB97X-D/6-31G(d,p) level using the Gaussian 09 (Revision D.01) code.[247] The range-separation parameter (ω) was optimized following the IP tuning procedure.[218, 219] The value of ω for the isolated **PNDI2Tz** repeat unit is 0.17 $Bohr^{-1}$. Using this ω value, the torsion potentials (PES) between (i) the NDI and BTz units and (ii) the two thiazole units were calculated at 5° intervals (from 0° to 180°), by fixing the dihedral angles as shown in **Figure 3.7a** and relaxing all other geometric degrees of freedom. The N-substituted side-chains of the NDI units were replaced with methyl groups to reduce computational cost since these side chains have negligible impact on the geometric and optical properties of the isolated polymer backbone. The torsion potential between NDI and BTz (**Figure 3.7a**) has a minimum around 120º dihedral angle (with the nearest thiazole sulfur pointing towards an NDI oxygen), and is relatively flat (within 0.6 kcal/mol, *i.e.*, kT at room temperature) between 60º and 140º.

On the other hand, the torsion potential between the two thiazole units strongly favors the *anti*-coplanar structure. Overall, the NDI-thiazole interactions point to the **PNDI2Tz** polymer backbone being non-planar in the solid state. This contrasts with the **N2200** backbone that is expected to be more planar.[248, 249] In comparison, the 5,5'-bithiazole analog **P(NDI2OD-T2)**, where the thiazole nitrogen atoms point towards the NDI units, has a broad and flat potential profile at $\theta \approx 90^{o}$, making for a nearly orthogonal torsion angle between the NDI and 5,5'-BTz units and indicating a large degree of conformational disorder.[246] These results demonstrate the significant impact isomeric

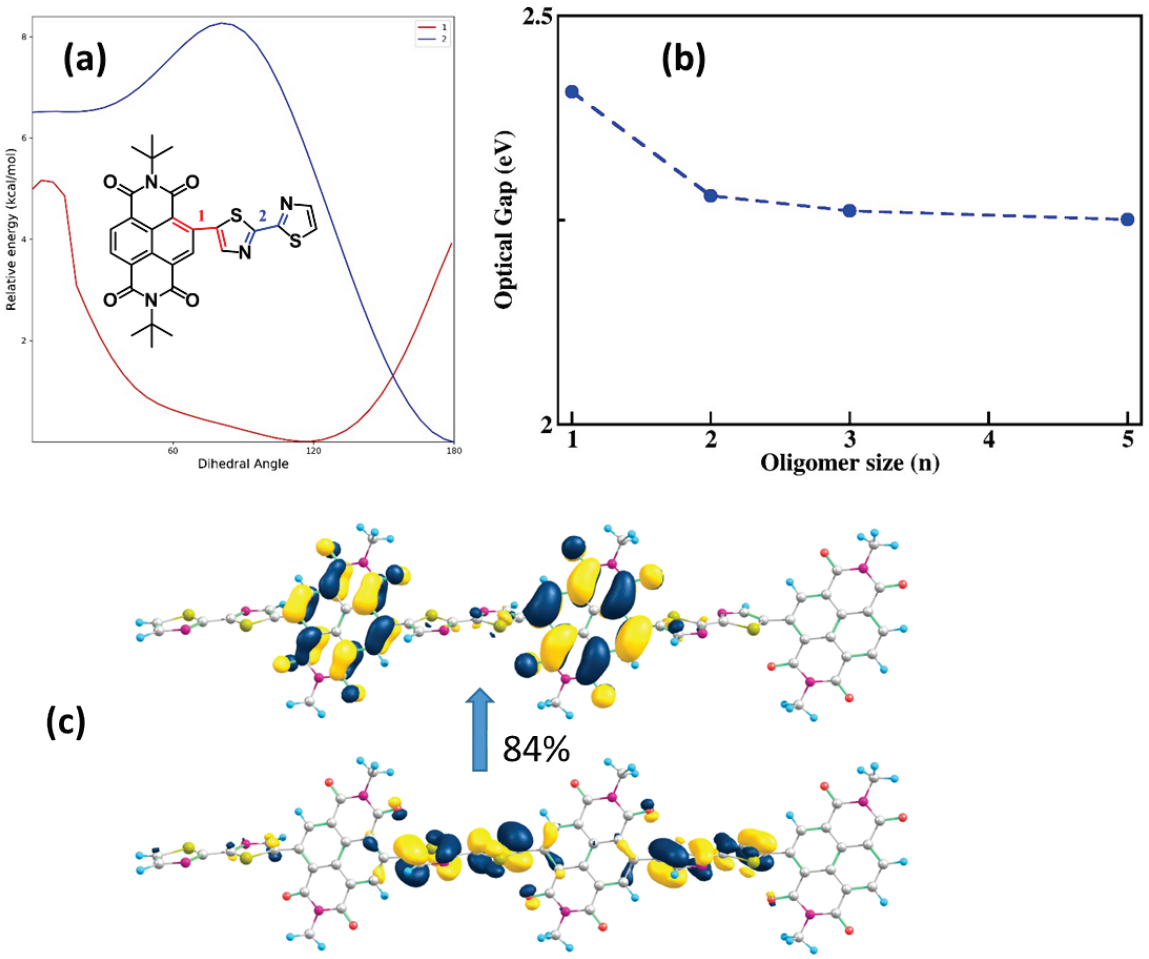

Figure 3.7. a) Torsion potentials related to the rotation of the adjacent units in the monomer of **PNDI2Tz**; relative energies determined at the tuned-ωB97X-D/6-31G(d,p) level. b) Evolution of the optical gap *vs.* oligomer size for **PNDI2Tz** as calculated at the TD-DFT (tuned-ωB97X-D/6-31G(d,p)// ωB97X-D/6-31G(d,p) level of theory). (c) TD-DFT (tuned-ωB97X-D) natural transition orbitals (bottom: hole wavefunction; top: electron wavefunction) with the largest contribution to the $S_0 \rightarrow S_1$ transition in the **PNDI2Tz** trimer.

structures can have on the equilibrium geometry of the final polymers, which in turn can influence the electronic performance of the materials.

The optical properties of **PNDI2Tz** were calculated at the time-dependent DFT (TD-DFT) level. The influence of the dielectric medium was modeled within the self-consistent reaction field (SCRF) framework (taking into account a dielectric constant, ε = 4.71, equivalent to chloroform, to maintain consistency with experiment) and using the

integral equation formalism of the polarizable continuum model (IEF-PCM).[250] **Figure 3.7b** illustrates the convergence of the optical gap as a function of the oligomer length of NDI2Tz; convergence is nearly reached at the level of the trimer already and extrapolation to the polymer gives a value of 2.26 eV, which is to be compared with an experimental optical absorption onset of 2.04 eV in the pristine thin-film**. Figure 3.7c** displays the DFT-calculated tuned-ωB97X-D natural transition orbitals (with the largest weight) for the S_0 to S_1 transition in the trimer of **PNDI2Tz**. The hole localizes essentially over bithiazole units and the electron over NDI units; this coupled-oscillator picture of the lowest optical transition rationalizes the weak solvatochromism experimentally observed.[251]

3.3.5 Thin-film morphology and solid-state crystallinity

PNDI2Tz thin-film microstructures were investigated by two-dimensional grazing incidence wide angle X-ray scattering (GIWAXS) (**Figure 3.8**). Films were prepared by blade coating *p*-xylene-solutions of **PNDI2Tz** onto Si substrates (300 nm SiO_2 dielectric on heavily *p*-doped Si). **PNDI2Tz** is a predominantly face-on polymer evidenced by the diffraction peak on the z-axis (out-of-plane). Polymer thin films are largely amorphous, with limited crystallinity as suggested by the absence of well-defined diffraction patterns along the q_{xy} (in-plane) axis. Thermal annealing (150 °C, 30 min) does not appear to improve the molecular packing as well as expected. This is likely due to the twisted conjugated backbone that prevents packing of polymer molecules into highly ordered aggregates. A lamellar *d*-spacing of 29.76 Å and π-π stacking distance of 3.60 Å can be derived from the diffraction peak at q_{xy}= 0.211 $Å^{-1}$ and q_z = 1.75 Å of the pristine film. The annealed film (150 °C, 30 min) possesses more well-defined peaks with higher peak intensities for both lamellar packing and π-π stacking diffractions. The π-π stacking

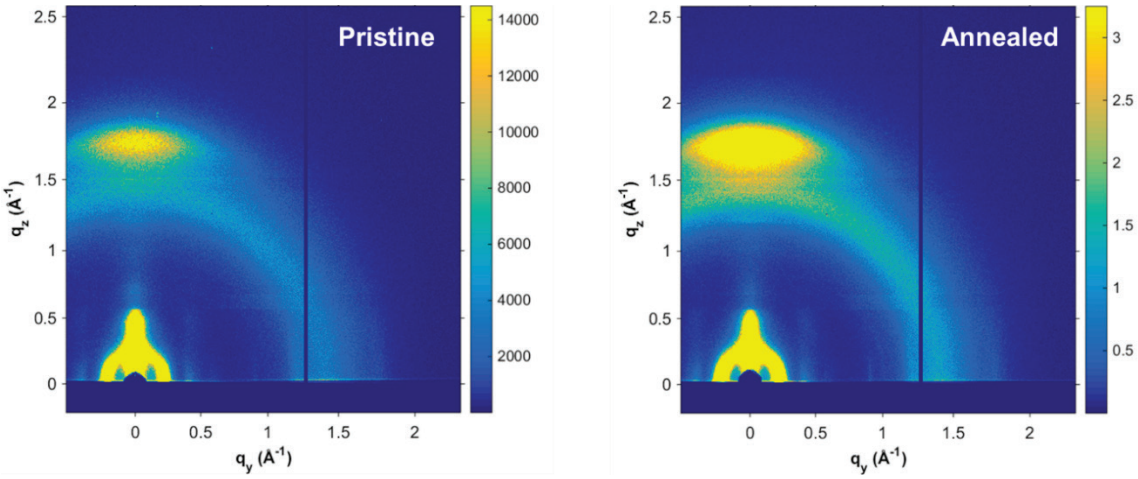

Figure 3.9. Grazing-incidence wide-angle X-ray scattering (GIWAXS) results of pristine and annealed **PNDI2Tz** on Si wafers.

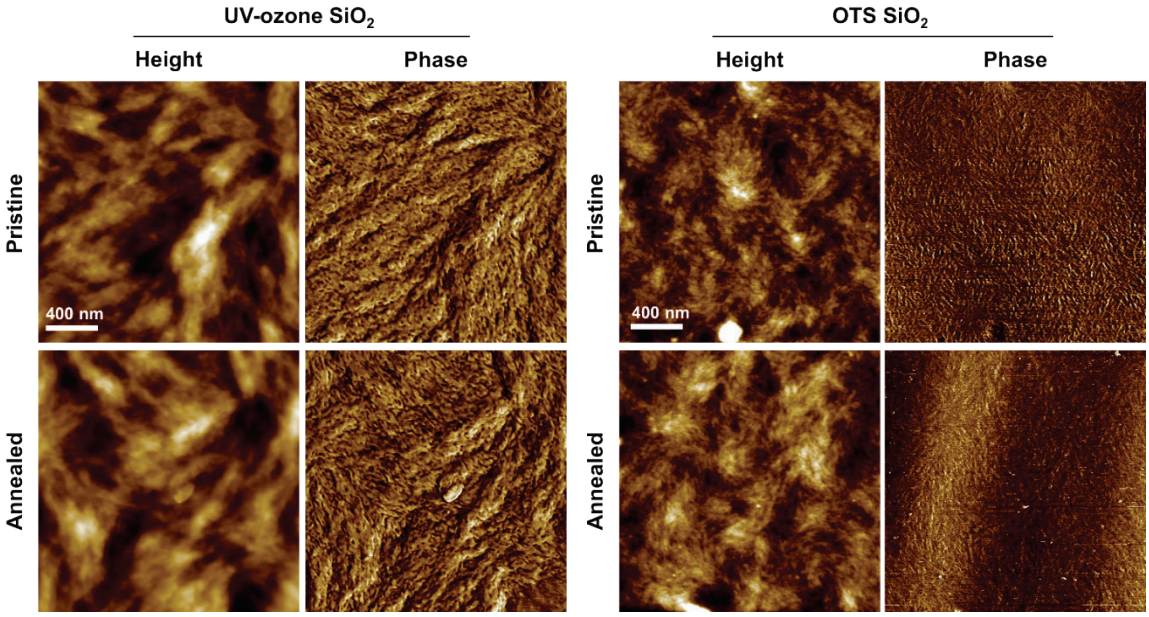

Figure 3.8. Atomic force microscopy (AFM) images of **PNDI2Tz** films cast on UV-ozone SiO_2 surfaces and OTS-processed SiO_2 surfaces.

distance for annealed films was similar, 3.58 Å, to that for as-deposited polymers, while the lamellar stacking distance was shorter, 29.18 Å.

The surface morphologies of **PNDI2Tz** polymer films were explored using tapping-mode atomic force microscopy (AFM), as shown in **Figure 3.9**. Polymer films

were blade coated onto either UV-ozone cleaned Si substrates (300 nm SiO_2 dielectric on heavily *p*-doped Si), or Si substrates processed with octadecyltrichlorosilane (OTS). Films fabricated on UV-ozone treated Si substrates exhibit larger sized features than films cast onto OTS surfaces. Films on OTS display a more nanofibrillar morphology with short nanofibers. Also, films coated on OTS treated substrates displayed significantly lower surface roughness (R_a = 0.87 nm ± 0.15 nm) than films cast on UV-ozone cleaned SiO_2 (R_a = 1.72 nm ± 0.43 nm). Thermal annealing up to 150 °C did not appear to alter thin film surface morphology, possibly due to the amorphous nature of **PNDI2Tz** polymer leading to no change in crystallinity before and after thermal treatment.

3.3.6 Charge Transport Performance

PNDI2Tz was dissolved into *p*-xylene (4-6 mg/mL) and blade-coated onto Si/SiO_2 substrates with pre-evaporated source and drain electrodes to fabricate bottom-gate-bottom-contact (BGBC) organic field-effect transistors (OFETs). For blade-coated films, 8-15 μL of polymer solution (4-6 mg/mL) was added on one side of a glass slide or wafer that had been sitting on the heating stage for at least 5 minutes to ensure the substrate was at the programmed temperature. In this study, only blade coating was performed due to poor film formation via spin coating methods. For the fabrication of bottom-gate/bottom-contact organic thin-film transistors, highly n-doped (100) silicon wafers with a 300 nm thermally grown oxide gate dielectric film were used as device substrates. Au source and drain contacts (50 nm of Au contacts with 3 nm of Cr as the adhesion layer) with fixed channel dimensions (50 μm in length and 2000 μm in width) were deposited via e-beam evaporation using a photolithography lift-off process. The Si/SiO_2 substrates were washed via bath sonication (Branson® Ultrasonic Bath, 230 Vac, 50 Hz) sequentially in acetone,

methanol and isopropyl alcohol for 15 min, followed by treatment in UV-ozone for 30 min (Novascan® PSD-UV - Benchtop UV-Ozone Cleaner). The general treatments [90] were employed for the treatment of gate dielectric layers using three self-assembled monolayers. The capacitances of the dielectric layers were measured using an Agilent 4284A Precision LCR meter.

Semiconducting thin films were fabricated via blade-coating at 100 °C to improve solvent evaporation and thin film formation on passivated surfaces. During the blade-coating process, 5 to 10 μL of semiconductor solution (4-6 mg/mL) was cast onto a heated substrate (1.5 cm × 1.5 cm). The angle between the glass blade and the substrate was set to be ca. 8°. Thin film formation was optimized by controlling different solution-shearing conditions such as substrate temperature and blade-coating speed. The blade-coated substrates were placed in a vacuum oven at 55 °C overnight to remove residual solvent. Film thickness was characterized using a Bruker DektakXTTM Stylus Profilometer. Film thickness varied with respect to fabrication methods.

OFET electronic characteristics were measured using an Agilent 4155C semiconductor parameter analyzer inside a N_2 filled glovebox. Charge carrier mobilities (μ), threshold voltages (V_{th}) and on/off ratios ($I_{on/off}$) were calculated in the saturation regime. he reported values are the average of 15 different devices with the standard deviation recorded. Each mobility data point was obtained by casting **PNDI2Tz** thin films onto 10-12 separate OFET devices. Electron mobilities were measured on all devices prepared on octadecyltrichlorosilane (OTS) passivated substrates. It is noted that no electron mobilities were measurable on bare SiO_2 surfaces, most likely due to the presence

of hydroxyl groups which serve as charge traps.[252] OTS treated devices displayed the highest mobilities.

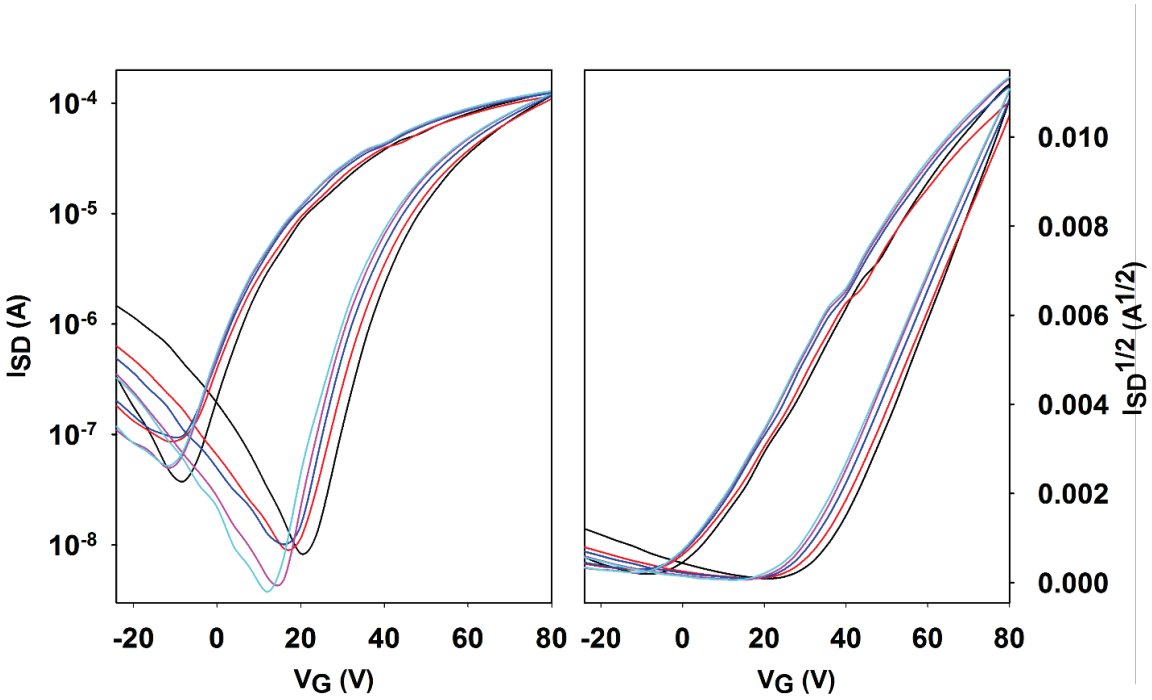

Figure 3.10. PNDI2Tz transfer curves measured on bottom-gate-bottom-contact OFETs (devices were coated at 3 mm/s; five device results overlapped showing consistent performances; devices are annealed in a N_2 glovebox at 150 °C for 30 min followed by cooling).

While OFETs were fabricated with shearing in both directions (parallel and perpendicular to channel width); shearing direction had no apparent impact on charge carrier mobility, most likely due to the relatively amorphous nature of the films. Note that conjugated polymer charge transport performance is known to depend on overall film morphology, which includes polymer orientation, polymer-polymer orientation, polymer domain orientation, and aggregated domain connectivity.[253] As noticed in **Figure 3.10**, transfer curves show consistent performance with hysteresis which derives from the imperfect morphologies between thin film and OTS-processed dielectric layers.[252, 254, 255] We believe that the slightly twisted conjugated backbone in **PNDI2Tz** compared to the

more planar backbone of **N2200** hindered effective organization of **PNDI2Tz** into structures having a higher degree of π-π interactions that would be expected to lead to effective intramolecular charge transport. Future studies focused on X-ray scattering of **PNDI2Tz** and **N2200** thin films are expected to elucidate fundamental differences in **PNDI2Tz** and **N2200** OFET charge transport behavior.

3.4 Conclusion

In this chapter, we reported the synthetic route to, and key properties of, a thiazole-based *n*-channel conjugated polymer, **PNDI2Tz**. The polymer featured low HOMO (-5.78 eV) and LUMO (−3.39 to −3.59 eV) levels; and based upon computational studies, possesses a slightly twisted backbone with clear donor-acceptor character. **PNDI2Tz** OFETs were also fabricated and characterized demonstrating unipolar *n*-channel characteristics with a field-effect mobility as high as 5.30×10^{-2} $cm^2V^{-1}s^{-1}$, a slightly lower value compared to the benchmark *n*-channel material **N2200**. Further studies related to the polymer solid state packing and charge transport mechanism are under way. Computational modeling revealed significant differences in the equilibrium geometries of NDI polymers synthesized with isomeric bithiazole units. These differences would be expected to influence materials electronic performance and demonstrate how seemingly minor molecular structural differences can influence polymer organization and self-assembly, which in turn impacts electronic performance in devices. The fundamental insights derived from synergistic, tightly coupled computational and experimental investigations presented here are expected to provide a foundation for the identification of robust and manufacturable materials for flexible electronics applications.

CHAPTER 4. NANOFIBER FORMATION IN NAPHTHALENE DIIMIDE-THIAZOLE BASED CONJUGATED POLYMER OFETS VIA DIELECTRIC SURFACE PROCESSING

4.1 Abstract

Self-assembled monolayers (SAMs) are becoming an essential component of organic electronics devices, such as organic photovoltaics (OPVs) and organic field-effect transistors (OFETs), due to their impacts on interface energetics and thin film interfacial morphology. This chapter focuses on interface engineering and its influence on thin film morphology and OFET performance. SAMs of three organic molecules presenting different surface properties were prepared on silicon dioxide surfaces to explore the impact of surface effects. The charge transport performance of three different, but structurally similar donor-acceptor conjugated polymers were studied as a function of SAM molecular composition in OFET applications. Seemingly, the formation of conjugated polymer nanofiber network is promoted by SAM layer surface effects. A combination of surface energy effects and buried interface effects promotes desirable polymer packing in solid state. In addition, surface energy seems to have direct impact that can enhance molecular packing and conjugated polymer π-π interactions. Low energy surfaces appear particularly favorable from an energetic standpoint for conjugated polymers to form tight nanofiber networks that enhance charge carrier mobilities.

4.2 Introduction

As discussed in the chapters above, organic semiconducting materials, and the organic field-effect transistors (OFETs) they facilitate, have received tremendous attention in recent years because of their promising future applications in several technology sectors.[119, 231-234] As a number of organic *p*-channel (hole transporting) and ambipolar semiconductors with relatively high hole mobilities ($\mu > 1$ $cm^2V^{-1}s^{-1}$) have become commercialized,[62, 63, 65] attention is shifting to the design and development of their *n*-channel (electron transporting) counterparts.[119, 235, 236] In addition, investigations associated with semiconductor solution processing methods, device fabrication techniques and device architectures are of significant interest.[14, 256-258] Notably, *n*-channel organic semiconductors are sensitive to electron charge traps that can negatively impact device performance.[63, 259] Thus, methods to reduce such traps, particularly in organic photovoltaic (OPV)[20, 21, 204] and OFET devices are required for the development of robust systems.[260, 261] As one example, surface defects and surface functionalities such as hydroxyl groups are known trap sites, which can be reduced through substrate surface passivation prior to semiconductor deposition using commodity chemicals such as octadecyltrichlorosilane (OTS) and hexamethyldisilazane (HMDS).[63, 262]

Operationally, surface passivation simply changes the nature of substrate surface chemical functionalities, which may in turn impact substrate surface energy. For instance, OTS, with its long alkyl side chain, more effectively reduces substrate surface energy when compared with HMDS.[263] In turn, surface chemistry coupled with surface energy will impact polymer orientation (edge-on *vs.* face-on), surface wetting, the thin film formation process and ultimately final film morphology[264-266], all of which are determining factors

for device performance. Frequently, OTS has been used as an adhesion promoter and dielectric surface passivation agent in the fabrication of polymer semiconductor based OFETs; additionally, the alkyl silane has been reported to afford improved charge carrier mobility in comparison to other surface passivation layers.[267, 268] Bao and co-workers have developed patterned substrates with hydrophobic and hydrophilic sections to promote conjugated small molecule single crystal formation which leading to high performing small molecule OFETs. [186, 187] Fu et al reported that the long alkyl chains in OTS can interact with side chains on polymers, promoting polymer molecules to form desirable face-on orientation when polymer PDBTz and pTBTD-5DH are deposited onto OTS-processed SiO_2 surfaces.[76, 82, 169] Kline et al reported the buried interface effect with SAM-processed substrate surface which significantly varies the concentration of highly oriented conjugated polymer crystalline phases. Their study revealed that the polymer morphology at the buried interface can be different from that in the bulk of the thin films, and further impact charge transport in thin-film devices.[170] Studies have also shown that processed substrate surface energies can impact grain size and surface morphology of organic semiconductor thin films

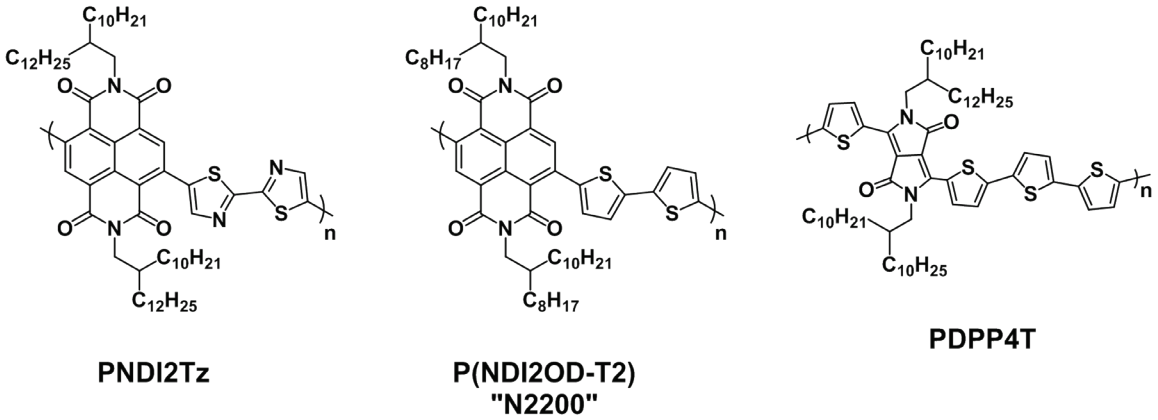

Figure 4.1. Chemical structures of conjugated polymers studied, **PNDI2Tz** (left), **P(NDI2OD-T2)** (middle), and **PDPP4T** (right).

and subsequently, device performance.[101, 269, 270] Nevertheless, definitive relationships between processing conditions, surface passivation effects and OFET performance have not been identified; and thus guidelines for the design of effective process protocols remain elusive.

In this chapter, the impacts of substrate surface energy, processing conditions and device performance were investigated and key relationships have been identified. Specifically, the phenomena were interrogated using thin-film transistor devices fabricated using the recently reported *n*-channel polymer, poly (naphthalenediimide-bithiazole) (**PNDI2Tz**) (structure shown in **Figure 4.1**).[271] In addition, the applicability of the findings for effective processing of alternative donor (D) – acceptor (A) polymers was demonstrated using a naphthalene-diimide based *n*-channel material, namely poly(naphthalene-diimide) (**PNDI2OD-T2, "N2200"**)[14] (synthesized by Carolyn Buckley in collaboration) and a benchmark *p*-channel conjugated polymer, poly(diketopyrrolopyrroledione-terthiophene) (**PDPP4T**)[56]. Substrate surface energy was manipulated using three commonly used silane surface passivation agents, namely, OTS, PTS (phenyltrichlorosilane), and HMDS. The results provide significant insight into key structure-process-property relationships surrounding the use of surface passivation materials and their consequential impact on semiconducting polymer charge transport performance.

4.3 Results and Discussions

4.3.1 Semiconducting polymer synthesis

The electron deficient thiazole ring was recently introduced as a viable acceptor in the search for efficient electron transporting semiconducting polymers.[76, 90, 120, 271] Previous

studies explored the copolymerization of thiazoles with electron donors such as thiophene and thienothiophene, and the electron acceptor, diketopyrrolopyrrole (DPP), revealing the potential of thiazoles as valuable units in organic electronic materials.[90, 121, 239-241] Recently, thiazole was co-polymerized with a 2-decyltetradecyl substituted NDI through Stille step-growth polymerization to afford **PNDI2Tz**.[271] Synthesized **PNDI2Tz** has a molecular weight (number average molecular weight, Mn) of 49.3 kD and polydispersities (PDI, *Đ*) of 3.3. **N2200** and **PDPP4T** were synthesized via literature procedures[56, 69] (**N2200**: Mn = 53 kD, PDI = 1.3; **PDPP4T**: Mn=29.1 kD, PDI = 2.4).

4.3.2 Dielectric layer processing

Processed SiO_2 surface energies were as follows: OTS (21.99 ± 1.97 mJ/m^2), PTS (28.63 ± 0.83 mJ/m^2), and HMDS (35.77 ± 2.23 mJ/m^2) (**Figure 4.2**). For blade-coated films, 8-15 μL of polymer solution (4-6 mg/mL) was added on one side of a glass slide or wafer that had been sitting on the heating stage for at least 5 minutes to ensure the substrate was at the programmed temperature. In this study, only blade coating was performed due to poor film formation *via* spin coating methods. For the fabrication of bottom-gate/bottom-contact organic thin-film transistors, highly *n*-doped (100) silicon wafers with a 300 nm thermally grown oxide gate dielectric film were used as device substrates. Au source and drain contacts (50 nm of Au contacts with 3 nm of Cr as the adhesion layer) with fixed channel dimensions (50 μm in length and 2000 μm in width) were deposited *via e*-beam

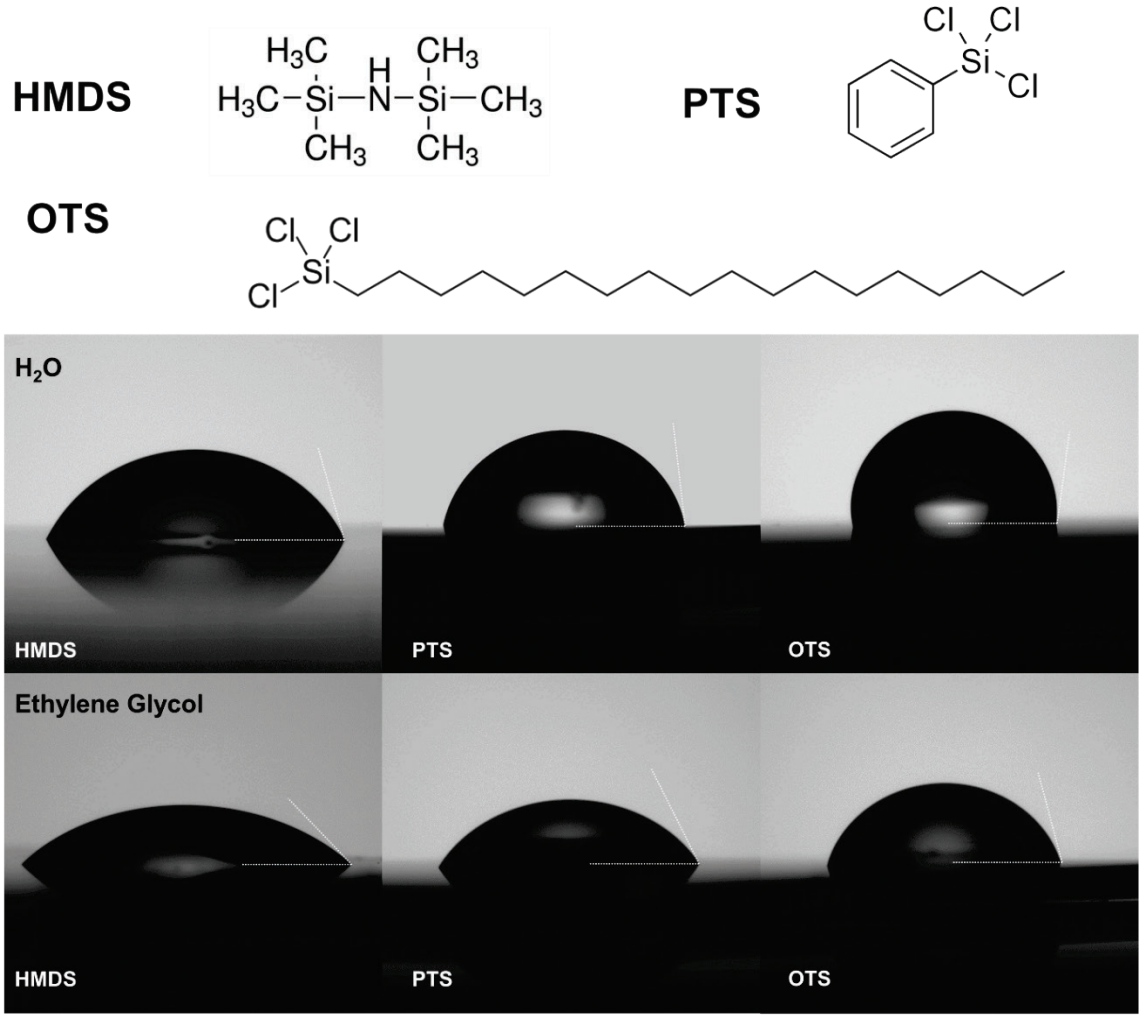

Materials	Water(°)	EG(°)	γ_s_d	γ_s_p	γ_s (mJ/m^2)
HMDS	68.38	48.08	18.68	17.09	35.77
PTS	80.23	57.88	9.75	18.88	28.63
OTS	99.13	74.20	2.01	19.98	21.99

Figure 4.2. a) Chemical structures of hexamethyldisilazane (HMDS), phenyltrichlorosilane (PTS) and octadecyltrichlorosilane (OTS); b) Optical images showing the contact angles of the HMDS, PTS and OTS processed SiO_2 surfaces and surface free energy calculation results. Contact angles in table is the average value of 8 measured spots.

evaporation using a photolithography lift-off process. The Si/SiO_2 substrates were washed *via* bath sonication (Branson® Ultrasonic Bath, 230 V_{ac}, 50 Hz) sequentially in acetone,

methanol and isopropyl alcohol for 15 min, followed by treatment in UV-ozone for 30 min (Novascan® PSD-UV - Benchtop UV-Ozone Cleaner). The general treatments [90] were employed for the treatment of gate dielectric layers using three self-assembled monolayers (OTS, PTS and HMDS). The capacitances of the dielectric layers were measured using an Agilent 4284A Precision LCR meter.

4.3.3 Polymer thin-film microstructures and morphology

PNDI2Tz thin-films were prepared by blade coating the respective polymer solutions at elevated temperature (100 °C). At room temperature, resultant films were inhomogeneous, while no film formation was obtained using spin-coating due to poor wetting of polymer solution on SAM-treated SiO_2. The microstructure and thin-film

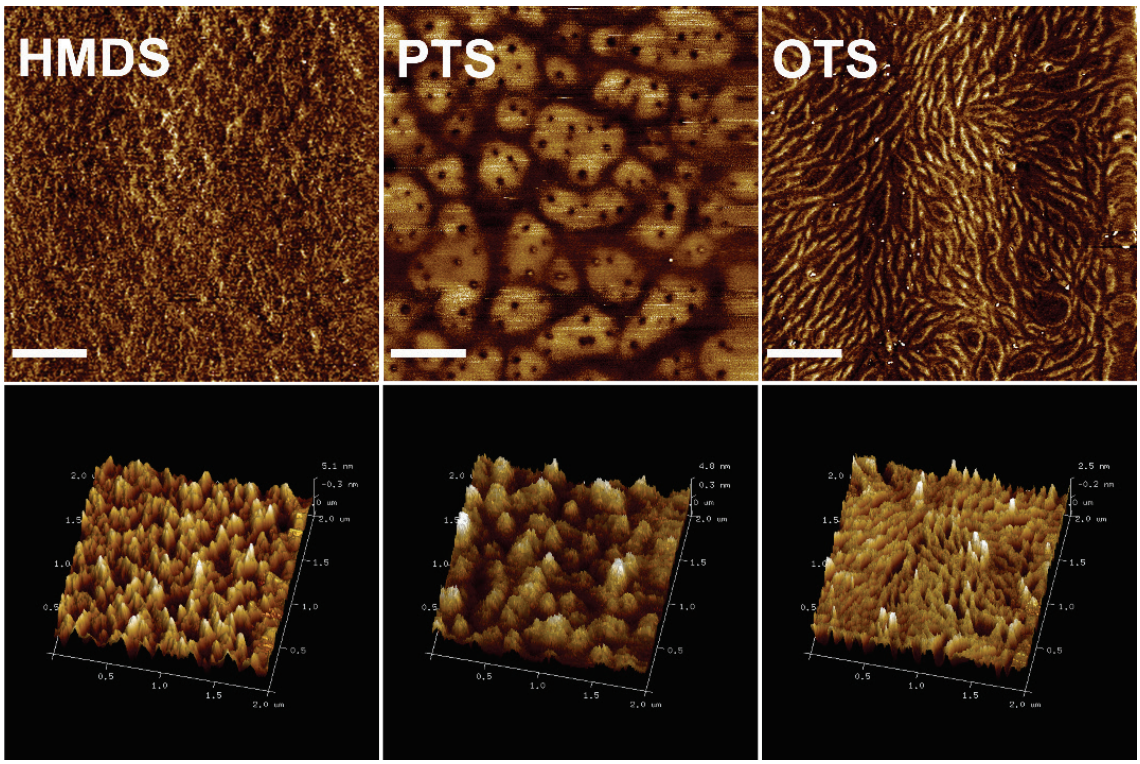

Figure 4.3. AFM images of **PNDI2Tz** thin films fabricated on HMDS, PTS and OTS surfaces showing the development of polymer nanofiber network. Bottom row is the three-dimensional representation of the height images for clear view. Scale bars are all 400 nm.

morphology were studied by atomic force microscopy (AFM) (**Figure 4.3**) and grazing-incidence wide angle X-ray scattering (GIWAXS) (**Figure 4.4**). AFM phase and height images of blade coated **PNDI2Tz** (**Figure 4.3**), demonstrated the evolution of thin- film morphology from a relatively featureless film to one with clearly defined **PNDI2Tz** networked nanofibers. In the current investigation, similar nanofiber network formation was observed, and more detailed discussion is presented in Chapter 4.3.4 – "Process Versatility", below.

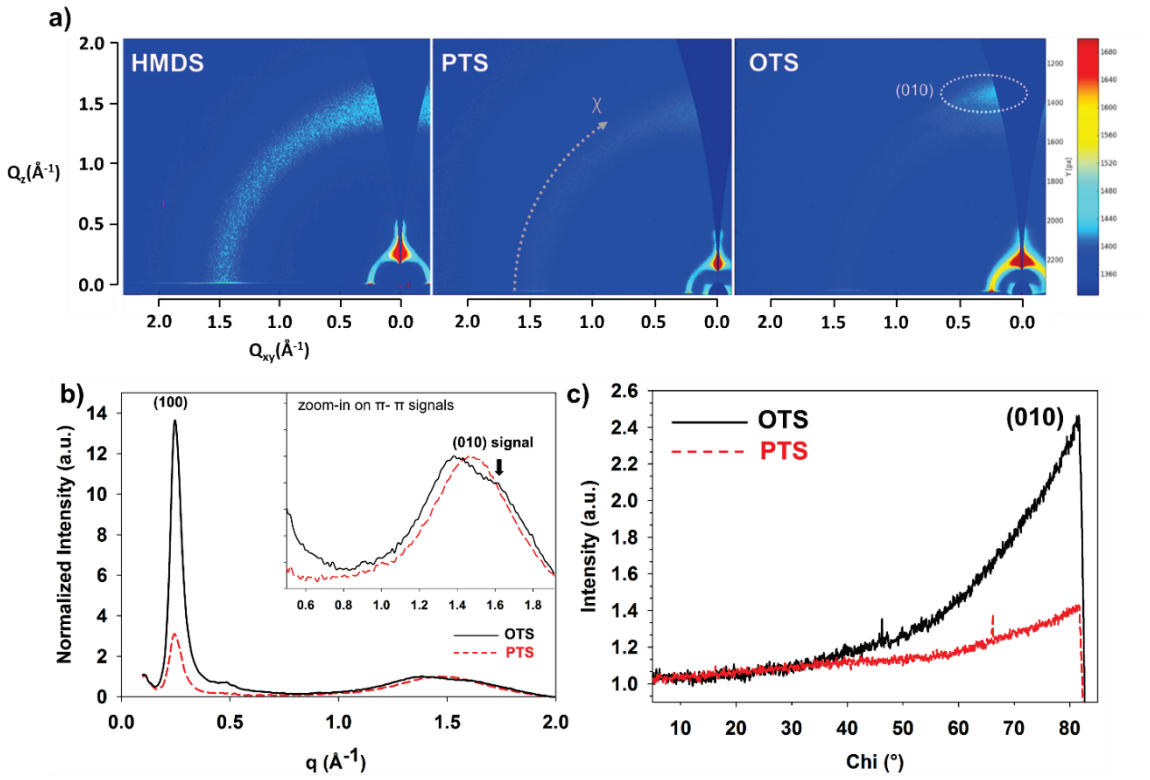

Figure 4.4. a) GIWAXS image of **PNDI2Tz** thin-films on HMDS, PTS and OTS processed SiO_2 surfaces; b) 1D line cut along Chi = 15° with zoomed-in plot on q_z = 0.6~1.8 Å^{-1}; c) π- π stacking Chi plot from *xy*-plane (Chi = 0°) to *z*-axis (Chi = 90°).

PNDI2Tz nanofibers exhibited large, substrate surface chemistry dependent variations in density and scale (**Figure 4.3**). On either bare SiO_2 or HMDS treated surfaces, only nanoscale granular-like features were observed upon blade coating the **PNDI2Tz** solutions; PTS passivation afforded polymer surfaces with only somewhat more structure. In contrast, OTS treated substrates facilitated **PNDI2Tz** nanofiber formation at blade coating speeds above 1 mm/s (**Figure 4.5**). As the coating speed increased up to 4 mm/s, an interconnected nanofiber network was formed. When the coated speed was increased further, no homogeneous film formation was discerned. The AFM results highlight the influence of substrate interface chemistry and likely, surface energy on the development of conjugated polymer thin-film morphology. In addition, AFM height images (**Figure 4.3**) show clear variations in surface morphology. The results suggest that more surface features

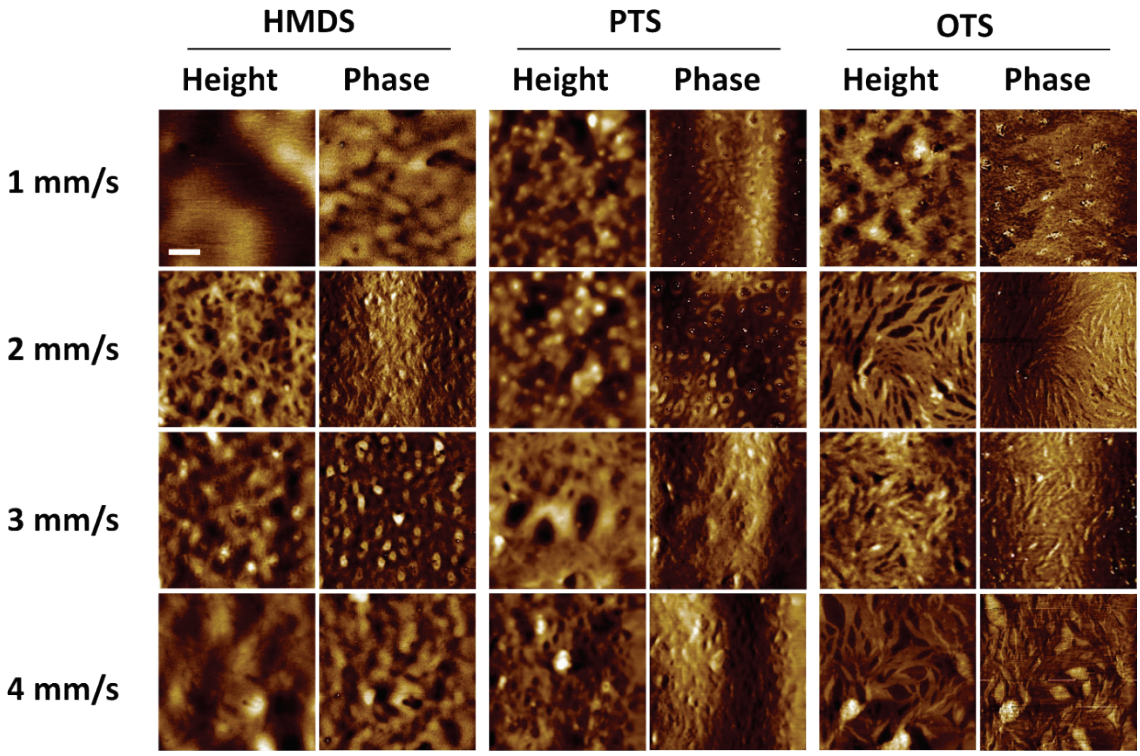

Figure 4.5. PNDI2Tz AFM height and phase image with blade coating speeds. Scale bar is 400 nm.

derived from nanofibers can be attained *via* high temperature solution shearing, especially under higher blade coating speed (3 mm/s). (**Figure 4.5**).

GIWAXS profiles of **PNDI2Tz** thin-films presented (100) reflection peaks along the out-of-plane (q_z) direction, corresponding to polymer lamellar stacking orientated normal to the substrate (**Figure 4.4**). However, halo-like patterns are apparent along the azimuthal angle at (100) peak, indicating a distribution of polymer orientations within the film.[258, 272]. GIWAXS scans also revealed that blade-coated films possess a low degree of order compared to many semi-crystalline conjugated polymers; note the faint (010) diffraction and absence of higher order (300) and (400) lamellar packing peaks. This may be due to the larger dihedral angle between the thiazole and NDI units, which introduces twisting in the conjugated backbone. In addition, the alkyl side chain branch point is closer to the NDI units and thus steric hindrance effects may prevent formation of a semi-crystalline film.[82] The 1D GIWAXS integration profiles (with background strip) are presented in **Figure 4.4b**. Strong (100) peaks at q_z = ca. 25 Å were observed for all thin

Table 4.1. Electron transporting properties of **PNDI2Tz** based OFET devices fabricated under high temperature blade coating conditions on processed wafer devices.

	Glass processing	Surface Energy, γ_s (mJ/m^2)	Bladecoating speed (mm/s)	Bladecoating temperature (°C)	Thermal Anneal	Mobility (cm^{2}V^{-1}s^{-1})
A	OTS	21.99	0.5	R.T.	no	9.03E-03 ± 2.08E-03
B	OTS		0.5	R.T.	yes	1.12E-02 ± 1.12E-03
C	OTS		1	100	-	1.57E-02 ± 1.26E-03
D	OTS		2	100	-	1.29E-02 ± 2.19E-03
E	OTS		3	100	-	7.05E-02 ± 5.43E-03
F	OTS		5	100	-	1.06E-02 ± 2.09E-03
G	PTS	28.63	3	100	-	3.82E-02 ± 4.97E-03
H	HMDS	35.77	3	100	-	1.62E-02 ± 1.49E-03

films. The calculated average (100) *d*-spacing for high temperature blade-coated polymer films on OTS treated surfaces was slightly smaller than that obtained for PTS counterparts, namely, 24.74 Å *vs.* 25.86 Å, respectively. Further on OTS, **PNDI2Tz** exhibited a significantly stronger signal in the (010) direction, as the signal along q = 1.5-1.7 $Å^{-1}$ was integrated across all azimuthal angles. OTS treated substrates also provided for **PNDI2Tz** films having a somewhat shorter π-π stacking distance of 3.87 Å (q = 1.623 $Å^{-1}$). Together, GIWAXS and AFM data strongly suggest that the lower energy OTS surfaces promote the formation of tightly packed conjugated polymer structures.

*4.3.4 **PNDI2Tz** Charge Transport Performance*

Blade coated **PNDI2Tz** based OFET devices were fabricated by shearing polymer solutions in both the parallel and perpendicular direction relative to channel width. Shearing direction did not appear to impact mobility (μ), conceivably due to the somewhat isotropic nature of the as formed nanofiber network (AFM results, *vide supra*). For each processed surface (including the pristine SiO_2), 10 devices were coated with each **PNDI2Tz** solution at 100 °C and each coating speed. The electron transport performance results are presented in **Table 4.1** and **Figure 4.6.** No electron mobility (μ_e) was discernable on bare SiO_2 surfaces, most likely due to the presence of hydroxyl groups which serve as charge traps.

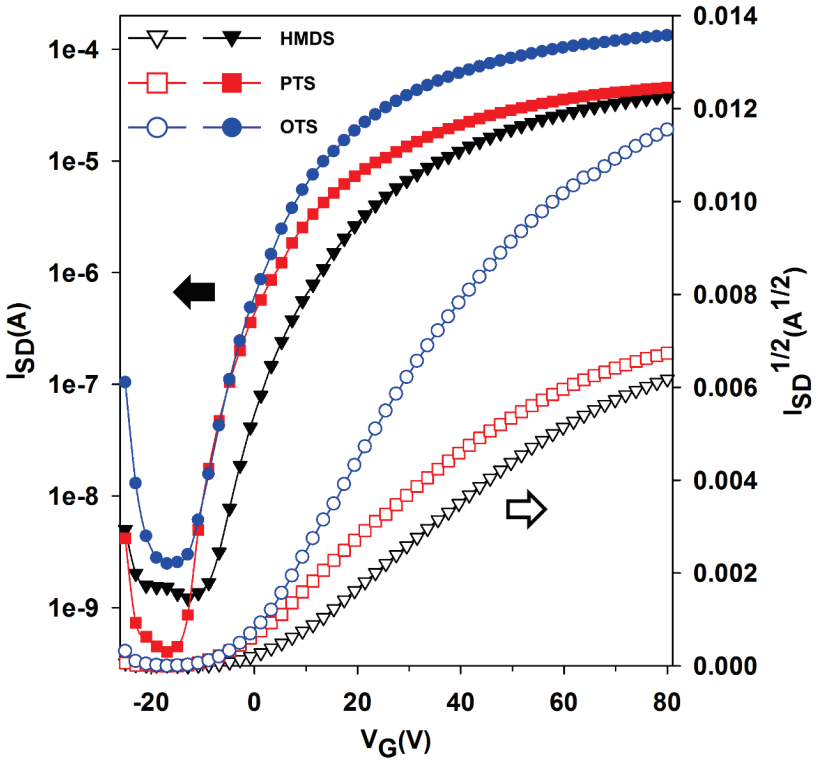

Figure 4.6. Transfer curve of **PNDI2Tz** devices coated on HMDS, PTS and OTS processed bottom-gate-bottom-contact transistors. Solid dots are I_D vs V_G curve, and hollow-dots are $I_D^{1/2}$ vs V_G curve. Devices were fabricated at a blade-coating speed of 3 mm/s.

No OTS treated devices consistently displayed the highest mobilities, and the results appear well-correlated with enhanced nanofiber formation as observed by AFM. Upon increasing shearing speed from 1 to 3 mm/s, average μ_e increased from 1.57×10^{-2} $cm^2V^{-1}s^{-1}$ to 7.05×10^{-2} $cm^2V^{-1}s^{-1}$. Continuing to increase shearing speed from 4 to 5 mm/s led to decreased μ_e (1.06×10^{-2} $cm^2V^{-1}s^{-1}$) as a result of poor film formation, *i.e.*, formation of isolated polymer domains. As a result, 3 mm/s was selected as the optimized coating speed. From examination of the results in **Table 4.1**, films fabricated on OTS treated surfaces exhibited a 2-to-5 fold increase in μ_e vs the same semiconducting polymer deposited on PTS or HMDS treated substrates.

4.3.5 Process Versatility-comparison with benchmark D-A conjugated polymers

To investigate whether the trends identified for **PNDI2Tz** are generally applicable to other D-A polymer semiconductors, two alternative conjugated polymers were evaluated, namely, the hole transport conjugated polymer, **PDPP4T**[56], and the electron transport material, **PNDI2OD-T2**[14, 69], also known as **N2200** (**Figure 4.7**). Polymer solutions having a concentration of 4-6 mg/mL were prepared using *p*-xylene as solvent. Thin films were blade coated under optimized speeds (2 - 4 mm/s) at 100 °C on OTS-passivated surfaces. AFM images (**Figure 4.7** 2 to 5 μm viewing area) confirmed the

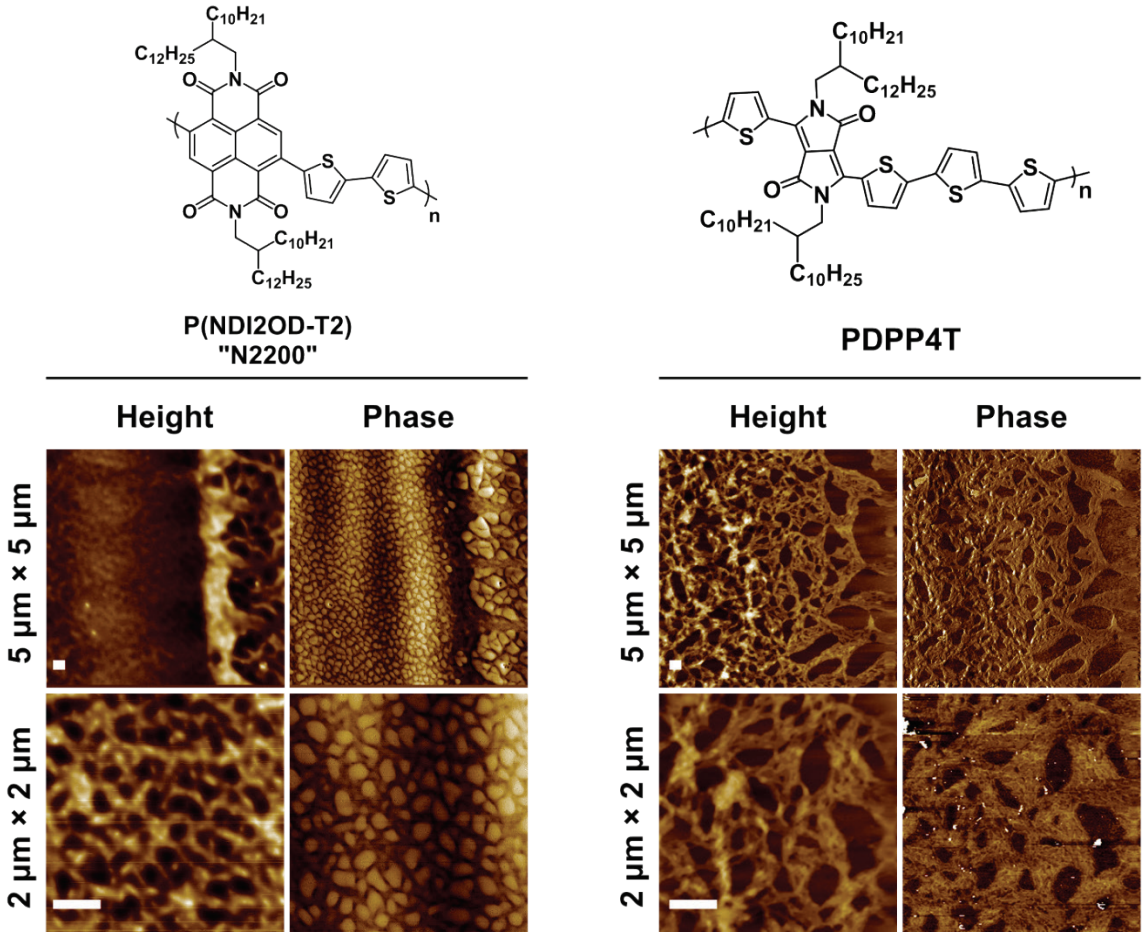

Figure 4.7. AFM height and phase images of two other polymers (**N2200**/n-channel, **PDPP4T**/p-channel) indicating the formation of nanofiber networks on OTS-processed devices at blade-coating speed of 3 mm/s and 4 mm/s, respectively. Scale bar is 400 nm.

presence of high density nanofiber networks in both systems. Due to polymer solubility differences, however, the morphologies differed somewhat from those observed for **PNDI2Tz**. Importantly, AFM images of both polymers showed similar network structure emerging under the blade coating conditions used here.

While overall morphology was different, the fabrication strategy developed for **PNDI2Tz** effected an increase in mobility for both **PDPP4T** and **N2200** (**Table 4.2** and **Figure 4.8**). Further process optimization is expected to provide for additional enhancements. Similar to **PNDI2Tz** transport performance, improved hole and electron transport performance for **PDPP4T** and **N2200**, respectively, is attributed to enhanced nanofiber network formation, particularly on low energy surfaces. For instance, **PDPP4T** mobility was only 0.28 $cm^2V^{-1}s^{-1}$ on HMDS passivated surfaces, while OTS-processed devices exhibited $\mu = 1.41$ $cm^2V^{-1}s^{-1}$, or in other words, a 5-fold increase. Similarly, **N2200** exhibited a 4-fold increase in mobility, from 0.047 $cm^2V^{-1}s^{-1}$ to 0.216 $cm^2V^{-1}s^{-1}$, for HMDS *vs.* OTS-processed OFETs. The mobilities measured here were lower than the highest values reported due to differences in device architecture, significant enhancements in

Table 4.2. OFET performances of **PDPP4T** and **N2200** under proposed blade coating conditions (same as the highest performing condition in **Table 4.1**).

		μ_{avg} (μ_{max}) ($cm^2V^{-1}s^{-1}$)	V_{th}(V)	$I_{ON/OFF}$
PDPP4T	HMDS	0.28 ± 0.04 (0.32)	-27.4 ± 1.3	10^4
	OTS	1.41 ± 0.17 (1.68)	-33.2 ± 3.6	10^4-10^5
N2200	HMDS	0.047 ± 0.022 (0.068)	11.4 ± 0.9	10^3
	OTS	0.216 ± 0.039 (0.277)	25.3 ± 1.4	10^4

OFET performance, directly correlated with interface chemistry and surface energy, were achieved in all three systems examined in this study.

4.3.6 Nanofiber Formation and Charge Transport

Semiconducting polymer charge transport performance is generally believed to be highly dependent upon overall film morphology, which includes the orientation of individual polymer chains relative to the substrate surface, orientation of chains with respect to each other, the level of aggregation of polymer chains into π-π stacked structures/domains and connectivity between aggregated domains.[253] Blade coating semiconductors from solution is a readily scalable thin-film deposition method known to enhance fiber alignment, fiber long-range and short-range order, and charge transport due

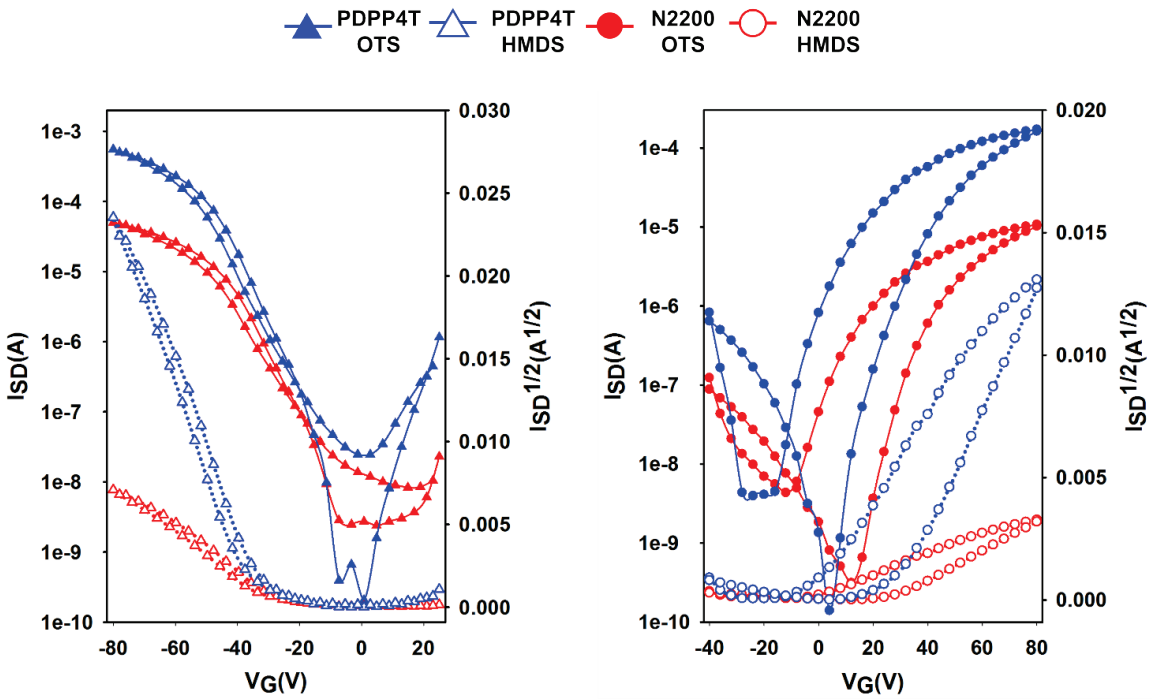

Figure 4.8. Transfer curves of **PDPP4T** (*p*-channel), and **N2200** (*n*-channel) showing processing versatility. Solid lines are source-drain current of OFETs, and dashed lines are source-drain current square roots.

to shear force.[273-275] The versatility of blade coating also allows for use of a wide range of solvents and easy control of substrate temperature. While the impact of shear forces on selected D-A conjugated polymers has been investigated, few studies have explored the role of substrate surface energy.

Here, three different, yet structurally similar D-A conjugated polymers were used to demonstrate the impact of substrate temperature, shear forces and interface chemistry/surface energy on charge transport performance. In all cases under optimized shear conditions, passivation of the device substrate to afford a lower energy surface led to fibril formation and enhanced charge transport performance. For the polymers investigated in this study, fabrication of thin-films on any processed surface was problematic when using *p*-xylene as solvent at room temperature. While solution deposition on higher energy surfaces (HMDS and PTS) *vs.* the OTS lower energy counterpart afforded more continuous semiconductor films, charge transport was impeded. With an increase in substrate temperature to enhance solvent evaporation, the polymer inks were able to consistently form uniform films, even on low energy surfaces. As temperature increased, more reliable and consistent film formation was achieved on HMDS surfaces and PTS surfaces; high quality films on OTS surfaces were formed up to100 °C.

Substrate temperature, blade speed and substrate surface energy, in combination impacted ultimate thin-film morphology, nanofiber formation in particular. As demonstrated by AFM imaging (**Figure 4.3** and **Figure 4.5**), nanofiber formation, density and orientation varied significantly with shearing speed. An 'optimized' microstructure, favorable to charge transport was obtained at a blade speed of 3 mm/s, which afforded the highest observed mobility for all polymer examined here. Under these conditions,

particularly on the lower energy OTS surface, networked nanofiber structures were attained. At higher blade coating speed, film formation was impacted due to solvent cohesion effects, relative to solvent evaporation. As substrate temperature increases, the solvent evaporates at a faster rate, leaving many microvoids in the film, thus exposing the substrate as the solute polymer chains self-assemble into tighter bundles driven by surface tension. Therefore, as solvent evaporates, polymer nanofiber formation was enhanced on lower energy surfaces. While this process enhances polymer nanofiber formation, overall processing conditions must be balanced to afford interconnected, uniform films. In addition, AFM results indicate the presence of aggregated nanofiber interactions within the fibril network. More obvious interactions were found in samples fabricated with a coating speed of 3 mm/s. (**Figure 4.3**) GIWAXS results revealed that the lamellar and π-π stacking distance both decreased for **PNDI2Tz** films fabricated on OTS *vs.* PTS and HMDS

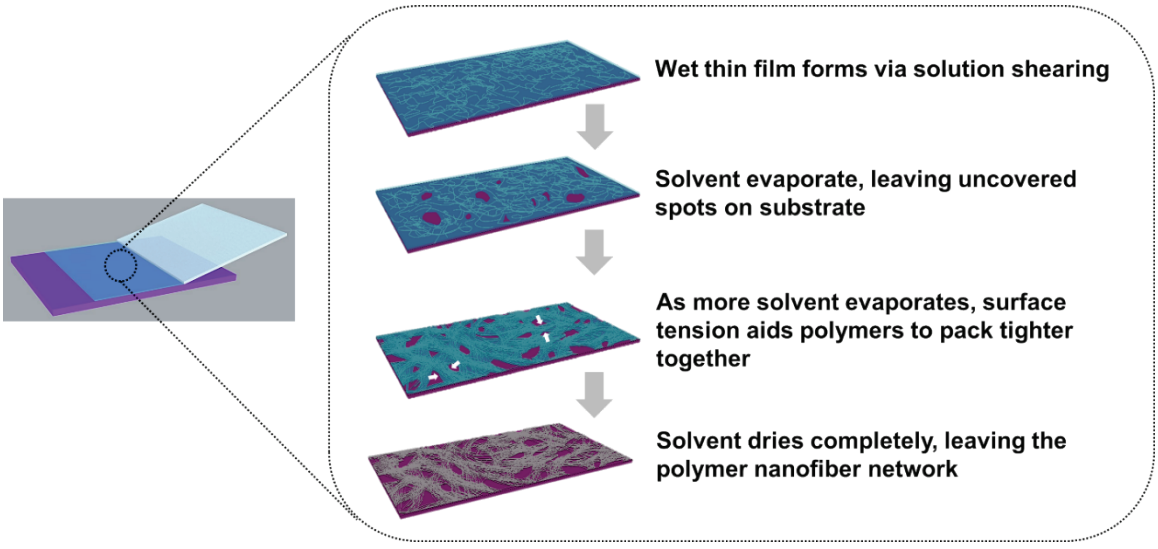

Figure 4.9. Schematic representation of the proposed conjugated polymer nanofiber network formation process on OTS-processed substrates.

surfaces, which implies that the molecular backbones and side chains became increasingly close-packed under the 'optimized' conditions.

Figure 4.9 presents a mechanistic, schematic representation of the evolution of film morphology with enhanced polymer nanofiber formation on an OFET device substrate. The synergistic effects of shear stress, cohesion, and high temperature aided film formation were expected to promote formation of a microstructure favorable for charge transport. Here, thin film devices fabricated on different energy surfaces were studied: shear at high temperature combined with use of a lower energy surface was favorable for thin film deposition and enhanced nanofiber network formation. From a fluid dynamics perspective, flow viscosity varied significantly with a change in the dimensions of the confined structure.[276] Molecular chain extension and intense π-π intermolecular stacking can be expected due to the effects of shear stress, solvent evaporation behavior, and polymer-substrate interfacial interactions. The hypothesis presented here is supported by AFM and GIWAXS analysis, as well as photophysical characterization. To further understand the synergistic effects of shear stress and low energy surface effects, *in-situ* characterization strategies, e.g., X-ray diffraction and neutron scattering, will be utilized in the future studies.

The phenomenon observed with high temperature blade coating is closely related to flow-induced changes in solvent evaporation and polymer conformation. In particular, enhanced solvent evaporation on low energy surfaces would be expected to promote self-assembly in polymer films. Below room temperature, solvents evaporate at slower rates which can lead to the formation of more uniform wet thin films. As solvent dries gradually, polymers would precipitate out and form a homogeneous polymer thin film. Under high

temperature blade coating condition, solvent evaporates much faster leaving voids within thin films. On higher energy surfaces, the polymer solution wets the surface well enough to form wet uniform films under shear stress. Low energy surfaces suppress the wetting phenomenon leading to inhomogeneous film formation. As polymer solution dries out, certain areas on the surface are left uncovered. Nevertheless, the polymers are 'pushed together' due to cohesion of the solvent so that the overall driving force enhances nanofiber formation.

These studies further support the design concept and hypothesis presented for solution based processing of conjugated polymers.[277] The shear speed dependent experiment (surface structure analysis in **Figure 4.5** and charge transport performance in **Table 4.1**) supports the importance of shear stress. Combined with the GIWAXS and AFM images, inter-fiber connections may have been formed during the high temperature coating process. Furthermore, the inter-fiber connections that would be afforded by the nanofiber network morphology provide additional support to the growing body of evidence that inter-grain polymer nanofibers play a major role in determining polymer macroscopic mobility, given the improved charge transport performance demonstrated. A similar mechanism is expected to be at play for the electron transport materials, obvious bundle-like structures can be observed in **Figure 4.9**. Thus, blade coating on low energy surfaces will lead to desirable microstructures on the molecular scale through to the mesoscale, and up to the macro scale with a range of a few hundred micrometers.

4.4 Conclusion

In this chapter, we reported the enhanced conjugated polymer nanofiber formation on low energy surfaces. Through experiments on multiple conjugated polymers in non-halogenated solvents, significant mobility enhancements were attained. By systematically analyzing polymer thin film morphologies, a mechanistic explanation of previously reported results of performance enhancements in OFETs fabricated on low energy surfaces was provided. The formation of conjugated polymer nanofiber bundles on low energy surfaces are due to the synergistic effects of solution shearing and interface chemistry / surface effects. Given the synergistic effects of shear flow with surface processing techniques, such processing studies can play an important role in the desired large scale fabrication of soft electronics on various surfaces.

CHAPTER 5. THIAZOLE-NAPHTHALENE DIIMIDE CONJUGATED POLYMERS FOR ACID SENSING APPLICATIONS

5.1 Abstract

Functional π-conjugated materials, especially stimuli-responsive π-conjugated materials have been used extensively for chemical sensors, and a π-conjugated system leads to a change in molecular geometry and/or electronic structure that can be detected as a change in either the optical or electrical properties. In this chapter, **PNDI2Tz** is reported as an acid sensing material. In addition, **PNDI2Tz** *n*-channel OFETs were fabricated and device electronic responses against gas phase Lewis acid, boron trifluoride were investigated. **PNDI2Tz** shows high response to BF_3 gas by forming Lewis acid-base adduct which can significant reduced electron transport in OFETs. **PNDI2Tz**-based OFET exhibit a pure electron mobility of 0.05 $cm^2V^{-1}s^{-1}$ at normal working state. In the presence of 60 ppm BF_3, **PNDI2Tz** OFET-based gas sensor is turned off within 100 seconds. The turn-on/turn-off cycle can be repeated for over 50 times with insignificant harm to **PNDI2Tz** OFET sensor.

5.2 Introduction

Functional π-conjugated materials, especially stimuli-responsive π-conjugated materials have been used extensively for chemical sensors,[278] where selective interaction between a target analyte (*i.e.* biological macromolecules, ions, particles) and a π-conjugated system leads to a change in molecular geometry and/or electronic structure that

can be detected as a change in either the optical or electrical properties. For example, π-conjugated compounds have been used for selective ion sensing of iodine/mercury[279] and zinc[280, 281], where specific compound-analyte interactions lead to a change in either the absorption or fluorescence of the complex system. Interactions between π-conjugated compounds and stimuli, such as biological systems, can also be used to for sensing applications[282]. In addition, π-conjugated materials can detect pH changes in solution through the halochromic effect, in which materials changes color upon addition of protons[283].

Among a variety of π-conjugated structures, thiazoles have recently gained increasing attention since nitrogen incorporation in the thiazole rings can impart control over frontier molecular orbital energies[284], and also facilitate directed intermolecular interactions in both solutions[285, 286] and the solid-state[75, 287]. The basic nitrogen of thiazoles can be utilized for developing halochromic materials which show a change in optical absorption as a result of acid-base interactions. The general mechanism for the halochromic

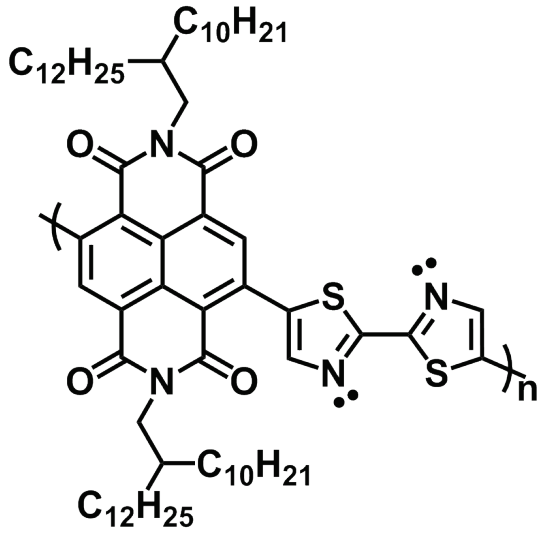

Figure 5.1. Chemical structure of PNDI2Tz showing nitrogen atom lone pairs.

response of thiazole-based compounds is based on the activation of intramolecular charge transfer absorption that results from protonation (or interaction with Lewis acid) of the nitrogen in thiazole. Therefore, π-conjugated structures with strong built-in donor–acceptor interactions tend to exhibit a more pronounced halochromic effect due to an enhanced ability to redistribute charge density and promote charge-transfer (CT) absorption[283]. In addition, thiazoles have been proven as a promising building block for new generation conjugated polymers for organic electronic applications, such as organic photovoltaics (OPV)[64, 207, 288], and organic field-effect transistors (OFET)[76, 90, 121].

In this study, we focused on investigating the halochromic effect of a newly synthesized donor-acceptor (D-A) conjugated polymer, **PNDI2Tz** with respect to acids in solution and acidic gas fumes in the solid state (**Figure 5.1**). We discovered a pronounced halochromic behavior where significantly different optical responses were observed. By investigating **PNDI2Tz**'s halochromic behavior, we proposed **PNDI2Tz**'s acid sensing mechanism. Furthermore, we studied **PNDI2Tz** for promising OFET-based sensor for an acidic gas, boron trifluoride (BF_3).

5.3 Experimental

5.3.1 Materials and Measurements

PNDI2Tz was synthesized and prepared by previous literatures[69, 70]. All reagents and solvents were purchased from commercial sources, and were of reagent grade. All acids were purchased from commercial sources, and were of reagent grade. Chloroform, dichloromethane, toluene, *p*-xylene (PX), isopropanol, tetrahydrofuran (THF), dimethylformamide (DMF), chlorobenzene, 1,2-dichorobenzene (*o*-DCB), and 1,2,4-

trichlorobenzene (TCB) were purchased as anhydrous grade solvents from Sigma-Aldrich. THF was distilled from sodium benzophenone in a solvent purification system (SPS). 2-Bromothiazole was purchased from Scientific Matrix. Tetrabutylammonium bromide (*n*-Bu4NBr), *n*,*n*-diisopropylethylamine (DIPEA), diisopropylamine (DIPA), palladium(II) acetate ($Pd(OAc)_2$), tris(dibenzylideneacetone)- dipalladium(0) ($Pd_2(dba)_3$), tri(*o*-tolyl)phosphine (P(*o*-tolyl)$_3$), sodium diethyldithiocarbamate, and tetra-*n*-butylammonium hexafluorophosphate ([*n*-Bu_4N]+[PF_6]-) were purchased from Sigma-Aldrich. *N*-octadecyltrichlorosilane (OTS), was purchased from Gelest, Inc. Silica gel was purchased from Sorbent Technologies (Premium Rf™, porosity: 60A; particle size: 40-75 μm). Anhydrous chlorobenzene was degassed prior to use by a freeze-pump-thaw process.

All polymer thin films for UV-*vis* absorption characterization were prepared by spin-coating polymer solutions in *p*-xylene (5 mg/mL), and chloroform (5 mg/mL), onto pristine SiO_2 glass substrates and pre-treated glass coverslip substrates. Low concentration OTS solutions (0.1% v/v in toluene) were prepared within a glovebox filled with N_2. UV-ozone cleaned device substrates were transferred into a N_2 filled glovebox immediately after cleaning, and then submerged in the as prepared surface treatment solutions overnight at room temperature. The passivated substrates were then bath sonicated in toluene for 30 min, followed by blow drying with compressed air (after passing through a molecular sieve to filter off water and oil).

Thin films were blade-coated onto the substrates using an in-house blade coater (DMX-UMD-17/23 Firmware, Arcus Technology) equipped with a glass blade and temperature controlled heating stage. Polymers were first dissolved in *p*-xylene to prepare the active ink (5-10 mg/mL) and then coated onto processed glass slides (for UV-*vis*

studies), processed *p*-doped Si wafers (for GIWAXS studies), or processed OFET device substrates (for electronic property studies) at 100 °C. Blade coating speeds were programmed and precisely controlled by a DMX-UMD 23 controller from Arcus Technology. Blade height was controlled to be within a range of 45-55 μm, and blade angle was set to be 8° ± 1°. Heating during blade coating was achieved by embedded thermocouples with precise temperature control. For chloroform samples, the heating temperature was set at 45 ºC; for *p*-xylene samples, the temperature was set at 100 ºC.

5.3.2 UV-vis Measurements

For solution UV-*vis* spectroscopy, **PNDI2Tz** stock solution was prepared at a concentration of 0.5 mg/mL, equivalent of a repeating-unit molar concentration of 4.5×10^{-4} mol/L. Prepared stock solution was heated in a N_2 filled glovebox for 30 min to break all aggregates, followed with passing through a 0.2 μm PTFE filter. 1.8 mL diluted **PNDI2Tz** solution (4.5×10^{-5} mol/L) was then transferred to a 1 cm × 1 cm quartz cuvette with seal. Diluted acid solutions (1.02×10^{-3} M) in acetonitrile (MeCN) were prepared in similar fashion. A 5 μL GC gas tight syringe was used to transfer 2 μL of diluted solution to UV-*vis* cuvette. Between adding acid to UV-*vis* cuvette, gas tight syringe is rinsed with pure MeCN for 3 times, and then acid stock solution for 3 times.

For thin film UV-*vis* spectroscopy, **PNDI2Tz** in chloroform and *p*-xylene stock solution (4-6 mg/mL) were blade coated on UV-ozoned cleaned SiO_2 glass slides. For BF3 exposure experiments, we purged chamber with N_2 for 3 min to ensure anhydrous environment. Then, we injected 20 μL of anhydrous $BF_3{\cdot}OEt_2$ as source of BF_3 (concentration calculated by BF_3 as 281 ppm), and record the change in thin film UV-*vis* spectra. All waste BF_3 gas was properly neutralized by trimethylamine (TEA), and all

measurements were performed with good ventilation. A special gas chamber is built to fit in the N_2 glovebox with two gas inlets (BF_3 and N_2), and one outlet connected to a vial of trimethylamine solution to neutralize BF_3 (**Figure 5.2**).

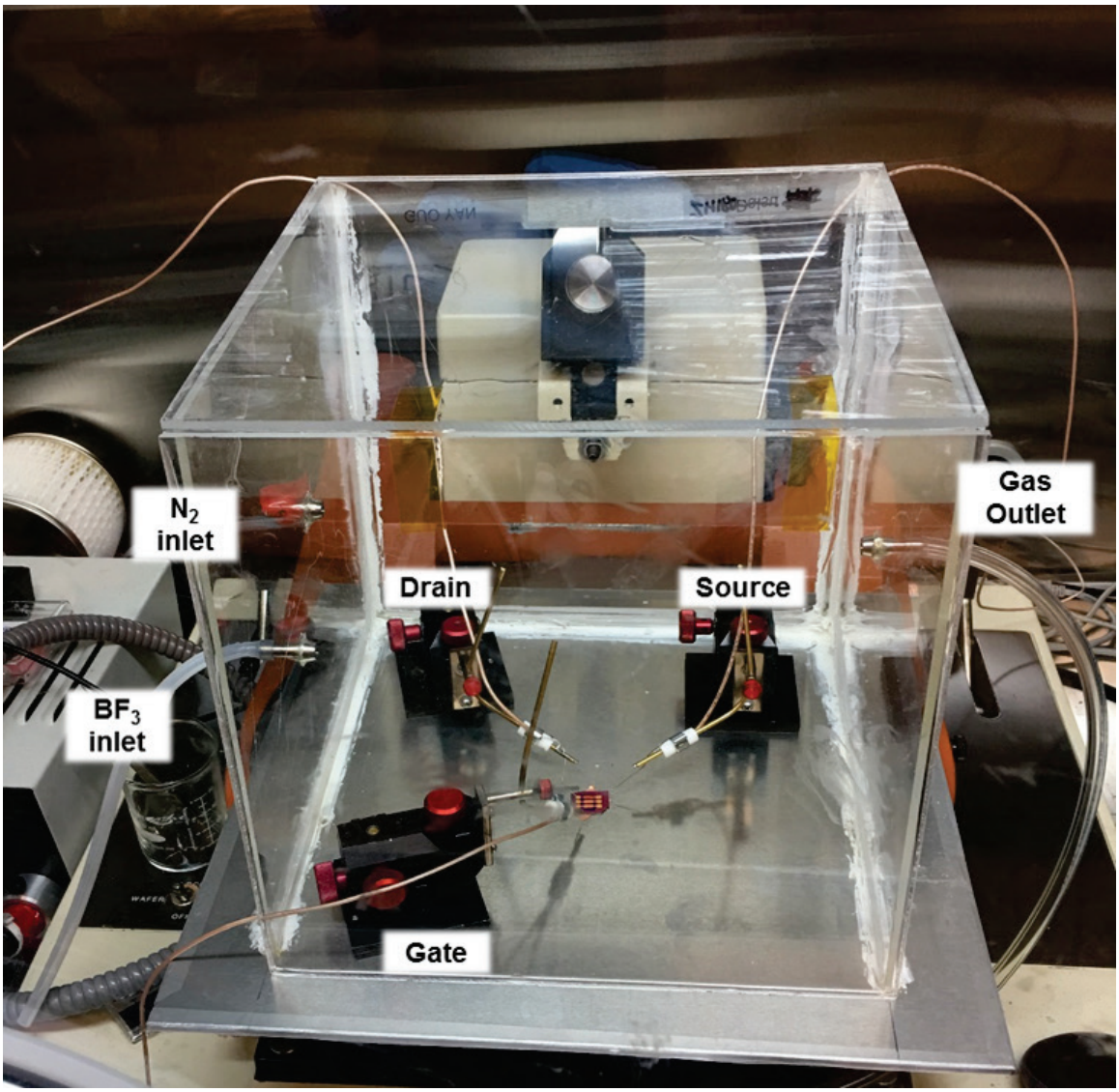

Figure 5.2. PNDI2Tz OFET-based BF_3 sensor in custom-built gas chamber for sensing test.

5.3.3 Thin Film Preparation and Device fabrication

All electrode evaporation processes were conducted on single-crystalline (100) Si wafers at Marcus Nanotechnology Center at Georgia Institute of Technology. For blade-coated films, 8-15 μL of polymer solution (4-6 mg/mL) was added on one side of a glass slide or wafer that had been sitting on the heating stage for at least 5 minutes to ensure the substrate was at the programmed temperature. In this study, only blade coating was performed due to poor film formation *via* spin coating methods. For the fabrication of bottom-gate/bottom-contact organic thin-film transistors, highly *n*-doped (100) silicon wafers with a 300 nm thermally grown oxide gate dielectric film were used as device substrates. Au source and drain contacts (50 nm of Au contacts with 3 nm of Cr as the adhesion layer) with fixed channel dimensions (50 μm in length and 2000 μm in width) were deposited *via e*-beam evaporation using a photolithography lift-off process. The Si/SiO_2 substrates were washed *via* bath sonication (Branson® Ultrasonic Bath, 230 V_{ac}, 50 Hz) sequentially in acetone, methanol and isopropyl alcohol for 15 min, followed by treatment in UV-ozone for 30 min (Novascan® PSD-UV - Benchtop UV-Ozone Cleaner).

Bottom-gate, bottom-contact architecture OFETs were fabricated as sensor devices. The polymer semiconductors were blade-coated from a 5 mg/mL *p*-xylene solution, and then were annealed at 150°C for 30 min in the glovebox. Au source/drain electrodes (W=2000 μm, L=50 μm) were used to measure the electrical performances of **PNDI2Tz**-based devices. The field-effect mobilities were calculated from the transfer curves for more than six devices in the saturation regime (V_G=45 V).

Semiconducting thin films were fabricated *via* blade-coating at 100 °C to improve solvent evaporation and thin film formation on passivated surfaces. During the blade-

coating process, 5 to 10 μL of semiconductor solution (5 mg/mL) was cast onto a heated substrate (1.5 cm × 1.5 cm). The angle between the glass blade and the substrate was set to be ca. 8°. Thin film formation was optimized by controlling different solution-shearing conditions such as substrate temperature and blade-coating speed. The blade-coated substrates were placed in a vacuum oven at 55 °C overnight to remove residual solvent.

OFET electronic characteristics were measured using an Agilent 4155C semiconductor parameter analyzer inside a N_2 filled glovebox. Charge carrier mobilities (μ), threshold voltages (V_{th}) and on/off ratios ($I_{on/off}$) were calculated in the saturation regime. The reported values are the average of 15 different devices with the standard deviation recorded. The microstructure and surface morphology of the thin-films were analyzed by atomic force microscope (AFM, Bruker Dimension Icon® Atomic Force Microscope, Mikromasch® AFM probe tips, 3.5 N/m, 135 kHz).

5.4 Results and Discussion

The synthesis of **PNDI2Tz** was reported previously,[271] **PNDI2Tz**and purified by Soxhlet extraction. The low-molecular-weight portions and residual catalyst impurities were removed by dissolution in ethanol, acetone, and hexane. The chloroform extracts were concentrated and precipitated in ethanol, and then the solids were collected as a product. **PNDI2Tz** shows a number-average molecular weight (M_n) of 49.3 kD with a PDI of 3.33, as determined by gel permeation chromatography (GPC) relative to polystyrene standards with chloroform as eluent.

*5.4.1 **PNDI2Tz** Halochromism in Solution*

PNDI2Tz-acid interactions were first investigated in solution with a variety of acids including sulfuric acid (H_2SO_4), trifluoroacetic acid (TFA) and nitric acid (HNO_3). We selected HNO_3 to study the mechanism associated with **PNDI2Tz**. Within 5 seconds subsequent addition of methanol (MeOH) resulted in an immediate change in color of the solution back to the original pink. (**Figure 5.3**) Such cycle could be repeated more than 5 times. In order to further investigate the mechanism associated with the observed color change, stoichiometric addition of nitric acid (1.02×10^{-3} M) in MeCN was performed, and the resultant changes were monitored by UV-*vis* spectroscopy.

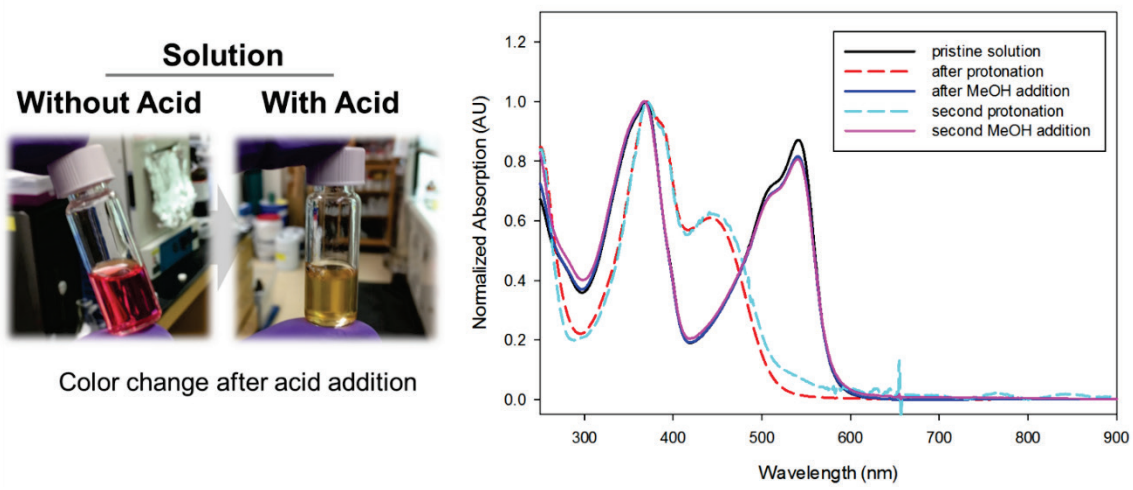

Figure 5.3. (left) **PNDI2Tz** halochromic effect in solution with HNO_3 addition; (right) UV-*vis* spectra of **PNDI2Tz** solution during acidification cycles.

As presented in **Figure 5.4**, when a total of 0.3 equivalents of nitric acid (relative to mole of **PNDI2Tz** in system) is added to a solution of **PNDI2Tz** in *p*-xylene, the color change was completed, and no further changes in color as determined by UV-*vis* were observed, suggesting a saturation threshold. Subsequent addition of MeOH, which acts as a Lewis base to bind with H^+, the **PNDI2Tz** solution immediately switches back to its

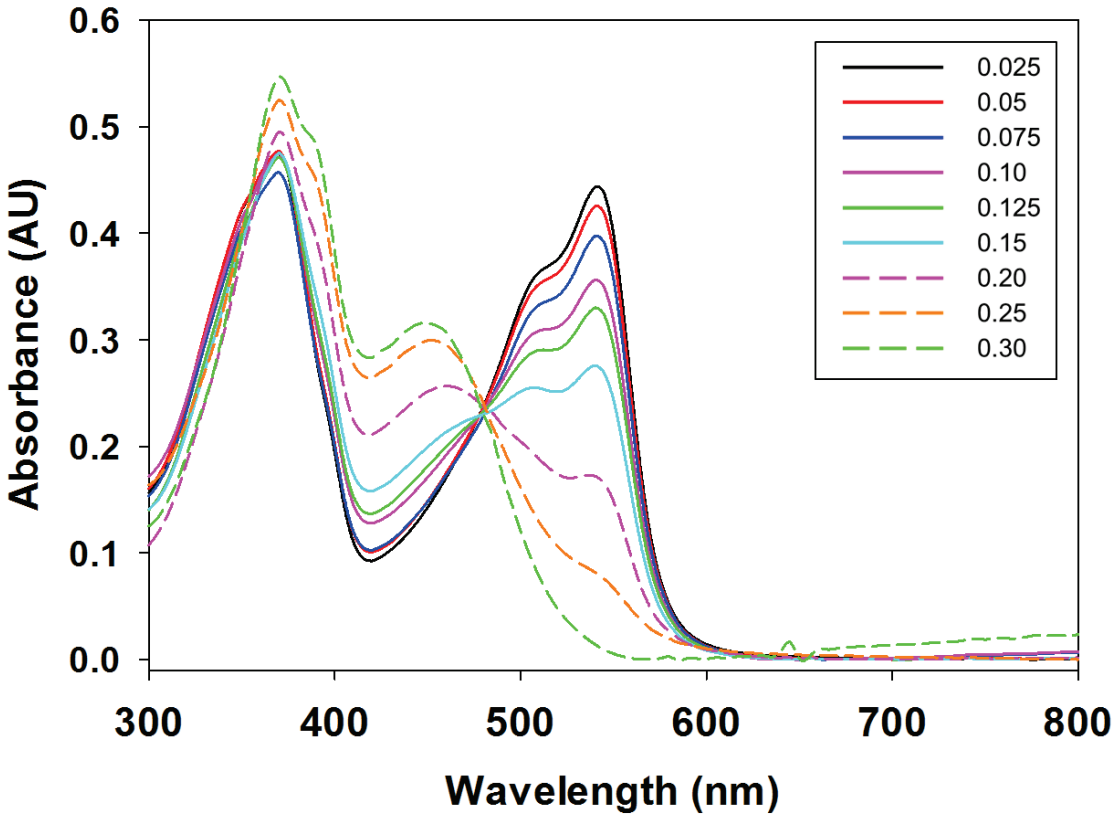

Figure 5.4. Stoichiometric addition of HNO_3 in **PNDI2Tz** solution with HNO_3 molar equivalences.

original pink color though some solution haziness was apparent, presumably due to polymer aggregation induced by MeOH, a poor solvent for **PNDI2Tz**. The result also indicates that **PNDI2Tz** is a weak Lewis base (LB) that forms a weak Lewis acid-Lewis base (LA-LB) adduct with H^+.

The addition of complementary ions ($NaNO_3$, KNO_3 in acetonitrile) results in no halochromic effect, confirming that H^+ is the active species involved in **PNDI2Tz** solution color change ($NaNO_3$ solubility in MeCN is 3 mmol/kg, and KNO_3 solubility in MeCN is 2.3 mmol/kg[289]). In the presence of H^+, the UV-*vis* absorption at 540 nm decreases in intensity, while that at 450 nm increases, indicating a gradual shift in the absorbing species.

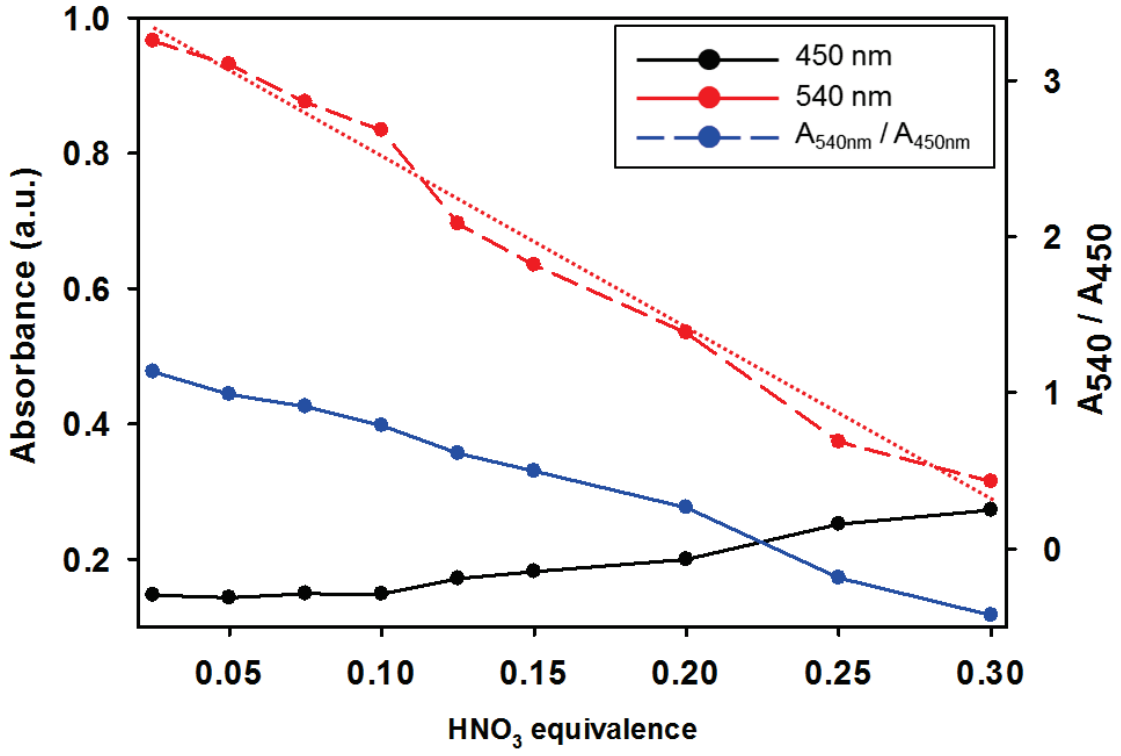

Figure 5.5. PNDI2Tz solution UV-*vis* relative absorbance (A_{540}/A_{450}) with respect to different HNO_3 molar equivalences.

The relative absorbance of (A_{540}/A_{450}) was used to evaluate the sensitivity of **PNDI2Tz** toward HNO_3 (**Figure 5.5**). At the incremental equivalence of 0.025 (relative to mole of **PNDI2Tz** in system), the **PNDI2Tz**system equilibrates after 12 aliquots of acid solution are added to the polymer, enabling a colorimetric sensing of H^+. The absorption measurements were taken immediately upon addition of acid, and the results are depicted in **Figure 5.5**. With increasing H^+ content in the solution mixture, **PNDI2Tz** response **PNDI2Tz**increases, and a linear relationship between (A_{540}/A_{450}) and the equivalence of H^+ (R^2=0.985) is observed. Thus, **PNDI2Tz** is may facilitate quantitative detection of H^+ in solution within the investigated concentration range[290].

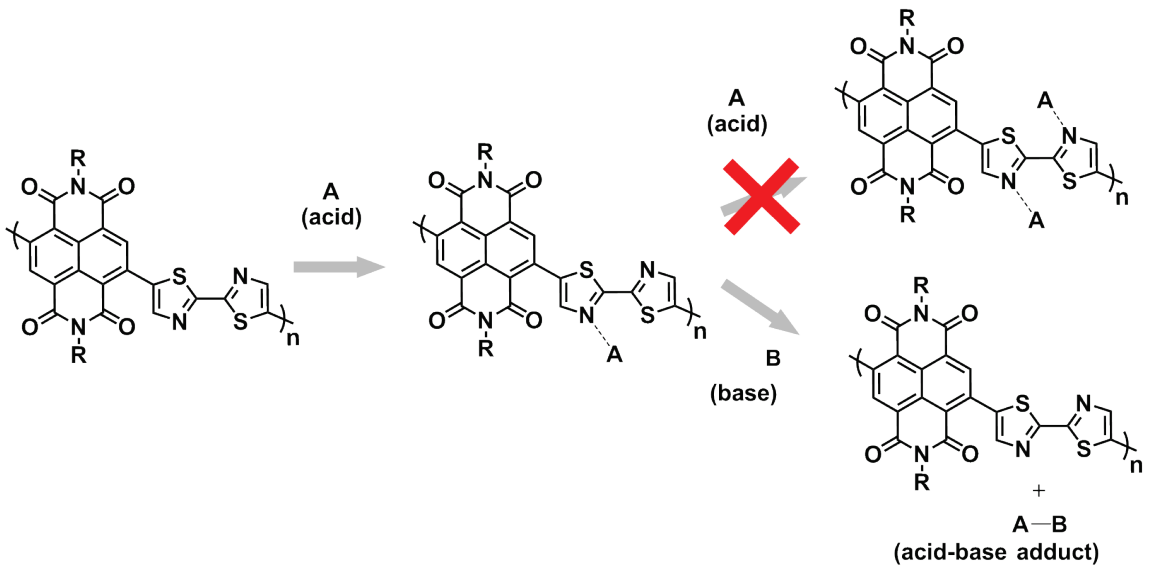

Figure 5.6. Proposed mechanism of PNDI2Tz interaction with acids.

During acidification, **PNDI2Tz** optical bandgap increased from 2.12 eV to 2.26 eV (pristine onset absorption at 584 nm, after acid onset absorption at 549 nm). In addition, we noticed an isosbestic point at ca. 485 nm. **(Figure 5.4)** The appearance of an isosbestic point indicates that the stoichiometry of the reaction remains unchanged during the course of the reaction or the physical change of the sample, and that no secondary reactions occur during the considered time range[291]. Since there are two nitrogen items in 2,2'-bithiazole for every **PNDI2Tz** repeating unit, the stepwise protonation of both bithiazole nitrogen species would lead to the formation of a mono-protonated intermediate species, resulting an absence of the isosbestic point. Therefore, the presence of this point indicates that the acidification process does not form any intermediate species. With respect to each repeating unit, the proton can only bind to one thiazole nitrogen atom, not both. (**Figure 5.6**).

*5.4.2 BF_3 Interaction with **PNDI2Tz** in Solid State*

We further extended the scope of the investigation of **PNDI2Tz** interaction with acidic species to include neutral Lewis acid (LA) species. BF_3 represents one industrially relevant and readily candidate. **PNDI2Tz** thin films were exposed to BF_3 fumes at room temperature, and the recovery process was studied. Due to the volatile nature and toxicity of BF_3 gas, fresh $BF_3{\cdot}OEt_2$ was used as the source of BF_3. A **PNDI2Tz** covered glass slide was treated with BF_3 fume in an isolation chamber, as described in *Section 5.4.1*. Prior to exposure to the Lewis acid, the **PNDI2Tz** thin film appears pink. As 20 µL $BF_3{\cdot}OEt_2$ (equivalent to 0.16 mmol BF_3) was added to the chamber, the thin film slowly changes color to yellow. Assuming BF_3 uniformly disperses throughout the chamber, the equivalent BF_3 concentration in the chamber was 281 ppm.

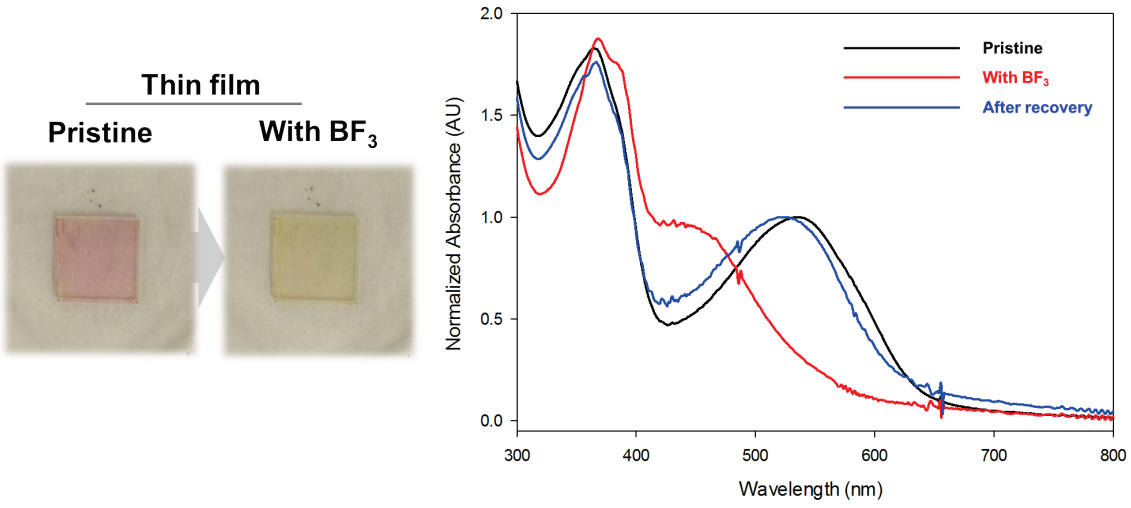

Figure 5.7. (left) **PNDI2Tz** halochromic effect in solid state with BF_3 fume; (right) UV-vis spectra of **PNDI2Tz** thin film during BF_3 cycles.

Subsequently, the **PNDI2Tz** film was transferred out of the chamber and left in the ambient at room temperature for 5 min. **PNDI2Tz**The color of **PNDI2Tz** switched back to

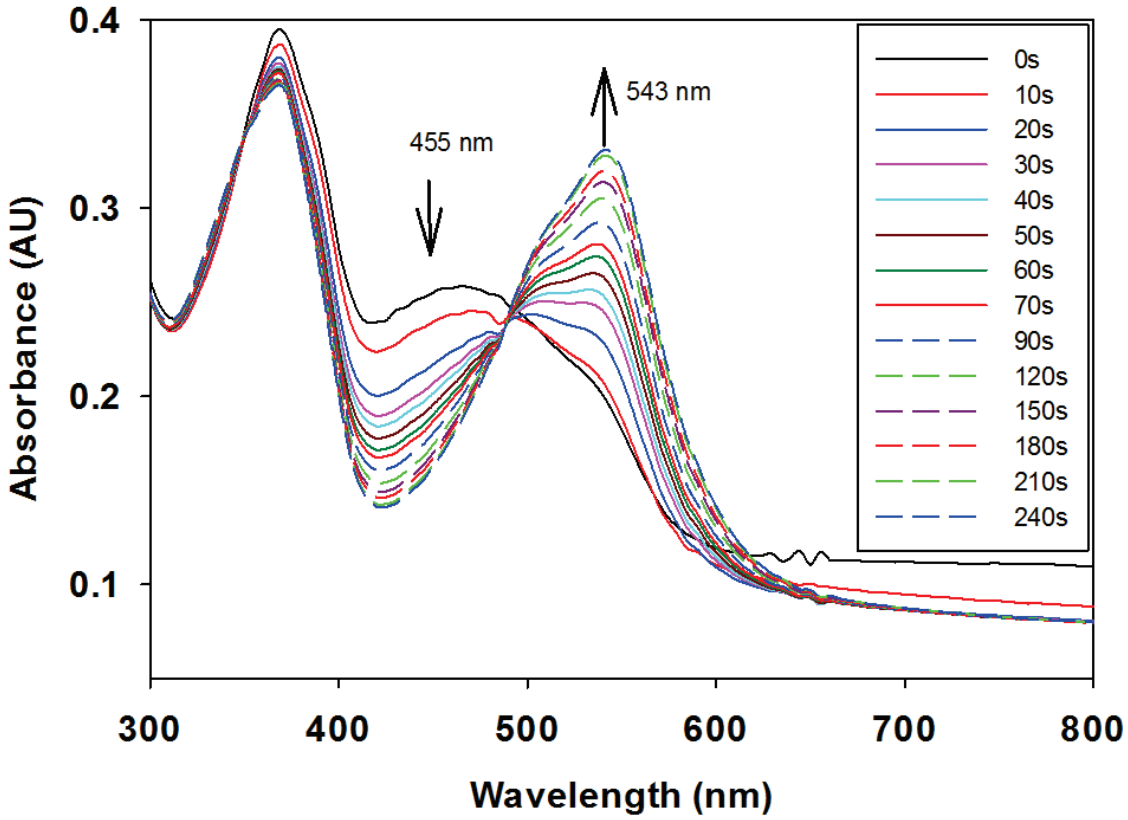

Figure 5.8. Overlaid UV-*vis* spectra of PNDI2Tz recovery process after BF_3 exposure.

the original pink. (**Figure 5.7**) The process appeared spontaneous, and addition of base was not required. As BF_3 evaporated from the **PNDI2Tz** film, the color change could be monitored by UV-*vis* spectroscopy. During the recovery process, the **PNDI2Tz** absorption at 543 nm increases in intensity, while the 455 nm band decreases, and an isosbestic point is apparent at 490 nm. The shoulder at 387 nm that is apparent in the Lewis acid treated film, eventually disappears after 240 s. The starting state and end state absorption patterns in the BF_3 exposure experiment are very similar, if not identical, to the **PNDI2Tz** acidification process in solution. Similarly, the **PNDI2Tz** optical bandgap increased from 2.04 eV to 2.16 eV (pristine **PNDI2Tz** thin film onset absorption at 607 nm, after BF_3 onset absorption at 575 nm). (**Figure 5.8**)

5.4.3 ***PNDI2Tz*** *OFET for BF_3 sensor*

PNDI2Tz OFET sensor is tested against BF_3 in a custom chamber. OFET was first cycled for 3~4 minutes by sweeping with gate voltage from -25 V to 80 V (15 to 20 front-and-back scans). When OFET transfer curve is stabilized, 5 µL $BF_3{\cdot}OEt_2$ fume is injected

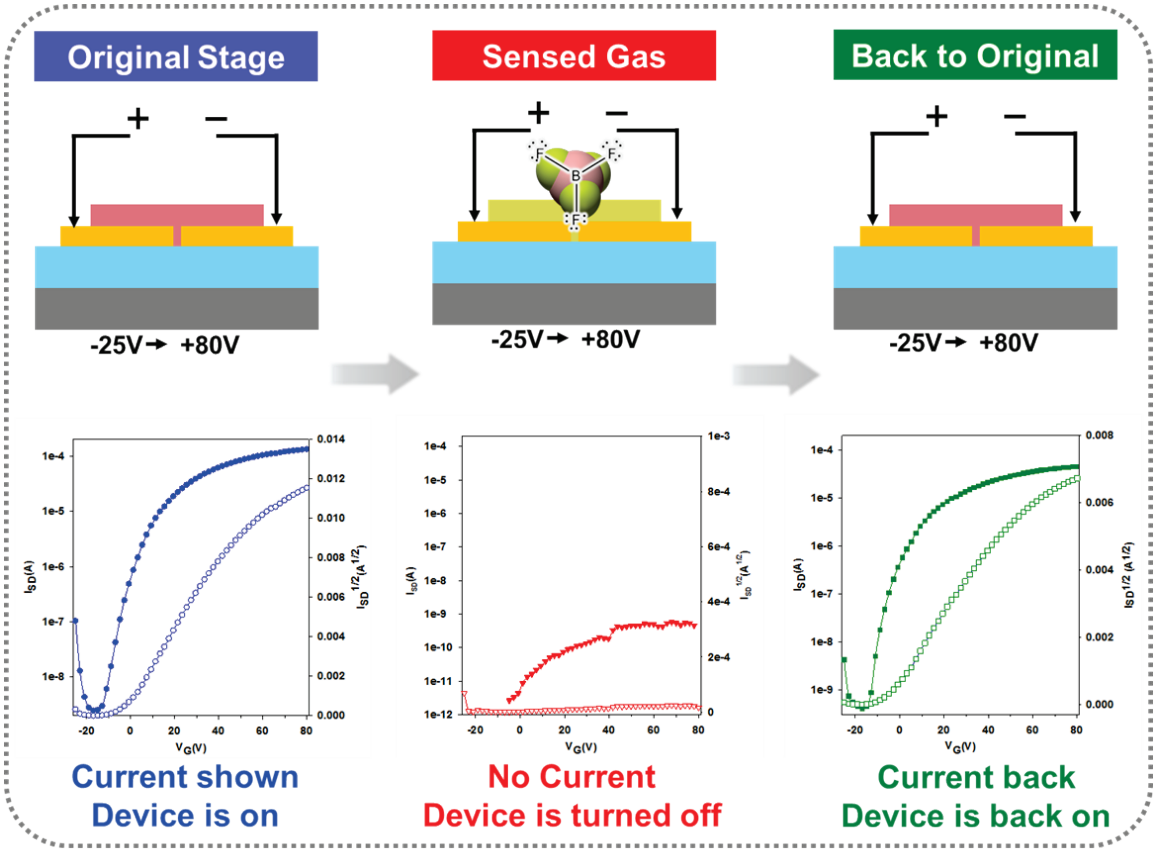

	Original Stage	Sensed Gas	Back-to-original
On-Current (I_{ON})	134 µA (± 21 µA)	Lower than 1 nA	98 µA (± 17 µA)
Threshold Voltage (V_{th})	-1.4 V (± 0.5V)	Not measurable	-2.8 V (± 1.7 V)
Mobility (μ_e^{FET})	0.043 cm^2/Vs (± 0.003 cm^2/Vs)	No mobility measured	0.035 cm^2/Vs (± 0.008 cm^2/Vs)

Figure 5.9. Demonstration of PNDI2Tz OFET-based BF_3 sensor with transfer curves.

in chamber (equivalent BF_3 concentration at 60 ppm). While OFET detects BF_3 fume, the transistor is turned off, showing reduced source-drain current (I_D) current to 10^{-8}~10^{-10} A, a 4~6 order of magnitude drop. For blank control experiments, anhydrous ether was pumped in chamber while OFET source-drain current is simultaneously monitored. OFET performed normally during the whole run, indicating BF_3 is the active species that turned off the transistor. After transistor is turned off, the transistor was transferred into the antechamber and left in vacuum (-30 mmHg) for 3 min and purged with pure N_2. Post testing on OFET shows that the OFET regains its transistor characters with similar I_D. (**Figure 5.9**).

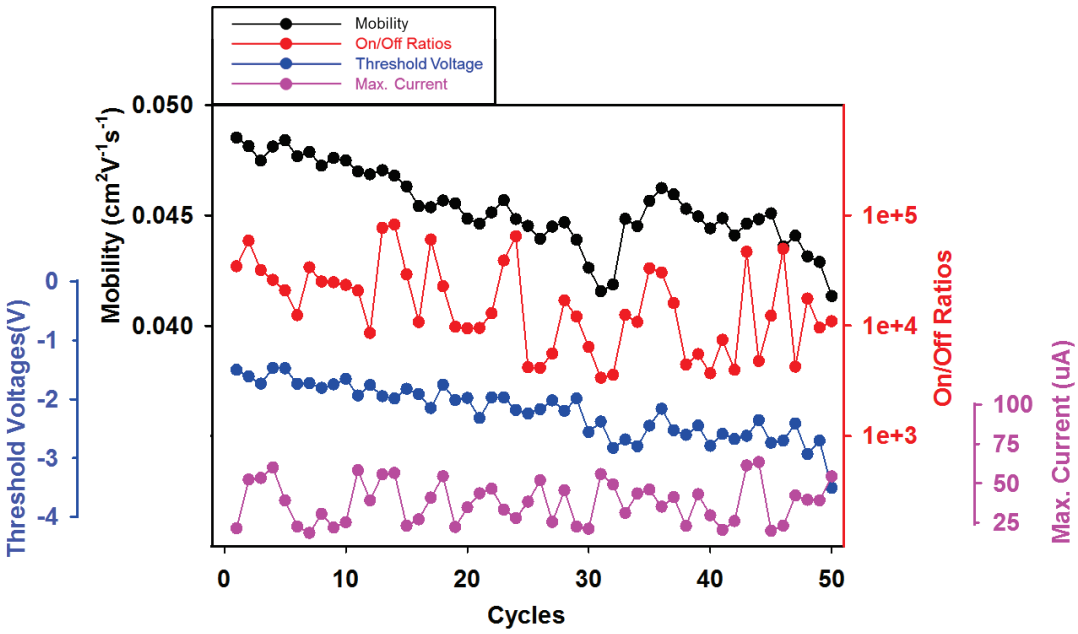

Figure 5.10. PNDI2Tz OFET-based BF3 sensor stability test and performance summary in 50 BF_3 treating cycles.

We tested the transistor for 50 cycles and recorded the mobility, highest I_D and threshold voltages of each run. (**Figure 5.10**) The I_D gradually decreased after 10 runs, but stayed above 20 μA, with increased threshold voltage (V_{th}) from -1 V to -4 V. OFET mobility stayed within a reasonable range with a slight drop, indicating the OFET sensor possess exhibits stable and robust performance. Control experiments with ether fumes were also conducted to ensure that the observed changes in OFET performance are not due to the addition of complementary species. Results shown in **Figure 5.11** illustrate the OFET source-drain current during the first 6 min after each species is added to the chamber. With anhydrous $BF_3 \cdot OEt_2$, **PNDI2Tz** OFET soon loses its transistor characteristics and the I_D

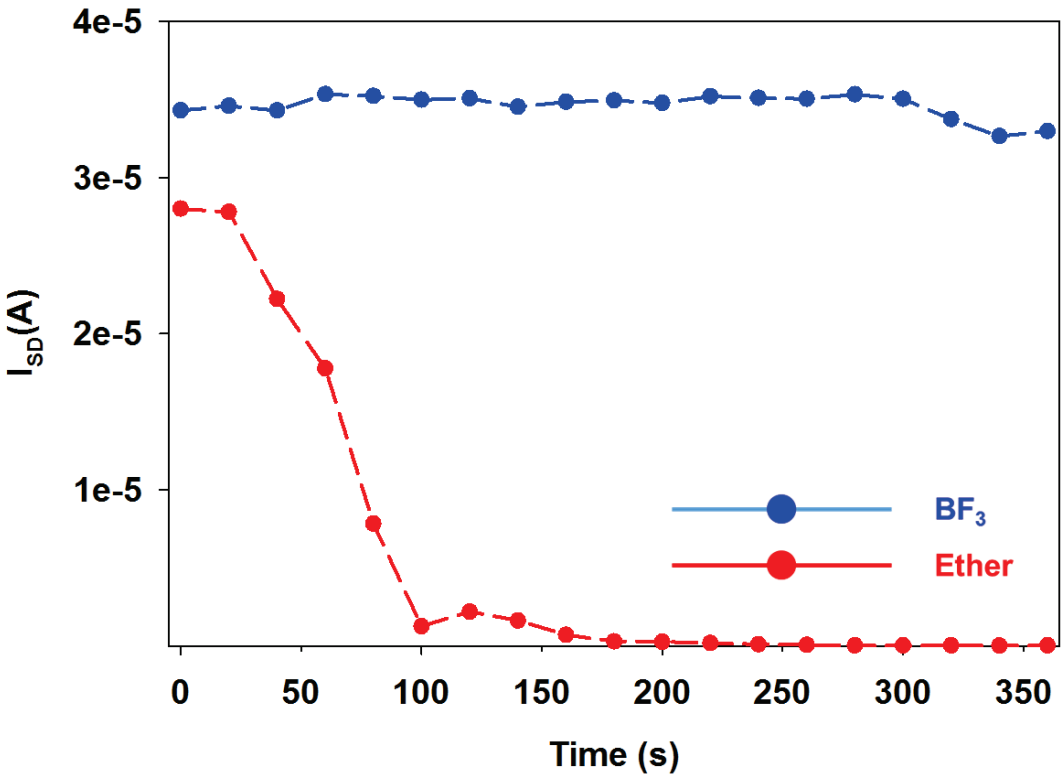

Figure 5.11. Real-time **PNDI2Tz** OFET source-drain current (I_D) with BF_3 fume addition and ether fume addition (as blank).

remained low for the remainder of the experiment; while with addition of anhydrous ether, **PNDI2Tz** OFETs perform well with no observed drop in I_D.

5.5 Conclusion

In conclusion, a newly synthesized conjugated polymer, **PNDI2Tz**, is reported as an acid sensing material. In addition, **PNDI2Tz** *n*-channel OFETs were fabricated and device electronic responses against exposure to the gas phase Lewis acid, boron trifluoride were investigated. **PNDI2Tz** shows high response to BF_3 gas through formation of a Lewis acid-base adduct which can significantly reduce electron transport in the semiconducting polymer. **PNDI2Tz**-based OFETs exhibit a pure electron mobility of 0.05 $cm^2V^{-1}s^{-1}$ under normal working conditions. In the presence of 60 ppm BF_3, the OFET is turned off within 60 seconds. The system appears robust, where the cycle can be repeated for over 50 times with insignificant harm to **PNDI2Tz** OFET performance. It is believed that the interactions between the nitrogen lone pairs in the bithiazole moiety and acids is the primary reason for both the halochromic effect and changes in electronical signals. This study revealed that **PNDI2Tz** possesses significant potential to pave the way for new, low-power OFET-based sensor designs aimed at detecting acidic species.

CHAPTER 6. CONCLUSIONS

This dissertation discusses the design, synthesis, and characterization of thiazole-containing π- conjugated semiconducting copolymers, the structure-process-properties of those polymers and their applications to OFET and OFET-based sensor devices.

Chapter 1 introduced the background of organic semiconductors and focused on recent advances with respect to the development of high-performance *n*-channel semiconducting polymers and summarized crucial methodologies in semiconducting polymer synthesis, characterization, and OFET device fabrication and processing.

Chapter 2 discussed the all-acceptor (A-A) design through homo-coupling of the electron deficient monomer, dibromo-bisthiazole-diketopyrrolopyrrole (DTzDPP) to afford **PDPP2Tz**, and incorporation of an electron deficient 2,2'-bithiazole moiety into an electron deficient DPP-thiazole system to afford **PDPP4Tz**. Even though the homo-coupled polymer **PDPP2Tz** did not show desirable OFET characteristics, the A-A copolymer, **PDPP4Tz** has a low HOMO energy level owing to the overall electron-poor nature of all building blocks. Polymer side chains impact the polymer solution processability and polymer inter-chain π-π interactions. A branched side chain having the branching position remote from the polymer backbone has the advantages of both improved solubility from branched units and effective π–π intermolecular interactions compared with those having branched chains close to the polymer backbone. A branched 5-decylheptadecyl (5-DH) side chain was incorporated into the polymer structure to enhance its solution processability, resulting a highly soluble polymer not only in common halogenated solvents, but also in more environmentally benign solvents

(xylenes, tetralin, toluene), which is more desirable for potential industrial applications. In addition, DFT calculations reveals that **PDPP4Tz** exhibits excellent planarity due to the small torsion angles between all ring units. X-ray scattering proves that **PDPP4Tz** thin films possess a high level of crystallinity in the solid state, which greatly enhanced its electron mobility (highest mobility measured as 0.067 $cm^2V^{-1}s^{-1}$ on BCBG OFET). This result indicated the potential of developing high-performance *n*-channel semiconducting polymers *via* an all-acceptor approach. This study demonstrated that 2,2'-bithiazole is a promising building block for future *n*-channel semiconducting polymers.

In Chapter 3, 2,2'-bithiazole is copolymerized with the electron deficient naphthalene diimide (NDI) group to afford a donor-acceptor (D-A) copolymer, **PNDI2Tz**. Polymer **PNDI2Tz** was obtained *via* palladium-catalyzed Stille polycondensation of a dibromo-substituted NDI derivative with distannyl-2,2'-bithiazole. The optical and electronic properties were investigated using UV-*vis* absorption spectroscopy and ultraviolet photoelectron spectroscopy. It was found that the polymers show very broad absorption bands in the 540 nm region, and **PNDI2Tz** has an optical bandgap of 1.87 eV. Computational analysis demonstrates that holes and electrons are mainly localized on the 2,2'-bithiazole and NDI units, respectively. Organic field-effect transistors fabricated with **PNDI2Tz** exhibit unipolar *n*-channel characteristics with mobility as high as 0.05 $cm^2V^{-1}s^{-1}$.

In Chapter 4, we focused on interface engineering and its influence on thin film morphology and OFET performance. Self-assembled monolayers (SAMs) of three organic molecules presenting different surface properties were prepared on silicon dioxide surfaces to explore the impact of surface effects. The electronic properties of three

different, but structurally similar donor-acceptor conjugated polymers were studied as a function of SAM molecular composition. Surface energy is shown to have direct impact on the formation of conjugated polymer nanofiber networks that can enhance molecular packing and conjugated polymer π-π interactions. Low energy surfaces are particularly favorable from an energetic standpoint for conjugated polymers to form tight nanofiber networks that enhance charge carrier mobilities.

In Chapter 5, we utilized **PNDI2Tz** as an acid sensing material, and studied its BF_3 sensing capability with an OFET-based gas sensor. **PNDI2Tz** was found to be a halochromic polymer when exposed to a variety of Brønsted acids and Lewis acids. We studied **PNDI2Tz** halochromic behavior in solution to understand the color changing mechanism. Furthermore, **PNDI2Tz** *n*-channel OFETs were fabricated and device electronic responses against the gas phase Lewis acid, boron trifluoride were investigated. **PNDI2Tz** shows high sensitivity to BF_3 gas through forming a Lewis acid-base adduct which can significant reduce electron transport in OFET configurations. **PNDI2Tz**-based OFETs exhibit a pure electron mobility of 0.05 $cm^2V^{-1}s^{-1}$ at normal working state. In the presence of 60 ppm BF_3, the OFET turns off within 60 seconds. The turn-on/turn-off cycle can be repeated for over 50 times with insignificant negative impact on **PNDI2Tz** OFET performance.

CHAPTER 7. FUTURE WORK

7.1 Structure-Property Relationship Study: Impacts of Thiazole/Thiophene on Diketopyrrolopyrrole Polymeric Semiconductor Fundamentals and Performance to Their Applications in OFETs

In this thesis, thiazole has been recognized as a promising building block for *n*-channel conjugated polymers. Thiazole-based conjugated polymers have shown to be suitable acceptor semiconductors for OFETs and sensors. One future project is to synthesize a series of thiophene/thiazole based conjugated polymers to systematically understand the structure-property relationships in terms of energy levels, solution processability, and device performance. In recent years, a series of high-efficiency donor polymers have been developed for single-junction organic photovoltaics (OPV) pushing power conversion efficiency (PCE) up to over 17%.[26, 27, 292-295] Nevertheless, the accepting components are still limited to mainly PCBM derivatives, **N2200** and a few other options.[28, 296, 297] Preliminary results have shown that **PDPP4T (P1)** and **PDPP4Tz (P4)** are unipolar polymers, while **PDPP2Tz2T (P2)** and **PDPP2T2Tz (P3)** are ambipolar polymers. (**Figure 7.1**) It is noted that **P1**, **P2** and **P3** are with 2-decyltetradecyl (2-DT) side chain, and **P4** is with 5-decylheptadecyl (5-DH) side chain. Preliminary characterization was conducted at this stage.

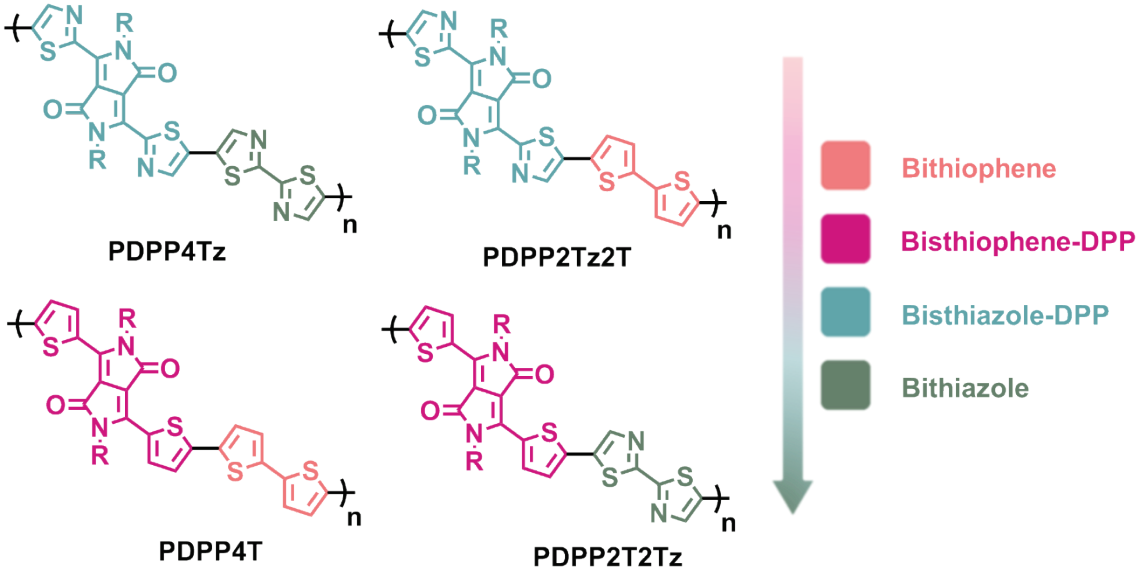

Figure 7.1. Chemical structure of four DPP-thiazole/thiophene polymers and building block electron deficiency in an increasing order.

Table 7.1. Chloroform gel permeation chromatography (GPC) results of DPP-thiazole/thiophene polymers.

	Retention Time[min]	Mn	Mw	Mz	Mw/Mn	Mz/Mw
PDPP4T	18.41	29,109	68,401	129760	2.35	1.897
PDPP2T2Tz	17.70	36,633	146,506	399828	3.999	2.729
PDPP2Tz2T	16.85	68,639	279,672	632966	4.075	2.263

All DPP-thiazole/thiophene polymers were characterized by gel permeation chromatography (GPC). (**Table 7.1**) **P1** and **P4** have lower molecular weights, meanwhile **P2** and **P3** have substantially higher molecular weights. As shown in solution and thin film UV-*vis*, DPP-thiazole/thiophene polymer absorption patterns exhibit a clear trend in their onset absorption and bandgap (**Figure 7.2** and **Table 7.2**). With ionization potentials

measured from ultraviolet photoelectron spectroscopy (UPS), the DPP-thiazole/thiophene polymer electron affinities were estimated.[76, 215]

Table 7.2. Photophysical characteristics of **PDPP4T (P1)**, **PDPP2Tz2T (P2)** and **PDPP2T2Tz (P3)**.

	Ionization Potential (eV)	UV-*vis* onset absorption (nm)	Optical Bandgap (eV)	Estimated Electron Affinity (eV)*
PDPP4T	4.64	908	1.37	3.27
PDPP2T2Tz	5.48	838	1.48	4.00
PDPP2Tz2T	4.85	857	1.45	3.40

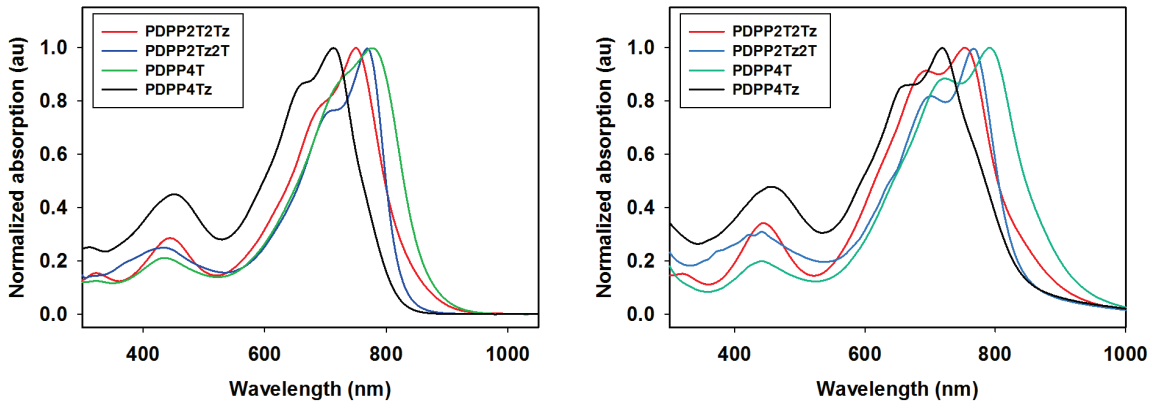

Figure 7.2. Solution and thin film UV-*vis* spectra of DPP-thiazole/thiophene polymers.

GIWAXS results demonstrate that all DPP-thiazole/thiophene polymers investigated here possess a high degree of crystallinity and preferable edge-on orientation in solid state. Polymer thin films cast on OTS-processed SiO_2 show enhanced crystallinity compared to those fabricated on UV-ozone treated SiO_2. (**Figure 7.3**) In the future, these polymers can be further characterized to further understand the impact of thiophene/thiazole on the energy levels of the polymers, the impact of nitrogen substitution *via* thiazole on the suitability of the polymers for incorporation into bulk heterojunction devices for the realization of all-polymer solar cells.

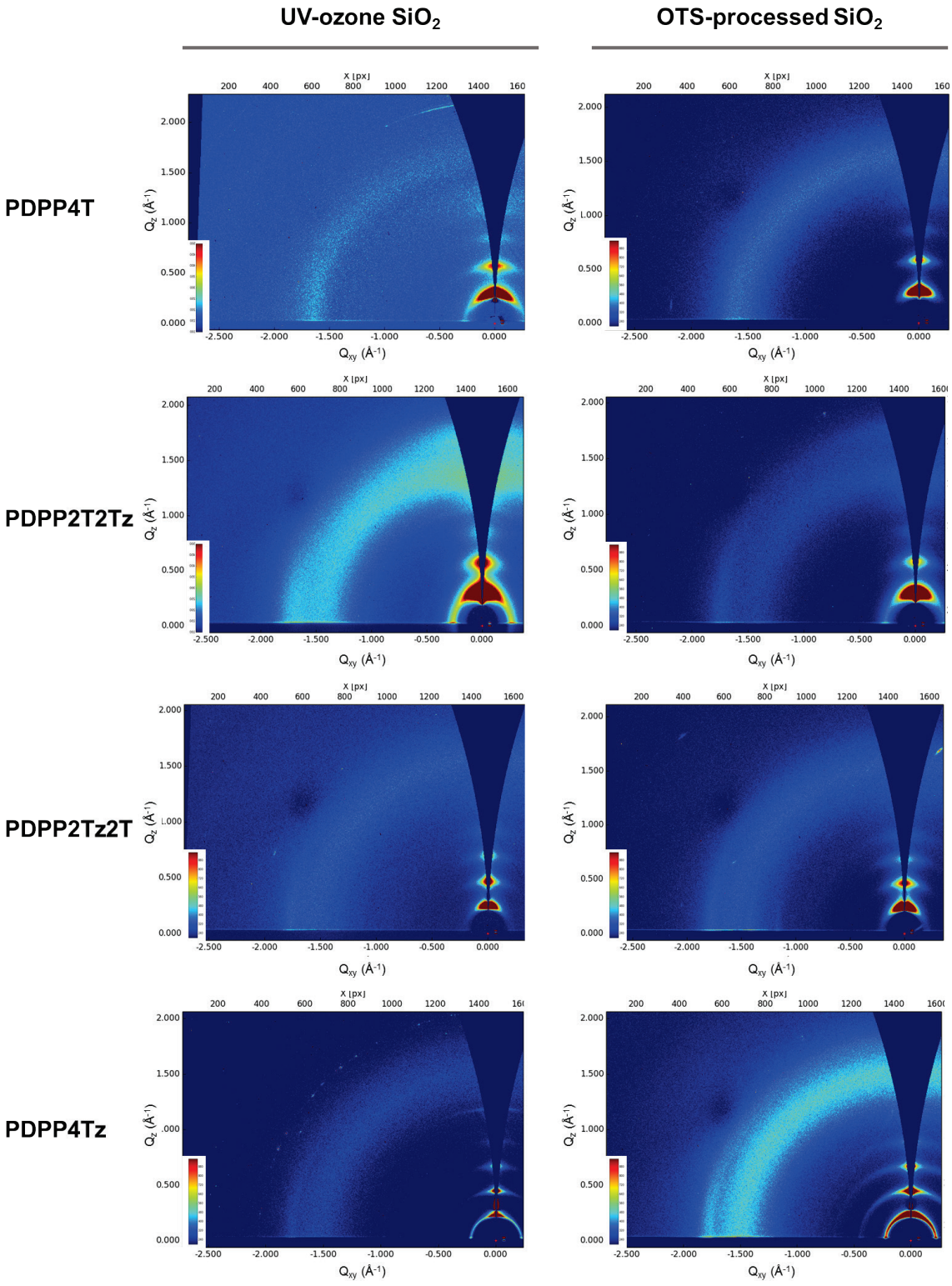

Figure 7.3. GIWAXS images of DPP-thiazole/thiophene polymers on UV-ozoned SiO_2 and OTS-processed SiO_2 substrates.

7.2 Investigation of Dielectric Layer Processing and Molecular Interactions at Interfaces and their Impacts to OFET Performance

Fluoroalkyl side chains are of interest in conjugated polymers because they have unique properties, such as hydrophobicity, rigidity, and thermal stability, as well as chemical and oxidative resistance and self-organization.[298-300] Alkyl and fluoroalkyl segments are both hydrophobic. When fluoroalkyl and alkyl chains are simultaneously introduced into a polymer, the two segments usually segregate, producing a highly ordered crystalline material.[301-303] Such behavior allows control over the molecular packing and may lead to highly ordered polymer thin films that can promote charge transport.

In order to further understand the surface effect, my proposed study is to synthesize two naphthalene diimide-bithiazole based conjugated polymers, one with an alkyl side chain and the other with a fluoroalkyl side chain. Three surface modifiers are proposed to

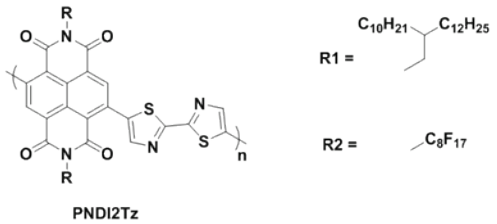

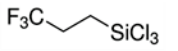

Trichloro(3,3,3-trifluoropropyl)silane (TFPS)

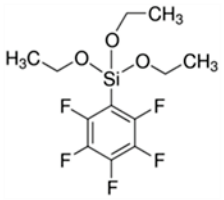

(Pentafluorophenyl)triethoxysilane (PFES)

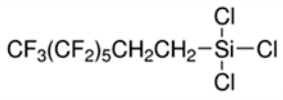

Trichloro(1H,1H,2H,2H-perfluorooctyl)silane (PFOS)

Scheme 7.1. Proposed **PNDI2Tz**-based conjugated polymer and fluoro- surface modifiers.

be used to understand the surface-polymer interaction: Trichloro(3,3,3-trifluoropropyl)silane (TFPS), trichloro(perfluorooctyl)silane (PFOS), and (pentafluororphenyl)triethoxysilane (PFES). (**Scheme 7.1**) This study will help to understand if the fluoro-surface modifiers could induce more order into the solid state structure and packing of conjugated polymers, and further, to enhance the OFET device performance of conjugated polymers. With different fluoro-alkyl chain length, it is possible to further understand the buried interface effect and surface energy effect on conjugated polymer self-assembly and orientation. PFES SAM may additionally interact with conjugated polymers through the π-system of the pentafluorophenyl ring which may lead to provide insights on the significance of electrostatic interactions between the dielectric layer and polymer.

7.3 Thiazole-based Conjugated Polymers for Metal Ion Sensor Applications

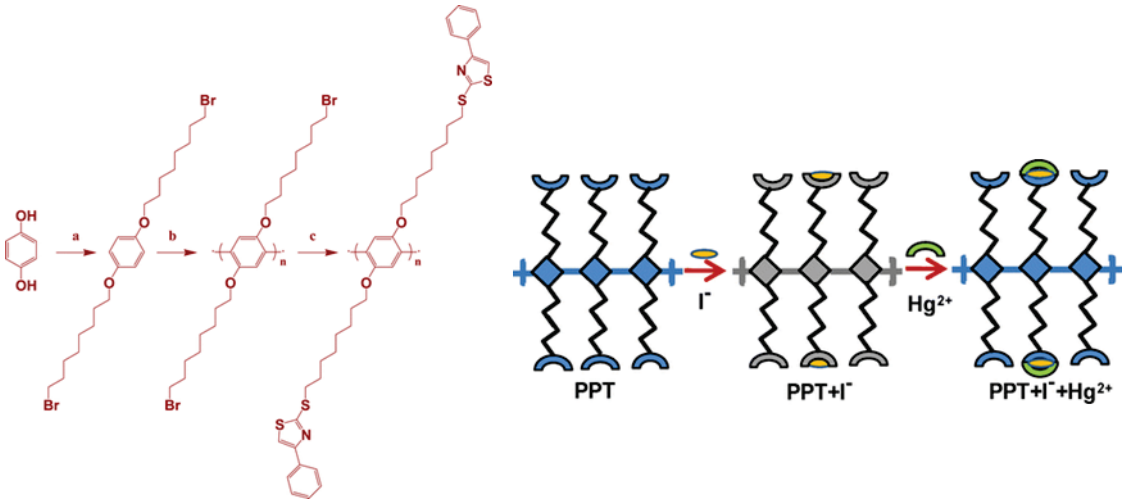

Figure 7.4. (left) Synthesis of Poly(1,4-bis-(8-(4-phenylthiazole-2-thiol)-octyloxy)-benzene: (a) K_2CO_3, dry acetone, 1,8-dibromooctane, 50 °C; (b) $FeCl_3$, nitrobenzene, RT; and (c) K_2CO_3, 4-phenylthiazole-2-thiol, THF, Reflux, 12 h; (right) proposed detection mechanism of mercury ion with PPT polymer. Reprinted from article *ACS Appl. Mater. Interfaces* **2013**, *5* (6), 2234-2240. Copyright 2013 American Chemical Society.

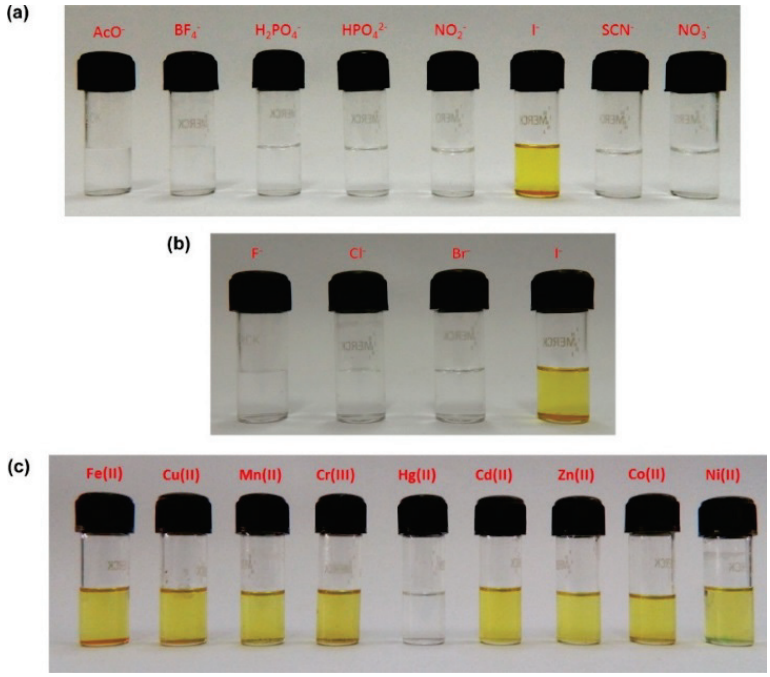

Figure 7.5. Color changes of PPT solution in a THF/water solution upon the addition of (a) anions and (b) halides; in both panels a and b. (c) Color changes of PPT–I^- solution in a THF/water solution upon the addition of metal salts in water. Reprinted with permission from *ACS Appl. Mater. Interfaces* **2013**, *5* (6), 2234-2240. Copyright 2013 American Chemical Society.

Hussain and co-workers report their synthetic approaches of a new conjugated poly-*p*-phenylene derivative strapped with 4-phenylthiazole-2-thiol, which can optically and visually detect the presence of iodide (I) and mercury (Hg) over a wide range of other competing ions in an aqueous medium.[279] (**Figure 7.4**) The neutral conjugated polymer poly(1,4-bis-(8-(4-phenylthiazole-2-thiol)-octyloxy)-benzene) (PPT) showed high optical activity in the presence of I^- and Hg^{2+}, which could be detected by fluorescence spectroscopy as well by colorimetric responses.

In the presence of very dilute Hg^{2+} salts, the yellow color of the solution disappears. (**Figure 7.5**) The PPT-based detection platform was further extended to solid state thin films. PPT-PS film also showed the ability to detect and respond to both iodide and

mercury salts. With such premise, thin films of such polymers can be cast onto OFET substrates. By incorporating the phenylthiazole units in the conjugated polymer design, we can expect the new conjugated polymer to respond to electronic signaling, such as a current change when sensing I^- and Hg^{2+} in aqueous or organic media. The detection limit of Hg^{2+} salt using the PPT polymer was found to be 2.1 nM in water. The detection of both iodide and mercury was also possible in solid state by using a membrane film prepared by mixing 1% PPT in polystyrene. This membrane changes color in the presence of iodide as well as mercury salts. These results confirm that the PPT polymer can be applied for the colorimetric as well as fluorometric sensing of I^- and Hg^{2+} ions in a complex environment in solution, as well as in the solid state, using a membrane film rapidly.

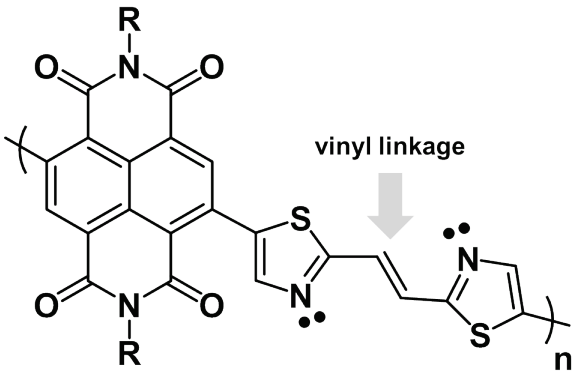

Figure 7.6. Proposed new NDI-thiazole based polymer with vinyl linkage for potential metal ion detection.

Given the reported results, one design approach for a thiazole-based conjugated polymer metal sensor is to introduce halides to the detection system. (**Figure 7.6**) In terms of synthesis, vinyl linkages between thiazole rings in 2,2'-bithiazole can be introduced to separate the nitrogen lone pair and sulfur antibonding orbital interactions and allow a change in polymer conformation without breaking the conjugation. The halochromism of

the new polymer as well as OFET performance in the presence of acid can then be studied and compared with **PNDI2Tz**.

APPENDIX. SYNTHESIS DETAILS

In this chapter, materials, instrumentation, and detailed synthesis of materials are provided.

A.1 Materials and general methods in PDPP2Tz and PDPP4Tz synthesis

Chloroform, dichloromethane, toluene, *p*-xylene (PX), isopropanol, tetrahydrofuran (THF), dimethylformamide (DMF), chlorobenzene and 1,2-dichorobenzene (*o*-DCB) were purchased as anhydrous grade solvents from Sigma-Aldrich. THF was distilled from sodium benzophenone in an solvent purification system (SPS). 2-Bromothiazole was purchased from Scientific Matrix. Tetrabutylammonium bromide (*n*-Bu4NBr), *N,N*-diisopropylethylamine (DIPEA), diisopropylamine (DIPA), palladium(II) acetate ($Pd(OAc)_2$), tris(dibenzylideneacetone)- dipalladium(0) ($Pd_2(dba)_3$), tri(o-tolyl)phosphine ($P(o\text{-tolyl})_3$), sodium diethyldithiocarbmate, and tetra-*n*-butylammonium hexafluorophosphate ($[n\text{-}Bu_4N]+[PF_6]-$) were purchased from Sigma-Aldrich. *N*-octadecyltrichlorosilane (OTS-18) was purchased from Gelest, Inc. Silica gel was purchased from Sorbent Technologies (Premium Rf™, porosity: 60A; particle size: 40-75 μm).

The synthetic procedures for the preparation of the 5-decylheptadecyl bromide side chains, 5,5'-bis(trimethylstannyl)-2,2'-bithiazole, and 2,5-bis(5-decylheptadecyl)-3,6-di(thiazole-2-yl)pyrrolo[3,4-c]pyrrole-1,4(2H,5H)-dione were modified from literature procedures[64, 76, 82]. Details of side chain synthesis and characterization can be found in previous literature[82, 90, 169, 271]. Nuclear magnetic resonance spectra of side chains, monomers and resulting polymers are listed in **Figure A1-A12**. Commercially available 2-bromothiazole was homocoupled to afford 2,2'-bithiazole[304], followed by metalation to

afford the distannane monomer, 5,5'-bis(trimethylstannyl)-2,2'-bithiazole [124]. The following content is the synthesis results and characterizations of precursors, monomers and polymers:

A.1.1 Synthesis of 5,5'-bis(trimethylstannyl)-2,2'-bithiazole

DIPA (0.45 mL, 3.12 mmol, 3.50 eq.) in THF (2 mL) was maintained under an argon atmosphere and cooled to -78 ˚C using a dry ice/acetone bath. Then, *n*-butyllithium (1.00 mL of a 2.5 M solution in hexane, 2.50 mmol, 2.80 eq.) was added in a dropwise manner. The resulting solution was then warmed to 0 °C using an ice-water bath and stirred at 0 °C for 30 min to afford lithium diisopropylamide (LDA). It was subsequently cooled to -78 ˚C in dry ice/acetone bath. Then, 2,2'-bithiazole (150 mg, 0.9 mmol, 1.00 eq.) in THF (3.9 mL) was added in a dropwise manner generating an orange solution. After stirring at -78 ˚C for 2 h, $SnMe_3Cl$ (3.25 mL of a 1.0 M solution in THF, 3.25 mmol, 3.64 eq.) was added in a dropwise manner. The resulting solution was then warmed to room temperature and stirred for 12 h. The solution was then poured into D.I. H_2O (50 mL), the mixture was extracted into CH_2Cl_2 (3 x 15 mL), washed with brine (3 × 15 mL), dried over anhydrous $MgSO_4$, filtered and then concentrated under reduced pressure using a rotary evaporator. The final product was washed with hexane at -78 ˚C and the final compound was isolated as a pale yellow solid (370 mg, yield: 85%). ^1H NMR (400 MHz, $CDCl_3$) δ 7.77 (s, 2 H), 0.41 (s, 18H).

A.1.2 Synthesis of 3,6-Bis-thiazol-2-yl-2,5-dihydro-pyrrolo[3,4-c]pyrrole-1,4-dione

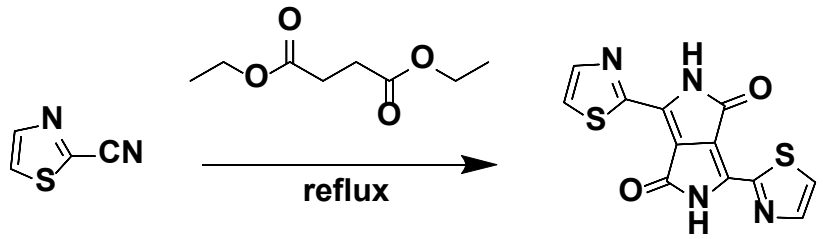

1.00 g of sodium metal were diced and carefully added into a 2-neck round bottom flask fit with a condenser. 40 mL of t-amyl alcohol was added in the flask with a stirrer. The reaction mixture was heated then overnight at 125 ^{o}C. 2.22 g (2.12 mL, 12.8 mmol) of diethyl succinate and 2.0 g (18.2 mmol) of 2-cyanothiazole were added into to 20 mL of t-amyl alcohol, then slowly added dropwise. The reaction mixture was then stirred at 110 ^{o}C for 8 hours. Mixture was cooled to room temperature afterwards, and the product was precipitated by pouring slowly into a mixture of 4.0 g glacial acetic acid, 100 mL of water, and 50 mL of methanol. The product was then filtered and washed with methanol followed by drying in a vacuum oven at 45 ^{o}C overnight to yield the product as a purple solid (1.18 g, 43%). MALDI-TOF calculated m/z = 301.99, found m/z = 301.47.

*A.1.3 Synthesis of 2,5-bis(5-decylheptadecyl)-3,6-di(thiazol-2-yl)-2,5-dihydropyrrolo-[3,4-c]pyrrole-1,4-dione (**3**)*

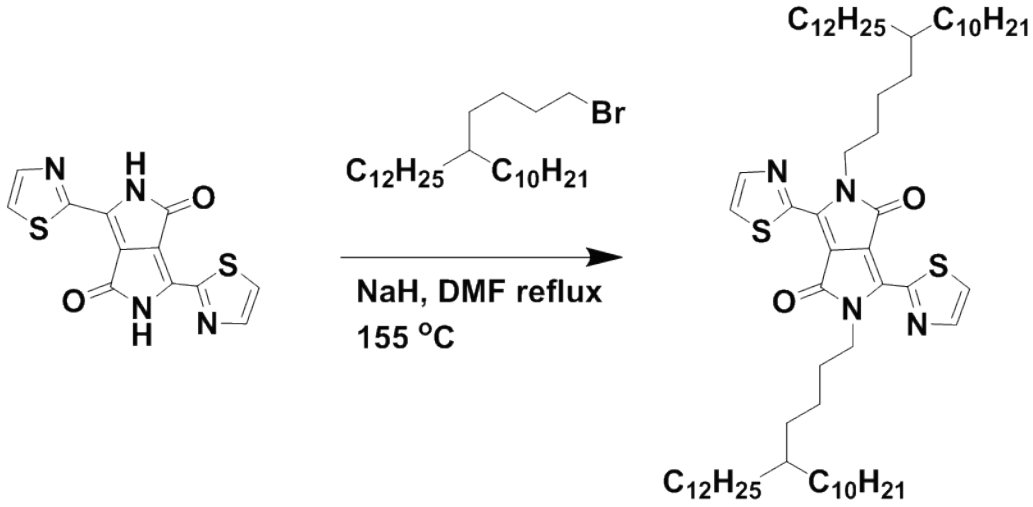

5-decyl-heptadecyl-bromide (6.08 g, 13.23 mmol, 4.00 eq.) was added into the mixture of 3,6-Bis-thiazol-2-yl-2,5-dihydro-pyrrolo[3,4-c]pyrrole-1,4-dione (1.00 g, 3.30 mmol, 1.00 eq.) and a 60% mineral oil suspension of NaH (0.39 g, 9.75 mmol) in anhydrous DMF (40 mL) under argon. The mixture was heated at reflux for 24 h, before cooling to room temperature. D.I. H_2O (100 mL) was added and the mixture was extracted into $CHCl_3$ (50 mL). The organic solution was washed with brine (3 x50 mL), dried over anhydrous $MgSO_4$, and concentrated under reduced pressure. The resulting dark residue was purified by column chromatography (silica gel, DCM). The product was recrystallized from isopropanol to afford the alkylated product as a purple solid (yield: 42 %). ^{1}H NMR (400 MHz, $CDCl_3$) δ: 8.07 (d, J = 2.4 Hz, 2H), 7.70 (d, J = 1.6, 2H), 4.40 (m, 4H), 1.68 (m, 4H), 1.32–1.19 (m, 90H), 0.87 (t, J = 6.8 Hz, 12H). ^{13}C NMR (400 MHz, $CDCl_3$) δ (ppm): 160.9, 155.3, 144.4, 137.6, 123.9, 110.5, 42.9, 37.3, 35.6, 33.3, 31.9, 30.2, 29.7, 26.2, 24.0, 22.7, 14.1. MALDI-TOF: calculated m/z = 1058.84, found 1057.71.

A.1.4 Synthesis of 3,6-bis(5-bromothiazol-2-yl)-2,5-bis(5-decylheptadecyl)-2,5-dihydropyrrolo[3,4-c]pyrrole-1,4-dione

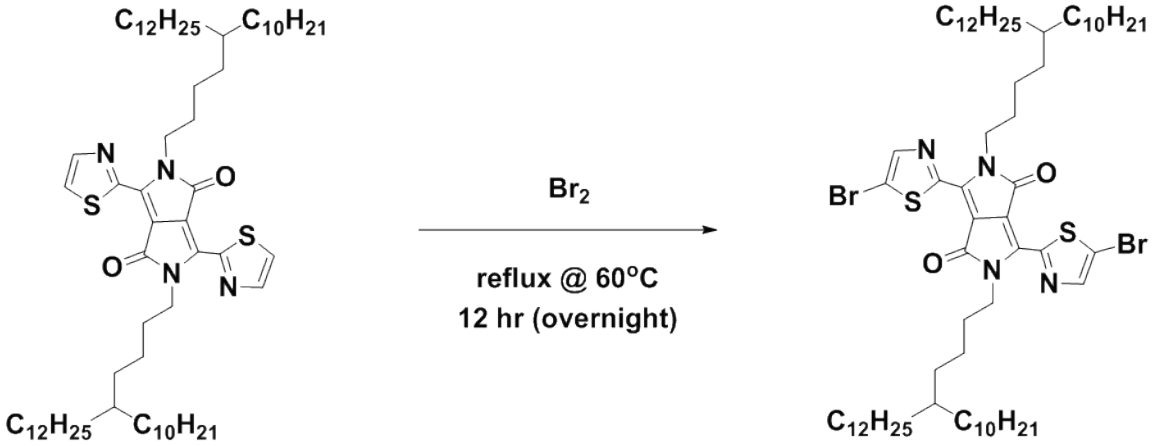

Sodium bicarbonate (0.435 g, 5.17 mmol) was added into a solution of alkylated bisthiazole diketopyrrolopyrrole (0.5 g, 0.47 mmol) in $CHCl_3$ (9 mL). A solution of Br_2 (0.75 g, 4.72 mmol) in $CHCl_3$ (9 mL) was added during a course of 20 min at 0 °C. The reaction mixture was stirred at 60 °C for 2 hr, followed by cooling to room temperature. A sodium thiosulfate solution (5.0 g in 20 mL H_2O) was added into the reaction mixture and stirred for 30 min to remove residual Br_2. The mixture was washed with brine (50 mL), followed by drying over anhydrous $MgSO_4$. The resulting solid was subjected to column chromatography (silica, eluent heptane/$CHCl_3$, v/v 60:40) to afford brominated monomer as titled product. The solid was dissolved in $CHCl_3$ (5 mL) and precipitated into methanol (100 mL) to afford pure product (0.32 g, 34 %) as a red solid. ^{1}H NMR (400 MHz, $CDCl_3$) δ (ppm): 7.93 (s, 2H), 4.31 (d, 4H), 1.65 (m, 2H), 1.50-1.20 (m, 90H), 0.87 (m, 12H). ^{13}C NMR (400 MHz, $CDCl_3$) δ (ppm): 160.7, 156.3, 136.6, 115.9, 110.7, 42.9, 37.3, 33.3, 30.2, 29.7, 26.7, 22.7, 14.1. MALDI-TOF: calculated m/z = 1216.66, found 1215.43.

A.1.4 Synthesis of poly(2,2'-bithiazole-3,6-bis(5-bithiazol-2-yl)-2,5-bis(5-decylheptadecyl)-2,5-dihydropyrrolo[3,4-c]pyrrole-1,4-dione) (PDPP4Tz)

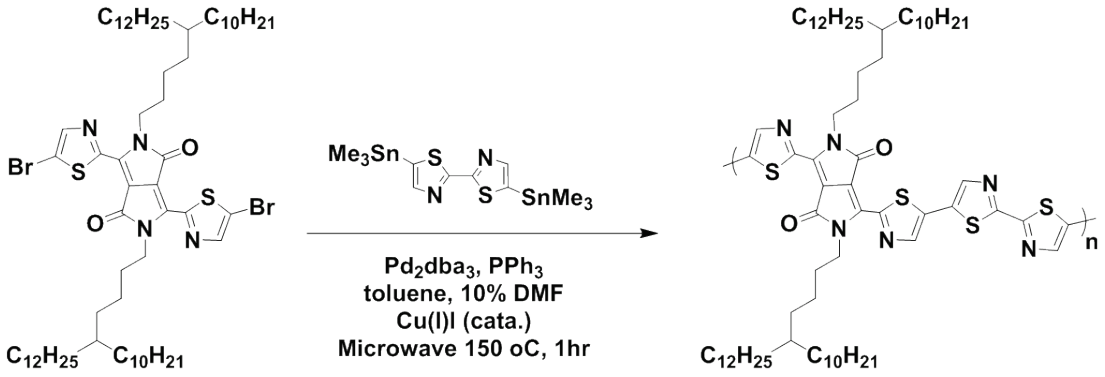

PDPP4Tz

To a degassed solution of monomer **3** (94.97 mg, 0.078 mmol), 5,5´- 5,5'-bis(trimethylstannyl)-2,2'-bithiazole (38.5 mg, 0.078 mmol) in toluene (2 mL) and DMF (0.2 mL), tris(dibenzylideneacetone)dipalladium(0) (2.11 mg, 2.3 μmol) and triphenylphosphine (2.44 mg, 9.3 μmol) were added. The mixture was set in a microwave reaction tube and reacted at 150 °C for 1 h, after which it was precipitated in methanol and filtered through a Soxhlet thimble. The polymer was extracted sequentially with acetone (24 hr), MeOH (24 hr), hexane (24 hr) and dichloromethane (12 hr), and then dissolved in chloroform. The chloroform solution was then precipitated into MeOH. Finally, the resulting polymer can be solubilized in chloroform and xylene for physical property characterization and device fabrication. Yield: 85.4 mg (87%) as a dark blue-green solid. ^{1}H NMR (400 MHz, $CDCl_3$) δ (ppm): 7.99, 7.89, 3.67, 1.51, 1.17, 0.80. Elemental analysis: calculated: C, 70.88%; H, 9.65%; N, 6.70%; found: C, 70.85%; H, 9.52%; N, 6.56%.

A.1.5 Synthesis of poly(3,6-bis(5-bithiazol-2-yl)-2,5-bis(5-decylheptadecyl)-2,5-dihydropyrrolo[3,4-c]pyrrole-1,4-dione)(PDPP2Tz)

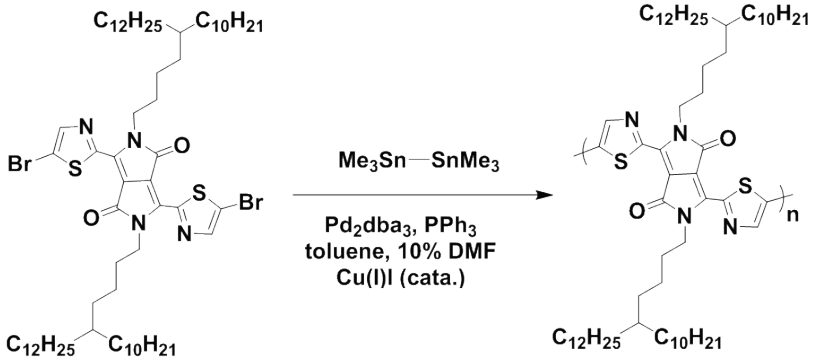

PDPP2Tz

To a degassed solution of monomer (247.2 mg, 0.20 mmol), hexamethylditin (65.6 mg, 0.20 mmol) in toluene (6 mL) and DMF (0.6 mL), tris(dibenzylideneacetone)dipalladium(0) (3.3 mg, 3.60 μmol) and triphenylphosphine (3.83 mg, 14.6 μmol) were added. The mixture was stirred at 120 °C for 16 h, after which it was precipitated in methanol and filtered through a Soxhlet thimble. The polymer was extracted sequentially with acetone (24 hr), MeOH (24 hr), hexane (24 hr) and dichloromethane (12 hr). The hexane portion and chloroform portion were collected. The more concentrated chloroform solution was then precipitated into MeOH, resulting a dark green solid. Finally, the resulting polymer can be solubilized in chloroform for physical property characterization. Yield: 85.4 mg (70%) as a dark blue-green solid. ^{1}H NMR (400 MHz, $CDCl_3$) δ (ppm): 8.00, 7.91, 3.70, 1.50(br), 1.20(br), 0.79.

A.2 Materials and general methods in PNDI2Tz synthesis

Chloroform, dichloromethane, toluene, *p*-xylene (PX), isopropanol, tetrahydrofuran (THF), *dimethylformamide* (DMF), chlorobenzene, 1,2-dichlorobenzene (*o*-DCB), and 1,2,4-trichlorobenzene (TCB) were purchased as anhydrous-grade solvents from Sigma-Aldrich. THF was distilled from sodium benzophenone in a solvent

purification system (SPS). 2-Bromothiazole was purchased from Scientific Matrix. Tetrabutylammonium bromide (*n*-Bu_4NBr), *n,n*-diisopropylamine (DIPEA), diisopropylamine (DIPA), palladium(II)acetate ($Pd(OAc)_2$), tris(dibenzylideneacetone)-dipalladium(0) ($Pd_2(dba)_3$, tri(*o*-tolyl)phosphine (P-(*o*-tolyl)$_3$), sodium diethyldithiocarbamate, and tetra-*n*-butylammonium hexafluorophosphate ([*n*-Bu_4N]+[PF_6]-) were purchased from Sigma-Aldrich. *N*-octadecyltrichlorosilane (OTS) was purchased from Gelest, Inc. Silica gel was purchased from Sorbent Technologies (Premium Rf™, porosity: 60A; particle size: 40-75 μm). Anhydrous chlorobenzene was degassed prior to use by a freeze-pump-thaw process.

Monomers were synthesized according to literature procedures.[14, 69, 70] **PNDI2Tz** was synthesized using modifications to reported procedures.[14, 90] Monomer and polymer nuclear magnetic resonance spectra were shown in **Figure A7-9**, **Figure A13** and **Figure A14**.

A.2.1 Synthesis of Poly(2,7-bis(2-decyltetradecyl)-4-methyl-9-(5'-methyl-[2,2'-bithiazol]-5-yl)benzo[lmn][3,8]phenanthroline-1,3,6,8(2H,7H)-tetraone):

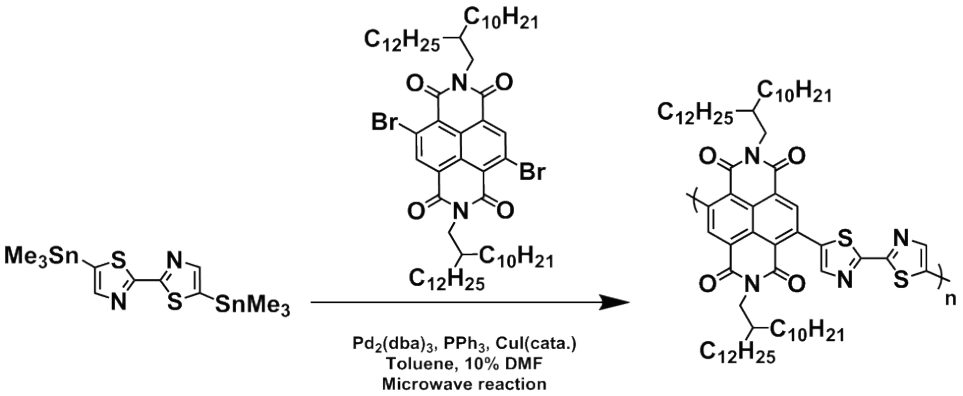

4,9-dibromo-2,7-bis(2-octyldodecyl)benzo[*lmn*][3,8]phenanthroline-1,3,6,8(2*H*, 7 *H*)-tetraone (500 mg, 0.44 mmol), *5,5'*-bis(trimethylstannyl)-*2,2'*-bithiazole (218 mg, 0.44

mmol), tris(dibenzylideneacetone) dipalladium(0) (12.1 mg, 0.013 mmol), triphenylphosphine (27.8 mg, 0.11 mmol), toluene (5 mL), dimethylformamide (0.5 mL) were added to a microwave reaction tube under nitrogen and sealed. The reaction tube was placed in a CEM Discover SP microwave reactor (1 hr, 150 $^{\circ}$C) and then removed. After cooling to room temperature, the viscous dark red reaction mixture was dissolved in chloroform and added dropwise to 250 mL methanol, and stirred vigorously for 1 hour. The precipitated solid was collected by vacuum filtration, and dried under reduced pressure for 24 hours. The solids were purified via subsequent Soxhlet extractions in 300 mL each of acetone, ethyl acetate, hexane, chloroform, and 1,2-dichlorobenzene (24 hours each). The chloroform fraction was concentrated and precipitated into methanol (350 mL), collected by vacuum filtration, and dried under reduced pressure for 24 hours to yield a deep red solid (216 mg, 44%). Mn = 49.3 kD (PDI = 3.33). ^{1}H NMR ($CDCl_3$, 400 MHz, ppm): δ= 8.85(s, 2H), 7.95 (s, 2H), 4.13 (br, 4H), 2.18 (br, 2H), 1.23 (br, 80H), 0.84 (br, 12H). Elemental Analysis: (Calculated) C, 73.87; H, 9.48; N, 5.07; S, 5.80; (Found) C, 73.93; H, 9.48; N, 5.01; S, 5.80; S, 5.71.

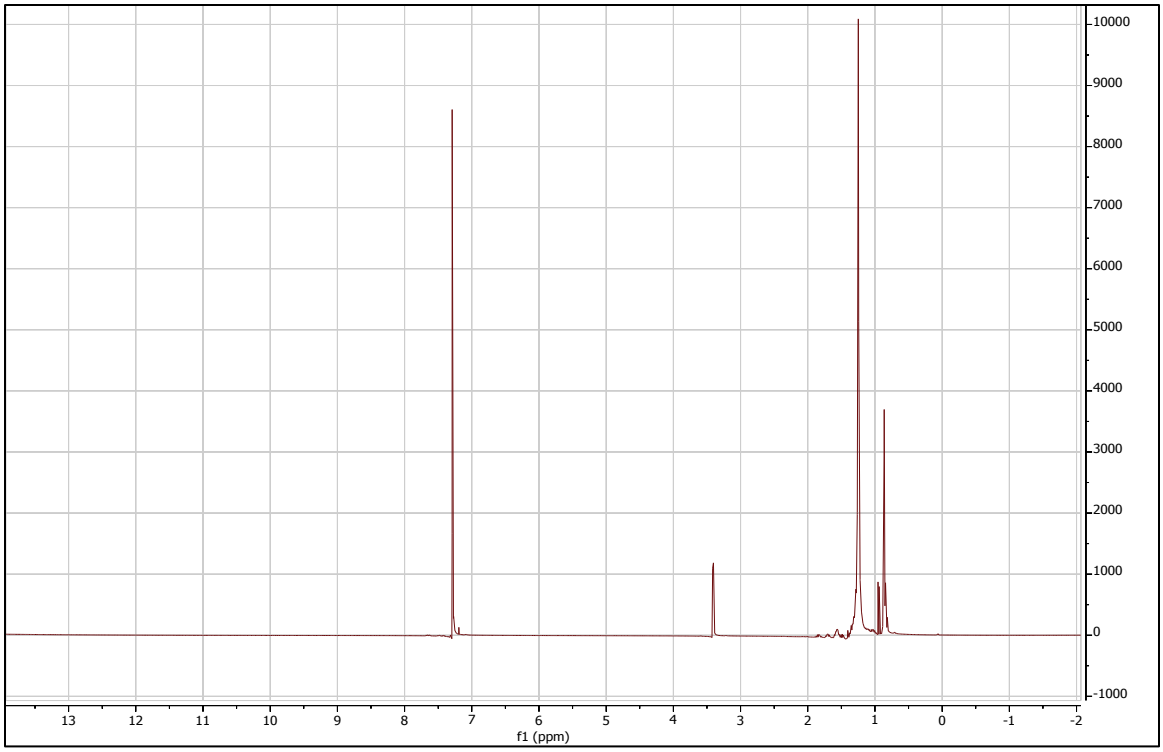

Figure A1. ^{1}H NMR of 11-(bromomethyl)tricosane

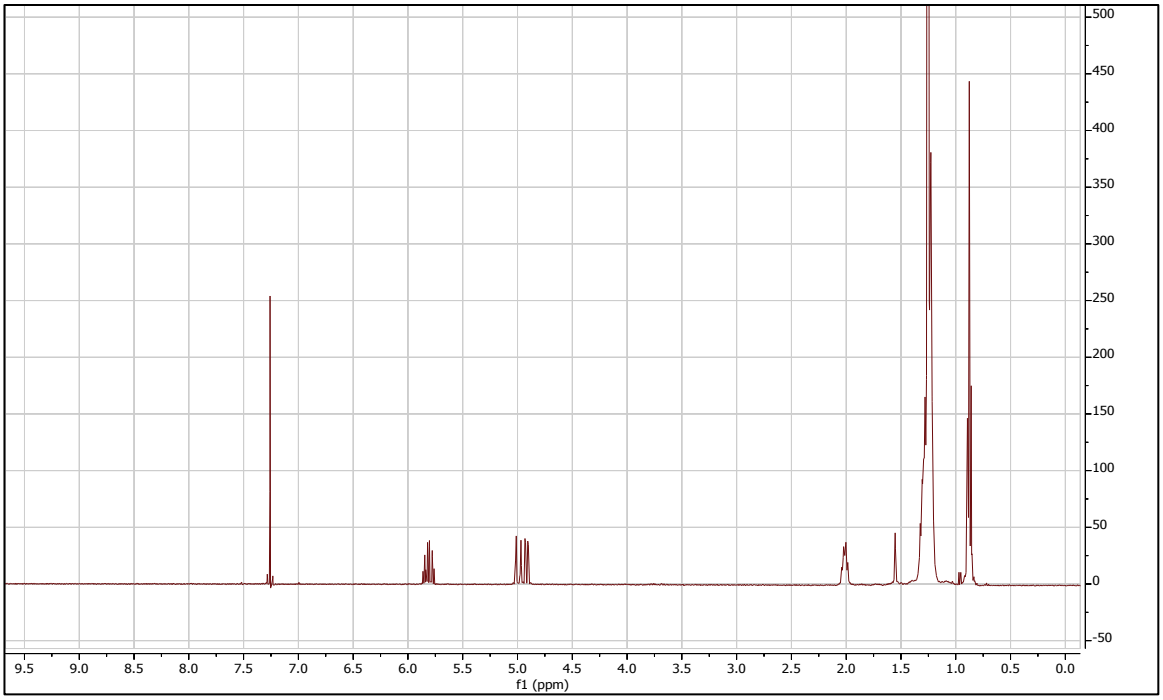

Figure A2. ^{1}H NMR of 11-(but-3-en-1-yl)tricosane

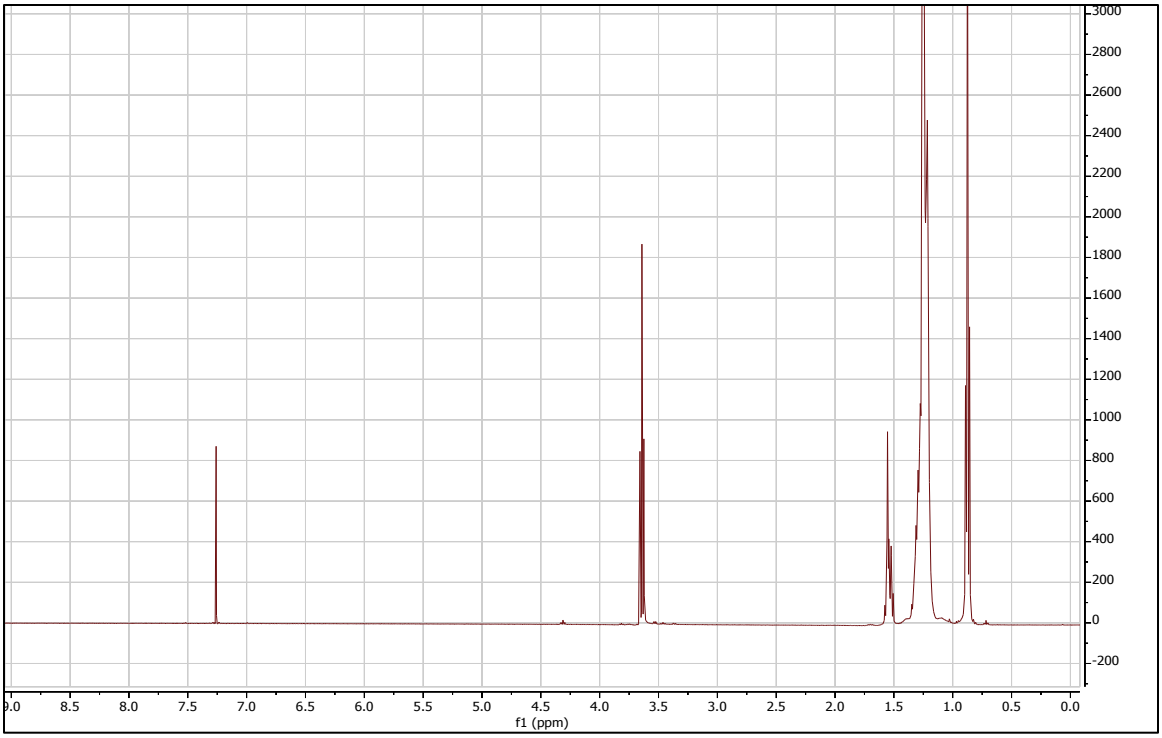

Figure A3. ^{1}H NMR of 5-decylheptadecan-1-ol

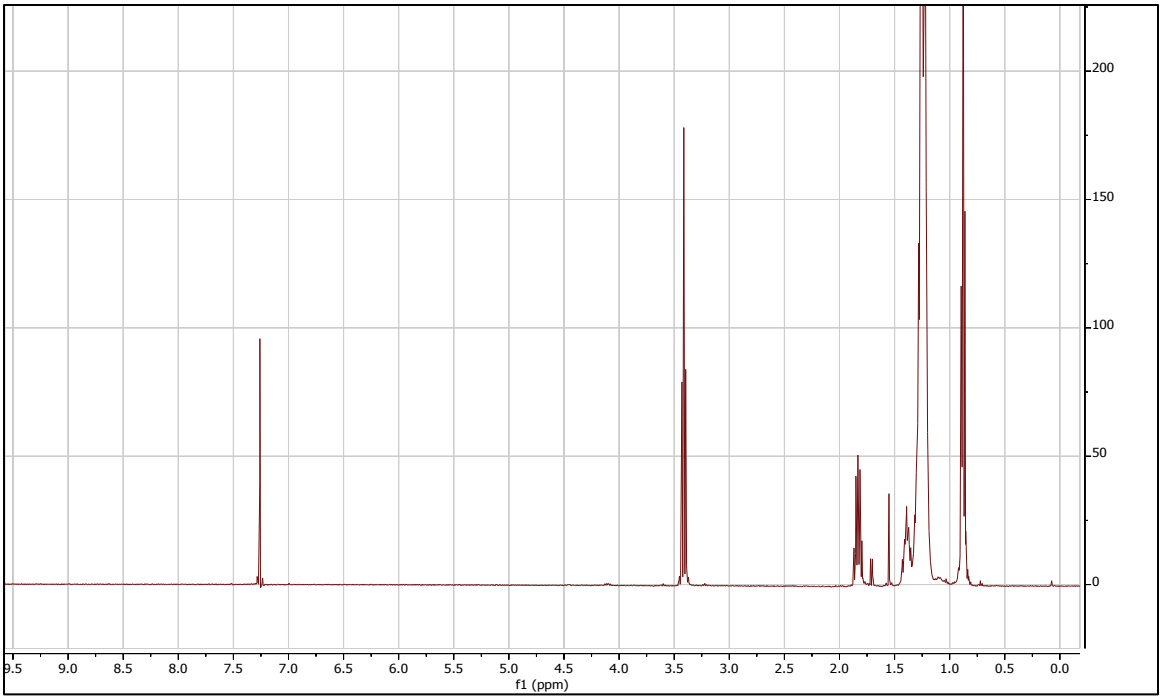

Figure A4. ^{1}H NMR of 11-(4-bromobutyl)tricosane

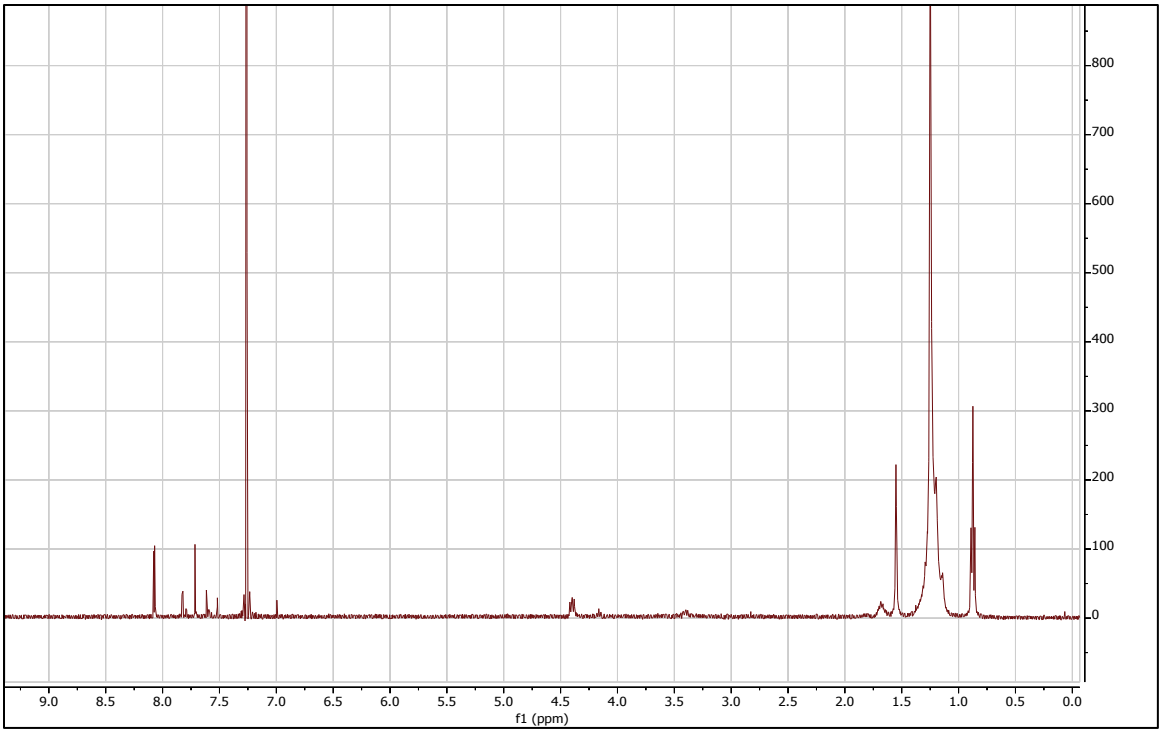

Figure A5. ^{1}H NMR of 2,5-bis(5-decylheptadecyl)-3,6-di(thiophen-2-yl)pyrrolo[3,4-c]pyrrole-1,4(2H,5H)-dione

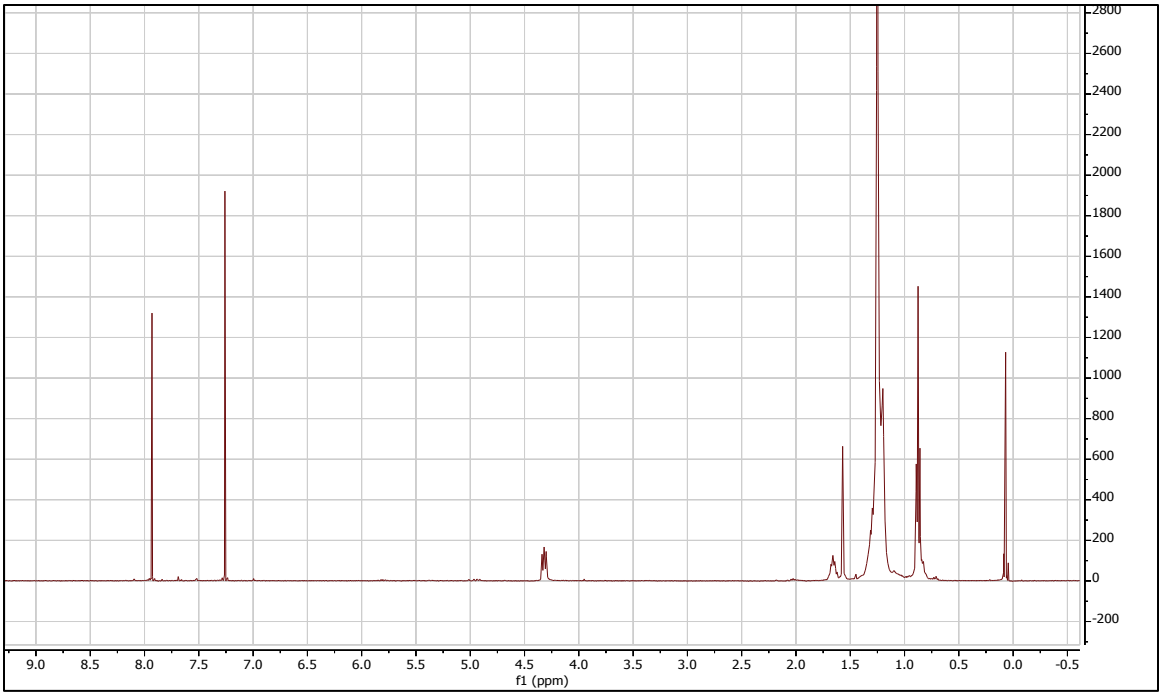

Figure A6. ^{1}H NMR of 3,6-bis(5-bromothiophen-2-yl)-2,5-bis(5-decylheptadecyl)-pyrrolo[3,4-c]pyrrole-1,4(2H,5H)-dione

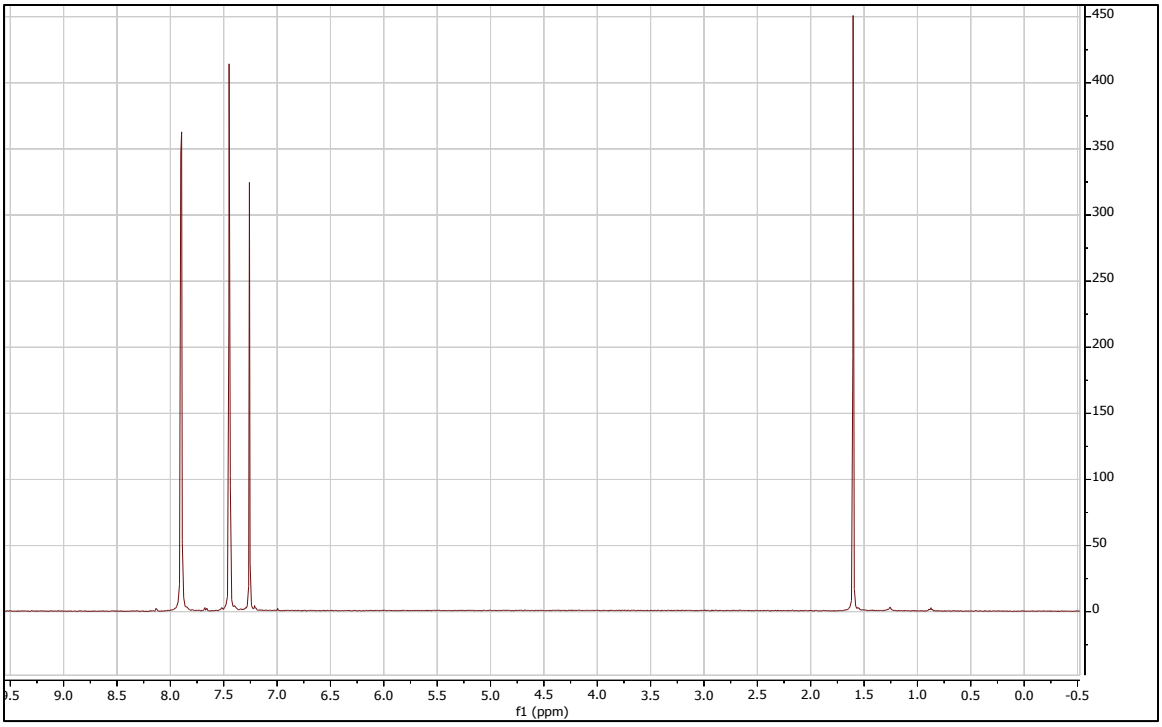

Figure A7. ^{1}H NMR of 2,2'-bithiazole

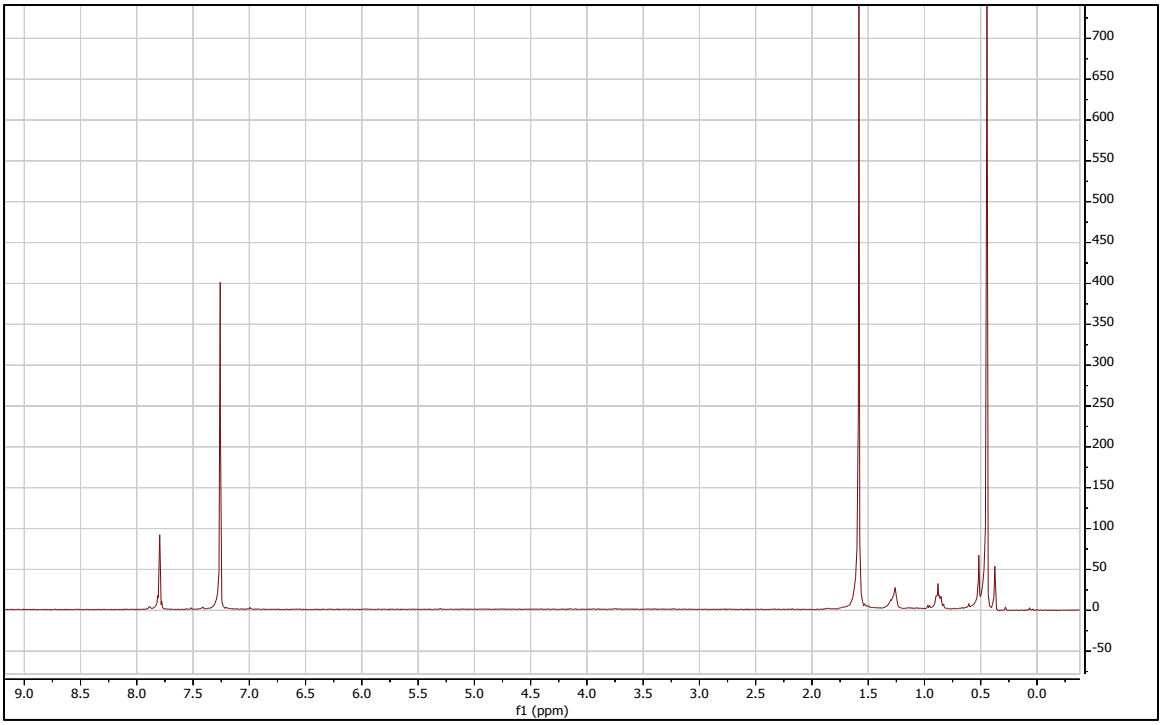

Figure A8. ^{1}H NMR of 5,5'-bis(trimethylstannyl)-2,2'-bithiazole

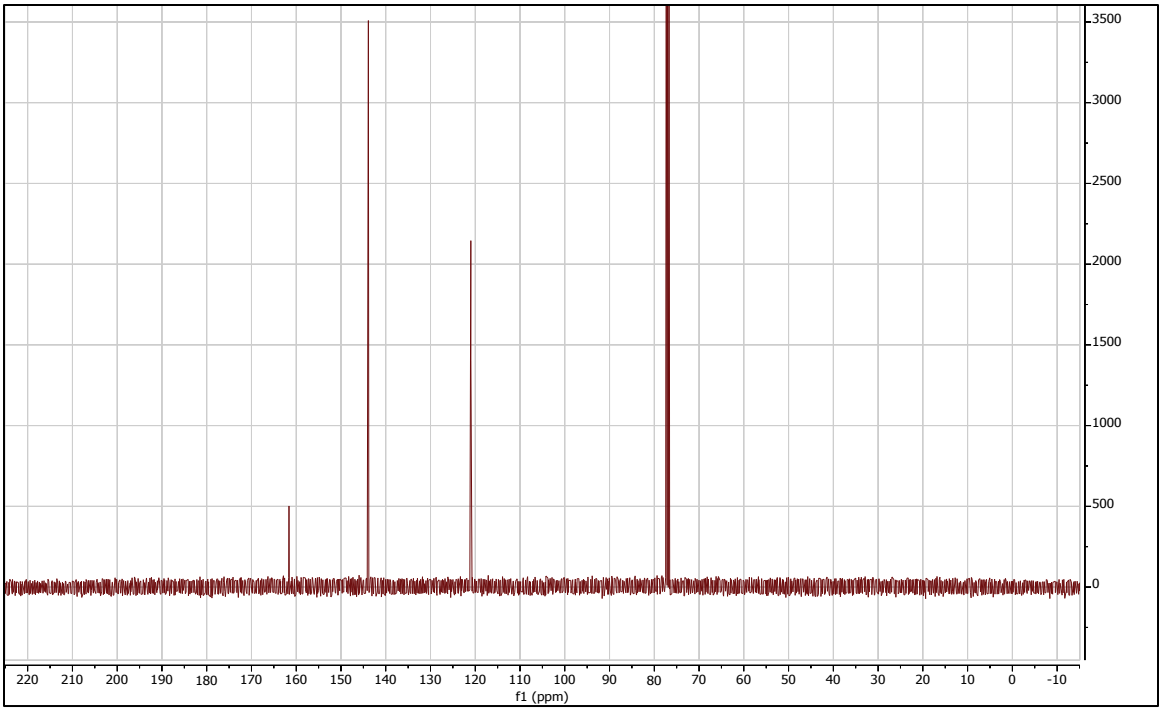

Figure A9. ^{13}C NMR of 5,5'-bis(trimethylstannyl)-2,2'-bithiazole

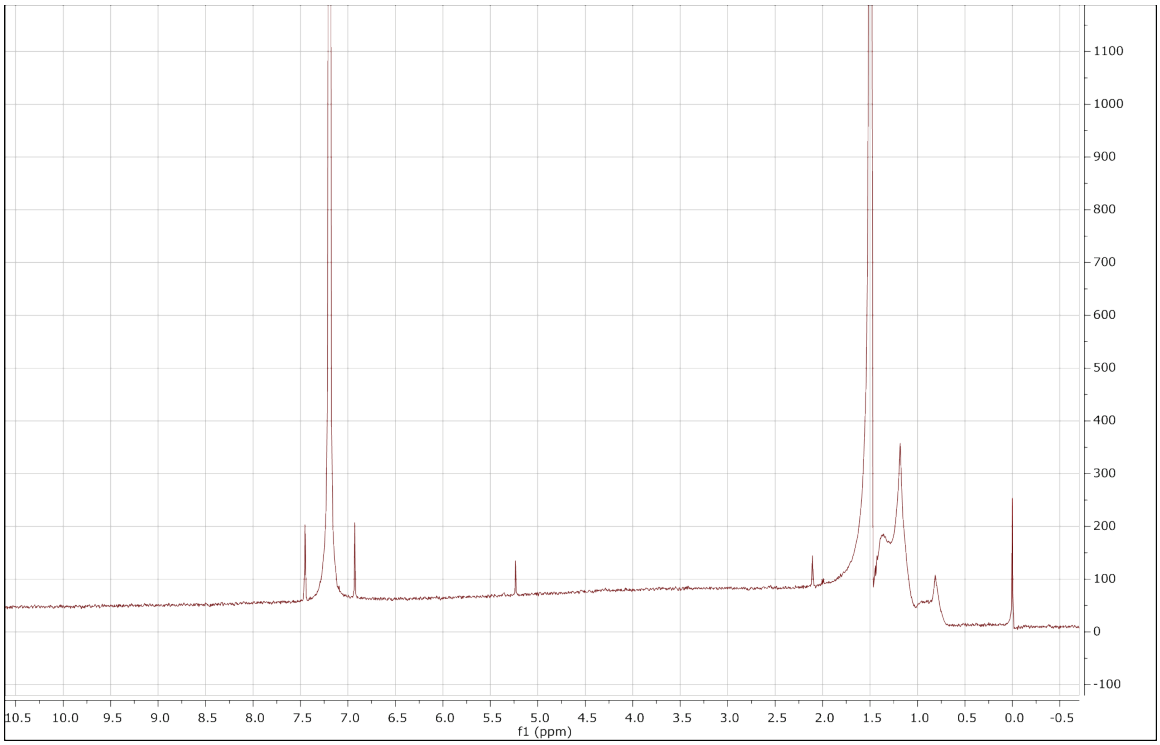

Figure A10. ^{1}H NMR of poly(3,6-bis(5-bithiazol-2-yl)-2,5-bis(5-decylheptadecyl)-2,5-dihydropyrrolo[3,4-c]pyrrole-1,4-dione) (**PDPP2Tz)**

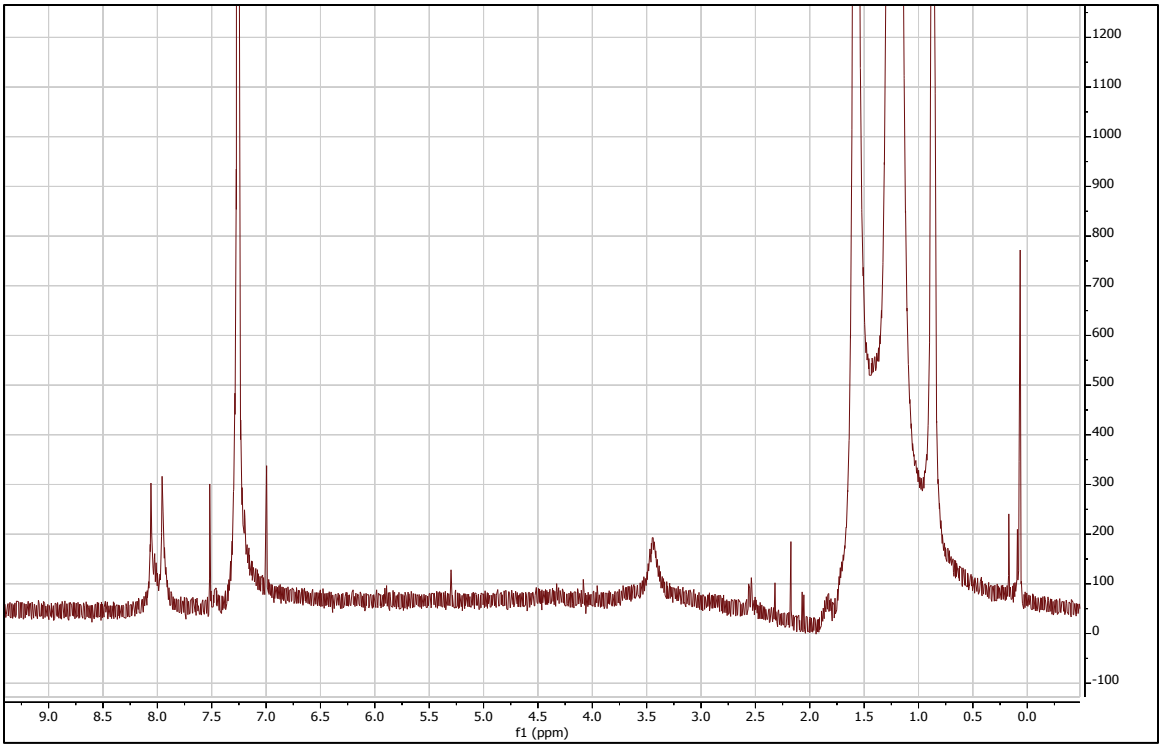

Figure A11. ^{1}H NMR of poly(2,2'-bithiazole-3,6-bis(5-bithiazol-2-yl)-2,5-bis(5-decylheptadecyl)-2,5-dihydropyrrolo[3,4-c]pyrrole-1,4-dione) (**PDPP4Tz**)

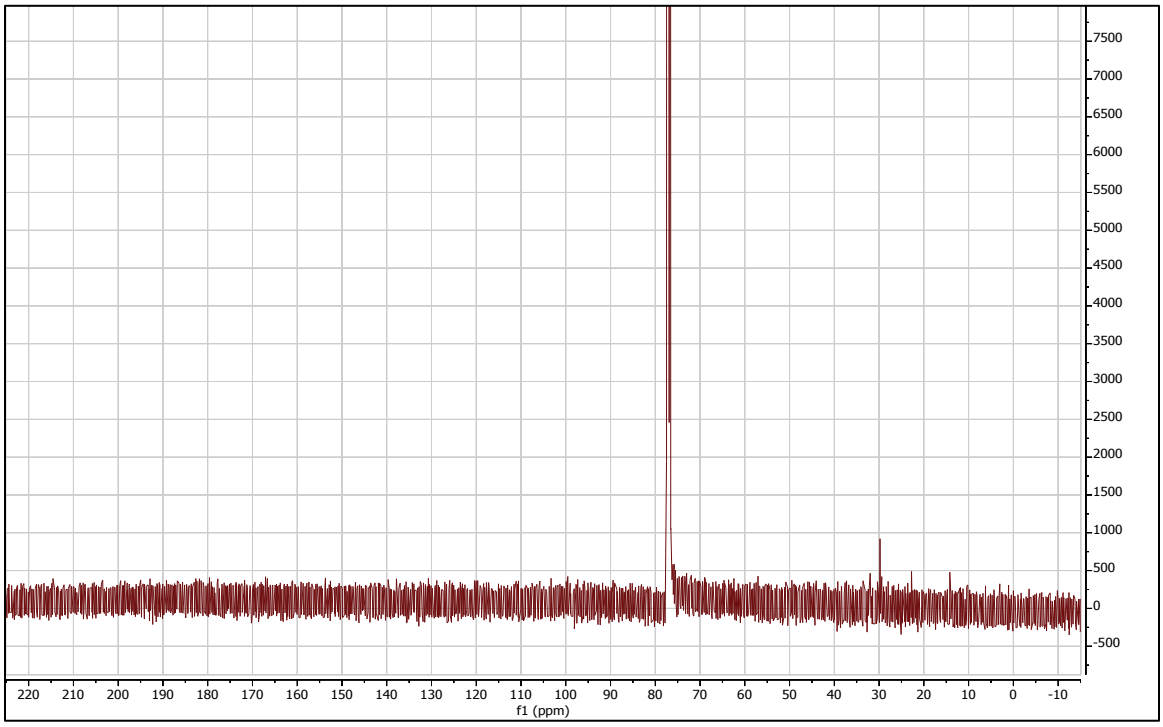

Figure A12. ^{13}C NMR of poly(2,2'-bithiazole-3,6-bis(5-bithiazol-2-yl)-2,5-bis(5-decylheptadecyl)-2,5-dihydropyrrolo[3,4-c]pyrrole-1,4-dione) (**PDPP4Tz**)

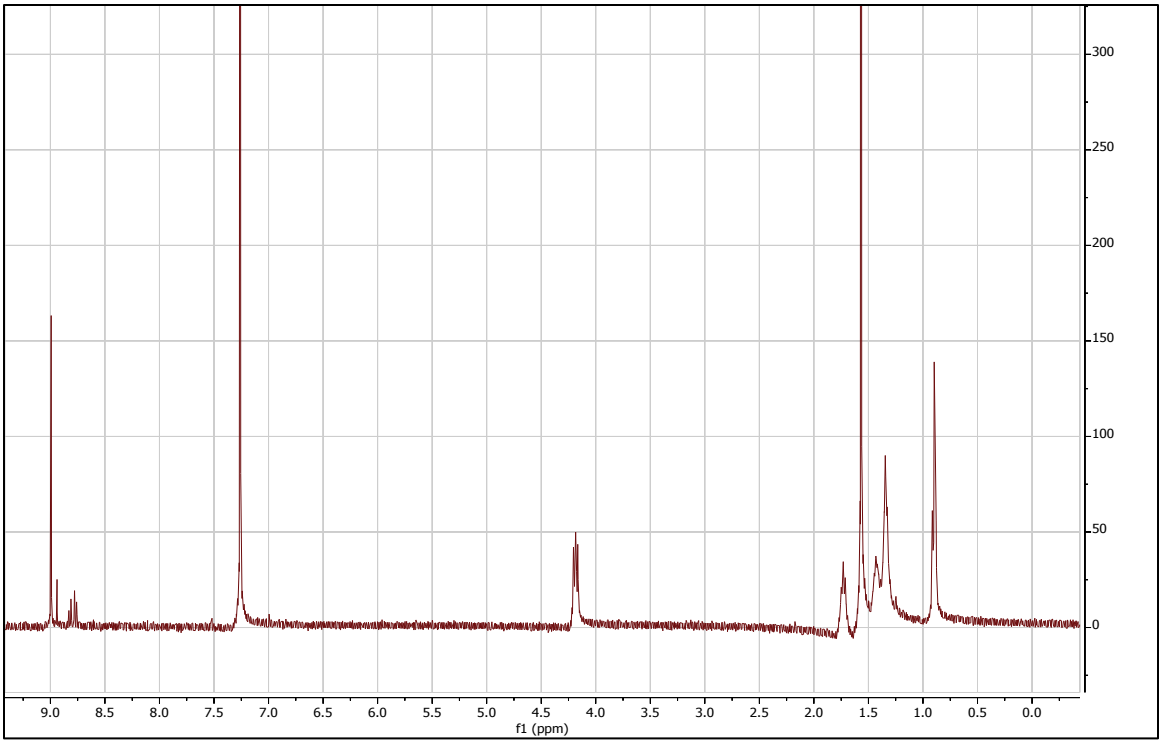

Figure A13. ^{1}H NMR of 4,9-dibromo-2,7-bis(2-decyltetradecyl)benzo[lmn][3,8]-phenanthroline-1,3,6,8(2H,7H)-tetraone

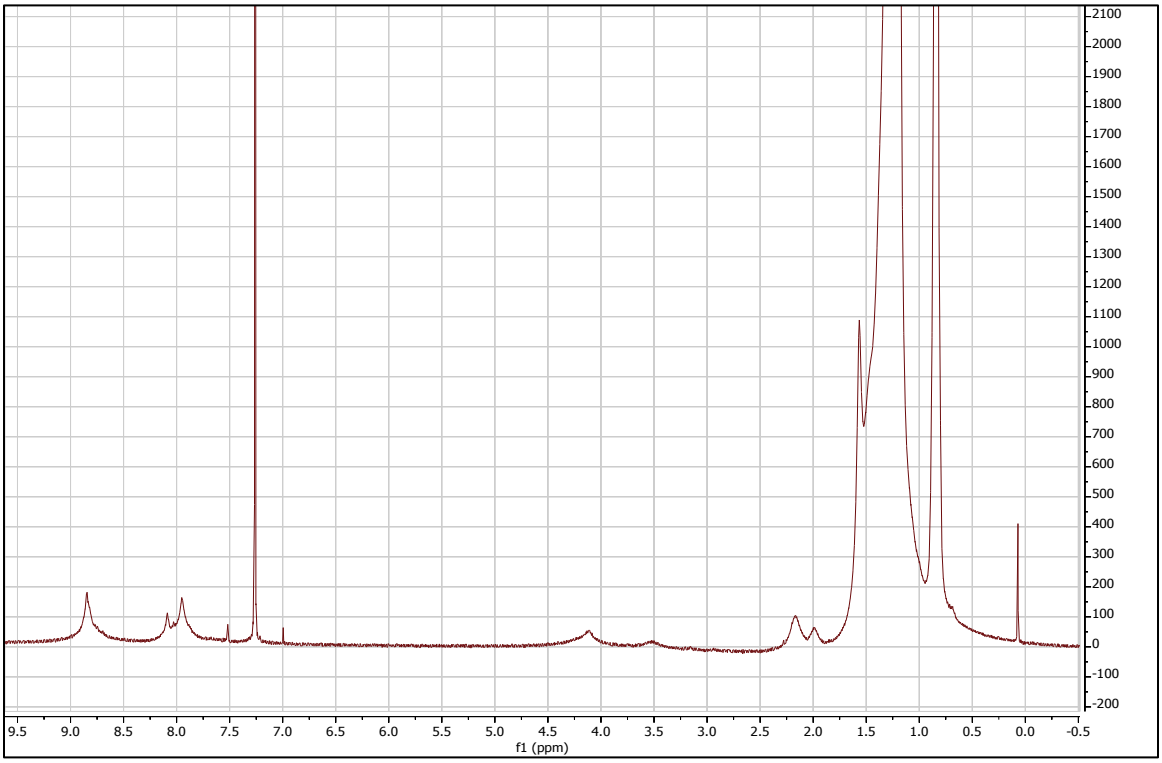

Figure A14. ^{1}H NMR of Poly(2,7-bis(2-decyltetradecyl)-4-methyl-9-(5′-methyl-[2,2′-bithiazol]-5yl)benzo[lmn][3,8]phenanthroline-1,3,6,8(2H,7H)-tetraone (**PNDI2Tz**)

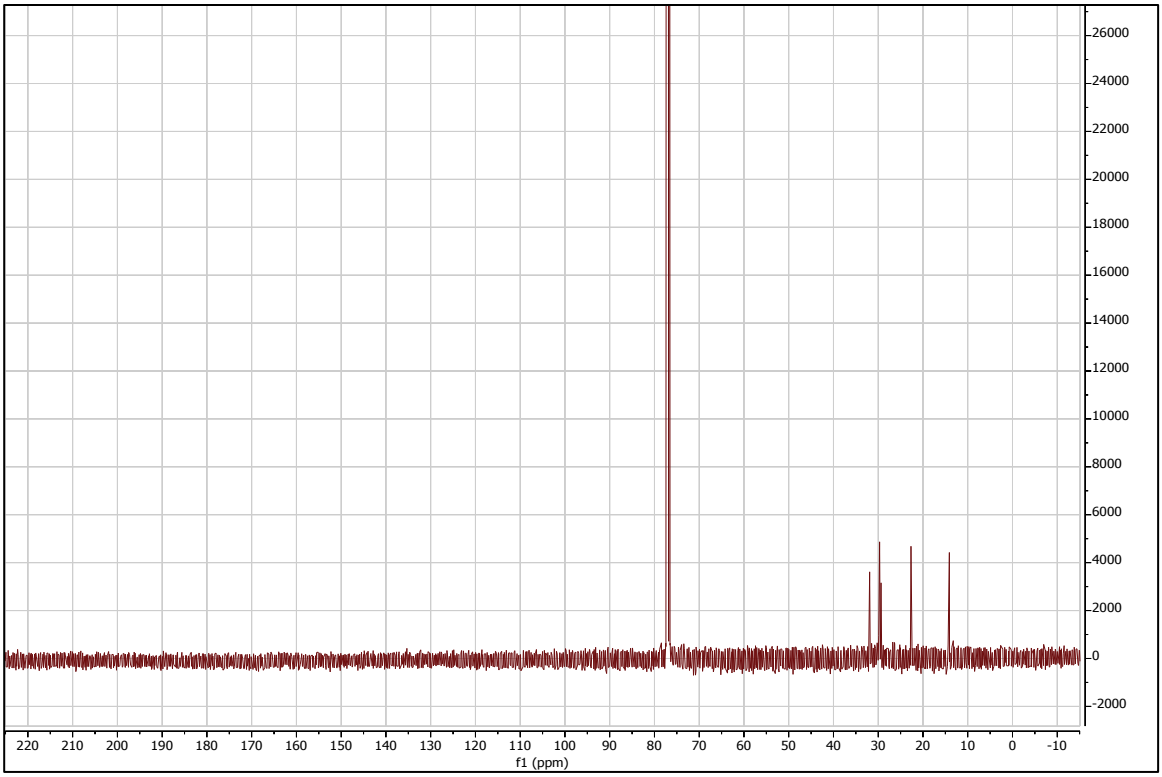

Figure A15. ^{13}C NMR of Poly(2,7-bis(2-decyltetradecyl)-4-methyl-9-(5′-methyl-[2,2′-bithiazol]-5yl)benzo[lmn][3,8]phenanthroline-1,3,6,8(2H,7H)-tetraone (**PNDI2Tz**)

REFERENCES

1. Salleo, A. Charge transport in polymeric transistors. *Mater. Today.* **2007,** 10 (3), 38-45.

2. Ashkenasy, G.; Cahen, D.; Cohen, R.; Shanzer, A.; Vilan, A. Molecular Engineering of Semiconductor Surfaces and Devices. *Acc. Chem. Res.* **2002,** 35 (2), 121-128.

3. Katz, H. E.; Bao, Z.; Gilat, S. L. Synthetic Chemistry for Ultrapure, Processable, and High-Mobility Organic Transistor Semiconductors. *Acc. Chem. Res.* **2001,** 34 (5), 359-369.

4. Zhang, J.; Xu, W.; Sheng, P.; Zhao, G.; Zhu, D. Organic Donor–Acceptor Complexes as Novel Organic Semiconductors. *Acc. Chem. Res.* **2017,** 50 (7), 1654-1662.

5. Coropceanu, V.; Cornil, J.; da Silva Filho, D. A.; Olivier, Y.; Silbey, R.; Brédas, J.-L. Charge Transport in Organic Semiconductors. *Chem. Rev.* **2007,** 107 (4), 926-952.

6. Ostroverkhova, O. Organic Optoelectronic Materials: Mechanisms and Applications. *Chem. Rev.* **2016,** 116 (22), 13279-13412.

7. Wang, C.; Dong, H.; Hu, W.; Liu, Y.; Zhu, D. Semiconducting π-Conjugated Systems in Field-Effect Transistors: A Material Odyssey of Organic Electronics. *Chem. Rev.* **2012,** 112 (4), 2208-2267.

8. Shirakawa, H.; Louis, E. J.; MacDiarmid, A. G.; Chiang, C. K.; Heeger, A. J. Synthesis of electrically conducting organic polymers: halogen derivatives of polyacetylene, (CH). *J. Chem. Soc., Chem. Commun.* **1977,** (16), 578-580.

9. Sirringhaus, H. 25th Anniversary Article: Organic Field-Effect Transistors: The Path Beyond Amorphous Silicon. *Adv. Mater.* **2014,** 26 (9), 1319-1335.

10. McGinness, J. E. Mobility Gaps: A Mechanism for Band Gaps in Melanins. *Science* **1972,** 177 (4052), 896.

11. McGinness, J.; Corry, P.; Proctor, P. Amorphous Semiconductor Switching in Melanins. *Science* **1974,** 183 (4127), 853.

12. Ong, B. S.; Wu, Y.; Liu, P.; Gardner, S. High-Performance Semiconducting Polythiophenes for Organic Thin-Film Transistors. *J. Am. Chem. Soc.* **2004,** 126 (11), 3378-3379.

13. Jones, B. A.; Facchetti, A.; Wasielewski, M. R.; Marks, T. J. Tuning Orbital Energetics in Arylene Diimide Semiconductors. Materials Design for Ambient Stability of n-Type Charge Transport. *J. Am. Chem. Soc.* **2007,** 129 (49), 15259-15278.

14. Yan, H.; Chen, Z.; Zheng, Y.; Newman, C.; Quinn, J. R.; Dotz, F.; Kastler, M.; Facchetti, A. A high-mobility electron-transporting polymer for printed transistors. *Nature* **2009,** 457 (7230), 679-86.

15. Dimitrakopoulos, C. D.; Malenfant, P. R. L. Organic Thin Film Transistors for Large Area Electronics. *Adv. Mater.* **2002,** 14 (2), 99-117.

16. Newman, C. R.; Frisbie, C. D.; da Silva Filho, D. A.; Brédas, J.-L.; Ewbank, P. C.; Mann, K. R. Introduction to Organic Thin Film Transistors and Design of n-Channel Organic Semiconductors. *Chem. Mater.* **2004,** 16 (23), 4436-4451.

17. Scully, S. R.; McGehee, M. D. Effects of optical interference and energy transfer on exciton diffusion length measurements in organic semiconductors. *J. Appl. Phys.* **2006,** 100 (3), 034907.

18. Najafov, H.; Lee, B.; Zhou, Q.; Feldman, L. C.; Podzorov, V. Observation of long-range exciton diffusion in highly ordered organic semiconductors. *Nat. Mater.* **2010,** 9 (11), 938.

19. Bakulin, A. A.; Rao, A.; Pavelyev, V. G.; van Loosdrecht, P. H. M.; Pshenichnikov, M. S.; Niedzialek, D.; Cornil, J.; Beljonne, D.; Friend, R. H. The Role of Driving Energy and Delocalized States for Charge Separation in Organic Semiconductors. *Science* **2012,** 335 (6074), 1340.

20. Lu, L.; Zheng, T.; Wu, Q.; Schneider, A. M.; Zhao, D.; Yu, L. Recent Advances in Bulk Heterojunction Polymer Solar Cells. *Chem. Rev.* **2015,** 115 (23), 12666-731.

21. Nicolai, H. T.; Kuik, M.; Wetzelaer, G. A.; de Boer, B.; Campbell, C.; Risko, C.; Bredas, J. L.; Blom, P. W. Unification of trap-limited electron transport in semiconducting polymers. *Nat. Mater.* **2012,** 11 (10), 882-7.

22. Lüssem, B.; Keum, C.-M.; Kasemann, D.; Naab, B.; Bao, Z.; Leo, K. Doped Organic Transistors. *Chem. Rev.* **2016,** 116 (22), 13714-13751.

23. Usta, H.; Facchetti, A.; Marks, T. J. n-Channel Semiconductor Materials Design for Organic Complementary Circuits. *Acc. Chem. Res.* **2011,** 44 (7), 501-510.

24. Potje-Kamloth, K. Semiconductor Junction Gas Sensors. *Chem. Rev.* **2008,** 108 (2), 367-399.

25. Katz, H. E.; Lovinger, A. J.; Johnson, J.; Kloc, C.; Siegrist, T.; Li, W.; Lin, Y. Y.; Dodabalapur, A. A soluble and air-stable organic semiconductor with high electron mobility. *Nature* **2000,** 404 (6777), 478.

26. Meng, L.; Zhang, Y.; Wan, X.; Li, C.; Zhang, X.; Wang, Y.; Ke, X.; Xiao, Z.; Ding, L.; Xia, R.; Yip, H.-L.; Cao, Y.; Chen, Y. Organic and solution-processed tandem solar cells with 17.3% efficiency. *Science* **2018,** 361 (6407), 1094-1098.

27. Cui, Y.; Yao, H.; Gao, B.; Qin, Y.; Zhang, S.; Yang, B.; He, C.; Xu, B.; Hou, J. Fine-Tuned Photoactive and Interconnection Layers for Achieving over 13% Efficiency in a Fullerene-Free Tandem Organic Solar Cell. *J. Am. Chem. Soc.* **2017,** 139 (21), 7302-7309.

28. Zhao, W.; Li, S.; Zhang, S.; Liu, X.; Hou, J. Ternary Polymer Solar Cells based on Two Acceptors and One Donor for Achieving 12.2% Efficiency. *Adv. Mater.* **2016,** 29 (2), 1604059.

29. Reineke, S.; Lindner, F.; Schwartz, G.; Seidler, N.; Walzer, K.; Lussem, B.; Leo, K. White organic light-emitting diodes with fluorescent tube efficiency. *Nature* **2009,** 459 (7244), 234-238.

30. Lo, S.-C.; Burn, P. L. Development of Dendrimers: Macromolecules for Use in Organic Light-Emitting Diodes and Solar Cells. *Chem. Rev.* **2007,** 107 (4), 1097-1116.

31. Yuen, J. D.; Kumar, R.; Zakhidov, D.; Seifter, J.; Lim, B.; Heeger, A. J.; Wudl, F. Ambipolarity in Benzobisthiadiazole-Based Donor–Acceptor Conjugated Polymers. *Adv. Mater.* **2011,** 23 (33), 3780-3785.

32. Xu, W.; Hu, Z.; Liu, H.; Lan, L.; Peng, J.; Wang, J.; Cao, Y. Flexible All-organic, All-solution Processed Thin Film Transistor Array with Ultrashort Channel. *Scientific Reports* **2016,** 6, 29055.

33. Smith, J.; Hamilton, R.; Qi, Y.; Kahn, A.; Bradley, D. D. C.; Heeney, M.; McCulloch, I.; Anthopoulos, T. D. The Influence of Film Morphology in High-Mobility Small-Molecule:Polymer Blend Organic Transistors. *Adv. Funct. Mater.* **2010,** 20 (14), 2330-2337.

34. OLED TV. https://www.youtube.com/watch?v=SPLFzEHvqd4 Access date

35. 3D printed solar cell. https://www.greenoptimistic.com/3d-printed-solar-cells/ Access date September 26,**2018**

36. COPE organic electronic printed on flexible substrate. http://s2.cope.gatech.edu/hg/item/63912 Access date September 26,**2018**

37. Wang, L.; Fine, D.; Sharma, D.; Torsi, L.; Dodabalapur, A. Nanoscale organic and polymeric field-effect transistors as chemical sensors. *Anal. Bioanal. Chem.* **2006,** 384 (2), 310-321.

38. Zhang, L.; Fonari, A.; Liu, Y.; Hoyt, A.-L. M.; Lee, H.; Granger, D.; Parkin, S.; Russell, T. P.; Anthony, J. E.; Brédas, J.-L.; Coropceanu, V.; Briseno, A. L.

Bistetracene: An Air-Stable, High-Mobility Organic Semiconductor with Extended Conjugation. *J. Am. Chem. Soc.* **2014,** 136 (26), 9248-9251.

39. Facchetti, A. Polymer donor–polymer acceptor (all-polymer) solar cells. *Mater. Today.* **2013,** 16 (4), 123-132.

40. Nielsen, C. B.; Turbiez, M.; McCulloch, I. Recent Advances in the Development of Semiconducting DPP-Containing Polymers for Transistor Applications. *Adv. Mater.* **2012,** 25 (13), 1859-1880.

41. Li, Y.; Sonar, P.; Murphy, L.; Hong, W. High mobility diketopyrrolopyrrole (DPP)-based organic semiconductor materials for organic thin film transistors and photovoltaics. *Energy Environ. Sci.* **2013,** 6 (6), 1684-1710.

42. Cheng, X.; Caironi, M.; Noh, Y.-Y.; Wang, J.; Newman, C.; Yan, H.; Facchetti, A.; Sirringhaus, H. Air Stable Cross-Linked Cytop Ultrathin Gate Dielectric for High Yield Low-Voltage Top-Gate Organic Field-Effect Transistors. *Chem. Mater.* **2010,** 22 (4), 1559-1566.

43. Yan, Z.; Sun, B.; Li, Y. Novel stable (3E,7E)-3,7-bis(2-oxoindolin-3-ylidene)benzo[1,2-b:4,5-b′]difuran-2,6(3H,7H)-dione based donor–acceptor polymer semiconductors for n-type organic thin film transistors. *Chem. Commun. (Cambridge, U. K.)* **2013,** 49 (36), 3790-3792.

44. Martínez Hardigree, J. F.; Katz, H. E. Through Thick and Thin: Tuning the Threshold Voltage in Organic Field-Effect Transistors. *Acc. Chem. Res.* **2014,** 47 (4), 1369-1377.

45. Sokolov, A. N.; Tee, B. C. K.; Bettinger, C. J.; Tok, J. B. H.; Bao, Z. Chemical and Engineering Approaches To Enable Organic Field-Effect Transistors for Electronic Skin Applications. *Acc. Chem. Res.* **2012,** 45 (3), 361-371.

46. Horowitz, G.; Hajlaoui, R.; Bouchriha, H.; Bourguiga, R.; Hajlaoui, M. The Concept of "Threshold Voltage" in Organic Field-Effect Transistors. *Adv. Mater.* **1998,** 10 (12), 923-927.

47. Koch, N.; Vollmer, A.; Duhm, S.; Sakamoto, Y.; Suzuki, T. The Effect of Fluorination on Pentacene/Gold Interface Energetics and Charge Reorganization Energy. *Adv. Mater.* **2007,** 19 (1), 112-116.

48. Biniek, L.; Chochos, C. L.; Leclerc, N.; Hadziioannou, G.; Kallitsis, J. K.; Bechara, R.; Leveque, P.; Heiser, T. A [3,2-b]thienothiophene-alt-benzothiadiazole copolymer for photovoltaic applications: design, synthesis, material characterization and device performances. *J. Mater. Chem.* **2009,** 19 (28), 4946-4951.

49. Brocorens, P.; Van Vooren, A.; Chabinyc, M. L.; Toney, M. F.; Shkunov, M.; Heeney, M.; McCulloch, I.; Cornil, J.; Lazzaroni, R. Solid-State Supramolecular

Organization of Polythiophene Chains Containing Thienothiophene Units. *Adv. Mater.* **2009,** 21 (10-11), 1193-1198.

50. McCulloch, I.; Heeney, M.; Chabinyc, M. L.; DeLongchamp, D.; Kline, R. J.; Cölle, M.; Duffy, W.; Fischer, D.; Gundlach, D.; Hamadani, B.; Hamilton, R.; Richter, L.; Salleo, A.; Shkunov, M.; Sparrowe, D.; Tierney, S.; Zhang, W. Semiconducting Thienothiophene Copolymers: Design, Synthesis, Morphology, and Performance in Thin-Film Organic Transistors. *Adv. Mater.* **2009,** 21 (10-11), 1091-1109.

51. McCulloch, I.; Heeney, M.; Bailey, C.; Genevicius, K.; MacDonald, I.; Shkunov, M.; Sparrowe, D.; Tierney, S.; Wagner, R.; Zhang, W.; Chabinyc, M. L.; Kline, R. J.; McGehee, M. D.; Toney, M. F. Liquid-crystalline semiconducting polymers with high charge-carrier mobility. *Nat. Mater.* **2006,** 5 (4), 328.

52. Pan, H.; Li, Y.; Wu, Y.; Liu, P.; Ong, B. S.; Zhu, S.; Xu, G. Low-Temperature, Solution-Processed, High-Mobility Polymer Semiconductors for Thin-Film Transistors. *J. Am. Chem. Soc.* **2007,** 129 (14), 4112-4113.

53. Li, Y.; Singh, S. P.; Sonar, P. A High Mobility P-Type DPP-Thieno[3,2-b]thiophene Copolymer for Organic Thin-Film Transistors. *Adv. Mater.* **2010,** 22 (43), 4862-4866.

54. Osaka, I.; Sauvé, G.; Zhang, R.; Kowalewski, T.; McCullough, R. D. Novel Thiophene-Thiazolothiazole Copolymers for Organic Field-Effect Transistors. *Adv. Mater.* **2007,** 19 (23), 4160-4165.

55. Zhu, Y.; Champion, R. D.; Jenekhe, S. A. Conjugated Donor−Acceptor Copolymer Semiconductors with Large Intramolecular Charge Transfer: Synthesis, Optical Properties, Electrochemistry, and Field Effect Carrier Mobility of Thienopyrazine-Based Copolymers. *Macromolecules* **2006,** 39 (25), 8712-8719.

56. Li, Y.; Sonar, P.; Singh, S. P.; Soh, M. S.; van Meurs, M.; Tan, J. Annealing-Free High-Mobility Diketopyrrolopyrrole−Quaterthiophene Copolymer for Solution-Processed Organic Thin Film Transistors. *J. Am. Chem. Soc.* **2011,** 133 (7), 2198-2204.

57. Li, Y.; Sonar, P.; Singh, S. P.; Zeng, W.; Soh, M. S. 3,6-Di(furan-2-yl)pyrrolo[3,4-c]pyrrole-1,4(2H,5H)-dione and bithiophene copolymer with rather disordered chain orientation showing high mobility in organic thin film transistors. *J. Mater. Chem.* **2011,** 21 (29), 10829-10835.

58. Sonar, P.; Singh, S. P.; Li, Y.; Ooi, Z.-E.; Ha, T.-j.; Wong, I.; Soh, M. S.; Dodabalapur, A. High mobility organic thin film transistor and efficient photovoltaic devices using versatile donor–acceptor polymer semiconductor by molecular design. *Energy Environ. Sci.* **2011,** 4 (6), 2288-2296.

59. Meager, I.; Ashraf, R. S.; Rossbauer, S.; Bronstein, H.; Donaghey, J. E.; Marshall, J.; Schroeder, B. C.; Heeney, M.; Anthopoulos, T. D.; McCulloch, I. Alkyl Chain Extension as a Route to Novel Thieno[3,2-b]thiophene Flanked Diketopyrrolopyrrole Polymers for Use in Organic Solar Cells and Field Effect Transistors. *Macromolecules* **2013,** 46 (15), 5961-5967.

60. Tang, A.; Li, L.; Lu, Z.; Huang, J.; Jia, H.; Zhan, C.; Tan, Z. a.; Li, Y.; Yao, J. Significant improvement of photovoltaic performance by embedding thiophene in solution-processed star-shaped TPA-DPP backbone. *Journal of Materials Chemistry A* **2013,** 1 (18), 5747-5757.

61. Carsten, B.; Szarko, J. M.; Lu, L.; Son, H. J.; He, F.; Botros, Y. Y.; Chen, L. X.; Yu, L. Mediating Solar Cell Performance by Controlling the Internal Dipole Change in Organic Photovoltaic Polymers. *Macromolecules* **2012,** 45 (16), 6390-6395.

62. Gao, Y.; Zhang, X.; Tian, H.; Zhang, J.; Yan, D.; Geng, Y.; Wang, F. High Mobility Ambipolar Diketopyrrolopyrrole-Based Conjugated Polymer Synthesized Via Direct Arylation Polycondensation. *Adv. Mater.* **2015,** 27 (42), 6753-6759.

63. Li, J.; Zhao, Y.; Tan, H. S.; Guo, Y.; Di, C. A.; Yu, G.; Liu, Y.; Lin, M.; Lim, S. H.; Zhou, Y.; Su, H.; Ong, B. S. A stable solution-processed polymer semiconductor with record high-mobility for printed transistors. *Sci Rep* **2012,** 2, 754.

64. Li, W.; Roelofs, W. S. C.; Turbiez, M.; Wienk, M. M.; Janssen, R. A. J. Polymer Solar Cells with Diketopyrrolopyrrole Conjugated Polymers as the Electron Donor and Electron Acceptor. *Adv. Mater.* **2014,** 26 (20), 3304-3309.

65. Yao, J.; Yu, C.; Liu, Z.; Luo, H.; Yang, Y.; Zhang, G.; Zhang, D. Significant Improvement of Semiconducting Performance of the Diketopyrrolopyrrole–Quaterthiophene Conjugated Polymer through Side-Chain Engineering via Hydrogen-Bonding. *J. Am. Chem. Soc.* **2016,** 138 (1), 173-185.

66. Yi, Z.; Wang, S.; Liu, Y. Design of High-Mobility Diketopyrrolopyrrole-Based π-Conjugated Copolymers for Organic Thin-Film Transistors. *Adv. Mater.* **2015,** 27 (24), 3589-3606.

67. Gao, L.; Zhang, Z.-G.; Xue, L.; Min, J.; Zhang, J.; Wei, Z.; Li, Y. All-Polymer Solar Cells Based on Absorption-Complementary Polymer Donor and Acceptor with High Power Conversion Efficiency of 8.27%. *Adv. Mater.* **2016,** 28 (9), 1884-1890.

68. Getmanenko, Y. A.; Singh, S.; Sandhu, B.; Wang, C.-Y.; Timofeeva, T.; Kippelen, B.; Marder, S. R. Pyrrole[3,2-d:4,5-d[prime or minute]]bisthiazole-bridged bis(naphthalene diimide)s as electron-transport materials. *J. Mater. Chem. C.* **2014,** 2 (1), 124-131.

69. Guo, X.; Watson, M. D. Conjugated polymers from naphthalene bisimide. *Org. Lett.* **2008,** 10 (23), 5333-6.

70. Guo, X. G.; Kim, F. S.; Seger, M. J.; Jenekhe, S. A.; Watson, M. D. Naphthalene Diimide-Based Polymer Semiconductors: Synthesis, Structure-Property Correlations, and n-Channel and Ambipolar Field-Effect Transistors. *Chem. Mater.* **2012,** 24 (8), 1434-1442.

71. Kobaisi, M. A.; Bhosale, S. V.; Latham, K.; Raynor, A. M.; Bhosale, S. V. Functional Naphthalene Diimides: Synthesis, Properties, and Applications. *Chem. Rev.* **2016,** 116 (19), 11685-11796.

72. Chen, Z.; Zheng, Y.; Yan, H.; Facchetti, A. Naphthalenedicarboximide- vs Perylenedicarboximide-Based Copolymers. Synthesis and Semiconducting Properties in Bottom-Gate N-Channel Organic Transistors. *J. Am. Chem. Soc.* **2009,** 131 (1), 8-9.

73. Facchetti, A. π-Conjugated Polymers for Organic Electronics and Photovoltaic Cell Applications. *Chem. Mater.* **2011,** 23 (3), 733-758.

74. Wang, Y.; Hasegawa, T.; Matsumoto, H.; Mori, T.; Michinobu, T. D-A1-D-A2 Backbone Strategy for Benzobisthiadiazole Based n-Channel Organic Transistors: Clarifying the Selenium-Substitution Effect on the Molecular Packing and Charge Transport Properties in Electron-Deficient Polymers. *Adv. Funct. Mater.* **2017,** 27 (33), 1701486-n/a.

75. Black, H. T.; Perepichka, D. F. Crystal Engineering of Dual Channel p/n Organic Semiconductors by Complementary Hydrogen Bonding. *Angewandte Chemie International Edition* **2014,** 53 (8), 2138-2142.

76. Fu, B.; Wang, C.-Y.; Rose, B. D.; Jiang, Y.; Chang, M.; Chu, P.-H.; Yuan, Z.; Fuentes-Hernandez, C.; Kippelen, B.; Brédas, J.-L.; Collard, D. M.; Reichmanis, E. Molecular Engineering of Nonhalogenated Solution-Processable Bithiazole-Based Electron-Transport Polymeric Semiconductors. *Chem. Mater.* **2015,** 27 (8), 2928-2937.

77. Mei, J.; Bao, Z. Side Chain Engineering in Solution-Processable Conjugated Polymers. *Chem. Mater.* **2014,** 26 (1), 604-615.

78. Yang, H.; Shin, T. J.; Yang, L.; Cho, K.; Ryu, C. Y.; Bao, Z. Effect of Mesoscale Crystalline Structure on the Field-Effect Mobility of Regioregular Poly(3-hexyl thiophene) in Thin-Film Transistors. *Adv. Funct. Mater.* **2005,** 15 (4), 671-676.

79. Huang, H.; Yang, L.; Facchetti, A.; Marks, T. J. Organic and Polymeric Semiconductors Enhanced by Noncovalent Conformational Locks. *Chem. Rev.* **2017,** 117 (15), 10291-10318.

80. Liu, J.; Mikhaylov, I. A.; Zou, J.; Osaka, I.; Masunov, A. E.; McCullough, R. D.; Zhai, L. Insight into how molecular structures of thiophene-based conjugated polymers affect crystallization behaviors. *Polymer* **2011,** 52 (10), 2302-2309.

81. Guo, X.; Puniredd, S. R.; Baumgarten, M.; Pisula, W.; Müllen, K. Rational Design of Benzotrithiophene-Diketopyrrolopyrrole-Containing Donor-Acceptor Polymers for Improved Charge Carrier Transport. *Adv. Mater.* **2013,** 25 (38), 5467-5472.

82. Fu, B.; Baltazar, J.; Sankar, A. R.; Chu, P.-H.; Zhang, S.; Collard, D. M.; Reichmanis, E. Enhancing Field-Effect Mobility of Conjugated Polymers Through Rational Design of Branched Side Chains. *Adv. Funct. Mater.* **2014,** 24 (24), 3734-3744.

83. Nishinaga, S.; Mori, H.; Nishihara, Y. Phenanthrodithiophene–Isoindigo Copolymers: Effect of Side Chains on Their Molecular Order and Solar Cell Performance. *Macromolecules* **2015,** 48 (9), 2875-2885.

84. Holliday, S.; Donaghey, J. E.; McCulloch, I. Advances in Charge Carrier Mobilities of Semiconducting Polymers Used in Organic Transistors. *Chem. Mater.* **2014,** 26 (1), 647-663.

85. Chen, H.; Hurhangee, M.; Nikolka, M.; Zhang, W.; Kirkus, M.; Neophytou, M.; Cryer, S. J.; Harkin, D.; Hayoz, P.; Abdi-Jalebi, M.; McNeill, C. R.; Sirringhaus, H.; McCulloch, I. Dithiopheneindenofluorene (TIF) Semiconducting Polymers with Very High Mobility in Field-Effect Transistors. *Adv. Mater.* **2017,** 29 (36), 1702523.

86. Zhao, Y.; Guo, Y.; Liu, Y. 25th Anniversary Article: Recent Advances in n-Type and Ambipolar Organic Field-Effect Transistors. *Adv. Mater.* **2013,** 25 (38), 5372-5391.

87. Quinn, J. T. E.; Zhu, J.; Li, X.; Wang, J.; Li, Y. Recent progress in the development of n-type organic semiconductors for organic field effect transistors. *J. Mater. Chem. C.* **2017,** 5 (34), 8654-8681.

88. Kronemeijer, A. J.; Gili, E.; Shahid, M.; Rivnay, J.; Salleo, A.; Heeney, M.; Sirringhaus, H. A Selenophene-Based Low-Bandgap Donor–Acceptor Polymer Leading to Fast Ambipolar Logic. *Adv. Mater.* **2012,** 24 (12), 1558-1565.

89. Shi, Y.; Guo, H.; Qin, M.; Zhao, J.; Wang, Y.; Wang, H.; Wang, Y.; Facchetti, A.; Lu, X.; Guo, X. Thiazole Imide-Based All-Acceptor Homopolymer: Achieving High-Performance Unipolar Electron Transport in Organic Thin-Film Transistors. *Adv. Mater.* **2018,** 30 (10), 1705745.

90. Yuan, Z. B.; Fu, B. Y.; Thomas, S.; Zhang, S. Y.; DeLuca, G.; Chang, R.; Lopez, L.; Fares, C.; Zhang, G. Y.; Bredas, J. L.; Reichmanis, E. Unipolar Electron Transport Polymers: A Thiazole Based All-Electron Acceptor Approach. *Chem. Mater.* **2016,** 28 (17), 6045-6049.

91. Shi, K.; Zhang, F.; Di, C.-A.; Yan, T.-W.; Zou, Y.; Zhou, X.; Zhu, D.; Wang, J.-Y.; Pei, J. Toward High Performance n-Type Thermoelectric Materials by Rational Modification of BDPPV Backbones. *J. Am. Chem. Soc.* **2015,** 137 (22), 6979-6982.

92. Zhao, X.; Zhan, X. Electron transporting semiconducting polymers in organic electronics. *Chem. Soc. Rev.* **2011,** 40 (7), 3728-3743.

93. Zhou, E.; Cong, J.; Wei, Q.; Tajima, K.; Yang, C.; Hashimoto, K. All-Polymer Solar Cells from Perylene Diimide Based Copolymers: Material Design and Phase Separation Control. *Angewandte Chemie International Edition* **2011,** 50 (12), 2799-2803.

94. Sonar, P.; Fong Lim, J. P.; Chan, K. L. Organic non-fullerene acceptors for organic photovoltaics. *Energy Environ. Sci.* **2011,** 4 (5), 1558-1574.

95. Yang, Y.; Zhang, G.; Luo, H.; Yao, J.; Liu, Z.; Zhang, D. Highly Sensitive Thin-Film Field-Effect Transistor Sensor for Ammonia with the DPP-Bithiophene Conjugated Polymer Entailing Thermally Cleavable tert-Butoxy Groups in the Side Chains. *ACS Appl. Mater. Interfaces* **2015,** 8 (6), 3635-43.

96. Higginbotham, H. F.; Maniam, S.; Langford, S. J.; Bell, T. D. M. New brightly coloured, water soluble, core-substituted naphthalene diimides for biophysical applications. *Dyes Pigm.* **2015,** 112, 290-297.

97. Hendsbee, A. D.; McAfee, S. M.; Sun, J.-P.; McCormick, T. M.; Hill, I. G.; Welch, G. C. Phthalimide-based [small pi]-conjugated small molecules with tailored electronic energy levels for use as acceptors in organic solar cells. *J. Mater. Chem. C.* **2015,** 3 (34), 8904-8915.

98. Gross, Y. M.; Trefz, D.; Tkachov, R.; Untilova, V.; Brinkmann, M.; Schulz, G. L.; Ludwigs, S. Tuning Aggregation by Regioregularity for High-Performance n-Type P(NDI2OD-T2) Donor–Acceptor Copolymers. *Macromolecules* **2017,** 50 (14), 5353-5366.

99. Koeckelberghs, G.; De Cremer, L.; Vanormelingen, W.; Dehaen, W.; Verbiest, T.; Persoons, A.; Samyn, C. Improved synthesis of N-alkyl substituted dithieno[3,2-b:2′,3′-d]pyrroles. *Tetrahedron* **2005,** 61 (3), 687-691.

100. Lu, C.; Chen, H.-C.; Chuang, W.-T.; Hsu, Y.-H.; Chen, W.-C.; Chou, P.-T. Interplay of Molecular Orientation, Film Formation, and Optoelectronic Properties on Isoindigo- and Thienoisoindigo-Based Copolymers for Organic Field Effect Transistor and Organic Photovoltaic Applications. *Chem. Mater.* **2015,** 27 (19), 6837-6847.

101. Lei, T.; Cao, Y.; Fan, Y.; Liu, C.-J.; Yuan, S.-C.; Pei, J. High-Performance Air-Stable Organic Field-Effect Transistors: Isoindigo-Based Conjugated Polymers. *J. Am. Chem. Soc.* **2011,** 133 (16), 6099-6101.

102. Stalder, R.; Mei, J.; Subbiah, J.; Grand, C.; Estrada, L. A.; So, F.; Reynolds, J. R. n-Type Conjugated Polyisoindigos. *Macromolecules* **2011,** 44 (16), 6303-6310.

103. Kim, R.; Amegadze, P. S. K.; Kang, I.; Yun, H.-J.; Noh, Y.-Y.; Kwon, S.-K.; Kim, Y.-H. High-Mobility Air-Stable Naphthalene Diimide-Based Copolymer Containing Extended π-Conjugation for n-Channel Organic Field Effect Transistors. *Adv. Funct. Mater.* **2013,** 23 (46), 5719-5727.

104. Zhao, Z.; Yin, Z.; Chen, H.; Zheng, L.; Zhu, C.; Zhang, L.; Tan, S.; Wang, H.; Guo, Y.; Tang, Q.; Liu, Y. High-Performance, Air-Stable Field-Effect Transistors Based on Heteroatom-Substituted Naphthalenediimide-Benzothiadiazole Copolymers Exhibiting Ultrahigh Electron Mobility up to 8.5 cm V−1 s−1. *Adv. Mater.* **2016,** 29 (4), 1602410.

105. Lei, T.; Xia, X.; Wang, J.-Y.; Liu, C.-J.; Pei, J. "Conformation Locked" Strong Electron-Deficient Poly(p-Phenylene Vinylene) Derivatives for Ambient-Stable n-Type Field-Effect Transistors: Synthesis, Properties, and Effects of Fluorine Substitution Position. *J. Am. Chem. Soc.* **2014,** 136 (5), 2135-2141.

106. Voronina, Y. K.; Krivolapov, D. B.; Bogdanov, A. V.; Mironov, V. F.; Litvinov, I. A. An unusual conformation of 1,1′-dimethyl-isoindigo in crystals. *J. Struct. Chem.* **2012,** 53 (2), 413-416.

107. Yang, J.; Wang, H.; Chen, J.; Huang, J.; Jiang, Y.; Zhang, J.; Shi, L.; Sun, Y.; Wei, Z.; Yu, G.; Guo, Y.; Wang, S.; Liu, Y. Bis-Diketopyrrolopyrrole Moiety as a Promising Building Block to Enable Balanced Ambipolar Polymers for Flexible Transistors. *Adv. Mater.* **2017,** 29 (22), 1606162.

108. Shi, L.; Guo, Y.; Hu, W.; Liu, Y. Design and effective synthesis methods for high-performance polymer semiconductors in organic field-effect transistors. *Materials Chemistry Frontiers* **2017,** 1 (12), 2423-2456.

109. Kang, I.; Yun, H.-J.; Chung, D. S.; Kwon, S.-K.; Kim, Y.-H. Record High Hole Mobility in Polymer Semiconductors via Side-Chain Engineering. *J. Am. Chem. Soc.* **2013,** 135 (40), 14896-14899.

110. Al Kobaisi, M.; Bhosale, S. V.; Latham, K.; Raynor, A. M.; Bhosale, S. V. Functional Naphthalene Diimides: Synthesis, Properties, and Applications. *Chem. Rev.* **2016,** 116 (19), 11685-11796.

111. Bhosale, S. V.; Jani, C. H.; Langford, S. J. Chemistry of naphthalene diimides. *Chem. Soc. Rev.* **2008,** 37 (2), 331-342.

112. Würthner, F. Perylene bisimide dyes as versatile building blocks for functional supramolecular architectures. *Chem. Commun. (Cambridge, U. K.)* **2004,** (14), 1564-1579.

113. Huang, C.; Barlow, S.; Marder, S. R. Perylene-3,4,9,10-tetracarboxylic Acid Diimides: Synthesis, Physical Properties, and Use in Organic Electronics. *The Journal of Organic Chemistry* **2011,** 76 (8), 2386-2407.

114. Suraru, S.-L.; Burschka, C.; Würthner, F. Diindole-Annulated Naphthalene Diimides: Synthesis and Optical and Electronic Properties of Syn- and Anti-Isomers. *The Journal of Organic Chemistry* **2014,** 79 (1), 128-139.

115. Würthner, F.; Stolte, M. Naphthalene and perylene diimides for organic transistors. *Chem. Commun. (Cambridge, U. K.)* **2011,** 47 (18), 5109-5115.

116. Zhan, X.; Facchetti, A.; Barlow, S.; Marks, T. J.; Ratner, M. A.; Wasielewski, M. R.; Marder, S. R. Rylene and Related Diimides for Organic Electronics. *Adv. Mater.* **2010,** 23 (2), 268-284.

117. Guo, X. G.; Zhou, N. J.; Lou, S. J.; Smith, J.; Tice, D. B.; Hennek, J. W.; Ortiz, R. P.; Navarrete, J. T. L.; Li, S. Y.; Strzalka, J.; Chen, L. X.; Chang, R. P. H.; Facchetti, A.; Marks, T. J. Polymer solar cells with enhanced fill factors. *Nat. Photonics* **2013,** 7 (10), 825-833.

118. Tao, T.; Peng, Y.-X.; Huang, W.; You, X.-Z. Coplanar Bithiazole-Centered Heterocyclic Aromatic Fluorescent Compounds Having Different Donor/Acceptor Terminal Groups. *The Journal of Organic Chemistry* **2013,** 78 (6), 2472-2481.

119. Zhang, J.; Xu, W.; Sheng, P.; Zhao, G.; Zhu, D. Organic Donor-Acceptor Complexes as Novel Organic Semiconductors. *Acc. Chem. Res.* **2017**,

120. Su, H.-L.; Sredojevic, D. N.; Bronstein, H.; Marks, T. J.; Schroeder, B. C.; Al-Hashimi, M. Bithiazole: An Intriguing Electron-Deficient Building for Plastic Electronic Applications. *Macromol. Rapid Commun.* **2017,** 38 (10), 1600610-n/a.

121. Lin, Y.; Fan, H.; Li, Y.; Zhan, X. Thiazole-Based Organic Semiconductors for Organic Electronics. *Adv. Mater.* **2012,** 24 (23), 3087-3106.

122. Liu, Y.; Dong, H.; Jiang, S.; Zhao, G.; Shi, Q.; Tan, J.; Jiang, L.; Hu, W.; Zhan, X. High Performance Nanocrystals of a Donor–Acceptor Conjugated Polymer. *Chem. Mater.* **2013,** 25 (13), 2649-2655.

123. Mamada, M.; Nishida, J.-i.; Kumaki, D.; Tokito, S.; Yamashita, Y. n-Type Organic Field-Effect Transistors with High Electron Mobilities Based on Thiazole−Thiazolothiazole Conjugated Molecules. *Chem. Mater.* **2007,** 19 (22), 5404-5409.

124. Wolf, M. O.; Wrighton, M. S. Tunable Electron Density at a Rhenium Carbonyl Complex Coordinated to the Conducting Polymer Poly[5,5'-(2-thienyl)-2,2'-bithiazole]. *Chem. Mater.* **1994,** 6 (9), 1526-1533.

125. Yamamoto, T.; Suganuma, H.; Maruyama, T.; Inoue, T.; Muramatsu, Y.; Arai, M.; Komarudin, D.; Ooba, N.; Tomaru, S.; Sasaki, S.; Kubota, K. pi-conjugated and light emitting poly(4,4'-dialkyl-2,2'-bithiazole-5,5'-diyl)s and their analogues comprised of electron-accepting five-membered rings. Preparation, regioregular structure, face-to-face stacking, and electrochemical and optical properties. *Chem. Mater.* **1997,** 9 (5), 1217-1225.

126. Jung, I. H.; Jung, Y. K.; Lee, J.; Park, J.-H.; Woo, H. Y.; Lee, J.-I.; Chu, H. Y.; Shim, H.-K. Synthesis and electroluminescent properties of fluorene-based copolymers containing electron-withdrawing thiazole derivatives. *Journal of Polymer Science Part A: Polymer Chemistry* **2008,** 46 (21), 7148-7161.

127. Johansson, M. P.; Olsen, J. Torsional Barriers and Equilibrium Angle of Biphenyl: Reconciling Theory with Experiment. *J. Chem. Theory Comput.* **2008,** 4 (9), 1460-1471.

128. Bronstein, H.; Hurhangee, M.; Fregoso, E. C.; Beatrup, D.; Soon, Y. W.; Huang, Z.; Hadipour, A.; Tuladhar, P. S.; Rossbauer, S.; Sohn, E.-H.; Shoaee, S.; Dimitrov, S. D.; Frost, J. M.; Ashraf, R. S.; Kirchartz, T.; Watkins, S. E.; Song, K.; Anthopoulos, T.; Nelson, J.; Rand, B. P.; Durrant, J. R.; McCulloch, I. Isostructural, Deeper Highest Occupied Molecular Orbital Analogues of Poly(3-hexylthiophene) for High-Open Circuit Voltage Organic Solar Cells. *Chem. Mater.* **2013,** 25 (21), 4239-4249.

129. Usta, H.; Sheets, W. C.; Denti, M.; Generali, G.; Capelli, R.; Lu, S.; Yu, X.; Muccini, M.; Facchetti, A. Perfluoroalkyl-Functionalized Thiazole–Thiophene Oligomers as N-Channel Semiconductors in Organic Field-Effect and Light-Emitting Transistors. *Chem. Mater.* **2014,** 26 (22), 6542-6556.

130. Ando, S.; Nishida, J.-i.; Tada, H.; Inoue, Y.; Tokito, S.; Yamashita, Y. High Performance n-Type Organic Field-Effect Transistors Based on π-Electronic Systems with Trifluoromethylphenyl Groups. *J. Am. Chem. Soc.* **2005,** 127 (15), 5336-5337.

131. Balan, B.; Vijayakumar, C.; Saeki, A.; Koizumi, Y.; Seki, S. p/n Switching of Ambipolar Bithiazole–Benzothiadiazole-Based Polymers in Photovoltaic Cells. *Macromolecules* **2012,** 45 (6), 2709-2719.

132. He, Y.; Hong, W.; Li, Y. New building blocks for π-conjugated polymer semiconductors for organic thin film transistors and photovoltaics. *J. Mater. Chem. C.* **2014,** 2 (41), 8651-8661.

133. Hong, W.; Sun, B.; Guo, C.; Yuen, J.; Li, Y.; Lu, S.; Huang, C.; Facchetti, A. Dipyrrolo[2,3-b:2′,3′-e]pyrazine-2,6(1H,5H)-dione based conjugated polymers for ambipolar organic thin-film transistors. *Chem. Commun. (Cambridge, U. K.)* **2013,** 49 (5), 484-486.

134. Chen, M. S.; Niskala, J. R.; Unruh, D. A.; Chu, C. K.; Lee, O. P.; Fréchet, J. M. J. Control of Polymer-Packing Orientation in Thin Films through Synthetic Tailoring of Backbone Coplanarity. *Chem. Mater.* **2013,** 25 (20), 4088-4096.

135. Cai, K.; Xie, J.; Zhao, D. NIR J-Aggregates of Hydroazaheptacene Tetraimides. *J. Am. Chem. Soc.* **2014,** 136 (1), 28-31.

136. Guo, C.; Quinn, J.; Sun, B.; Li, Y. An indigo-based polymer bearing thermocleavable side chains for n-type organic thin film transistors. *J. Mater. Chem. C.* **2015,** 3 (20), 5226-5232.

137. Street, R. A.; Northrup, J. E.; Salleo, A. Transport in polycrystalline polymer thin-film transistors. *Physical Review B* **2005,** 71 (16), 165202.

138. Rivnay, J.; Jimison, L. H.; Northrup, J. E.; Toney, M. F.; Noriega, R.; Lu, S.; Marks, T. J.; Facchetti, A.; Salleo, A. Large modulation of carrier transport by grain-boundary molecular packing and microstructure in organic thin films. *Nat. Mater.* **2009,** 8 (12), 952-958.

139. Salleo, A.; Kline, R. J.; DeLongchamp, D. M.; Chabinyc, M. L. Microstructural Characterization and Charge Transport in Thin Films of Conjugated Polymers. *Adv. Mater.* **2010,** 22 (34), 3812-3838.

140. Rivnay, J.; Noriega, R.; Northrup, J. E.; Kline, R. J.; Toney, M. F.; Salleo, A. Structural origin of gap states in semicrystalline polymers and the implications for charge transport. *Physical Review B* **2011,** 83 (12), 121306.

141. Rivnay, J.; Salleo, a.; Mannsfeld, S.; Miller, C.; Toney, M. Determination of Organic Semiconductor Microstructure from the Molecular to Device Scale with Quantitative X-Ray Scattering and Absorption Analyses. *Chem. Rev.* **2012,** 112, 5488.

142. Noriega, R.; Rivnay, J.; Vandewal, K.; Koch, F. P. V.; Stingelin, N.; Smith, P.; Toney, M. F.; Salleo, A. A general relationship between disorder, aggregation and charge transport in conjugated polymers. *Nat. Mater.* **2013,** 12, 1038.

143. Sirringhaus, H.; Brown, P. J.; Friend, R. H.; Nielsen, M. M.; Bechgaard, K.; Langeveld-Voss, B. M. W.; Spiering, A. J. H.; Janssen, R. A. J.; Meijer, E. W.; Herwig, P.; de Leeuw, D. M. Two-dimensional charge transport in self-organized, high-mobility conjugated polymers. *Nature* **1999,** 401 (6754), 685.

144. Sirringhaus, H. Device Physics of Solution-Processed Organic Field-Effect Transistors. *Adv. Mater.* **2005,** 17 (20), 2411-2425.

145. Rivnay, J.; Mannsfeld, S. C. B.; Miller, C. E.; Salleo, A.; Toney, M. F. Quantitative Determination of Organic Semiconductor Microstructure from the Molecular to Device Scale. *Chem. Rev.* **2012,** 112 (10), 5488-5519.

146. Noriega, R.; Rivnay, J.; Vandewal, K.; Koch, F. P. V.; Stingelin, N.; Smith, P.; Toney, M. F.; Salleo, A. A general relationship between disorder, aggregation and charge transport in conjugated polymers. *Nat. Mater.* **2013,** 12 (11), 1038-1044.

147. Vandewal, K.; Albrecht, S.; Hoke, E. T.; Graham, K. R.; Widmer, J.; Douglas, J. D.; Schubert, M.; Mateker, W. R.; Bloking, J. T.; Burkhard, G. F.; Sellinger, A.; Fréchet, J. M. J.; Amassian, A.; Riede, M. K.; McGehee, M. D.; Neher, D.; Salleo, A. Efficient charge generation by relaxed charge-transfer states at organic interfaces. *Nat. Mater.* **2014,** 13 (1), 63-68.

148. Barford, W.; Marcus, M. Perspective: Optical spectroscopy in π-conjugated polymers and how it can be used to determine multiscale polymer structures. *The Journal of Chemical Physics* **2017,** 146 (13), 130902.

149. Torricelli, F.; Ghittorelli, M.; Smits, E. C. P.; Roelofs, C. W. S.; Janssen, R. A. J.; Gelinck, G. H.; Kovács-Vajna, Z. M.; Cantatore, E. Ambipolar Organic Tri-Gate Transistor for Low-Power Complementary Electronics. *Adv. Mater.* **2015,** 28 (2), n/a-n/a.

150. Zhou, X.; Ai, N.; Guo, Z. H.; Zhuang, F. D.; Jiang, Y. S.; Wang, J. Y.; Pei, J. Balanced Ambipolar Organic Thin-Film Transistors Operated under Ambient Conditions: Role of the Donor Moiety in BDOPV-Based Conjugated Copolymers. *Chem. Mater.* **2015,** 27 (5), 1815-1820.

151. Hammock, M. L.; Chortos, A.; Tee, B. C. K.; Tok, J. B. H.; Bao, Z. 25th Anniversary Article: The Evolution of Electronic Skin (E-Skin): A Brief History, Design Considerations, and Recent Progress. *Adv. Mater.* **2013,** 25 (42), 5997-6038.

152. Benight, S. J.; Wang, C.; Tok, J. B. H.; Bao, Z. Stretchable and self-healing polymers and devices for electronic skin. *Prog. Polym. Sci.* **2013,** 38 (12), 1961-1977.

153. Guo, C. Synthesis and Performance Characterization of Polymer Semiconductors for Organic Thin Film Transistors. University of Waterloo, 2015.

154. Ebnesajjad, S., 15 - Applications in Microelectronics Industry. In *Melt Processible Fluoroplastics*, Ebnesajjad, S., Ed. William Andrew Publishing: Norwich, NY, 2003; pp 509-530.

155. Bent, S. F., Chapter 5 - Semiconductor Surface Chemistry. In *Chemical Bonding at Surfaces and Interfaces*, Nilsson, A., Pettersson, L. G. M., Nørskov, J. K., Eds. Elsevier: Amsterdam, 2008; pp 323-395.

156. Dechun, Z., 4 - Chemical and photophysical properties of materials for OLEDs. In *Organic Light-Emitting Diodes (OLEDs)*, Buckley, A., Ed. Woodhead Publishing: 2013; pp 114-142.

157. Bhattacharyya, B., Chapter 10 - Microdevices Fabrication for Microelectromechanical Systems and Other Microengineering Applications. In *Electrochemical Micromachining for Nanofabrication, MEMS and Nanotechnology*, Bhattacharyya, B., Ed. William Andrew Publishing: 2015; pp 185-204.

158. Ebisawa, F.; Kurokawa, T.; Nara, S. Electrical properties of polyacetylene/polysiloxane interface. *J. Appl. Phys.* **1983,** 54 (6), 3255-3259.

159. Braga, D.; Horowitz, G. High-Performance Organic Field-Effect Transistors. *Adv. Mater.* **2009,** 21 (14-15), 1473-1486.

160. Takayasu, S.; Tsuyoshi, S.; Takao, S., *Organic Field-Effect Transistors*. CRC Press: 2007; p 529-550.

161. Jia, H.; Pant, G. K.; Gross, E. K.; Wallace, R. M.; Gnade, B. E. Gate induced leakage and drain current offset in organic thin film transistors. *Organic Electronics* **2006,** 7 (1), 16-21.

162. Chen, Z.; Lee, M. J.; Shahid Ashraf, R.; Gu, Y.; Albert-Seifried, S.; Meedom Nielsen, M.; Schroeder, B.; Anthopoulos, T. D.; Heeney, M.; McCulloch, I.; Sirringhaus, H. High-Performance Ambipolar Diketopyrrolopyrrole-Thieno[3,2-b]thiophene Copolymer Field-Effect Transistors with Balanced Hole and Electron Mobilities. *Adv. Mater.* **2012,** 24 (5), 647-652.

163. Horowitz, G. Organic Field-Effect Transistors. *Adv. Mater.* **1999,** 10 (5), 365-377.

164. Di, C.-a.; Liu, Y.; Yu, G.; Zhu, D. Interface Engineering: An Effective Approach toward High-Performance Organic Field-Effect Transistors. *Acc. Chem. Res.* **2009,** 42 (10), 1573-1583.

165. Love, J. C.; Estroff, L. A.; Kriebel, J. K.; Nuzzo, R. G.; Whitesides, G. M. Self-Assembled Monolayers of Thiolates on Metals as a Form of Nanotechnology. *Chem. Rev.* **2005,** 105 (4), 1103-1170.

166. Chang, J.-F.; Sun, B.; Breiby, D. W.; Nielsen, M. M.; Sölling, T. I.; Giles, M.; McCulloch, I.; Sirringhaus, H. Enhanced Mobility of Poly(3-hexylthiophene) Transistors by Spin-Coating from High-Boiling-Point Solvents. *Chem. Mater.* **2004,** 16 (23), 4772-4776.

167. Kim, D. H.; Lee, B.-L.; Moon, H.; Kang, H. M.; Jeong, E. J.; Park, J.-I.; Han, K.-M.; Lee, S.; Yoo, B. W.; Koo, B. W.; Kim, J. Y.; Lee, W. H.; Cho, K.; Becerril, H. A.; Bao, Z. Liquid-Crystalline Semiconducting Copolymers with Intramolecular Donor−Acceptor Building Blocks for High-Stability Polymer Transistors. *J. Am. Chem. Soc.* **2009,** 131 (17), 6124-6132.

168. Um, H. A.; Shin, J.; Lee, T. W.; Cho, M. J.; Choi, D. H. Modulation of carrier mobility of diketopyrrolopyrrole and quaterthiophene containing copolymer with

self-assembled monolayers on gate dielectrics of thin film transistors. *Synth. Met.* **2013,** 184, 61-67.

169. Fu, B. DESIGN AND SYNTHESES OF HOLE AND ELECTRON TRANSPORT DONOR-ACCEPTOR POLYMERIC SEMICONDUCTORS AND THEIR APPLICATIONS TO ORGANIC FIELD-EFFECT TRANSISTORS. Ph.D. Thesis, Georgia Institute of Technology, Atlanta, Georgia, U.S.A., 2015.

170. Joseph Kline, R.; McGehee, M. D.; Toney, M. F. Highly oriented crystals at the buried interface in polythiophene thin-film transistors. *Nat. Mater.* **2006,** 5, 222.

171. Chua, L.-L.; Ho, P. K. H.; Sirringhaus, H.; Friend, R. H. High-stability ultrathin spin-on benzocyclobutene gate dielectric for polymer field-effect transistors. *Appl. Phys. Lett.* **2004,** 84 (17), 3400-3402.

172. Roberts, M. E.; Queraltó, N.; Mannsfeld, S. C. B.; Reinecke, B. N.; Knoll, W.; Bao, Z. Cross-Linked Polymer Gate Dielectric Films for Low-Voltage Organic Transistors. *Chem. Mater.* **2009,** 21 (11), 2292-2299.

173. Schwartz, G.; Tee, B. C. K.; Mei, J.; Appleton, A. L.; Kim, D. H.; Wang, H.; Bao, Z. Flexible polymer transistors with high pressure sensitivity for application in electronic skin and health monitoring. *Nature Communications* **2013,** 4, 1859.

174. Sakanoue, T.; Sirringhaus, H. Band-like temperature dependence of mobility in a solution-processed organic semiconductor. *Nat. Mater.* **2010,** 9 (9), 736.

175. Hwang, D. K.; Fuentes-Hernandez, C.; Kim, J.; Potscavage, W. J.; Kim, S.-J.; Kippelen, B. Top-Gate Organic Field-Effect Transistors with High Environmental and Operational Stability. *Adv. Mater.* **2011,** 23 (10), 1293-1298.

176. Lu, G.; Blakesley, J.; Himmelberger, S.; Pingel, P.; Frisch, J.; Lieberwirth, I.; Salzmann, I.; Oehzelt, M.; Di Pietro, R.; Salleo, A.; Koch, N.; Neher, D. Moderate doping leads to high performance of semiconductor/insulator polymer blend transistors. *Nature Communications* **2013,** 4, 1588.

177. Yoon, M.-H.; Kim, C.; Facchetti, A.; Marks, T. J. Gate Dielectric Chemical Structure−Organic Field-Effect Transistor Performance Correlations for Electron, Hole, and Ambipolar Organic Semiconductors. *J. Am. Chem. Soc.* **2006,** 128 (39), 12851-12869.

178. Kim, C.; Wang, Z.; Choi, H.-J.; Ha, Y.-G.; Facchetti, A.; Marks, T. J. Printable Cross-Linked Polymer Blend Dielectrics. Design Strategies, Synthesis, Microstructures, and Electrical Properties, with Organic Field-Effect Transistors as Testbeds. *J. Am. Chem. Soc.* **2008,** 130 (21), 6867-6878.

179. Veres, J.; Ogier, S. D.; Leeming, S. W.; Cupertino, D. C.; Mohialdin Khaffaf, S. Low-k Insulators as the Choice of Dielectrics in Organic Field-Effect Transistors. *Adv. Funct. Mater.* **2003,** 13 (3), 199-204.

180. Ortiz, R. P.; Facchetti, A.; Marks, T. J. High-k Organic, Inorganic, and Hybrid Dielectrics for Low-Voltage Organic Field-Effect Transistors. *Chem. Rev.* **2010,** 110 (1), 205-239.

181. Facchetti, A.; Yoon, M. H.; Marks, T. J. Gate Dielectrics for Organic Field-Effect Transistors: New Opportunities for Organic Electronics. *Adv. Mater.* **2005,** 17 (14), 1705-1725.

182. Kim, N.; Potscavage, W. J.; Domercq, B.; Kippelen, B.; Graham, S. A hybrid encapsulation method for organic electronics. *Appl. Phys. Lett.* **2009,** 94 (16), 163308.

183. Kim, N.; Graham, S. Development of highly flexible and ultra-low permeation rate thin-film barrier structure for organic electronics. *Thin Solid Films* **2013,** 547, 57-62.

184. Yuan, Y.; Giri, G.; Ayzner, A. L.; Zoombelt, A. P.; Mannsfeld, S. C. B.; Chen, J.; Nordlund, D.; Toney, M. F.; Huang, J.; Bao, Z. Ultra-high mobility transparent organic thin film transistors grown by an off-centre spin-coating method. *Nature Communications* **2014,** 5, 3005.

185. Kim, D. H.; Lee, D. Y.; Lee, H. S.; Lee, W. H.; Kim, Y. H.; Han, J. I.; Cho, K. High-Mobility Organic Transistors Based on Single-Crystalline Microribbons of Triisopropylsilylethynyl Pentacene via Solution-Phase Self-Assembly. *Adv. Mater.* **2007,** 19 (5), 678-682.

186. Li, H.; Tee, B. C. K.; Giri, G.; Chung, J. W.; Lee, S. Y.; Bao, Z. High-Performance Transistors and Complementary Inverters Based on Solution-Grown Aligned Organic Single-Crystals. *Adv. Mater.* **2012,** 24 (19), 2588-2591.

187. Giri, G.; Park, S.; Vosgueritchian, M.; Shulaker, M. M.; Bao, Z. High-Mobility, Aligned Crystalline Domains of TIPS-Pentacene with Metastable Polymorphs Through Lateral Confinement of Crystal Growth. *Adv. Mater.* **2013,** 26 (3), 487-493.

188. Chen, J.; Tee, C. K.; Shtein, M.; Martin, D. C.; Anthony, J. Controlled solution deposition and systematic study of charge-transport anisotropy in single crystal and single-crystal textured TIPS pentacene thin films. *Organic Electronics* **2009,** 10 (4), 696-703.

189. Verilhac, J.-M.; LeBlevennec, G.; Djurado, D.; Rieutord, F.; Chouiki, M.; Travers, J.-P.; Pron, A. Effect of macromolecular parameters and processing conditions on supramolecular organisation, morphology and electrical transport properties in thin layers of regioregular poly(3-hexylthiophene). *Synth. Met.* **2006,** 156 (11), 815-823.

190. O'Connor, B.; Kline, R. J.; Conrad, B. R.; Richter, L. J.; Gundlach, D.; Toney, M. F.; DeLongchamp, D. M. Anisotropic Structure and Charge Transport in Highly

Strain-Aligned Regioregular Poly(3-hexylthiophene). *Adv. Funct. Mater.* **2011,** 21 (19), 3697-3705.

191. Chang, M.; Choi, D.; Fu, B.; Reichmanis, E. Solvent Based Hydrogen Bonding: Impact on Poly(3-hexylthiophene) Nanoscale Morphology and Charge Transport Characteristics. *ACS Nano* **2013,** 7 (6), 5402-5413.

192. Diao, Y.; Shaw, L.; Bao, Z.; Mannsfeld, S. C. B. Morphology control strategies for solution-processed organic semiconductor thin films. *Energy Environ. Sci.* **2014,** 7 (7), 2145-2159.

193. Cho, S.; Lee, K.; Yuen, J.; Wang, G.; Moses, D.; Heeger, A. J.; Surin, M.; Lazzaroni, R. Thermal annealing-induced enhancement of the field-effect mobility of regioregular poly(3-hexylthiophene) films. *J. Appl. Phys.* **2006,** 100 (11), 114503.

194. Fu, Y.; Lin, C.; Tsai, F.-Y. High field-effect mobility from poly(3-hexylthiophene) thin-film transistors by solvent–vapor-induced reflow. *Organic Electronics* **2009,** 10 (5), 883-888.

195. Kim, D. H.; Park, Y. D.; Jang, Y.; Yang, H.; Kim, Y. H.; Han, J. I.; Moon, D. G.; Park, S.; Chang, T.; Chang, C.; Joo, M.; Ryu, C. Y.; Cho, K. Enhancement of Field-Effect Mobility Due to Surface-Mediated Molecular Ordering in Regioregular Polythiophene Thin Film Transistors. *Adv. Funct. Mater.* **2005,** 15 (1), 77-82.

196. Kline, R. J.; McGehee, M. D.; Kadnikova, E. N.; Liu, J.; Fréchet, J. M. J.; Toney, M. F. Dependence of Regioregular Poly(3-hexylthiophene) Film Morphology and Field-Effect Mobility on Molecular Weight. *Macromolecules* **2005,** 38 (8), 3312-3319.

197. Himmelberger, S.; Vandewal, K.; Fei, Z.; Heeney, M.; Salleo, A. Role of Molecular Weight Distribution on Charge Transport in Semiconducting Polymers. *Macromolecules* **2014,** 47 (20), 7151-7157.

198. Nielsen, C. B.; Holliday, S.; Chen, H.-Y.; Cryer, S. J.; McCulloch, I. Non-Fullerene Electron Acceptors for Use in Organic Solar Cells. *Acc. Chem. Res.* **2015,** 48 (11), 2803-12.

199. Yi, Z.; Ma, L.; Li, P.; Xu, L.; Zhan, X.; Qin, J.; Chen, X.; Liu, Y.; Wang, S. Enhancing the organic thin-film transistor performance of diketopyrrolopyrrole-benzodithiophene copolymers via the modification of both conjugated backbone and side chain. *Polym. Chem.* **2015,** 6 (30), 5369-5375.

200. Gao, L.; Zhang, Z. G.; Xue, L.; Min, J.; Zhang, J.; Wei, Z.; Li, Y. All-Polymer Solar Cells Based on Absorption-Complementary Polymer Donor and Acceptor with High Power Conversion Efficiency of 8.27%. *Adv. Mater.* **2016,** 28 (9), 1884-90.

201. Bijleveld, J. C.; Zoombelt, A. P.; Mathijssen, S. G. J.; Wienk, M. M.; Turbiez, M.; de Leeuw, D. M.; Janssen, R. A. J. Poly(diketopyrrolopyrrole−terthiophene) for Ambipolar Logic and Photovoltaics. *J. Am. Chem. Soc.* **2009,** 131 (46), 16616-16617.

202. Zhou, E.; Cong, J.; Wei, Q.; Tajima, K.; Yang, C.; Hashimoto, K. All-polymer solar cells from perylene diimide based copolymers: material design and phase separation control. *Angew Chem Int Ed Engl* **2011,** 50 (12), 2799-803.

203. Sonar, P.; Lim, J. P. F.; Chan, K. L. Organic non-fullerene acceptors for organic photovoltaics. *Energy Environ. Sci.* **2011,** 4 (5), 1558-1574.

204. Facchetti, A. Polymer donor-polymer acceptor (all-polymer) solar cells. *Mater. Today.* **2013,** 16 (4), 123-132.

205. Zhao, Y.; Zhao, X.; Roders, M.; Qu, G.; Diao, Y.; Ayzner, A. L.; Mei, J. Complementary Semiconducting Polymer Blends for Efficient Charge Transport. *Chem. Mater.* **2015,** 27 (20), 7164-7170.

206. Bronstein, H.; Chen, Z.; Ashraf, R. S.; Zhang, W.; Du, J.; Durrant, J. R.; Shakya Tuladhar, P.; Song, K.; Watkins, S. E.; Geerts, Y.; Wienk, M. M.; Janssen, R. A. J.; Anthopoulos, T.; Sirringhaus, H.; Heeney, M.; McCulloch, I. Thieno[3,2-b]thiophene−Diketopyrrolopyrrole-Containing Polymers for High-Performance Organic Field-Effect Transistors and Organic Photovoltaic Devices. *J. Am. Chem. Soc.* **2011,** 133 (10), 3272-3275.

207. Hendriks, K. H.; Li, W.; Heintges, G. H. L.; van Pruissen, G. W. P.; Wienk, M. M.; Janssen, R. A. J. Homocoupling Defects in Diketopyrrolopyrrole-Based Copolymers and Their Effect on Photovoltaic Performance. *J. Am. Chem. Soc.* **2014,** 136 (31), 11128-11133.

208. Chou, N.; Kim, Y.; Kim, S. A Method to Pattern Silver Nanowires Directly on Wafer-Scale PDMS Substrate and Its Applications. *ACS Appl. Mater. Interfaces* **2016,** 8 (9), 6269-76.

209. Lei, T.; Dou, J.-H.; Cao, X.-Y.; Wang, J.-Y.; Pei, J. Electron-Deficient Poly(p-phenylene vinylene) Provides Electron Mobility over 1 cm2 V–1 s–1 under Ambient Conditions. *J. Am. Chem. Soc.* **2013,** 135 (33), 12168-12171.

210. Politis, J. K.; Curtis, M. D.; Gonzalez, L.; Martin, D. C.; He, Y.; Kanicki, J. Synthesis and Characterization of Conjugated, n-Dopable, Bithiazole-Containing Polymers. *Chem. Mater.* **1998,** 10 (6), 1713-1719.

211. Yamamoto, T.; Komarudin, D.; Arai, M.; Lee, B. L.; Suganuma, H.; Asakawa, N.; Inoue, Y.; Kubota, K.; Sasaki, S.; Fukuda, T.; Matsuda, H. Extensive studies on pi-stacking of poly(3-alkylthiophene-2,5-diyl)s and poly(4-alkylthiazole-2,5-diyl)s by optical spectroscopy, NMR analysis, light scattering analysis, and X-ray crystallography. *J. Am. Chem. Soc.* **1998,** 120 (9), 2047-2058.

212. Karikomi, M.; Kitamura, C.; Tanaka, S.; Yamashita, Y. New Narrow-Bandgap Polymer Composed of Benzobis(1,2,5-thiadiazole) and Thiophenes. *J. Am. Chem. Soc.* **1995,** 117 (25), 6791-6792.

213. Lee, B.-L.; Yamamoto, T. Syntheses of New Alternating CT-Type Copolymers of Thiophene and Pyrido[3,4-b]pyrazine Units: Their Optical and Electrochemical Properties in Comparison with Similar CT Copolymers of Thiophene with Pyridine and Quinoxaline. *Macromolecules* **1999,** 32 (5), 1375-1382.

214. Li, H.; Duan, Y.; Coropceanu, V.; Bredas, J.-L. Electronic structure of the pentacene–gold interface: A density-functional theory study. *Organic Electronics* **2009,** 10 (8), 1571-1578.

215. Bredas, J.-L. Mind the gap! *Mater. Horiz.* **2014,** 1 (1), 17-19.

216. Anthony, J. E.; Facchetti, A.; Heeney, M.; Marder, S. R.; Zhan, X. n-Type Organic Semiconductors in Organic Electronics. *Adv. Mater.* **2010,** 22 (34), 3876-3892.

217. Frisch, M. J.; Trucks, G. W.; Schlegel, H. B.; Scuseria, G. E.; Robb, M. A.; Cheeseman, J. R.; Scalmani, G.; Barone, V.; Mennucci, B.; Petersson, G. A.; Nakatsuji, H.; Caricato, M.; Li, X.; Hratchian, H. P.; Izmaylov, A. F.; Bloino, J.; Zheng, G.; Sonnenberg, J. L.; Hada, M.; Ehara, M.; Toyota, K.; Fukuda, R.; Hasegawa, J.; Ishida, M.; Nakajima, T.; Honda, Y.; Kitao, O.; Nakai, H.; Vreven, T.; Montgomery Jr., J. A.; Peralta, J. E.; Ogliaro, F.; Bearpark, M. J.; Heyd, J.; Brothers, E. N.; Kudin, K. N.; Staroverov, V. N.; Kobayashi, R.; Normand, J.; Raghavachari, K.; Rendell, A. P.; Burant, J. C.; Iyengar, S. S.; Tomasi, J.; Cossi, M.; Rega, N.; Millam, N. J.; Klene, M.; Knox, J. E.; Cross, J. B.; Bakken, V.; Adamo, C.; Jaramillo, J.; Gomperts, R.; Stratmann, R. E.; Yazyev, O.; Austin, A. J.; Cammi, R.; Pomelli, C.; Ochterski, J. W.; Martin, R. L.; Morokuma, K.; Zakrzewski, V. G.; Voth, G. A.; Salvador, P.; Dannenberg, J. J.; Dapprich, S.; Daniels, A. D.; Farkas, Ö.; Foresman, J. B.; Ortiz, J. V.; Cioslowski, J.; Fox, D. J. *Gaussian 09, Revision D.01*, Gaussian, Inc.: Wallingford, CT, USA, 2013.

218. Stein, T.; Kronik, L.; Baer, R. Reliable Prediction of Charge Transfer Excitations in Molecular Complexes Using Time-Dependent Density Functional Theory. *J. Am. Chem. Soc.* **2009,** 131 (8), 2818-2820.

219. Körzdörfer, T.; Brédas, J.-L. Organic Electronic Materials: Recent Advances in the DFT Description of the Ground and Excited States Using Tuned Range-Separated Hybrid Functionals. *Acc. Chem. Res.* **2014,** 47 (11), 3284-3291.

220. Dovesi, R.; Orlando, R.; Erba, A.; Zicovich-Wilson, C. M.; Civalleri, B.; Casassa, S.; Maschio, L.; Ferrabone, M.; De La Pierre, M.; D'Arco, P.; Noël, Y.; Causà, M.; Rérat, M.; Kirtman, B. CRYSTAL14: A program for the ab initio investigation of crystalline solids. *Int. J. Quantum Chem.* **2014,** 114 (19), 1287-1317.

221. Zhao, Y.; Truhlar, D. G. The M06 suite of density functionals for main group thermochemistry, thermochemical kinetics, noncovalent interactions, excited

states, and transition elements: two new functionals and systematic testing of four M06-class functionals and 12 other functionals. *Theor. Chem. Acc.* **2008,** 120 (1), 215-241.

222. Schimka, L.; Harl, J.; Kresse, G. Improved hybrid functional for solids: The HSEsol functional. *The Journal of Chemical Physics* **2011,** 134 (2), 024116.

223. Peintinger, M. F.; Oliveira, D. V.; Bredow, T. Consistent Gaussian basis sets of triple-zeta valence with polarization quality for solid-state calculations. *J. Comput. Chem.* **2013,** 34 (6), 451-459.

224. Monkhorst, H. J.; Pack, J. D. Special points for Brillouin-zone integrations. *Phys. Rev. B* **1976,** 13 (12), 5188-5192.

225. Hsu, B. B.-Y.; Cheng, C.-M.; Luo, C.; Patel, S. N.; Zhong, C.; Sun, H.; Sherman, J.; Lee, B. H.; Ying, L.; Wang, M.; Bazan, G.; Chabinyc, M.; Brédas, J.-L.; Heeger, A. The Density of States and the Transport Effective Mass in a Highly Oriented Semiconducting Polymer: Electronic Delocalization in 1D. *Adv. Mater.* **2015,** 27 (47), 7759-7765.

226. Dovesi, R.; Orlando, R.; Erba, A.; Zicovich-Wilson, C. M.; Civalleri, B.; Casassa, S.; Maschio, L.; Ferrabone, M.; De La Pierre, M.; D'Arco, P.; Noël, Y.; Causà, M.; Rérat, M.; Kirtman, B. CRYSTAL14: A program for the ab initio investigation of crystalline solids. *Int. J. Quantum Chem.* **2014,** 114 (19), 1287-1317.

227. Hsu, B. B.-Y.; Cheng, C.-M.; Luo, C.; Patel, S. N.; Zhong, C.; Sun, H.; Sherman, J.; Lee, B. H.; Ying, L.; Wang, M.; Bazan, G.; Chabinyc, M.; Brédas, J.-L.; Heeger, A. The Density of States and the Transport Effective Mass in a Highly Oriented Semiconducting Polymer: Electronic Delocalization in 1D. *Adv. Mater.* **2015,** 27 (47), 7759-7765.

228. Stein, T.; Kronik, L.; Baer, R. Reliable Prediction of Charge Transfer Excitations in Molecular Complexes Using Time-Dependent Density Functional Theory. *J. Am. Chem. Soc.* **2009,** 131 (8), 2818-2820.

229. Körzdörfer, T.; Brédas, J.-L. Organic Electronic Materials: Recent Advances in the DFT Description of the Ground and Excited States Using Tuned Range-Separated Hybrid Functionals. *Acc. Chem. Res.* **2014,** 47 (11), 3284-3291.

230. Lei, T.; Dou, J.-H.; Cao, X.-Y.; Wang, J.-Y.; Pei, J. A BDOPV-Based Donor–Acceptor Polymer for High-Performance n-Type and Oxygen-Doped Ambipolar Field-Effect Transistors. *Adv. Mater.* **2013,** 25 (45), 6589-6593.

231. Bao, Z.; Locklin, J., *Organic Field-Effect Transistors*. CRC Press: 2007.

232. Kurosawa, T.; Chiu, Y. C.; Zhou, Y.; Gu, X. D.; Chen, W. C.; Bao, Z. A. Impact of Polystyrene Oligomer Side Chains on Naphthalene Diimide-Bithiophene

Polymers as n-Type Semiconductors for Organic Field-Effect Transistors. *Adv. Funct. Mater.* **2016,** 26 (8), 1261-1270.

233. Knopfmacher, O.; Hammock, M. L.; Appleton, A. L.; Schwartz, G.; Mei, J.; Lei, T.; Pei, J.; Bao, Z. Highly stable organic polymer field-effect transistor sensor for selective detection in the marine environment. *Nat Commun* **2014,** 5, 2954.

234. Sirringhaus, H. 25th anniversary article: organic field-effect transistors: the path beyond amorphous silicon. *Adv. Mater.* **2014,** 26 (9), 1319-35.

235. Shi, K.; Zhang, F.; Di, C. A.; Yan, T. W.; Zou, Y.; Zhou, X.; Zhu, D.; Wang, J. Y.; Pei, J. Toward High Performance n-Type Thermoelectric Materials by Rational Modification of BDPPV Backbones. *J. Am. Chem. Soc.* **2015,** 137 (22), 6979-82.

236. Lee, W.-Y.; Wu, H.-C.; Lu, C.; Naab, B. D.; Chen, W.-C.; Bao, Z. n-Type Doped Conjugated Polymer for Nonvolatile Memory. *Adv. Mater.* **2017,** 29 (16), 1605166.

237. Mirabal Rafael, A.; Vanderzwet, L.; Abuadas, S.; Emmett Michael, R.; Schipper, D. Dehydration Polymerization for Poly(hetero)arene Conjugated Polymers. *Chemistry – A European Journal* **2018,** 0 (0), 12231-12235.

238. Hernandez, V.; Lopez Navarrete, J. T. Ab initio study of torsional potentials in 2,2'-bithiophene and 3,4'- and 3,3'-dimethyl-2,2'-bithiophene as models of the backbone flexibility in polythiophene and poly(3-methylthiophene). *The Journal of Chemical Physics* **1994,** 101 (2), 1369-1377.

239. Shoaee, S.; Subramaniyan, S.; Xin, H.; Keiderling, C.; Tuladhar, P. S.; Jamieson, F.; Jenekhe, S. A.; Durrant, J. R. Charge Photogeneration for a Series of Thiazolo-Thiazole Donor Polymers Blended with the Fullerene Electron Acceptors PCBM and ICBA. *Adv. Funct. Mater.* **2013,** 23 (26), 3286-3298.

240. Mishra, S. P.; Palai, A. K.; Kumar, A.; Srivastava, R.; Kamalasanan, M. N.; Patri, M. Highly Air-Stable Thieno[3,2-b]thiophene-Thiophene-Thiazolo[5,4-d]thiazole-Based Polymers for Light-Emitting Diodes. *Macromol. Chem. Phys.* **2010,** 211 (17), 1890-1899.

241. Lee, S. K.; Cho, J. M.; Goo, Y.; Shin, W. S.; Lee, J.-C.; Lee, W.-H.; Kang, I.-N.; Shim, H.-K.; Moon, S.-J. Synthesis and characterization of a thiazolo[5,4-d]thiazole-based copolymer for high performance polymer solar cells. *Chem. Commun. (Cambridge, U. K.)* **2011,** 47 (6), 1791-1793.

242. Saaidia, A.; Saidani, M. A.; Hleli, E.; Alam, S.; Ulbricht, C.; Romdhane, S.; Ben Fredj, A.; Kästner, C.; Egbe, D. A. M.; Schubert, U. S.; Bouchriha, H.; Hoppe, H. Temperature-Tuning of Optical Properties and Molecular Aggregation in AnE-PVstat Copolymer Solution. *The Journal of Physical Chemistry C* **2018,** 122 (7), 3965-3969.

243. Kersting, R.; Lemmer, U.; Mahrt, R. F.; Leo, K.; Kurz, H.; Bässler, H.; Göbel, E. O. Femtosecond energy relaxation in \ensuremath{\pi}-conjugated polymers. *Phys. Rev. Lett.* **1993,** 70 (24), 3820-3823.

244. Hansen, W. N.; Hansen, G. J. Absolute half-cell potential: A simple direct measurement. *Phys. Rev. A* **1987,** 36 (3), 1396-1402.

245. Cardona Claudia, M.; Li, W.; Kaifer Angel, E.; Stockdale, D.; Bazan Guillermo, C. Electrochemical Considerations for Determining Absolute Frontier Orbital Energy Levels of Conjugated Polymers for Solar Cell Applications. *Adv. Mater.* **2011,** 23 (20), 2367-2371.

246. Wang, S.; Sun, H.; Erdmann, T.; Wang, G.; Fazzi, D.; Lappan, U.; Puttisong, Y.; Chen, Z.; Berggren, M.; Crispin, X.; Kiriy, A.; Voit, B.; Marks Tobin, J.; Fabiano, S.; Facchetti, A. A Chemically Doped Naphthalenediimide-Bithiazole Polymer for n-Type Organic Thermoelectrics. *Adv. Mater.* **2018,** 30 (31), 1801898.

247. M. J. Frisch, G. W. T., H. B. Schlegel, G. E. Scuseria, M. A. Robb, J. R. Cheeseman, G. Scalmani, V. Barone, G. A. Petersson, H. Nakatsuji, X. Li, M. Caricato, A. Marenich, J. Bloino, B. G. Janesko, R. Gomperts, B. Mennucci, H. P. Hratchian, J. V. Ortiz, A. F. Izmaylov, J. L. Sonnenberg, D. Williams-Young, F. Ding, F. Lipparini, F. Egidi, J. Goings, B. Peng, A. Petrone, T. Henderson, D. Ranasinghe, V. G. Zakrzewski, J. Gao, N. Rega, G. Zheng, W. Liang, M. Hada, M. Ehara, K. Toyota, R. Fukuda, J. Hasegawa, M. Ishida, T. Nakajima, Y. Honda, O. Kitao, H. Nakai, T. Vreven, K. Throssell, J. A. Montgomery, Jr., J. E. Peralta, F. Ogliaro, M. Bearpark, J. J. Heyd, E. Brothers, K. N. Kudin, V. N. Staroverov, T. Keith, R. Kobayashi, J. Normand, K. Raghavachari, A. Rendell, J. C. Burant, S. S. Iyengar, J. Tomasi, M. Cossi, J. M. Millam, M. Klene, C. Adamo, R. Cammi, J. W. Ochterski, R. L. Martin, K. Morokuma, O. Farkas, J. B. Foresman, and D. J. Fox *Gaussian 09, revision D. 01*, Gaussian, Inc., Wallingford CT: 2009.

248. Fazzi, D.; Caironi, M. Multi-length-scale relationships between the polymer molecular structure and charge transport: the case of poly-naphthalene diimide bithiophene. *Phys. Chem. Chem. Phys.* **2015,** 17 (14), 8573-8590.

249. Fazzi, D.; Caironi, M.; Castiglioni, C. Quantum-Chemical Insights into the Prediction of Charge Transport Parameters for a Naphthalenetetracarboxydiimide-Based Copolymer with Enhanced Electron Mobility. *J. Am. Chem. Soc.* **2011,** 133 (47), 19056-19059.

250. Scalmani, G.; Frisch, M. J. Continuous surface charge polarizable continuum models of solvation. I. General formalism. *J. Chem. Phys.* **2010,** 132 (11), 114110.

251. Pandey, L.; Doiron, C.; Sears, J. S.; Bredas, J.-L. Lowest excited states and optical absorption spectra of donor-acceptor copolymers for organic photovoltaics: a new picture emerging from tuned long-range corrected density functionals. *Phys. Chem. Chem. Phys.* **2012,** 14 (41), 14243-14248.

252. Lee, S.; Koo, B.; Shin, J.; Lee, E.; Park, H.; Kim, H. Effects of hydroxyl groups in polymeric dielectrics on organic transistor performance. *Appl. Phys. Lett.* **2006,** 88 (16), 162109.

253. Shaw, L.; Hayoz, P.; Diao, Y.; Reinspach, J. A.; To, J. W.; Toney, M. F.; Weitz, R. T.; Bao, Z. Direct Uniaxial Alignment of a Donor-Acceptor Semiconducting Polymer Using Single-Step Solution Shearing. *ACS Appl. Mater. Interfaces* **2016,** 8 (14), 9285-96.

254. Chua, L.-L.; Zaumseil, J.; Chang, J.-F.; Ou, E. C. W.; Ho, P. K. H.; Sirringhaus, H.; Friend, R. H. General observation of n-type field-effect behaviour in organic semiconductors. *Nature* **2005,** 434 (7030), 194.

255. Park, H.; Kwon, J.; Kang, B.; Kim, W.; Kim, Y.-H.; Cho, K.; Jung, S. Control of Concentration of Nonhydrogen-Bonded Hydroxyl Groups in Polymer Dielectrics for Organic Field-Effect Transistors with Operational Stability. *ACS Appl. Mater. Interfaces* **2018,** 10 (28), 24055-24063.

256. Zhang, G. Y.; Hui, H. Y.; Chu, P. H.; Yuan, Z. B.; Chang, R.; Risteen, B.; Yang, H.; Reichmanis, E. From Staple Food to Flexible Substrate to Electronics: Rice as a Biocompatible Precursor for Flexible Electronic Components. *Chem. Mater.* **2016,** 28 (23), 8475-8479.

257. Kleinhenz, N.; Persson, N.; Xue, Z. Z.; Chu, P. H.; Wang, G.; Yuan, Z. B.; McBride, M. A.; Choi, D.; Grover, M. A.; Reichmanis, E. Ordering of Poly(3-hexylthiophene) in Solutions and Films: Effects of Fiber Length and Grain Boundaries on Anisotropy and Mobility. *Chem. Mater.* **2016,** 28 (11), 3905-3913.

258. Wang, G.; Chu, P. H.; Fu, B.; He, Z.; Kleinhenz, N.; Yuan, Z.; Mao, Y.; Wang, H.; Reichmanis, E. Conjugated Polymer Alignment: Synergisms Derived from Microfluidic Shear Design and UV Irradiation. *ACS Appl. Mater. Interfaces* **2016,** 8 (37), 24761-72.

259. Fukuda, K.; Takeda, Y.; Mizukami, M.; Kumaki, D.; Tokito, S. Fully solution-processed flexible organic thin film transistor arrays with high mobility and exceptional uniformity. *Sci Rep* **2014,** 4, 3947.

260. Ito, Y.; Virkar, A. A.; Mannsfeld, S.; Oh, J. H.; Toney, M.; Locklin, J.; Bao, Z. Crystalline ultrasmooth self-assembled monolayers of alkylsilanes for organic field-effect transistors. *J. Am. Chem. Soc.* **2009,** 131 (26), 9396-404.

261. Yan, Y.; Huang, L. B.; Zhou, Y.; Han, S. T.; Zhou, L.; Sun, Q.; Zhuang, J.; Peng, H.; Yan, H.; Roy, V. A. Surface Decoration on Polymeric Gate Dielectrics for Flexible Organic Field-Effect Transistors via Hydroxylation and Subsequent Monolayer Self-Assembly. *ACS Appl. Mater. Interfaces* **2015,** 7 (42), 23464-71.

262. Tiwari, S. P.; Knauer, K. A.; Dindar, A.; Kippelen, B. Performance comparison of pentacene organic field-effect transistors with SiO2 modified with

octyltrichlorosilane or octadecyltrichlorosilane. *Organic Electronics* **2012,** 13 (1), 18-22.

263. Lim, S. C.; Kim, S. H.; Lee, J. H.; Kim, M. K.; Kim, D. J.; Zyung, T. Surface-treatment effects on organic thin-film transistors. *Synth. Met.* **2005,** 148 (1), 75-79.

264. Jimison, L. H.; Salleo, A.; Chabinyc, M. L.; Bernstein, D. P.; Toney, M. F. Correlating the microstructure of thin films of poly[5,5-bis(3-dodecyl-2-thienyl)-2,2-bithiophene] with charge transport: Effect of dielectric surface energy and thermal annealing. *Physical Review B* **2008,** 78 (12), 125319.

265. Meredig, B.; Salleo, A.; Gee, R. Ordering of Poly(3-hexylthiophene) Nanocrystallites on the Basis of Substrate Surface Energy. *ACS Nano* **2009,** 3 (10), 2881-2886.

266. Huang, L.; Wang, G.; Zhou, W.; Fu, B.; Cheng, X.; Zhang, L.; Yuan, Z.; Xiong, S.; Zhang, L.; Xie, Y.; Zhang, A.; Zhang, Y.; Ma, W.; Li, W.; Zhou, Y.; Reichmanis, E.; Chen, Y. Vertical Stratification Engineering for Organic Bulk-Heterojunction Devices. *ACS Nano* **2018,** 12 (5), 4440-4452.

267. Chang, J. F.; Sun, B. Q.; Breiby, D. W.; Nielsen, M. M.; Solling, T. I.; Giles, M.; McCulloch, I.; Sirringhaus, H. Enhanced mobility of poly(3-hexylthiophene) transistors by spin-coating from high-boiling-point solvents. *Chem. Mater.* **2004,** 16 (23), 4772-4776.

268. Umeda, T.; Kumaki, D.; Tokito, S. Surface-energy-dependent field-effect mobilities up to 1 cm2/V s for polymer thin-film transistor. *J. Appl. Phys.* **2009,** 105 (2), 024516.

269. Yang, S. Y.; Shin, K.; Park, C. E. The Effect of Gate-Dielectric Surface Energy on Pentacene Morphology and Organic Field-Effect Transistor Characteristics. *Adv. Funct. Mater.* **2005,** 15 (11), 1806-1814.

270. Cheng, X.; Noh, Y.-Y.; Wang, J.; Tello, M.; Frisch, J.; Blum, R.-P.; Vollmer, A.; Rabe, J. P.; Koch, N.; Sirringhaus, H. Controlling Electron and Hole Charge Injection in Ambipolar Organic Field-Effect Transistors by Self-Assembled Monolayers. *Adv. Funct. Mater.* **2009,** 19 (15), 2407-2415.

271. Yuan, Z.; Buckley, C.; Thomas, S.; Zhang, G.; Bargigia, I.; Wang, G.; Fu, B.; Silva, C.; Brédas, J.-L.; Reichmanis, E. A Thiazole–Naphthalene Diimide Based n-Channel Donor–Acceptor Conjugated Polymer. *Macromolecules* **2018,** 51 (18), 7320-7328.

272. DeLongchamp, D. M.; Kline, R. J.; Fischer, D. A.; Richter, L. J.; Toney, M. F. Molecular characterization of organic electronic films. *Adv. Mater.* **2011,** 23 (3), 319-37.

273. Diao, Y.; Tee, B. C. K.; Giri, G.; Xu, J.; Kim, D. H.; Becerril, H. A.; Stoltenberg, R. M.; Lee, T. H.; Xue, G.; Mannsfeld, S. C. B.; Bao, Z. Solution coating of large-area organic semiconductor thin films with aligned single-crystalline domains. *Nat. Mater.* **2013,** 12 (7), 665-671.

274. Diao, Y.; Shaw, L.; Mannsfeld, S. C. B. Morphology Control Strategies for Solution- Processed Organic Semiconductor Thin Fi Lms. *Energy Environ. Sci.* **2014,** 7, 2145.

275. Wang, S.; Fabiano, S.; Himmelberger, S.; Puzinas, S.; Crispin, X.; Salleo, A.; Berggren, M. Experimental evidence that short-range intermolecular aggregation is sufficient for efficient charge transport in conjugated polymers. *Proceedings of the National Academy of Sciences* **2015,** 112 (34), 10599.

276. Nishizawa, T.; Lim, H. K.; Tajima, K.; Hashimoto, K. Highly uniaxial orientation in oligo(p-phenylenevinylene) films induced during wet-coating process. *J. Am. Chem. Soc.* **2009,** 131 (7), 2464-5.

277. Schroeder, C. M. Observation of Polymer Conformation Hysteresis in Extensional Flow. *Science* **2003,** 301 (5639), 1515.

278. McQuade, D. T.; Pullen, A. E.; Swager, T. M. Conjugated Polymer-Based Chemical Sensors. *Chem. Rev.* **2000,** 100 (7), 2537-2574.

279. Hussain, S.; De, S.; Iyer, P. K. Thiazole-Containing Conjugated Polymer as a Visual and Fluorometric Sensor for Iodide and Mercury. *ACS Appl. Mater. Interfaces* **2013,** 5 (6), 2234-2240.

280. Helal, A.; Kim, H.-S. Thiazole-based chemosensor: synthesis and ratiometric fluorescence sensing of zinc. *Tetrahedron Lett.* **2009,** 50 (39), 5510-5515.

281. Helal, A.; Kim, S. H.; Kim, H.-S. Thiazole sulfonamide based ratiometric fluorescent chemosensor with a large spectral shift for zinc sensing. *Tetrahedron* **2010,** 66 (52), 9925-9932.

282. Hanafi-Bagby, D.; Piunno, P. A. E.; Wust, C. C.; Krull, U. J. Concentration dependence of a thiazole orange derivative that is used to determine nucleic acid hybridization by an optical biosensor. *Anal. Chim. Acta* **2000,** 411 (1), 19-30.

283. Black, H. T.; Pelse, I.; Wolfe, R. M. W.; Reynolds, J. R. Halochromism and protonation-induced assembly of a benzo[g]indolo[2,3-b]quinoxaline derivative. *Chem. Commun. (Cambridge, U. K.)* **2016,** 52 (87), 12877-12880.

284. Takimiya, K.; Osaka, I.; Nakano, M. π-Building Blocks for Organic Electronics: Revaluation of "Inductive" and "Resonance" Effects of π-Electron Deficient Units. *Chem. Mater.* **2014,** 26 (1), 587-593.

285. Blight, B. A.; Hunter, C. A.; Leigh, D. A.; McNab, H.; Thomson, P. I. T. An AAAA–DDDD quadruple hydrogen-bond array. *Nature Chem.* **2011,** 3, 244.

286. Schmuck, C.; Wienand, W. Self-Complementary Quadruple Hydrogen-Bonding Motifs as a Functional Principle: From Dimeric Supramolecules to Supramolecular Polymers. *Angewandte Chemie International Edition* **2001,** 40 (23), 4363-4369.

287. Luo, X.-Z.; Jia, X.-J.; Deng, J.-H.; Zhong, J.-L.; Liu, H.-J.; Wang, K.-J.; Zhong, D.-C. A Microporous Hydrogen-Bonded Organic Framework: Exceptional Stability and Highly Selective Adsorption of Gas and Liquid. *J. Am. Chem. Soc.* **2013,** 135 (32), 11684-11687.

288. Li, W.; An, Y.; Wienk, M. M.; Janssen, R. A. J. Polymer-polymer solar cells with a near-infrared spectral response. *Journal of Materials Chemistry A* **2015,** 3 (13), 6756-6760.

289. Acetonitrile with Silver nitrate, Potassium nitrate and Sodium nitrate. https://srdata.nist.gov/solubility/sol_detail.aspx?sysID=78_34 Access date

290. Yao, Z.; Hu, X.; Huang, B.; Zhang, L.; Liu, L.; Zhao, Y.; Wu, H.-C. Halochromism of a Polythiophene Derivative Induced by Conformational Changes and Its Sensing Application of Carbon Dioxide. *ACS Appl. Mater. Interfaces* **2013,** 5 (12), 5783-5787.

291. McNaught, A. D.; Wilkinson, A., *IUPAC. Compendium of Chemical Terminology, 2nd ed. (the "Gold Book")*. Blackwell Scientific Publications: Oxford, 1997; Vol. 79.

292. Li, S.; Ye, L.; Zhao, W.; Zhang, S.; Mukherjee, S.; Ade, H.; Hou, J. Energy-Level Modulation of Small-Molecule Electron Acceptors to Achieve over 12% Efficiency in Polymer Solar Cells. *Adv. Mater.* **2016,** 28 (42), 9423-9429.

293. Liu, X.; Li, X.; Li, Y.; Song, C.; Zhu, L.; Zhang, W.; Wang, H.-Q.; Fang, J. High-Performance Polymer Solar Cells with PCE of 10.42% via Al-Doped ZnO Cathode Interlayer. *Adv. Mater.* **2016,** 28 (34), 7405-7412.

294. Zhao, W.; Qian, D.; Zhang, S.; Li, S.; Inganäs, O.; Gao, F.; Hou, J. Fullerene-Free Polymer Solar Cells with over 11% Efficiency and Excellent Thermal Stability. *Adv. Mater.* **2016,** 28 (23), 4734-4739.

295. Zhao, W.; Li, S.; Yao, H.; Zhang, S.; Zhang, Y.; Yang, B.; Hou, J. Molecular Optimization Enables over 13% Efficiency in Organic Solar Cells. *J. Am. Chem. Soc.* **2017,** 139 (21), 7148-7151.

296. Wang, Q.; Zhang, S.; Xu, B.; Li, S.; Yang, B.; Yuan, W.; Hou, J. Efficient Fullerene-Free Polymer Solar Cells Based on Alkylthio Substituted Conjugated Polymers. *The Journal of Physical Chemistry C* **2017,** 121 (9), 4825-4833.

297. Sun, C.; Pan, F.; Bin, H.; Zhang, J.; Xue, L.; Qiu, B.; Wei, Z.; Zhang, Z.-G.; Li, Y. A low cost and high performance polymer donor material for polymer solar cells. *Nature Communications* **2018,** 9 (1), 743.

298. Hong, X.; Tyson, J. C.; Middlecoff, J. S.; Collard, D. M. *Macromolecules* **1999,** 32, 4232.

299. Hong, X. M.; Collard, D. M. *Macromolecules* **2000,** 33, 6916.

300. Hong, X. M.; Tyson, J. C.; Collard, D. M. *Macromolecules* **2000,** 33, 3502.

301. Middlecoff, J. S.; Collard, D. M. *Synth. Met.* **1997,** 84, 221.

302. Wang, B.; Watt, S.; Hong, M.; Domercq, B.; Sun, R.; Kippelen, B.; Collard, D. M. *Macromolecules* **2008,** 41, 5156.

303. Geng, Y.; Wei, Q.; Hashimoto, K.; Tajima, K. *Chem. Mater.* **2011,** 23, 4257.

304. Hassan, J.; Lavenot, L.; Gozzi, C.; Lemaire, M. A convenient catalytic route to symmetrical functionalized bithiophenes. *Tetrahedron Lett.* **1999,** 40 (5), 857-858.